ISSN 1068-3755, Surface Engineering and Applied Electrochemistry, 2010, Vol. 46, No. 6, pp. 535–537. © Allerton Press, Inc., 2010.

ELECTRICAL PRECISION TREATMENT OF MATERIALS

The Impact of High Energy Ion Irradiation upon CO Gas Sensitivity of Nanostructured GaN Epilayers[1]

O. S. Volciuc[a, b], V. Popa[a, b], I. M. Tiginyanu[b, c], V. A. Skuratov[d], M. Cho[a], and D. Pavlidis[a]

[a] *Department of High-Frequency Electronics, Technical University Darmstadt, Darmstadt, Merckstr. 25, 64283 Darmstadt, Germany*

[b] *National Center for Materials Study and Testing, Technical University of Moldova, Stefan cel Mare 168, MD-2004 Chisinau, Republic of Moldova*

[c] *Laboratory of Nanotechnology, Institute of Electronic Engineering and Nanotechnologies, Academy 3/3, MD-2028 Chisinau, Republic of Moldova*

[d] *Flerov Laboratory of Nuclear Reactions, Joint Institute for Nuclear Research, ul. Joliot Curie 6, Dubna, Moscow oblast, 141980 Russia*

e-mail: lesichin@yahoo.com

Received May 10, 2010

Abstract—Photoelectrochemically nanostructured GaN epilayers were found to exhibit good sensitivity towards CO in the temperature range from 180 to 280°C. We show that subjection of nanostructured GaN samples to 166 MeV Xe^{+23} ion irradiation causes considerable reduction of the gas sensitivity, while post-irradiation rapid thermal annealing results in sensitivity restoration, the effect being dependent upon the dose of irradiation and annealing temperature. A 50% restoration of the relative sensitivity is demonstrated after rapid thermal annealing for 1 min at 800°C in samples irradiated by Xe^{+23} ions at a dose of 10^{12} cm^{-2}.

DOI: 10.3103/S1068375510060013

INTRODUCTION

GaN is a high temperature material with excellent potential for use in various fields including high power electronics, light emitting devices, and sensors. It exhibits pronounced chemical stability and radiation hardness, the latter property being considerably enhanced by nanostructuring of the compound by means of photoelectrochemical (PEC) etching techniques [1]. Recently we found that nanostructuring is an effective tool for improving the sensitivity and selectivity of GaN-based gas sensors [2]. This paper reports the investigation of the influence of high energy heavy ion irradiation and subsequent annealing on CO gas sensitivity of photoelectrochemically nanostructured GaN epilayers.

EXPERIMENTAL DETAILS

The unintentionally doped GaN layers used in our experiments were grown by low-pressure metalorganic chemical-vapor deposition (MOCVD) on (0001) *c*-plane sapphire substrates. The thickness of the layers was 2.7 μm and the concentration of free electrons was of about 10^{17} cm^{-3}. Ti/Au ohmic contacts of concentric annular design were deposited by lift-off on the GaN epilayers. Subsequently the samples were subjected to PEC etching in 0.1 M of KOH solution for 20 min at room temperature under illumination of a 350 W Hg lamp focused on a spot of 5 mm in diameter. The obtained morphology represents a uniform distribution of conical nanostructures, as illustrated in Fig. 1. The origin of these nanostructures is related to threading dislocations inherent to GaN epilayers grown on lattice-mismatched substrates [3]. The electrochemically treated samples were irradiated at room temperature by 166 MeV Xe^{+23} ions at doses 10^{10}, 10^{11} and 10^{12} cm^{-2}. The irradiation was carried out on the IC-100 cyclotron at the Joint Institute for Nuclear Research in Dubna, Russia. After ion irradiation and preliminary gas sensitivity exploration, the GaN samples were subjected to rapid thermal annealing in N_2 atmosphere for 1 min. For the gas response investigation the samples were mounted in a cell where the CO gas concentration was varied from 200 to 2000 ppm, whereas the sample temperature was increased from 180 to 280°C.

RESULTS AND DISCUSSION

The relative sensitivity S was calculated using the equation:

$$S = \frac{R_{N_2} - R_{CO}}{R_{N_2}} \times 100\%,$$

[1] The article is published in the original.

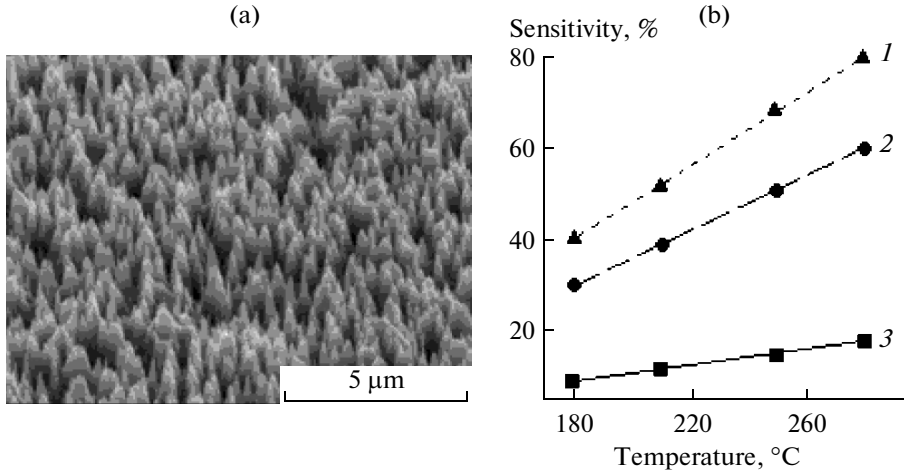

Fig. 1. The morphology of PEC nanostructured GaN and gas response towards 200, 1000 and 2000 ppm of CO before Xe^{+23} ion irradiation. (*1*) 2000 ppm CO; (*2*) 1000 ppm CO; (*3*) 200 ppm CO.

where R_{N_2} is the electrical resistance in nitrogen as a carrier gas, while R_{CO} is the resistance in CO gas environment.

The sensitivity of PEC etched GaN layers to CO concentration was found to be linear before ion irradiation. The gas sensitivity as a function of sensor temperature is illustrated in Fig. 1. The sensor response time was in the range of 2–3 s, whereas the recovery time did not exceed 10 s at 280°C.

After ion irradiation, the gas sensitivity was reduced to 17% at the dose of 10^{10} cm^{-2}, and even to 6% for the samples subjected to ion irradiation at the dose of 10 cm^{-2} (Fig. 2). This corresponds to the diminution of the sensitivity by at least ten times in comparison with the sensitivity of non-irradiated samples (Fig. 1). The drastic reduction of the sensitivity is expected to be caused by the large number of lattice defects induced by ion irradiation in the sensitive layer of GaN which is located at the base of conical structures.

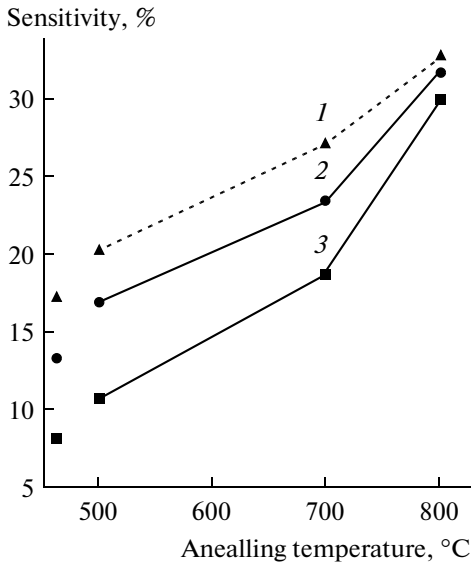

Fig. 2. The gas response of PEC nanostructured GaN toward 1000 ppm of CO for 3 doses of Xe irradiation. The initial three points represents data for the samples before annealing. (*1*) Dose 10^{10}; (*2*) Dose 10^{11}; (*3*) Dose 10^{12} cm^{-2}; CO = 1000 ppm; T_s = 280°C.

An effective method for curing the defects induced by high energy ion irradiation is thermal annealing [4]. The annealing-induced restoration of the crystal lattice is particularly effective for nanostructured semiconductor materials. The results of our investigation prove to confirm this trend. From the data illustrated in Fig. 2 it can be seen that for the highest dose of 10^{12} cm^{-2} the rapid thermal annealing at 800°C leads to 50% restoration of the sensitivity parameter in comparison with the non-irradiated samples.

The high energy Xe irradiation influences not only the sensitivity parameter, but also the recovery time of the gas sensor. In our case, the response time was in the range of 2–3 s before and after 10^{12} cm^{-2} Xe irradiation, while the recovery time was found to be in the range of 35–36 s after this high dose irradiation and of about 22 s after subsequent rapid thermal annealing at 800°C (Fig. 3).

CONCLUSIONS

Host defects created in nanostructured GaN epilayers by high energy Xe^{+23} ion irradiation lead to considerable deterioration of the CO gas sensitivity which is caused probably by irradiation-induced changes in the surface properties of GaN nanostructures. It should be noted that the mechanism of high energy particle interaction with nanostructured GaN require

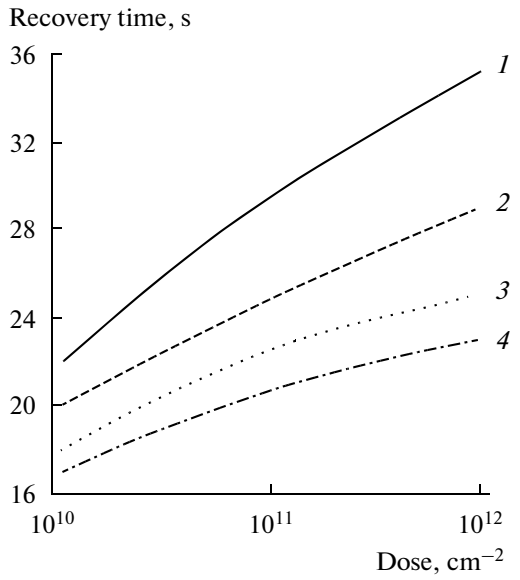

Fig. 3. The influence of Xe irradiation and rapid thermal annealing on recovery time of the nanostructured GaN based gas sensor. (*1*) after Xe irradiation; (*2*) after tr. an. 500°C; (*3*) after tr. an. 700°C; (*4*) after tr. an. 800°C; CO = 1000 ppm.

further investigation since the observed increase in the conductivity of these layer after irradiation could involve different specifics. Nevertheless, the results presented in this report are promising from the point of view of potential applications of nanostructured GaN in gas sensor electronics operating in high energy ion irradiation environment.

ACKNOWLEDGMENTS

One of the authors (O. Volciuc) would like to thank the NATO Science for Peace and Security Programme for the financial support under Reintegration grant no. 983328. V. Popa acknowledges the Ale[ander von Humboldt Foundation support. The financial support from the Supreme Council for Research and Technological Development of Moldova is also acknowledged.

REFERENCES

1. Ursaki, V.V., Tiginyanu, I.M., Volciuc, O., Popa, V., Skuratov, V.A., and Morkoç, H., Nanostructuring Induced Enhancement of Radiation Hardness in GaN Epilayers, *Appl. Phys. Lett.*, 2007, no. 90, p. 161 908.
2. Popa, V., Tiginyanu, I.M., Ursaki, V.V., Volciuc, O., and Morkoç, H., A GaN-Based Two-Sensor Array for Methane Detection in an Ethanol Environment, *Semicond. Sci. Technol.*, 2006, no. 21, p. 1518.
3. Youtsey, C., Romano, L.T., Molnar, R.J., and Adesida, I., Rapid Evaluation of Dislocation Densities in n-Type GaN Films Using Photoenhanced Wet Etching, *Appl. Phys. Lett.,* 1999, no. 74, p. 3537.
4. Pan, Z., Li, L.H., Zhang, W., Lin, Y.W., Wu, R.H., and Ge, W., Effect of Rapid Thermal Annealing on GaInNAs/GaAs Quantum Wells Grown by Plasma-Assisted Molecular-Beam Epitaxy, *Appl. Phys. Lett.*, 2000, no. 77, p. 1280.

ISSN 1068-3755, Surface Engineering and Applied Electrochemistry, 2010, Vol. 46, No. 6, pp. 538–546. © Allerton Press, Inc., 2010.
Original Russian Text © N.I. Tsyntsaru, Zh.I. Bobanova, D.M. Kroitoru, V.F. Cheban, G.I. Poshtaru, A.I. Dikusar, 2010, published in Elektronnaya Obrabotka Materialov, 2010, No. 6, pp. 8–16.

ELECTRICAL PRECISION TREATMENT OF MATERIALS

Effect of a Multilayer Structure and Lubrication on the Tribological Properties of Coatings of Fe–W Alloys

N. I. Tsyntsaru[a], Zh. I. Bobanova[a], D. M. Kroitoru[a], V. F. Cheban[b], G. I. Poshtaru[b], and A. I. Dikusar[a]

[a] *Institute of Applied Physics, Academy of Sciences of Moldova, ul. Akademiei 5, Chisinau, MD-28 Republic of Moldova*

[b] *Technical University of Moldova, bul. Stefan cel Mare 180, Chisinau, MD-2009, Republic of Moldova*

e-mail: ashra_nt@yahoo.com

Received April 21, 2010

Abstract—The methods for expanding the use of nanocrystalline electrolytic Fe–W alloys by creating a multilayer structure and using oil lubrication were studied. It was shown that lubricants can reduce the coefficient of friction and oxygen penetration into the sliding pairs, thus enhancing the wear resistance behaviour of Fe– W coatings as compared to that at dry friction, when the surface tribo-oxidation dominates. The electrodeposition of multilayer Fe–W/Cu coatings from a single bath was shown to be feasible. The tribological and mechanical properties of such coatings were investigated. The multilayer structure was found to improve the wear resistance characteristics of the coatings even at dry friction and at a relatively high normal load of 10 N.

DOI: 10.3103/S1068375510060025

INTRODUCTION

The induced codeposition of metals of the iron group with refractory metals (W and Mo) [1–3] from citrate solutions can be used as an effective method for obtaining coatings that have improved corrosion and tribological characteristics [4–8]. Recently, such coatings have been regarded to be an alternative to electrolytic chromium coatings owning to the fact that the ecological conditions of their obtainment are safer as compared to those of electrolytic chromium from toxic electrolytes [9].

Such coatings are primarily amorphous (nanocrystalline) [3, 10–14], which is a peculiarity of Fe–W alloys. Their mechanical properties at deposition from various electrolytes in the range of current densities of 10–350 mA/cm^2 and deposition temperatures of 40–90°C [3, 7, 9, 10, 14] were studied previously. Maximum values of the microhardness were obtained for the coatings from a citrate-ammonia electrolyte deposited at 70°C.

Materials known as multilayer coatings have also been an object of intensive studies lately. Such materials, which consist of alternating nanoscale layers of various metals and alloys, have improved physicomechanical, optical, electric, magnetic, and magnetooptical properties as compared with the traditional alloys [15–20]. Multilayer coatings of micrometric and nanometric sizes [23–28] may be produced by electrodeposition.

This study is aimed at a comparative examination of the mechanical and tribological properties of coatings made of iron-tunglten alloys and chromium at their friction with a lubricant, and Fe–W/Cu coatings at dry friction.

EXPERIMENTAL

The Fe–W and Fe–W/Cu alloys were deposited from electrolytes A and B.

(A) The electrodeposition of Fe–W coatings was performed from an electrolyte of the following composition, (g/l): iron sulfate $FeSO_4 \cdot 7H_2O$)—55; sodium wolframate ($Na_2WO_4 \cdot 2H_2O$)—132; sodium citrate ($Na_3C_6H_5O_7$)—112; citric acid ($C_6H_8O_7$)—33. The pH of the obtained solution was adjust to 7.6–7.8 using ammonia. The current density was 1–5 A/dm^2.

(B) The electrodeposition of the Fe–W/Cu coatings was performed from a single bath (electrolyte A) with the addition of copper sulfate ($CuSO_4 \cdot 5H_2O$) with a concentration less (by weight) by 100 times than that of iron sulfate. The pH of the obtained solution was adjust to a value of 7. The deposition was carried out from a cell with unseparated anode and cathode spaces under galvanostatic conditions at 70°C. A stainless steel plate served as the anode. The thickness of the coatings varied in the range of ~8–15 μm depending on the current density of the deposition.

The Fe–W and Fe–W/Cu coatings were deposited onto substrates of two types. In order to study the mechanical and triblogical characteristics, the electrodeposition of the coatings was performed on mechanically polished St3 steel. For the polarization measurements, copper electrodes were used as the substrate. The substrate was degreased in an ultrasonic bath with acetone followed by degreasing in water with

a soft detergent and then rinsed prior to the electrodeposition. After that, the substrate was applied to a nickel underlayer from a nickel-plating electrolyte that contained $NiCl_2 \cdot 6H_2O$ 240 g/l + HCl 80 g/l for 1 min.

Polarization curves were obtained from the B electrolyte in a three-electrode cell with an unseparated anode and cathode space on a Parstat 2273 potentiostat. A saturated silver-chloride electrode served as the reference electrode in relation to which the potential values were measured. The polarization curves were read at a potential sweep of 2 mV/s on a copper wire cathode. On the basis of the obtained polarization curves (Fig. 1), the optimal currents of the deposition for copper were also calculated for the Fe–W alloys from the limiting current of the diffusion. The polarization curve of the deposition was used to experimentally select a galvanostatic mode of the deposition. The electrodepositon of the multilayer coatings was performed in the pulse-galvanostatic mode (table). In all of the experiments, the current density in the electrodeposition of the alloys and copper was constant. After the period of the electrodeposition of the copper (t_{Cu}) and the alloy (t_{FeW}), there was a pause (t_{pause}) (Fig. 2, table).

The roughness of the surfaces of the deposited coatings was studied using (WYKO NT 3300) noncontact white light interferometry. The same methods were applied for the determination of the extent of wear volume after fretting tests on the coatings. The hardnesss was defined on a Nano-Hardness Tester, CSM.

Testing of the Coatings at Dry Friction

The friction and wear of the electrolytic coatings that were deposited on the St3 steel were estimated based on the dry bi-directional ball-on-flat sliding tests (fretting mode 1). The electroplated multilayer coatings were tested under the following conditions: the normal force was 10 N, the amplitude of the displacement of the counterbody was 200 μm, the frequency of the reciprocal motion was 5 Hz, and the number of cycles was 50000. The coatings were exposed to friction at oscillation against a fixed counterbody, which was a 10-mm-diameter corundum ball with an elasticity modulus of 300 GPa. All of the tests were performed at an environmental temperature of 23 ± 2°C and 50% relative humidity. The coatings were prepared for the friction tests: they were degreased in acetone and ethanol and dried. After the testing, the coatings were cleansed in an ultrasonic bath with ethanol to remove wear debris prior to examining the wear profiles.

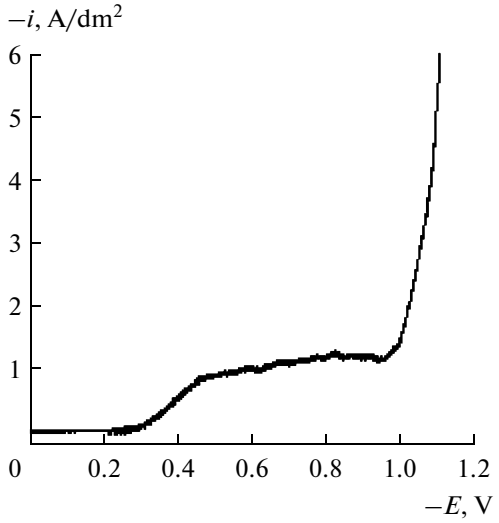

Fig. 1. Polarization curve of the electrodeposition of the Fe–W/Cu alloy that was obtained on a plate electrode from electrolyte B.

Testing the Coatings for Wear Resistance in the Presence of Oils

The tests were performed on an MVPD-1KPI laboratory facility according to the methods of [29]. The wear test conditions are: upper immobile cylindrical specimen (of 10.04 mm diameter with a 30-mm-long working part) coated with Fe–W on the flat surface of

Conditions of the electrodeposition and the roughness of the multilayer coatings

Deposition mode Fe–W/Cu	t_{Cu}, s	i_{Cu}, A/dm²	$t_{Fe–W}$, s	t_{pause}, s	$i_{Fe–W}$, A/dm²	Thickness of the layers, nm	R_a, μm
1	45		6.8	19.5		~10	0.98
2	180	0.1	34	10	2	~50	2.01
3	360		68	10		~100	0.09

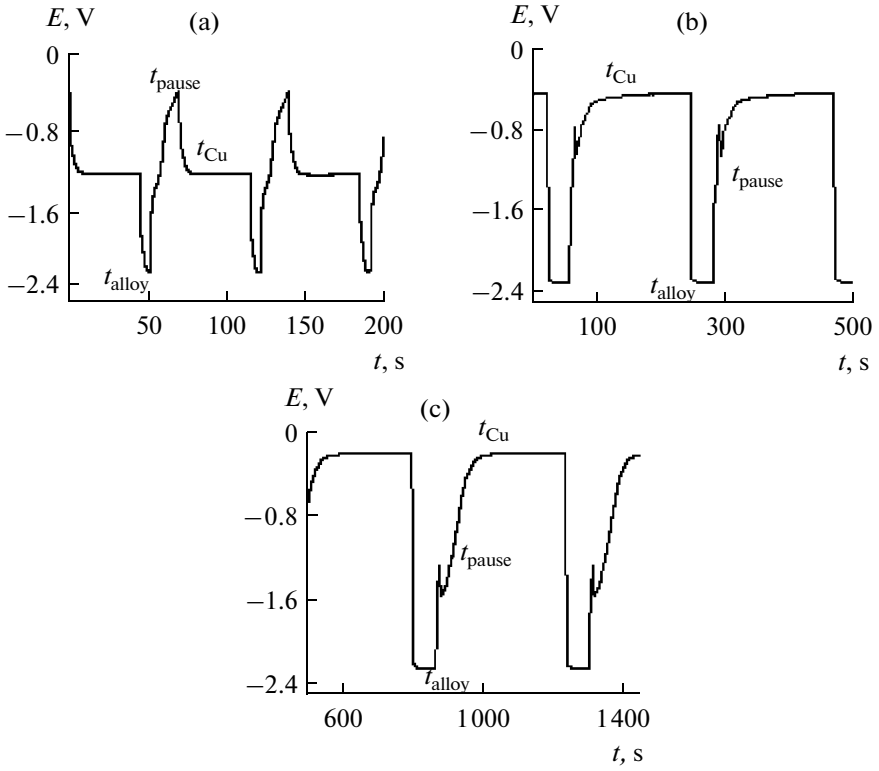

Fig. 2. Typical curves of the dependency of the potential on the time at the pulse-galvanostatic electrodeposition of Fe–W/Cu coatings in modes *1–3*. The potential is indicated without an ohmic component.

the lower specimen of quenched 45 steel (the HRC was 46–47, and the sizes were 110 × 50 mm), which was performed a reciprocal motion (at a frequency of 280 double strokes/min with a 100-mm peak-to-peak displacement amplitude) under a load of 300 N. The friction couples were lubricated with M-10 G_2K oil. The oil was supplied by a programed control mini-feeder, which ensured the accuracy of the oil expenditure and the synchronism of its being fed into the zone of the friction. The linear wear of the Fe–W specimens and the electrolytic chromium at the end of the testing was determined with regard to the average width of the wear area using a PMT-3 microscope.

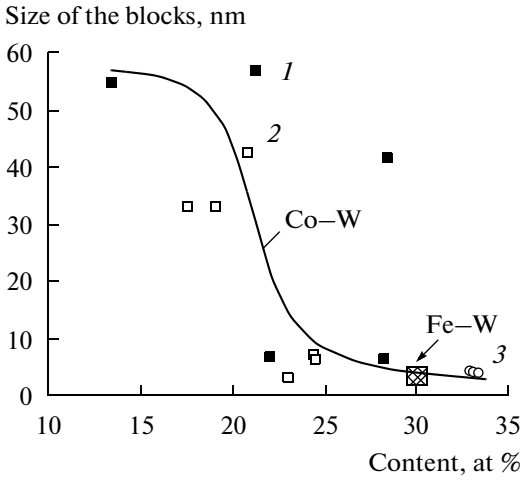

Fig. 3. Effect of the W concentration in the Co–W and Fe–W alloys on the size of the blocks (of a grain) that were electrodeposited at direct (*DC*) and pulse (*PC*) currents of the electrodeposition. (*1*) *DC*, pH 6.7; (*2*) *PC*, pH 6.7; (*3*) *DC*/*PC*, pH 8.

For comparison, the tribological characteristics of the Fe–W coatings that were deposited from the A electrolyte at a current density of 1 A/dm^2 and those from the chromium electrolyte (the standard electrolyte) at 55 A/dm^2 were determined.

RESULTS AND DISCUSSION

The Wear Study of the Coatings in the Presence of Oils

It was shown previously [30] that electrodeposited iron–tungsten alloys can be obtained in a nanocrystal state. Thus, at a tungsten concentration in the coating above 22–25% (at.), its grain size becomes less than 10 nm, which must lead to the change of the tribological and mechanical properties (Fig. 3 and 4 [31]). Indeed, such a small size of the grain enhances the hardness of the coatings, and its magnitude becomes comparable to (or even higher than) that of chromium coatings.

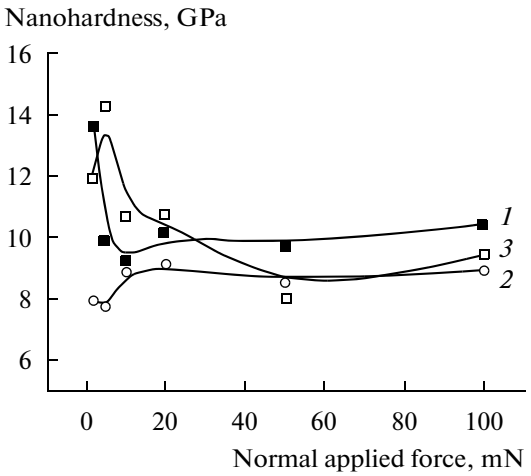

Fig. 4. Nanohardness that was measured at various loads of the indenter of the Fe–W and Co–W alloys and the Cr coatings; (*1*) Fe–W , (*2*) Co–W, and (*3*) Cr.

However, as the tribological tests of the iron-tungsten coatings showed, at the dry friction and a load of 2 N, such coatings undergo tribooxidation during the friction process (Fig. 5), which naturally interferes with their application. The Fe–W coatings undergo a high degree of wear (a darker color implies a larger depth in the image) resulting from the oxidation of the surface [30].

In order to expand the possibilities of using these alloys, we carried out investigations of the Fe–W – based alloys at their friction in the presence of oils, along with the variant of the multilayer coatings with copper.

One of the ways to decrease the wear is lubrication. The character of the behavior of the friction couples in the presence of oils greatly depends on the ability of the oil to penetrate into the area of the wear and remain there. The presence of oils substantially decreases oxygen's access to the area of contact in comparison with the degree of wear without lubrication, and this fact is found to be of special importance in the case of iron-based coatings [32].

In the context of the aforementioned, we studied the behavior of the Fe–W coatings in the presence of oils with a steel 45 counterbody. Indeed, the improvement of the tribological properties of the iron-tungsten coatings at friction in the presence of oils was noted. The friction coefficient decreases in the presence of oils to indicate the penetration of the lubricant into the contact area (Fig. 6). However, the friction coefficient that was measured is not so low as the one of the chromium coatings. This may be accounted for by the fact that the oxides that increase the friction coefficient [32] appear even in the presence of oils in the case of the Fe–W coatings, which affects the wear characteristics (Fig. 7).

It is seen that the depth of the wear of the Fe–W alloys deposited at various current densities is larger than that of the chromium coating (Fig. 7). Moreover, the Fe–W coatings deposited at higher current densities are characterized by a larger depth of wear, which is attributed to the somewhat higher tungsten content at the deposition at low current densities. Thus, even in the presence of oils at friction, the wear for the Fe–W coatings remains substantial, resulting, obviously, both from the choice of the oils for the given friction couple and the high load, which prevents reaching the required hydrodynamic mode at the given conditions of loading.

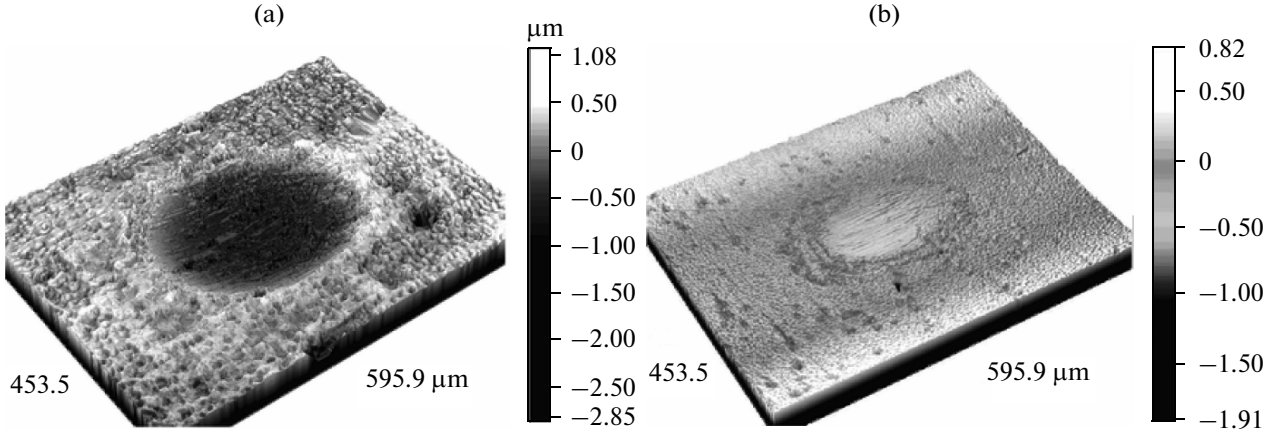

Fig. 5. The 3D images after the dry friction at 2 N and 10000 cycles of the electroplated coatings: (a) Fe–W (26 at % of W); (b) Co–W (24 at % of W).

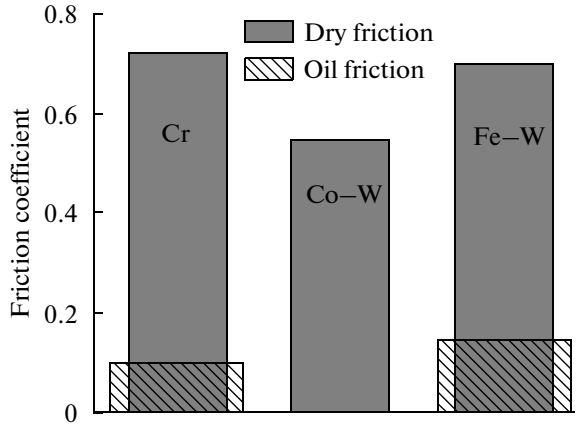

Fig. 6. Friction coefficient of the electroplated Fe–W, Co–W, and chromium coatings in the presence of oil.

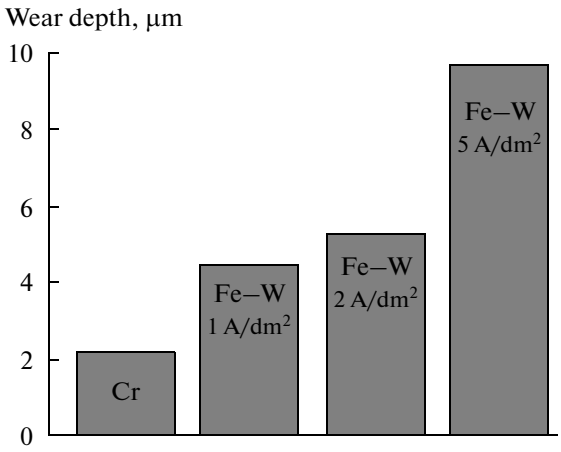

Fig. 7. Depth of wear of the electroplated Fe–W coatings at different current densities and coatings of electrolytic Cr. The friction tests were performed in the presence of oil and at a load of 300 N (after 21000 cycles).

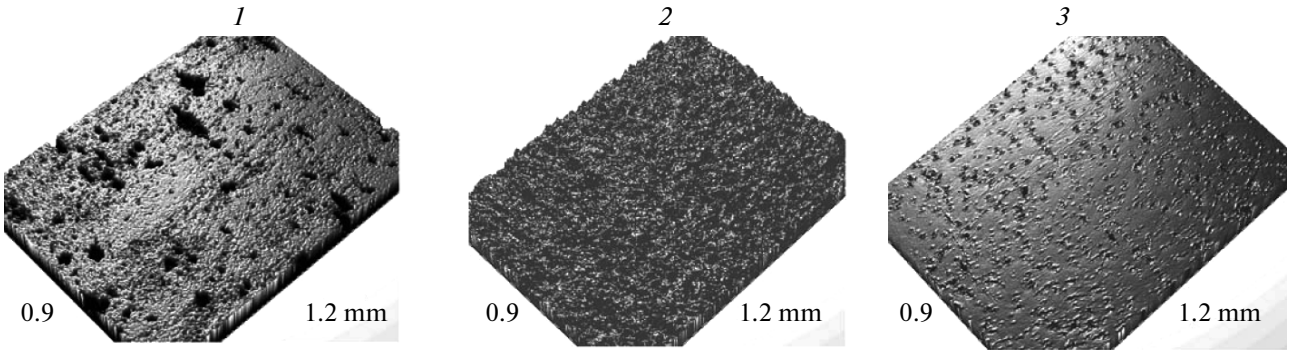

Fig. 8. The 3D images of the surfaces of the Fe–W/Cu multilayer coatings for modes 1–3 of the electrolysis and a layer's thickness in the multilayer coating, nm: 10 (*1*), 50 (*2*), and 100 (*3*).

Wear Study of the Fe–W/Cu Coatings at Dry Friction

The analysis of the tribological properties of the obtained multilayer Fe–W/Cu coatings was compared with electrodeposited Fe–W coating at 1 A/dm^2.

The study of the surfaces of the multilayer electrodeposited coatings showed that the roughness attains considerable values (Fig. 8 and the table), which is evidently specified by the nonuniformity of the obtained layers and the growth of the sizes of the grains at the deposition of the layers having a small thickness. In this case, high roughness is observed for individual layers with a thickness less than 100 nm. The finest roughness is observed at 100 nm, which is probably correlated with the more uniform deposition of the copper layers and the iron-tungsten alloy.

The sufficiently high roughness and nonuniformity of the coatings certainly must affect the tribological and mechanical properties. Thus, at the dry friction tests of the multilayer coatings at 10 N and 50000 cycles, the obtained wear track depend on the initial roughness of the coatings (Fig. 9). On the average, the wear depth at a given load was ~6 μm in 10-nm-thick layers, which is practically identical to the value of the wear depth for pure iron-tungsten coatings that were deposited at 1 A/dm^2. Note that, for the coatings having high roughness (as for instance in the case of a 50-nm-thick layer), one can hardly talk of the accuracy of the value of the wear depth (Fig. 9). Nevertheless, the layers with a thickness of less than 50 nm are found to not show any special improvement of the wear characteristics, which are correlated with the tribooxidation of the iron-tungsten coatings at dry friction.

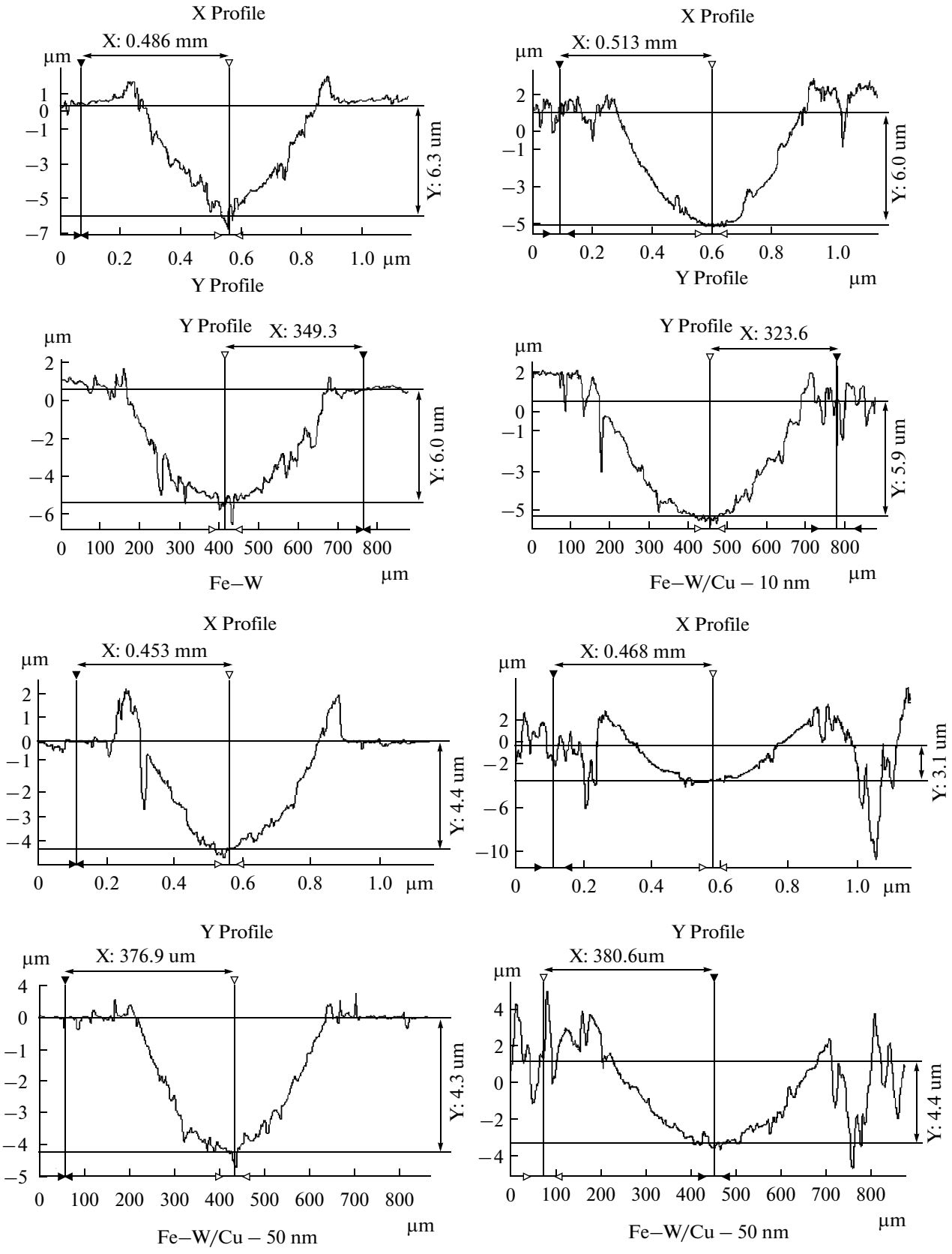

Fig. 9. Profiles of the multilayer coatings after the wear as measured in various directions for deposition modes 1–3 (table) and the Fe–W coating.

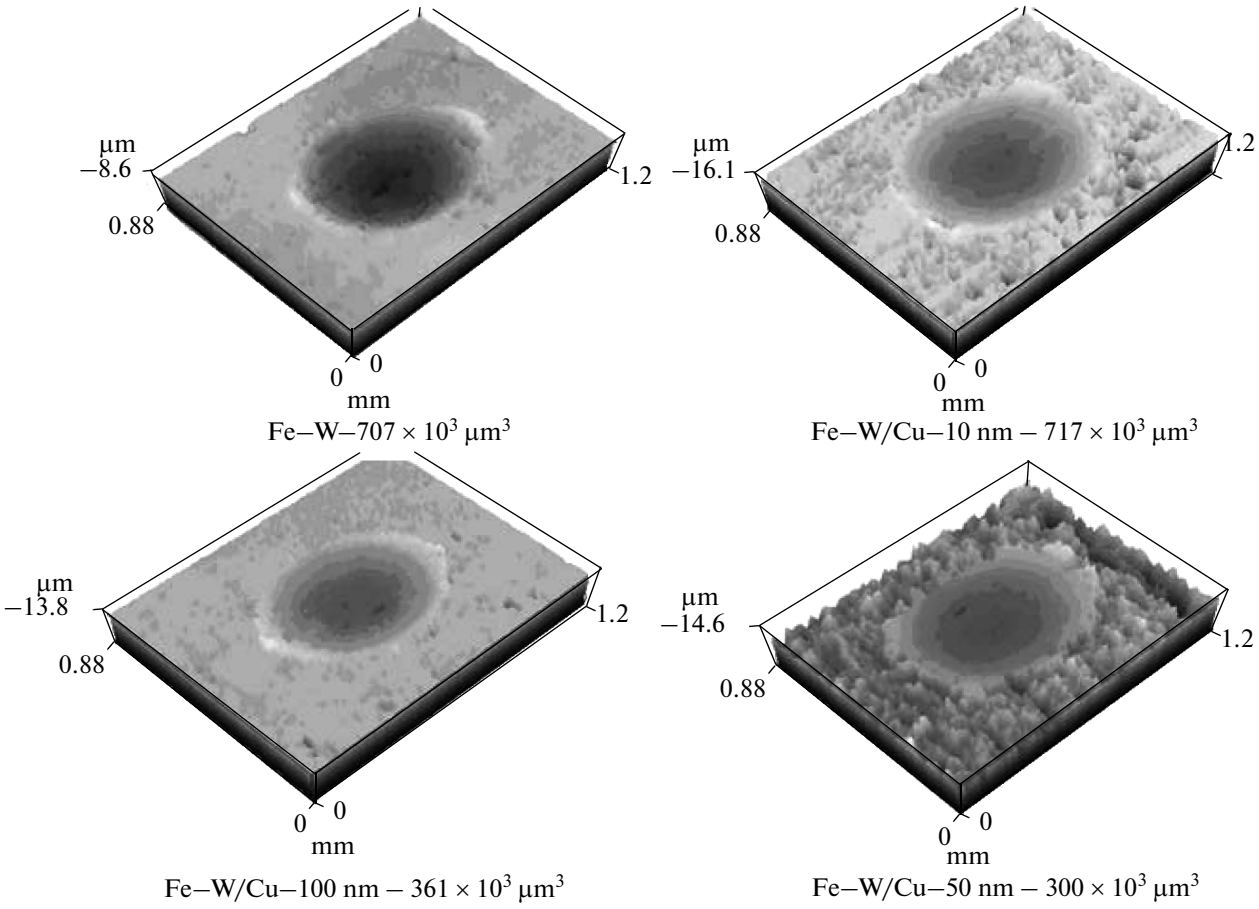

Fig. 10. The 3D images of the surfaces of the multilayer coatings and pure Fe–W after the tests for wear.

Thus, the volume of wear for the multilayer coatings with 10-nm-thick individual layers equals the wear for pure iron-tungsten coatings (Fig. 10). A decrease of the volume of the wear (Fig. 10) occurs at an increase of the thickness of the ingle layers with the minimum wear for 50-nm-thick layers.

The change of the friction coefficient of the multilayer coatings obtained at 10 N and an appropriate number of cycles is shown in Fig. 11. As is seen, for the specimen that was deposited with ~50-nm-thick layers, a certain decrease in the friction coefficient is observed as compared to the other coatings. This fact correlates with the lower value of the wear obtained for these coatings.

Hardness Measurement

The study of the mechanical properties, in particular, the hardness of the deposited multilayer coatings, was carried out using the multicycle method (MCM) on a Nano Indentation Tester. This method makes it possible to estimate the effect of various loads of the indenter (at different depths of penetration) on the hardness of the coatings. In this case, the hardness variation of a coating may be estimated in one area of the coating according to the thickness of the electrodeposit, instead of a few areas when using monoindentation. Figure 12 shows the results of the MCM study of the nanohardness of the multilayer coatings that were deposited in 1–3 modes of electrolysis (table). Copper is found to abruptly decrease the hardness of the multilayer coatings, particularly of those with 10-nm-thickness. This relates to the hardness obtained for the 50-nm-thick layers to a lesser degree. The values of the hardness of these coatings are practically identical to the hardness of the Fe–W coatings (Fig. 4). Note that high roughness makes it difficult to estimate the hardness. The data in Fig. 12 are presented for a more uniform area (Fig. 13a): the hardness estimation is found to be impossible over more rough areas (Fig. 13b).

CONCLUSIONS

The results of this study show the principle possibility for expanding the use of nanocrystalline Fe–W electroplating alloys. The friction coefficient and the penetration of oxygen to the friction surface are found to decreased at friction in the presence of lubricants. This makes it possible to improve the wear character-

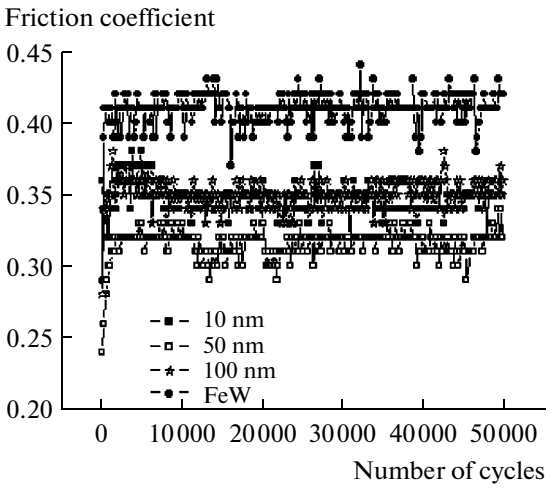

Fig. 11. Dependence of the friction coefficient on the number of cycles at dry friction using the method of "a ball along a plane" at 10 N for the Fe–W/Cu multilayer coatings and the Fe–W coatings.

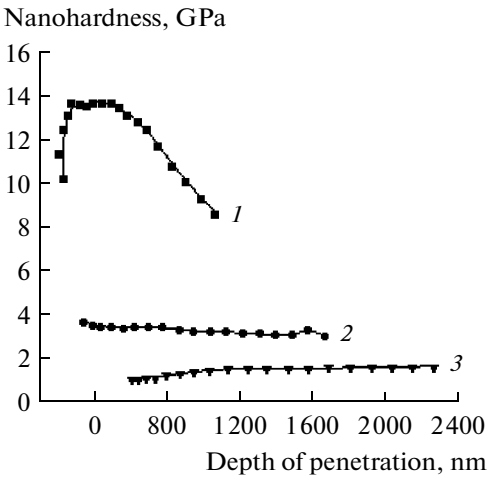

Fig. 12. Hardness measurements using a multicycle method (MCM) for modes *1–3* of the deposition of coatings (table) with the thickness of the layer, nm, being as follows: (*1*) 50; (*2*) 100; (*3*) 10. See the text for other details.

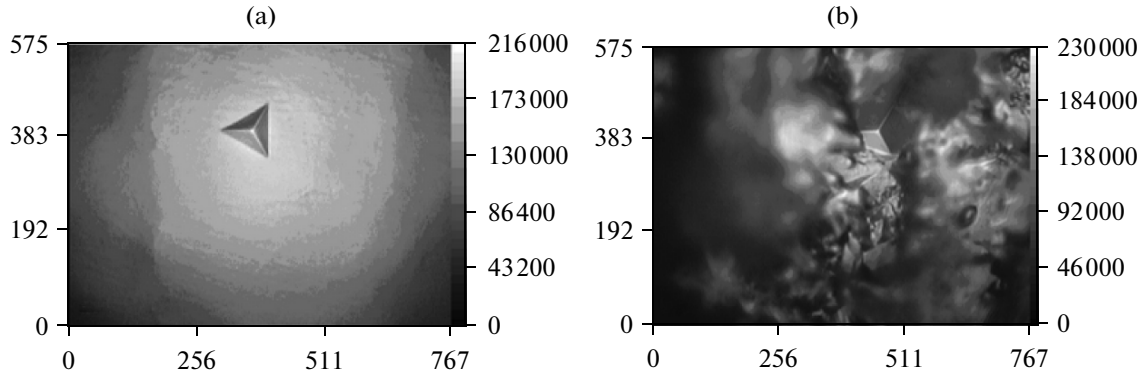

Fig. 13. Microstructure of the prints and adjacent zones after the indentation of the multilayer coatings using the MCM: (a, b) electrolysis mode 2 (prints in various areas of the coating).

istics of the Fe–W coatings versus the dry friction, when the surface tribooxidation is predominat.

The study of the tribological and mechanical properties of the multilayer Fe–W/Cu coatings by means of electrodeposition from a single bath leads to the improvement of the wear characteristics of the coatings even at dry friction and at a sufficiently high load of 10 N. The hardness of these coatings can be high in the case of the ~50-nm-thick individual layers, nevertheless of the copper presence.

ACKNOWLEDGMENTS

This research was performed within the framework of the State Program of the Academy of Sciences of the Republic of Moldova (project no. 09.836.05.06F) and the FP7-PEOPLE-2009-IRSES (proposal no. 247659).

The authors thank Dr X. Ye and M. Peeters (MTM Department, Catholic University, Leven, Belgium) for valuable advices' on tribological tests.

REFERENCES

1. Podlaha, E.J. and Landolt, D., Iduced Coodeposition I. An Experimental Investigation of Ni–Mo Alloys, *J. Electrochem. Soc.*,1996, vol. 143, p. 885.
2. Podlaha, E.J. and Landolt, D., Induced Coodeposition III. Molybdenum Alloys with Nickel, Cobalt, and Iron, *J. Electrochem. Soc.*,1997, vol. 144, p. 1672.
3. Donten, M., Cesiulis, H., and Stojek, Z., Electrodeposition and Properties of Ni–W, Fe–W and Ni–Fe–W Amorphous Alloys. A Comparative Study, *Electrochim. ACTA*, 2000, vol. 45, no. 20, p. 3389.
4. Bobanova, Zh.I., Dikusar, A.I., Cesiulis, H., Celis, J.P., Tsyntsaru, N.I., and Prosycevas, I., Micromechanical and Tribological Properties of Nanocrystalline Coatings

Electrodeposited from Citrate-Ammonia Solutions, *Russian J. Electrochem.*, 2009, vol. 45, no. 8, p. 895.

5. Brenner, A., Electrodeposition of Alloys, Volume II: Principles and Practice, Practical Considerations and Specific Information, *Electrodeposition of Alloys*, New York: Academic Press Inc., 1963.

6. Vas'ko, A.T., *Elektrokhimiya molibdena i vol'frama* (Electrochemistry of Molybdenum and Tungsten), Kiev: 1977.

7. Bondar', V.V., Grinina, V.V., and Pavlov, V.N., *Itogi nauki i tekhniki. Ser. Elektrokhimiya* (Results of Science and Engineering), Moscow: 1980.

8. Zakharov, A.A. and Vyacheslavov, P.M., *Elektroliticheskoe osazhdenie splavov* (Electrodeposition of Alloys), Leningrad: 1977.

9. Capel, H, Shipway, P.H., and Harris, S. J., Sliding Wear Behaviour of Electrodeposited Cobalt-Tungsten and Cobalt-Tungsten-Iron Alloys, *Wear*, 2003, vol. 255, p. 917.

10. Gambvurg, Yu.D., Zakharov, E.N., and Goryunov, G.E., Electrochemical Deposition, Structure and Properties of Iron-Tungsten Alloy, *Elektrocmim.*, 2001, vol. 37, no. 7, p. 789.

11. Zakharov, E.N. and Gamburg, Yu.D., Certain Patterns of Deposition of Iron-Tungsten Alloy from Citrate-Ammonia Solutions, *Electrokhim.*, 2005, vol. 41, no. 8, p. 1001.

12. Zakharov, E.N., Gamburg, Yu.D., Goryunov, G.E., and Lyakhov, E.F., Effect of Alkaline Metals and Ammomium on the Deposition Process and Structure of Iron-Tungsten Alloys, *Electrokhim.*, 2006, vol. 42, no. 8, p. 993.

13. Gamburg, Yu.D and Zakharov, E.N., Hydrogen Effect on Amorphisation of Iron-Tungsten alloys Obtained Using Electrochemical Synthesis, *Electrokhim.*, 2008, vol. 44, no. 6, p. 792.

14. Vyacheslavov, V.P., *Elektrochimicheskoe osazhdenie splavov* (Electrochemical Deposition of Alloys), Leningrad: Mashinostr., 1968.

15. Babich, M.N., Broto, J.M., Fert, A., Nguyen Van Dau F., Petroff, F., Eitenne, P., Creuzet, G., Friederich, A., and Chazelas, J., Giant Magnetoresistance of (001)Fe/(001)Cr Magnetic Superlattices, *Phys. Rev. Lett.,* 1988, vol. 61, p. 2472.

16. Ludwig, K., Hauch, J., Mattheis, R., Barholz, K.U., and Rieger, G., Adapting GMR Sensors for Integrated Devices, *Sens. Actuators A,* 2003, vol. 106, p. 17. Zhang, X., Misra, A., Wang, H., Shen, T.D., Nastasi, M., Mitchell, T.E., Hirth, J.P., Hoagland, R.G., and Embury, J.D., Enhanced Hardening in Cu/330 Stainless Steel Maltilayers by Nanoscale Twinning, *Acta Mater.*,2004, vol. 52, p. 995.

18. Anderson, P.M., Bingert, J.F., Misra, A., and Hirth, J.P., Rolling Texture in Nanoscale Cu/Nb Multilayers, *Acta Mater.*, 2003, vol. 51, p. 6059.

19. Lui, Z.J., Vyas, A., Lu, Y.H., and Shen, Y.G., Structural Properties of Sputter-Deposited CN_x/TiN Multilayer Films, *Thin Solid Films*, 2005, vol.479, p. 31.

20. Haseeb, A.S.M.A, Celis, J.P., and Roos, J.R., Fretting Wear of Metallic Multilayer Films, *Thin Solid Films,* 2003, vol. 444, p. 199.

21. Kirilova, I., Ivanov, I., and Rashkov, St., Anodic Behaviour of One and Two-Layer Coatings of Zn and Co Electrodeposited from Single and Dual Baths, *J. Appl. Electrochem.,* 1998, vol. 28, p. 637.

22. Jensen, J.D., Gabe, D.R., and Wilcox, G.D., The Practical Realization of Zinc-Iron Coatings, *Surf. Coat. Technol.*, 1998, vol. 105, p. 240.

23. Chawa, G., Wilcox, G.D., and Gabe, D.R., Compositionally Modulated Zinc Alloy Coatings for Corrosion Protection, *Trans. IMF*, 1998, vol. 76, p. 117.

24. Kalantary, M.R., Wilcox, G.D., and Gabe, D.R., Alternative Layers of Zinc and Nickel Electrodeposited to Protect Steel, *Br. Corrosion J.*, 1998, vol. 33, p. 197.

25. Herman, A.M., Mansour, M., and Badri, V., Deposition of Smooth Cu(In, Ga)Se_2 Films from Binary Multilayers, *Thin Solid Films*, 2000, vol. 361–362, p. 74.

26. Pasa, A.A. and Schwarzacher, W., Electrodeposition of Thin Films and Multilayers on Silicon, *Phys. Stat. Sol.,* 1999, vol. 173, p. 73.

27. Toth, Kadar E., Peter, L., Bescei, T., and Schwarzacher, W., Preparation and Magnetoresistance Characteristics of Electrodeposited Ni-Cu Alloys and Ni–Cu/Cu Multilayers, *J. Electrochem. Soc.*, 2000, vol. 147, p. 3311.

28. Jyoko, Y., Kashiwabara, S., Hayashi, Y., and Schwarzacher, W., Preparation of Perpendicular Magnetization Co/Pt Nanostructures by Electrodeposition, *Electrochem. Solid Stat. Lett.*, 1999, vol. 2, p. 67.

29. Azhder, V.V., Drozdov, Yu. N., Komendant, V.I., et al., Main Laws of Friction, Lubrication and Seizing at Accelerated and Decelerated Cyclic Sliding, *Trenie i Iznos*, 1988, vol. 9, no. 4, p. 581.

30. Tsyntsaru, N., Bobanova, J., Ye, X., Cesiulis, H., Dikusar, A., Prosycevas, I., and Celis, J.-P., Iron-Tungsten Alloys Electrodeposited under Direct Current from Citrate-Ammonia Plating Baths, *Surf. Coat. Technol.*, 2009, vol. 203, Issues 20–21, p. 2983.

31. Tsyntsaru, N., Cesiulis, H., Bobanova, J., Croitoru, D., Dikusar, A., and Celis, J.-P., Electrodeposition and Tribological Characterization of Nanostructured Co–W and Fe–W Alloys, *Proc. Int. Conf. BALTTRIB'2009, Kaunas*, 2009, p. 59.

32. Czupryk, W., Friction Transfer of Iron in Oxidative Wear Conditions During Lubricated Sliding, *Wear*, 2000, vol. 237, p. 288.

ISSN 1068-3755, Surface Engineering and Applied Electrochemistry, 2010, Vol. 46, No. 6, pp. 547–557. © Allerton Press, Inc., 2010.
Original Russian Text © Ph.I. Vysikaylo, 2010, published in Elektronnaya Obrabotka Materialov, 2010, No. 6, pp. 17–28.

ELECTRICAL PRECISION TREATMENT OF MATERIALS

Cumulation of de Broglie Waves of Electrons, Endoions and Endoelectrons of Fullerenes, and Resonances in the Properties of Nanocomposite Materials with Spatial Charge Layers

Ph. I. Vysikaylo

Technological Institute of Superhard and Novel Carbon Materials, ul. Tsentral'naya 7a, Troitsk, Moskovskaya obl., Russia
e-mail: filvys@rambler.ru

Received July 21, 2010

Abstract—The cumulation of de Broglie waves of electrons in hollow molecules (for example, C_{60}) has been investigated. The existence of negatively charged endoions of fullerenes with trapped electrons in the inner cavity (endoelectrons) is proved. The Schrodinger (Helmholtz) stationary equation for hollow polarized molecules is solved analytically. An endoelectron has a positive total energy, but, because of the polarization forces, it is localized (constantly cumulating) in the center of the hollow spherically symmetric molecule (C_{60}). The analytically calculated Eigen ψ-function and eigen energy determine the probability of finding an electron in the cavity of a hollow molecule. The Eigen energy of a quantum cavity (C_{60}) is compared with experimental studies of cross sections of electrons attachment to C_{60} dependencies on the electron energy. The importance of the polarization hollow molecules in the stabilization of the fullerene endoions with endoelectrons (with energies from 0.2 to 12 eV) is proved. The effect of the cumulation of electrons in the hollow of the molecule (the trap for electrons) can be used to control the concentration of the charge carriers, the thermal and electrical properties of semiconductors, and the hardening of materials with free electrons. The quantum properties of polarized cavities could cause the variation of the parameters of nanocomposites with a concentration of quantum modifiers (C_{60}).

DOI: 10.3103/S1068375510060037

INTRODUCTION

Fullerenes, nanotubes, clathrates, and onions comprise a peculiar class of nanostructures possessing a well-defined property of forming "traps" for other nanoobjects—separate atoms, molecules, or similar interleaved (matreshka) structures, for example, for endofullerenes (fullerenes with an enclosed atom or molecule) [1, 2].

To designate endofullerenes there is used the formula $M_k@C_n$ where M is the encapsulated atom or molecule, and the lower indices k and n indicate the number of such atoms and carbon atoms in a fullerene molecule, respectively. The used notation allows one to distinguish endohedral molecules from common chemical compounds, which, in the case of fullerenes, are designated by the symbol M_kC_n. In all the mentioned cases, the enclosed structures are formed by electrically neutral atoms and molecules which themselves consist of the layers of positive and negative charges complexly distributed in the space. (The foundations for such understanding or femtotechnologies with the layers of space charge were laid even by Rutherford early in the last century.) Yet, it is well known that the fullerene molecules are strong acceptors of electrons; the electron affinity of C_{60} is 2.7 eV [1]. Thus, the molecules of fullerenes can capture electrons and easily form chemical compounds. The electrons localize on the outside of a fullerene molecule due to the formation of a chemical bond. As the experiments show, there appears to be possible another "scenario" of the interaction between an electron and a fullerene (or another hollow molecule).

The characteristic dimension of the cell L of the C_{60} molecule (a pentagon or hexagon) is not more than 2.8 Å. This dimension corresponds to the minimum energy of the electron (~18 eV) (in the case of a de Broglie plane wave) needed to leave the inner bulk of C_{60} through these cells ($E = p^2/2m$, $p = (h/L)$, where h is the Planck constant, and m is the electron mass. If the electron has energy more than 18 eV, it can penetrate into a hollow molecule and leave it. It is logical to suppose the existence of some range of values of the electron resonance energies sufficient for the electron to penetrate into the molecule but not leave it.

In other words, fullerenes are traps for electrons possessing some resonance energy. The resonance capture into the inner cavity results in the formation of endoelectrons in fullerenes and other hollow molecules. This feature of hollow molecules—to play the role of traps for the electrons with resonance energies—opens up fresh opportunities to control the properties of composite materials (their parameters). Thus, selecting concentrations of hollow molecules (quantum resonators), for instance of a fullerene, it is

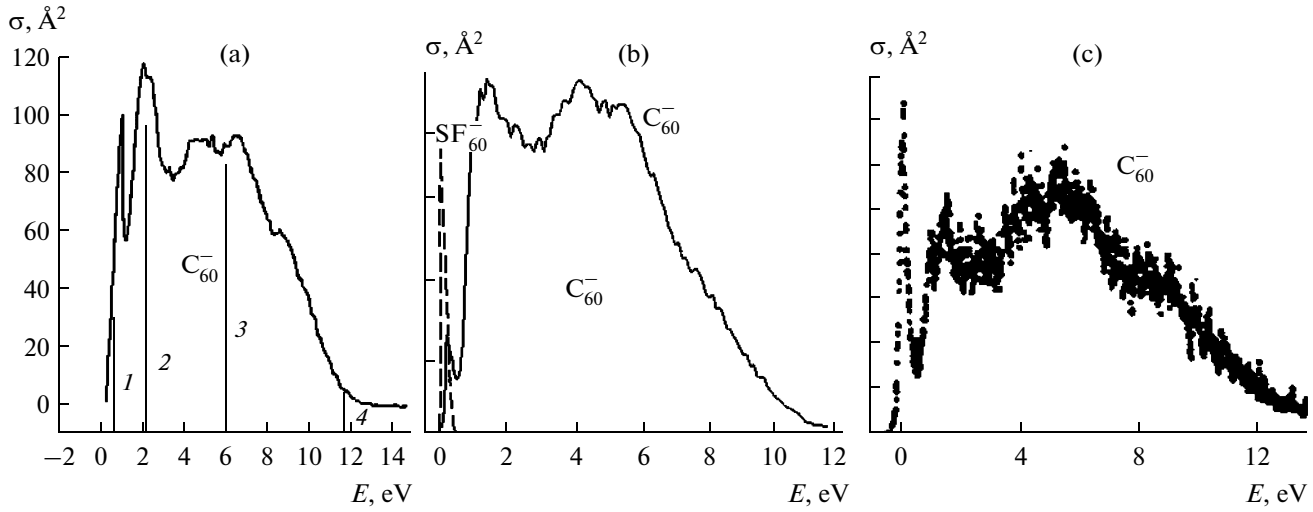

Fig. 1. Experimentally measured cross sections of the electron attachment to C_{60} versus its energy: (a) for C_{60} [6]. The straight solid vertical lines mark the intrinsic energies (with the main numbers $n = 1, 2, 3, 4$) calculated by (9) in view of the action of the forces of the polarization of C_{60} on stabilization of the fullerene endoion; (b) relative cross sections of the attachment of an electron to SF_6 and C_{60} for the flow of C_{60} ($T = 673$ K) [7]; (c) experimental curves of the efficient yield of the resonance capture of electrons by the C_{60} fullerene molecules [5].

possible to reduce the heat conduction of materials, to increase their strength characteristics forming double layers of spatial charge [3, 4], etc. The negative ion of a fullerene with an endoelectron or their system in the cavity can be called an endoion. The aim of this paper is to substantiate the possibility of such a "scenario." The analytical calculations and numerous experiments [5–7] (see the references in [6, 7]) count in favor of this assumption. Endohedrals were discovered almost simultaneously with fullerenes; as for the possible appearance of endoelectrons and, correspondingly, endoions of fullerenes and other hollow molecules, it was for the first time reported in [3, 4] in the form of a hypothesis and its good substantiation.

Interaction of C_{60} Molecules with Electrons

The interaction of C_{60} molecules with electrons has been studied in many works. Evidently, there is no other molecule (besides its derivatives and C_{70}) capable to form long-lived negative molecular ions (NMI) with the energy of the bombarding electrons up to 20 eV [5–7]. The mechanism of stabilization of NMI as regard to the electron removal at such a great excess energy stored in it is not clear yet [5–7] (see Fig. 1). Really, if the attachment to the fullerene molecules takes place according to the classic mechanism of an electron capture by a carbon atom into a potential well without deep penetration of the electron into the fullerene, there should be expected only a peak in the region of the small energy of electrons as is observed in the case of the SF_6 molecule (Fig. 1b). In the case of **a hollow** C_{60} molecule, there is quite another picture (Fig. 1). As in the experiments, there has been found the threshold of attachment of an activated electron to the C_{60} and C_{70} (Fig. 1); it could be involved the dissociative attachment mechanisms, requiring a certain energy of the electron activation. However, no decomposition products of C_{60} were found after a resonance electron was captured [6]. There is also no consensus of opinion among research workers regarding the mechanism of the resonance capture of slower (≈1–1.5 eV) electrons [5–7]. The resonance peaks in the cross sections of the attachments (see Fig. 1), according to [7], for C_{60} are observed in the experiments at the electron activation energies $E_n = 0.2$; 1.5; 4.5; 5.5; 8 eV.

If the first resonance level with $n = 1$ is clearly identified in Figs. 1a and 1b (in [6] it is pointed out that $E_1 = 0.24$ eV), the levels $n = 2–5$ mentioned in work [7] are established less accuratly, and the presence of them is doubted (so, the values $E_{2–5} = 2.25$; 3.8; 4.9; 6.1 eV are presented in [6]). Being in seemingly good agreement, the results of experimental works [5–7] substantially differ in the details of the resonance levels (Figs. 1a–1c). So, the energy of activation of the first resonance level of the C_{60} ion established in [6] is 0.24 eV, differing by 20% from the value presented in [7]. The relative magnitudes of the first peaks are several times different in relation to the second ones (Figs. 1a–1c). The author is inclined to believe that the results with the absolute values of the cross sections presented in [6] are more reliable, though even these data could be evidently refined in the course of further more accurate experiments. According to [6] (Fig. 1a), the effective radius of the polarization interaction exceeds the characteristic radius of the C_{60} molecule (0.36 nm), and, for the electrons with the energy of about 2 eV, it amounts up to 0.63 nm, exceeding the molecule's radius by $r_{ind} \approx 0.26$ nm. Undoubtedly,

this phenomenon is connected with the polarization forces arising between an external (exo-) electron and the C_{60} molecule polarized by this exoelectron (or another polarizing molecule). The polarization interaction results in the development of a standing spherical wave—an endoelectron—inside the molecule's cavity.

The interaction of the C_{60} molecule with an external electron in the case of the interaction with atoms of alkaline (or alkaline earth) metals is well studied. At room temperature, C_{60} crystallizes in the form of a face-centered cubic (FCC) lattice with relatively weak intermolecular bond forces. Such C_{60} molecular crystals are called fullerites. In a close-packed FCC structure (the lattice parameter is 1.417 nm), the C_{60} molecules are represented by balls of 1.002 nm radius. One C_{60} molecule is accounted for by one octahedral and two tetrahedral cavities of 0.206 and 0.112 nm radii, respectively. Such great cavities make fullerite promising for the synthesis of new compounds through the introduction of various atoms and molecules into them. Such an introduction is called an ntercalation [1]. If the intercalation of atoms results in the transfer of valence electrons to the C_{60} molecules, then such compounds are called fullerides and are designated by M_kC_{60}. Here, M = K, Rb, Cs, etc. Valence electrons are delocalized along the C_{60} shell producing molecular anions C_{60}^{-k} with the difference between the lengths of the double and single bonds reducing. The spectra of the light combination scattering (LCS) of such intercalated fullerenes displace into the low-frequency region in relation to the intramolecular spectra of fullerene molecules by nearly 6 cm^{-1} for each valence electron transmitted to the C_{60} molecule [8–10]. It is followed from the electron structure of the C_{60} molecule that, in the course of the reduction of C_{60}, the lowest free level t_{1u} is filled on which up to $k = 6$ electrons can be settled [1, 2, 11]. According to [8–11], it is believed that if there happens the capture of the electrons of a nanomaterial (metal or semiconductor) on the C_{60} shell (the electron sinks into a potential well) and the concentration of anions is comparable or exceeds the concentration of the C_{60} nondoped by electrons, then the spectrum of the C_{60} doped by electrons should also displace by 6 cm^{-1} to the captured electron [8–11]. However, if the electron with the energy $E > 0$ is thrown into the internal cavity of the fullerene due to the generation of polarization forces, which disappear when the electron penetrates into the hollow molecule, then such a shift could not be observed. Indeed, as is shown in this work, the endoelectron with the activation energy $E > 0.2$ eV is localized by the polarization forces in the center of the hollow molecules (with C_{60} as an example); does not produce chemical bonds with them; and, out of the boundaries of the localization region ($r \geq R$), the probability of its existence is zero (that is $\psi(r \geq R) \equiv 0$).

Interaction of an External Electron with Hollow Structures: The Cumulative–Topologic Mechanism of the Capture of an Electron in the Course of the Production of Endoions

In order to estimate the profile of the capture of an electron according to the mechanism of the form resonance, some investigators choose a spherically symmetric rectangular potential with the energy well in the whole cavity of the C_{60} (with the negative energy –2–3 eV, for example, [12] and the references in this paper). This is a mistake of the formulation of the problem, as there is no potential well in the internal cavity of C_{60}. The captured electron's energy E in the cavity constantly remains substantially more than zero. In these works, the C_{60} molecule's polarization favoring the permanent return (cumulation) of the captured electron to the center of the hollow structure is considered incorrectly. A potential well with the dimensions of a hollow molecule does not form. The action of the polarization forces results in the formation of a barrier (a quantum–coulomb focusing "mirror") reflecting the electron to the center of the hollow molecule. This polarized "mirror" (barrier) focusing the captured electron to the fullerene center is formed for a short instant by the synergetic (joint) fields of some bare positively charged ions of carbon atoms that appeared owing to the polarization of the molecule only at that moment when this endoelectron leaves the bulk of the hollow molecule (that is, becomes an exoelectron). Without the action of coulomb potentials, the electron moves inertially during the most time towards the center of the no longer polarized molecule. The value of the average electron polarizability of the C_{60} hollow molecules is large—$\alpha = 90 \times 10^{-30}$ m^3. The greatest mistake in the theoretical works is the fact that there is not taken into account the substantial internal region without a potential into which the electrons with the energy from 0.2 to 12 eV bombarding the molecule are thrown with the subsequent permanent reflection of them from the concave shell (the polarization "mirror").

The spherical potential well produced by the shell of carbon atoms is localized only at the molecule's surface with the shell's thickness dimensions and does not occupy the whole volume of the C_{60} molecule. The most internal volume of the C_{60} molecule is free from a coulomb potential (the shell). The potential is shell-type with the characteristic shell thickness on the order of the carbon atom diameter, that is less than 1 Å. Thus, it is the author's opinion that all quantum–mechanical computations carried out under the assumption that the coulomb potential well of the C_{60} molecule occupies the whole internal volume and the electron with the initial energy, for instance, 10 eV, immediately sinks into this well with the negative energy –2 eV are incorrect. (As will be proved in this work, the size of the reflecting shell's radius is determined by the polarization forces and exceeds the geometric radius of a hollow molecule.)

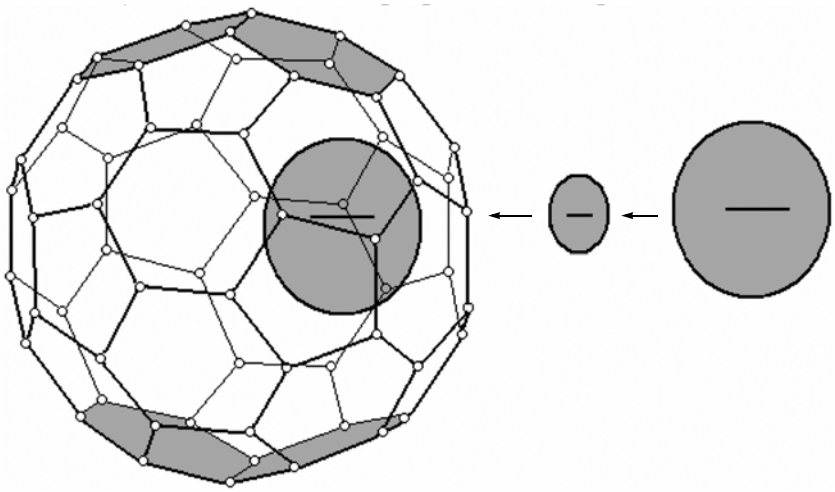

Fig. 2. The diagram of the cumulative throw off of an electron with the energy from 0.2 to 18 eV into the cavity of the C_{60} molecule and the resonance formation of the endoion $e_k@C_n$. The successive reduction of the length of the de Broglie wave of an electron bombarding the fullerene molecule polarized by it [4].

The author thinks that the mechanism of "the stabilization" of an electron with energy less than 18 eV colliding with the fullerene molecule is its removal into the internal cavity of the C_{60} molecule (Fig. 2) and the consequent localization of the electron, that is, the formation of a standing wave—an endoelectron—in the internal cavity of the C_{60}. The polarization of the C_{60} molecule and its geometric spherical shape (convex on the outside and concave on the inside) play a significant role in the process of the electron penetration into the fullerene. As is proved in this work, such geometry determines not only the width of the potential barrier but its height too (up to 18 eV).

Entering the internal region after the removal from the inner surface of the C_{60} molecule, the electron could not freely leave the closed molecule if its energy E is in the range of $0.2\ \text{eV} \le E \le 18$ eV. Only the capture of the electron into the C_{60} internal cavity as into a trap with the "mirrors" reflecting it to the center allows one to explain rationally the significant cross sections of the "attachment" (Fig. 1) at the energies of the electrons more than the ionization potential $I_{C60} = 7.6$ eV. The minimum kinetic energy of the electrons capable to be in the C_{60} molecule's internal bulk should be more than 0.2 eV. This is determined by the uncertainty principle and the C_{60} molecule's diameter: $D \approx 0.72$ nm ($R = 0.36$ nm).

In the resonance capture of an electron (within the mentioned range of its energies) by the C_{60} molecule and the corresponding production of an endoion $e_k@C_n$, there participate the following factors:

(1) the polarization of a fullerene (for example, the C_{60} molecule) with interaction with an incoming electron;

(2) the acceleration of the electron by a synergetic (joint) field of the ions of carbon atoms appearing owing to the polarization of C_{60} and its further acceleration to the center of a hollow molecule while moving in the region of a nucleus of one of the carbon atoms;

(3) the absence due to the geometric factor, of the polarization of a molecule with an electron inside (the molecule's surface is concave inside and convex outside).

After the molecule is polarized by the incoming electron, the latter is accelerated in the field of the carbon ion and acquires the kinetic energy necessary for the penetration and accumulation (cumulation) of electrons in the internal volume of the C_{60}. After the electron has passed around the ion's nucleus, it leaves the accelerating ion and flies into the C_{60} molecule's inner volume. Losing the kinetic energy, the endoelectron again "swells" inside the C_{60} molecule: its de Broglie characteristic wave grows (Fig. 2). In this case, it becomes nonpolarized again and the polarization potential disappears before the electron leaves the hollow molecule. The electron polarizes the C_{60} molecule more efficiently inside it than outside owing to the geometric factor. It is caused by the fact that the C_{60} molecule's inner surface is concave.

Such differences in the geometry of the electron shells for the outer and inner electrons determine the resonance dissipation of the inner electron by a dozen of the shell electrons (their number is inversely related to the electrons' kinetic energy or to the square of the de Broglie wave), and, for the outer electron, vice versa, they determine the possibility to be accelerated and focused to the center of the convex positively charged part of C_{60}. The energy of an endoelectron being about 0.2 eV, it could not polarize the molecule at all according to the Gauss theorem and interact with all the electrons of the C_{60} shell simultaneously. Thus, the "quantum–classic" endoelectron with the

energy from 0.2 eV entering into the C_{60} spherical molecule could not leave it if the fullerene cage is not broken. For the electron with the energy much more than 0.2 eV, the interaction takes place with the less number of electrons and thus the probability of its penetration through the C_{60} shell's potential barrier grows (with the electron energy increasing, the efficient shell barrier reduces). With the energy of the electron being more than 18 eV, it freely leaves the inner volume of the C_{60}.

Thus, the stabilization of a negative ion $e_k@C_n$ takes place owing to the cumulative throwing off of the incoming electrons by the nuclei of carbon atoms into the trap—the inner volume of a molecule—and the subsequent generation of polarization forces when the electron leaves the boundaries of the hollow molecule. This assumption is proved by the analytical investigations carried out in this work and their comparison with the experiments conducted in [5–7].

For a nanotube, the geometric factor of dissipation of an electron inside it has a 2D-dimension. The similar dissipation in a nanotube ensures the ballistic conduction of nanotubes. As thin extended quasi-one-dimensional and quasi-two-dimensional structures of complex geometry—nanotubes and nanofilms—were created in nanotechnology long ago, at the same time, a demand arose for the theoretical description of the behavior of an electron in the framework of such complex structures. It is believed in the theoretical models that, out of these regions, the wave function $\psi(r, t)$ of a quantum particle exponentially rapidly reduces (the model of soft walls) or is zero (the model of rigid walls). Above, we have substantiated the model of rigid walls for low-energy electrons (for example, $E_n < I_{C60}$) determined by the simultaneous interaction of an endoelectron with a lot of electrons of the C_{60} shell.

In some theoretical works, the solutions of a model of thin bent cylinder with a "twisted boundary" or a thin bent film have been considered in the adiabatic approximation [13]. It is convenient to characterize the scale difference in the thin extended structures by a small "adiabatic" parameter $\chi = D/L$, which is assumed to be little in [13]. Here, D is the diameter of the nanotube, and L is its length. Within the limits of these models, it is shown that the "geometric potential" or the existence of rigid walls in an empty waveguide produces an efficient attraction to the points of the greatest curvature of the axis. The term "geometric potential" was coined for the first time by V.P. Maslov in [14]. It is clear that, in the case of fullerenes, such a cumulation point is the center of a fullerene. As for the fullerene, the adiabaticity parameter $\chi = D/L$ becomes equal to 1; the generalized adiabatic principle for the description of the electron dynamics in bent nanostructures worked out in [13] is unsuitable for traps—fullerenes. In this case, $D = L$.

Yet, within the limits of a spherical model with rigid walls, it is possible to calculate the proper values of the resonance energy for endoelectrons and eigenfunctions for Helmholtz hollow quantum resonators. This proves the possibility of the formation of quantum traps (resonators) for electrons on the basis of hollow molecules (C_{60}, in particular). The trap is determined by the same geometric potential [14] reflecting the electron from the shell of a hollow molecule to its center. (It should be noted that the title of the work [14] "Asymtotics of Eigenfunctions of the Equation $\Delta u + k^2 u = 0$ with Boundary Layers on Equidistant Curves and Scattering of Electromagnetic Waves in Waveguides" serves this work—to find a solution for the case of C_{60}; see also (1).) Indeed, in such spherically concave (for the endoelectron) traps, an inner electron with energy of more than 18 eV can freely leave the internal cavity of a fullerene. Thus, in the case of a fullerene, the "geometric potential" efficiently focuses the electron to the center of the internal cavity and constantly reflects to the center already the inner one—the endoelectron. From the above mentioned considerations, one can select the height of the potential barrier—18 eV.

Interaction of an Endoelectron with Concave Nanostructures. The Mechanism of Reflection and Cumulation of the Fullerene Endoelectron by the Polarization "Mirror"

Let us calculate the influence of the "geometric potential" on the cumulation of the electrons to the center of the fullerene. Inside the fullerene, where the coulomb potential is zero, the electron with the total energy $E_n \sim 0.2$ eV can be considered as a closed by the shell spherically symmetric standing wave reflected to the center of the fullerene and described by the Schrodinger stationary equation and the Helmholtz equation [15, 16]:

$$\Delta\psi(r) + k_n^2\psi(r) = 0. \tag{1}$$

Here, $k_n^2 = 2E_n m/\hbar^2$, m is the electron mass.

The solution of equation (1) in the spherically symmetric case without considering the centrifugal potential ($l = 0$) is [16]:

$$\psi(r) = [A\cos(k_n r) + B\sin(k_n r)]/r. \tag{2}$$

As the boundary conditions on the internal boundary of the reflecting shell, in the model with an absolutely rigid shell, we lay the condition for the total internal reflection:

$$\begin{gathered}\psi(r \geq R) \equiv 0, \quad \text{where} \rightarrow \text{at} \quad r \leq R \\ \psi(r) = A\cos(k_n r)/r.\end{gathered} \tag{3}$$

According to [15, 16], in model (1)–(3), inside such a shell there should exist intrinsic discrete (reso-

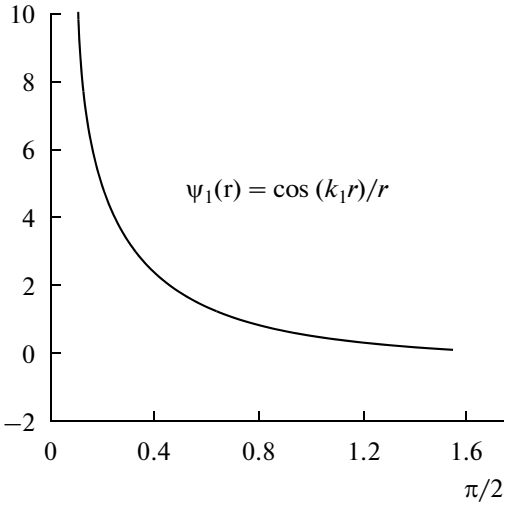

Fig. 3. The electron ψ-function versus the distance to the hollow molecule's center (*r* is in radians).

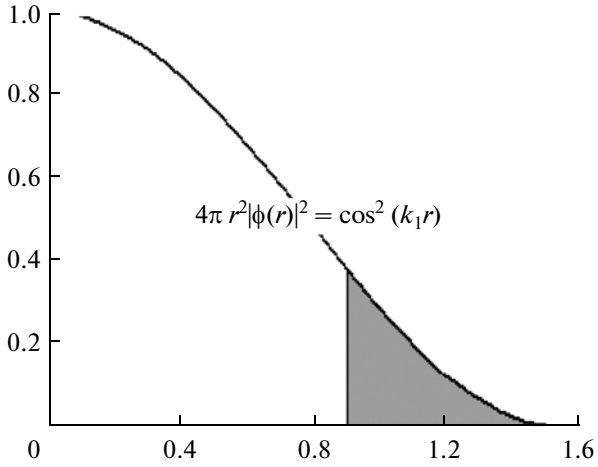

Fig. 4. The relative probability to find an electron in the C_{60} cavity versus the distance to the fullerene center. The relative probability of the presence of an electron outside the C_{60} shell is darkened.

nance) levels of energy for the electron closed by the shell with the activation energy $E_n \sim 0.2$ eV:

$$E_n = \pi^2(n-1/2)^2\hbar^2/2mR^2 = 0.37(n-1/2)^2/R^2\text{eV}, \quad n = 1, 2, 3\ldots. \tag{4}$$

According to (4), prescribing, for example, $R = 0.36$ nm (the radius of the C_{60} shell), we obtain at $n = 1-3$ the energy spectrum of the resonance levels of the captured electrons:

$$E_{n=1-3} = 0.71; 6.4; 17.7; \ldots \text{ eV}. \tag{5}$$

If the real thickness of the C_{60} shell is taken into account, the calculated energy of the levels increases 1.9 times, respectively:

$$E_{n=1-2} = 1.3; 12.0; \ldots \text{ eV}. \tag{6}$$

Infinite spectrum (5) or (6) is cut by the fact that, when the kinetic energy is more than 18 eV, the electron can freely leave the C_{60} as a de Broglie plane wave because its characteristic dimensions are comparable with the characteristic dimensions of the fullerene cell (Fig. 2). Even these results agree satisfactorily, to a first approximation, with the experiments [5–7] (Fig. 1). The results presented in [5] of the cumbersome numerical calculations according to the model dating back to the Thomas–Fermi model give the smallest energy of the oscillation mode for the case of C_{60} ~ 2.55 eV. Undoubtedly, it would be well to carry out numerical computations of the distribution of the electron density in C_{60} by the method of a density functional (see, for example, [17]) with the presence of an incoming electron. Yet, certain details of the cross section structure and the physics of the electron cumulation into hollow molecules can be refined further within the limits of an analytical model proposed by the author (1)–(4).

Space Distribution of an Electron in the Fullerene Molecule Cavity

Thus, the ψ-function by (3) is a function hyperbolically descending from the origin of the coordinates. However, from (3), it doesn't follow that the probability to find an electron at zero distance from the fullerene molecule's center is infinite. As we know [18], the probability that the electron is in the volume dV is $|\psi(r)|^2 dV = 4\pi r^2|\psi(r)|^2 dr$. Thus, the relative probability to find an electron in the spherical layer at a distance r from the fullerene molecule's center is determined by $\cos^2(k_n r)$ (Fig. 4). The maximum probability to find an electron in the hollow spherical molecule is actually achieved in its center, as the shell with such boundary conditions constantly reflects the electron to the structure center. The function $\psi(r)$ is not smooth at the origin of the coordinates and, what is more, is unlimited in the center of the focusing. The geometric potential of curved surfaces coined by V.Maslov in 1958 [14] operates in such a way in the case of hollow spherically symmetric molecules. It is this geometric potential that determines the cumulation of an electron to the center of the C_{60} structure and the peculiar features of the formation of the electron ψ-function in the fullerene cavity. The geometric potential turns into infinity at the origin of coordinates, and ψ(r) not only undergoes a kink but becomes infinite itself ($\cos(k_n r)/r \to \infty$ at $r \to 0$). The cumulation of an electron by the geometric potential is considered in this solution. Before determining the possible spectrum of the physical phenomena causing the appearance of this potential, we estimate the probability of the penetration of an electron through the potential barrier of the C_{60} shell.

Penetration through the "Geometric" Potential Barrier

The probability W of the penetration of an endoelectron through the "geometric" barrier is determined by a number of parameters [15]:

$$W \sim C\exp(-4\pi(2m(U-E))^{1/2}d/h)$$
$$\approx \exp(-1.08\times10^{10}(U-E_n)^{1/2}d).$$

One of them is the size of the barrier's characteristic width d [m], and the second one is the value of the potential U [eV]. Evidently, for the endoelectrons with the energy about 1 eV, d can be assumed equal to the radius of the $C_{60} \approx 0.36$ nm. Let the barrier height be 18 eV. According to these assumptions, the characteristic lifetime of the fullerene endoion is about $10^{-(8-9)}$ s. If there was coulomb repulsion between the tunneled electron and the fullerene, as in the case of the α-decay of atom nuclei, it would be almost impossible to detect the fullerene endoions, as by these estimations the electron lifetime inside the C_{60} is negligible. However, the decomposition of the fullerene endoion results in polarization of the so far neutral molecule of fullerene and the exoion focuses again to the center of the molecule by polarization forces. Thus, the ions with endoelectrons with the positive activation energy less than 12 eV exist during some period of time sufficient to detect and examine them [5–7] (Fig. 1). The polarization interaction between the C_{60} and the electron that has left the hollow molecule just now is responsible for their long existence. The polarization interaction returns the electron tunneled into the C_{60} shell back to the fullerene center if the energy of this electron is less than the energy of the polarization interaction between the electron and the fullerene molecule.

The polarization interaction of the C_{60} molecule with an external electron increases several times the efficient radius of the geometric potential; i.e., the electron radius is reflected back into the C_{60} molecule: $R \to R + r_{ind}$ with the lifetime growing correspondingly up to 10^{-4} s. Yet, for the electrons with the resonance activation energy E_n capable of being reflected specularly in the polarizing potential (mirror) of the C_{60} molecule, the lifetime in a hollow molecule grows even more times. This phenomenon of generation of a long-lived "soliton" in the region of C_{60} is proved by the resonance character of the attachment of the activated electrons, detected in the experiments, for instance, in [5–7] (Fig. 1), and by the analytic investigation being carried out in this work.

Polarization Interaction. Detailed Comparison of the Analytical Calculations with the Experimental Investigations

The efficient radius of the interaction of the C_{60} molecule with an electron can be estimated from the experimental data [6] (see Fig. 1a). According to the efficient cross section presented in Fig. 1a, the efficient radius of interaction $R_1 \approx (\sigma/\pi)^{1/2}$ is about 0.56 nm for the first resonance and $R_2 \approx 0.62$ for the second energy eigenvalue. Thus, the polarization interaction can substantially stabilize the fullerene endoion at certain energies of the endoelectron (not exceeding the energy of the polarization interaction) correlating well with the experimental observations [5–7].

Let us estimate $e\varphi_{ind}$, the characteristic energy of the polarization (induced) interaction of an electron with a fullerene molecule being polarized by it. The electric field of the C_{60} molecule dipole acting on the electron inducing the polarization of this very molecule [19] is

$$E(r) = 2P/r^3 = 2\alpha E(r)/r^3 = 2\alpha e/4\pi\varepsilon_0 r^5. \quad (7)$$

Integrating (7) with respect to r, we obtain the energy of the polarization interaction of the electron and the fullerene molecule $e\varphi_{ind}(r)$:

$$e\varphi(r) = -\alpha e^2/8\pi\varepsilon_0 r^4 = 0.065(r_0/r)^4 \text{ eV}. \quad (8)$$

Here, $r_0 = 1$, and r is measured in nm. Prescribing the distance from the electron to the fullerene molecule 0.26 nm, which corresponds to the maximum cross section of the electron's attachment to C_{60} (see Fig. 1a), we obtain $e\varphi(r_{ind} = 0.26) \approx 14$ eV. In the case of such energies, the de Broglie wave length (0.33 nm) is comparable with the radius of the fullerene molecule. Owing to the polarization of C_{60}, the further acceleration of the electron bombarding the fullerene takes place on several carbon ions (see p. 2), thusallowing the electron to penetrate into the inner cavity of the fullerene. On the other hand, if the energy of the incoming electron is more than the characteristic polarization energy ($e\varphi_{ind} \sim 14$ eV), the inertance of the electron with such kinetic energy can now counteract the polarizing forces. This should lead to a considerable decrease of the characteristic lifetime of the fullerene endoion depending on the endoelectron energy as its energy increases to about 14 eV. Such a regularity is actually observed in the experiments [5–7] (Fig. 1). Experimental observations [5–7] allow one to reach the conclusion that $e\varphi_{ind}$ for $C_{60} \sim 12$ eV.

Variation of the Mathematical Model to Consider the Polarization Interactions

Considering the polarization forces returning an electron back into C_{60}, it is possible to select the characteristic radius of a standing wave for the electron; not $R = 0.36$, but, for example, 0.26 nm more, that is, $R + r_{ind} = 0.62$ nm. In this case, the energy spectrum determined by the characteristic dimension of a polarization "well" according to (4) should be revised, hence,

$$E_{n=1-4} = 0.23;\ 2.1;\ 6.0;\ 11.8 \text{ eV}. \quad (9)$$

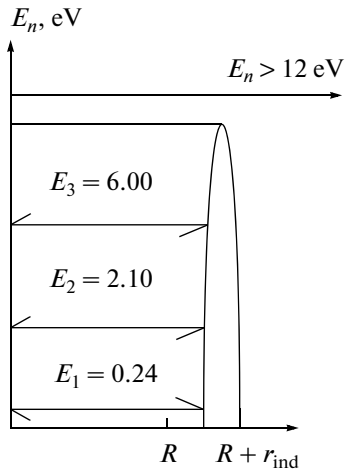

Fig. 5. The diagram of the revised model of the fullerene endoion considering the effect of the polarizing barrier ("mirror") and the corresponding increase (by r_{ind}) of the efficient dimension of the standing wave.

In the case of such variation, there is good correlation (9) with the experimental data presented in Figs. 1a and 1c. If we consider that r_{ind} for the first cross section peak is some smaller then for the second one, then the revised value $E_{n=1} \approx 0.28$ eV. Thus, during a part of time, 1 the electron is inside C_{60}, and, during the less part of time (Fig. 4), it is in the region of the action of the polarization forces determining the characteristic dimensions of the standing wave of the electron and the eigen energy spectrum of the spherical–symmetric quantum resonator for the electron (C_{60}). The revised model considering the polarization interaction between the C_{60} and the electron with energy $E_n \sim 0.2$ eV is presented in Fig. 5.

By the experimental observations (Fig. 1a), the resonance capture energy does not exceed 12 eV, thus, by (9), $k = 2n$; the principal number of endoelectrons stabilized by the polarization forces in the endoion $e_k@C_n$ does not exceed 6. According to [11], the C_{60}-k anions with $k = 6$ were not observed experimentally.

If there are created artificially some conditions under which fullerenes tightly cover a nanomaterial and the electrons can be on the surface of the nanomaterials only inside C_{60}, then the space charge layers modifying the integral properties of the composite materials containing hollow molecules can be formed in such materials.

The electric fields appearing round the endoions of fullerenes can several times (k times) exceed the electric fields around free electrons and reach or exceed the crystal fields (10^{10} V/m) on the surface of nanomaterials modified by endoions [4].

Modification of Properties of Nanomaterials at Formation of Double Layers of Spatial Charges on Their Surface

Under ordinary conditions, the C_{60} fullerene molecules form a crystal—fullerite [1]. In the last decade, the molecule of fullerene is the most often studied object by various spectral methods [1, 2]. Metal and semiconductor spraying by fullerene crystals—by fullerites—can results in a number of remarkable properties, in particular, in the coulomb melting of fullerites [3], the coulomb hardening of nanoobjects at their compression, a decrease of theheat conductance, growth of a nanomaterial's thermal resistance [4], etc. It can happen due to the capture of a substantial part of the nanoobject's electrons by fullerenes acting as traps for the electrons with energies in the range from 0.2 to 12 eV. The potential energy of the coulomb interaction of two charged ions in the fullerite with $k = 1$ is about 1.4 eV ($D \approx 1$ nm). By the results of this work, the accumulation of energy in the C_{60} cavity can reach $E_\Sigma = 2(E_1 + E_2 + E_3) \approx 17$ eV on one endoion $e_k@C_{60}$ with $k = 6$.

Calculations for Higher Fullerenes

Assuming that r_{ind} little changes in the case of higher fullerenes and its geometric efficient radius R is proportional to $N^{1/2}$ (N is the number of carbon atoms in the higher fullerene, where $4\pi R^2 \sim N$), the calculations of the eigen energies of the quantum resonators is a simple arithmetical problem. Spectrum (9) should be divided into the square of the geometric factor for the higher fullerene. This factor $\zeta_{70} = 1.03$ for C_{70}; $\zeta_{84} = 1.09$ and $\zeta_{90} = 1.12$.

So, for C_{70}, from (4) we obtain

$$E_{n=1-4} = 0.21;\ 1.9;\ 5.6;\ 11.1 \text{ eV}. \qquad (10)$$

Such reduction of the value of the resonance energy of the first peak for C_{70} is experimentally observed [5–7].

DEDUCTIONS

Quasi-stationary mutually resonant processes of cumulation and scattering (spray) of the de Broglie waves of electrons with **activation resonance energy** of such a dual fluctuating cumulative–dissipative process are for the first time analytically studied in this work. It is shown that the formation of a stationary standing wave occurs as the result of the localization of two resonance processes—cumulation and spray (dissipation)—in the region of a hollow molecule (the Helmholtz quantum resonator). The cumulation of the electron with nonzero energy to the center of a quantum resonator (hollow molecule) occurs due to the focusing polarization forces (polarization "mirrors" returning the electron to the molecule center). Polarization mirrors returning an electron to the fullerene center are determined by the generation of synergetic

(common) electric fields by a part of the positively charged fullerene cage. The displacement of the electron shell and the denudation of the positive charge of carbon atom nuclei happen at polarization. As a result of polarization, a part of the negative charge of the shell shifts into a far region from the electron that left the cavity. As the electron moves away from the center of the polarizing molecule, its energy decreases due to the action of the C_{60} dipole field, and the potential energy of the C_{60} electron shell grows. In this case, the kinetic energy of the electron is transferred into the energy of the C_{60} electron shell. The spray of endoelectrons from the C_{60} center is determined by their inertance (by an impulse or the total kinetic energy E_n, which is different from zero). The endoelectrons in endoions ($e_k@C_{60}$) have the positive total energy E_n, but, owing to the polarization forces acting on them on the part of the polarizing molecule, they are localized (constantly cumulate) to the center of this hollow spherically-symmetric molecule (for example, C_{60}).

The accomplished comparison of the analytically (see (9)) and experimentally found values of the resonance energies of the attachment to C_{60} [6] shows good agreement. Thus, for the first two resonances (Fig. 1a), the agreement does not exceed the experimental error [6] (≈10%). The conducted investigation has proved the importance not only of the polarization of a hollow molecule in the stabilization of an endoion of fullerene with endoelectrons with activation energy within the range from 0.2 to 12 eV but also the implication of the resonance (agreement) of the electron activation energy and the eigen energy of the Helmholtz quantum self-organizing resonator $e_k@C_{60}$ produced from C_{60} in the presence of an electron with the activation resonance energy.

The good agreement between the resonances was obtained experimentally, (Fig. 1a) and the eigen values of the energies of the quantum resonators calculated analytically by model (1)–(4) proposed by the author proved the possibility of the formation of negatively charged fullerene endoions $e_k@C_{60}$ with the captured electrons into the internal cavity (endoelectrons) with the resonance values of the activation energy.

The endoelectrons long-lived due to the resonance polarization interaction with C_{60} with the activation resonance energy in $e_k@C_{60}$ do not form chemical bonds with carbon atoms. Thus, we should not expect in the experiments any modification of the bonds and spectra of the C_{60} molecule in $e_k@C_{60}$ even at the level of 5–6 cm^{-1} for an electron, as in the case of intercalated fullerides [8–10], but it seems possible to study the resonance absorption in the energy range $\Delta E = E_i - E_{i-1}$, where $i = 2$ or 3 (Fig. 5)

The schrodinger stationary equation (Helmholtz homogeneous equation) (1) for hollow spherically symmetric molecules with regard for the polarization forces (coulomb "mirrors" suddenly appearing in the case of the tunneling of an electron through the C_{60} lattice) at the periphery of the polarizing molecules is analytically solved in this work as evidence for the phenomenon of cumulation of electrons in $e_k@C_{60}$ (see (3) and Fig. 5). Not only the eigen (resonance) values of the energy (9) but also the corresponding profiles of the eigen ψ-functions determining the probability of the existence of an electron in the molecule's cavity are calculated analytically. In accordance with this, there is analytically computed (3) the probability of the existence of an electron with the activation resonance energy in the cavity of a hollow molecule for a spherically symmetric quantum resonator (Fig. 4). It turns out that, regardless of the suppressing probability (≈70%) of the presence of an electron inside the fullerene molecule (Fig. 4), the efficient radius of an endoion exceeds the characteristic dimension of the molecule by the value r_{ind} due to the specificity of the dependence of the polarization forces on the distance to the polarizing molecule. As follows from the comparison of the analytical model and experiments [6] (Fig. 1a), the relative quantity $\zeta = (R + r_{ind})/R$—the scale correction for the polarization interaction (or simply the scale correction, according to terminology [12])—grows from $\zeta = 1.56$ up to $\zeta = 1.71$ with the increase of the incoming electron from 0.24 to 2.07 eV. Correspondingly, r_{ind} from the first resonance to the second one changes from 0.2 up to 0.26. It follows from the comparison of the analytical calculations and the experimental observations that the characteristic dimension of the efficient polarization of the C_{60} molecule (r_{ind}) (or the scale collection, according to terminology [12]) depends considerably on the energy of the incoming electron (if the values of the maximums in the attachment cross sections in [6] are measured with an accuracy of ≈10%). When the energies of the electrons are more than 8 eV, the attachment cross section sharply drops with the increase of the activation energy (Fig. 1) [5–7]. If the dependence of the efficient cross section of the attachment (the endoion radius) on the energy of an incoming electron is considered in the analytical model, the accuracy of the agreement of the energies of the first and the second resonances calculated by (4) with the experimentally established activation resonance energies is ≈90% (Fig. 1a).

Thus, in this work, there is proposed an actual **physical mechanism of resonance capture of an electron by polarizing hollow molecules** and its simple analytical model allowing one to find the spectrum of the activation of electrons and the eigen spectrum of the quantum resonator $e_{1-3}@C_{60}$ (see (9)) in agreement with the experimentally observed resonances in the cross sections of the electron attachment to C_{60} [6] with an accuracy not worse than ±10% (for $E_{1\text{ and }2}$). The proposed model allows one to carry out verification of the experimental results obtained in [5–7] and to refine the scale correction for the polarization interaction. It is proved in the work the importance of the polarization of a hollow molecule for the stabilization of an

endoion of fullerene with endoelectrons with the energy from 0.24 to 12 eV, as well as the significance of the resonance agreement of the eigen energies of the quantum resonator—fullerene—with the electron kinetic energy. The electron kinetic energy serves as the energy of activation of the oscillating resonance process (capture of the internal "soliton") formed by the resonance polarization barrier (the coulomb 'mirror').

The effect of the resonance interaction of hollow molecules with electrons with activation energies from 0.24 to 12 eV is determined by the following:

—the polarization interaction (the polarization coulomb "mirror" focusing electrons into the cavity);

—the geometry of a hollow molecule of fullerene, and

—the energy resonance (agreement of the eigen energy of the quantum resonator itself with the electron activation energy).

On the basis of the comparison of the experimental observations of the resonance attachment cross section [5–7] and the analytical calculations of the energy spectrum (see (9)), there is substantiated the possibility of the formation and long existence of endoions (or endoelectrons) of fullerene $e_k@C_{60}$ with $n = 3$ or $k = 6$ (according to the Pauli principle).

The effect of electron cumulation into hollow molecules (traps for electrons) can be used for control in semiconductors (concentration of charge carriers, thermal and electric properties) and for the hardening of materials with free electrons. The property of fullerenes to catch electrons and to form fullerene endoions of endoelectrons opens up the possibility to modify nanomaterials using coulomb forces and synergetic (intrinsic, general) electric fields [3, 4]. The author proves in his works [3, 4] that this femtotechnology of the microworld founded by Rutherford, who discovered a substantial partition of the charge in atoms, starts to show up considerably even in the nanoworld due to the quantum properties of the electron. The quantum properties of polarizing resonators (showing up in the dependence of the attachment cross section on the energy of the electrons) self-congruent with the resonance energy of the electron activation can determine the resonance (oscillatory) character of the variation of nanocomposite microparameters in relation to the volume concentration of quantum modifiers (for instance, C_{60}).

We have studied C_{60} as an example, the cumulation of the de Broglie waves (and of ψ-function) of electrons in polarizing, quantum, and spherical resonators—hollow molecules. The method tested for C_{60} and higher fullerenes can be used to simulate the phenomena determined by the polarization of molecules as in the case of nanotubes as well as other molecules with a great values of the polarizability (α). The mechanism of the resonance cumulative–dissipative capture of an electron and the formation of a negative ion $e_k@C_n$ with an electron inside the molecule cavity according to the diagram in Fig. 2 can be modified for the mechanism of the cumulative–dissipative capture into the internal cavity of polarizing atoms with the following formation of endohedral structures—fullerenes and nanotubes, inside which one or several electrons and atoms are enclosed. The obtained results can be used to describe the polarization processes between electrons with the activation resonance energy and any complex polarizing molecules.

In conformity with the available experiments [3–5], the performed analytic calculations and their perfect agreement with these experiments considering the polarization interactions in this work, there are classified quantum points, lines (wires), and wells according to the sign of the total energy of the lectrons at infinity from the quantum "box" capturing the electron (with $E > 0$ or with $E < 0$). In classic strictly finite quantum structures, the total energy of a quantum particle $E_n < 0$ (of FQ-particle) and in infinite quantum structures limited by polarization forces, the total energy of a quantum particle at the infinity from the polarizing quantum box $E_n > 0$, yet polarization forces localize such charged particles with resonant kinetic energies $E_n > 0$ (IQ-particles) in the region of the polarizable quantum "box" (Fig. 1). IQ-particles cumulate the total energy of the total energy of an electron coming from infinity in the region of the quantum "box". Contrastingly, FQ-particles are formed at cumulation of electrons and the unset of a part of the total electron energy (energy dissipation into the vicinity) in the form of the electromagnetic radiation.

The examined properties, determined by formation of charged endohedral structures and charged bilayers of such structures, in particular of negative ions $e_k@C_n$, on the surface of positively charging nanomaterials are of scientific and practical interest and call for further theoretical and detailed experimental investigations.

CONCLUSIONS

Based upon numerous experiments (see, for example, [5–7]) and references in these works, the author proved by the example of the resonance capture of an electron by a quantum resonator—C_{60}—that, in the microworld, there occurs self-organization of the cumulative–dissipative structures discovered and studied in the mesoworld in [20]. The cumulation structures under our investigation, unlike diffusion structures, discovered by Turing, are formed by the collapse to the center of convection currents [20], but not only in diffusion fluxes as in [21]. In cumulative–dissipative convective structures, there is possible the self-cumulation of mass, energy, impulse, charge, and electric field as determined by coulomb (polarization) forces. This idea is in outline stated by the author in [20] and detailed in this work with regard for the importance of quantum properties of electrons and quantum properties of the C_{60} resonator. Thus, in this

work it is once again proved the possibility of the self-focusing (cumulation) of a material determined not by gravitation forces but by electric forces,being 10^{40} times stronger than gravitation ones (and v/c times stronger than magnetic forces). E.I.Zababakhin [22], one of the creators of the most powerful bomb, could not expect such a powerful coulomb cumulation of the energy–mass–impulse fluxes.

ACKNOWLEDGMENTS

This work was carried out with the partial support of the Ministry of Education and Science of the Russian Federation, state contract no. 02.513.12.3061, and the Russian Foundation for Basic Research (project no. 09-08-13682-ofi_ts).

REFERENCES

1. Sidorov, L.N., Yurovskaya, M.A. et al., *Fullereny*, (Fullerenes), Moscow: Ekzamen, 2005.
2. Eletskii, A.V., Endohedral Structures, *Usp. Fiz. Nauk*, 2000, vol. 170, no. 2, p. 113–142.
3. Vysikaylo, Ph.I., Generation of a Fullerene Ion and Coulomb Melting of Fullerites, Abstracts of Papers, *Nauchno-prakticheskaya konferentsiya "Nanotekhnologii proizvodstvu—2009"*,Conf. "Nanotechnologies for Industry—2009), Fryazino, 2009, pp. 18–19.
4. Vysikaylo, Ph.I., Physical Fundamentals of Hardening of Materials by Space Charge Layers, *Elektr. Obrab. Mater.*, 2010, no. 4, pp. 4–12.
5. Tuktarov, R.F., Akhmet'yanov, R.F., Shikhovtseva, E.S., Lebedev, Ya.A., and Mazunov, V.A., Plasma Oscillations in Fullerene Molecules at Electron Capture, *Pis'ma Zh. Eksp. Teor. Fiz.*, 2005, vol. 81, no. 4, pp. 207–211.
6. Jaffke, T., Illenbergen, E., Lezius, M., Matejcik, S., Smith, D., and Mark, T.D., Formation of C_{60} and C_{70} by Free Electron Capture. Activation Energy and Effect of the Internal Energy on Lifetime, *Chem. Phys. Let.*, 1994, vol. 226, pp. 213–218.
7. Huang, J., Carman, H.S. and Compton, R.N., Low-Energy Electron Attachment to C_{60}, *J. Phys. Chem.*, 1995, vol. 99, p. 1719–1726.
8. Wang, K.A., Wang, Y., Dresselhaus, M.S., et al., Raman Scattering in C_{60} and Alkali–Metal–Doped C_{60} Films, *Phys. Rev. B*, 1992, vol. 45, p. 1955–1963.
9. Denisov, V.N., Mavrin, B.N., et al., Raman Scattering and Lattice Dynamics of Fullerides M_xC_{60}, *Optics and Spectroscopy*, 1994, vol. 76, no. 2, p. 242–253.
10. Dresselhaus, M.S., Dresselhaus, G., and Eklund, P.C., *Science of Fullerenes and Carbon Nanotubes*, London: Academic Press, 1995.
11. Reed, C.A. and Dolskar, R.D., Discrete Fulleride Anions and Fullerenium Cations, *Chem. Rev.*, 2000, vol. 100, pp. 1075–1120.
12. Nafikova, E.P., Asfandiarov, N.L., Fokin, A.I., and Lomakin, G.S., Usage of Integral Atom Model for Estimation of Life–Time of Negative Molecular Ions in Relation to Autoremoval of Electron, *Zh. Eksp. Teor. Fiz.*, 2002, vol. 122, no. 4(10), pp. 700–706.
13. Belov, V.V., Dobrokhotov, S.Yu., Maslov, V.P., and Tudorovskii, T.Ya., Generalized Adiabatic Principle For Description of Electron Dynamics in Bent Nanostructures, *Usp. Fiz. Nauk*, 2005, vol. 175, no. 9, p. 1004–1010.
14. Maslov, V.P., Asymtotics of Eigenfunctions of the Equation $\Delta u + k^2 u = 0$ with Boundary Layers on Equidistant Curves and Scattering of Electromagnetic Waves in Waveguides, *Dokl. AN SSSR*, 1958, vol. 123, p. 631–638.
15. Landau, L.D. and Lifshits, E.M., *Teoreticheskaya fizika*, (Theoretical Physics), vol. 3 of *Kvantovaya mekhanika. Nerelyativistskaya teoriya*, (Quantum Mechanics. Nonrelativistic Theory), Moscow: Fizmatlit, 1974.
16. Polyanin, A.D., *Spravochnik po lineinym uravneniyam matematicheskoi fiziki*, (Handbook of Linear Equations of Mathematical Physics), Moscow: Fizmatlit, 2001.
17. Yang, S., Yoon, M., et al., Electron Transfer and Localization in Endohedral Metallofullerenes: Ab initio Density Functional Theory Calculations, *Phys. Rev. B*, 2008, vol. 78, pp. 115435.
18. Gol'din, L.L. and Novikova, G.I., *Vvedenie v atomnuyu fiziku*, (Introduction into Atom Physics), Moscow: Gl. red. fiz.–mat. lit., 1969.
19. Landau, L.D. and Lifshits, E.M., *Teoreticheskaya fizika*, (Theoretical Physics), vol. 2 of *Teoriya polya*, (Theory of Field), Moscow: Fizmatlit, 2006.
20. Vysikaylo, Ph.I., Cumulation of Electric Field in Dissipative Structures in Gas–Discharge Plasma, *Zh. Eksp. Teor. Fiz.*, 2004, vol. 125, no. 5, pp. 1071–1081.
21. Turing, A.M., The Chemical Basis of the Morphogenesis, *Proc. Roy. Soc. B.*, 1952, vol. 273, pp. 37–71.
22. Zababakhin, E.I. and Zababakhin, I.E., *Yavleniya neogranichennoi kumulyatsii*, (Phenomena of Unlimited Cumulation), Moscow; Nauka, 1988.

ISSN 1068-3755, Surface Engineering and Applied Electrochemistry, 2010, Vol. 46, No. 6, pp. 558–569. © Allerton Press, Inc., 2010.
Original Russian Text © P.N. Belkin, 2010, published in Elektronnaya Obrabotka Materialov, 2010, No. 6, pp. 29–41.

ELECTRICAL SURFACE TREATMENT METHODS

Anode Electrochemical Thermal Modification of Metals and Alloys

P. N. Belkin

Nekrasov State University, ul. Pervogo Maya 14, Kostroma, 156961 Russia
e-mail: belkinp@yandex.ru

Received June 8, 2010

Abstract—This scientific review is devoted to the mechanism of the anode heating in aqueous electrolytes and its application for the heat and thermochemical treatment of steels and titanium alloys. The heating and electrochemical peculiarities of the anode hardening are considered, the technological possibilities for improving the operational properties using nitrohardening, carbonizing, or oxidation are described. A short history of the studies and designs including industrial devices for the technologies of the anode hardening is presented.

DOI: 10.3103/S1068375510060049

INTRODUCTION

This review is devoted to the scientific and engineering results of the anode chemical thermal treatment obtained based on the ideas of Boris Romanovich Lazarenko. The electric discharges were of primary importance among the plurality of his interests. The more so, as the thesis work of this scientist (a comparative analysis of the erosion stability of current conducting materials for enhancing the service time of electric contact devices) was the initial step towards his famous discovery. Making and breaking the electric contacts in a liquid was believed to decrease erosion, which failed to be confirmed. Instead, the discharges in both dielectric and conducting liquid media became of special of interest. In the 1960s, a research group that studied the discharges in aqueous electrolytes worked at the Institute of Applied Physics of the Moldova Academy of Sciences under the supervision of Academician B.P. Lazarenko. The role of the electric discharges arising in the electrolytic circuit breakers was determined, the specific nature of the gaseous discharge based on the electrolyte electrodes was revealed, and the contribution of the heat and electrochemical processes in the phenomena under study was defined. Those works were performed by A.A. Faktorovich and V.N. Duradzhi [1].

Further evolution of the subject was progressed by the wide contacts with scientific schools, which developed the application aspect of the discharge phenomena in electrolytes. Among the latter were the electrolyte heating for hardening or pressure treatment, chemical thermal modifying of metals and alloys, and purifying the surfaces from various impurities [2–4].

Real electrochemical thermal technologies started to be used in the Soviet Union at a Khar'kov tractor plant in the 1930s. The cathode version of the heating of the workpieces or blank parts was studied mainly as an electrochemical process. Scientists of Great Britain, France, Germany, India, and Japan started publishing materials dealing with the electrolytic heating of metals and alloys in the 1950s. About in that period, separate developments were patented, mostly by Japanese authors. The native results of the research of cathode heating phenomenon along with the proposed technical solutions and creation of the equipment for their realization were comprehended and described in the monographs of I.Z. Yasnogorodskii.

In the 1960s, V.S. Vanin showed the possibility of the effective use of the anode version of heating for the chemical thermal treatment. Gradually, this became a leading direction in the activity of the aforementioned group of the Moldavian research workers and other groups. In the modern *Chemical Encyclopedia*, the anode diffusion saturation is called an electrochemical thermal treatment. Below, the main aspects of the mechanism of this phenomenon and the variants of its practical use are considered.

THERMOPHYSICAL ASPECTS OF THE ANODE HEATING

Anode heating is realized in a three-phase system containing a vapor–gas shell (VGS) to separate the metal anode from the aqueous solution of the electrolyte. It is the VGS that the heat is released from owning to the current passage. Figure 1 shows the heat flows from the shell, where q_l is the density of the heat flow from the shell into the electrolyte solution; q_s denotes the density of the heat flow spent for the electrolyte evaporation; and q_a implies the density of the heat flow from the shell to the anode. Without a complete and stable shell, the anode heating up to temperatures of 200–250°C appears impossible. It is shown that the shell formation occurs due to the local boiling of the electrolyte in the anode region, where the major por-

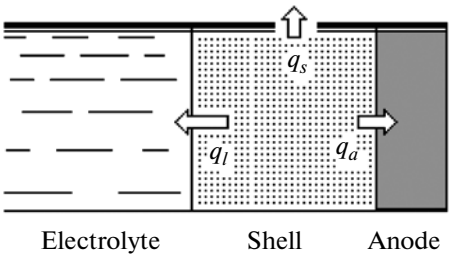

Fig. 1. Scheme of heat flows in an anode vapor–gas shell.

tion of the power source energy is released. The effect of the electrolysis gas liberation is relatively small. The requirements for the electrolyte content in which the heating of steel, titanium, and some other alloys is possible are established. A sufficiently high specific conductivity of a solution (no less than 0.5 Ohm^{-1} cm^{-1}), the temperature of the chemical decomposition of its components up to 400–500°C, and the undesirable high moisturizing of the treated metal with the electrolyte are necessary. The recommended value of the contact angle is no less than 50° [5].

A model of the anode heating in which the current passage is described by the electrical discharges in a vapor–gas medium is known [6]. Along with it, a conception of the emission of anions from the boiling electrolyte and their transfer onto a specimen–anode in the electric field used in this study was developed [7, 8]. The volume power of the heat source in the VGS can be expressed in various ways with or without account for the effect of the spatial charges, i.e., in accordance with Ohm's law [9]. The distribution of the temperature in the shell, as well as the volt–ampere (VAC) or voltage–temperature characteristics (VTC) of the anode heating may be calculated based on the solution of the equation of the heat conduction in the shell under various boundary conditions [10]. Typical VTC and VAC characteristics of the anode heating experimentally obtained are shown in Fig. 2.

The specific character of the anode heating consists in the fact that an increase in the voltage induces a growth of the power that is released despite a decrease in the current, which results from the VGS thickening, owning to the enhancement of the vapor generation. Such a dependence is observed on the VTC rising curve. The VTC decreasing curve is, obviously, correlated with a change of the VGS type of conductance. On the one hand, this site may be accounted for by the appearance of the electrical discharges, which induce sputtering of the electrolyte when its drops cool the anode–workpiece. On the other hand, the bombarding of the electrolyte surface by the iron ions upon the dissolution of the steel anode–workpiece may be responsible for the appearance of the cooling droplets.

The density of the heat flow from the shell into the electrolyte is proportional to the voltage of the heating. The description of the heat exchange between the shell and the workpiece is complicated by the absence of the material heat-release surface: its analog is a surface with a maximal temperature in the VGS [11], which makes it difficult to use the heat-transfer coefficient. The calculation of the density of the heat flow using the data of the experimental measurements of the temperature showed that the heat flow from the VGS into the anode–workpiece changes its sign at a certain value of the vertical coordinate (Fig. 3). The surface

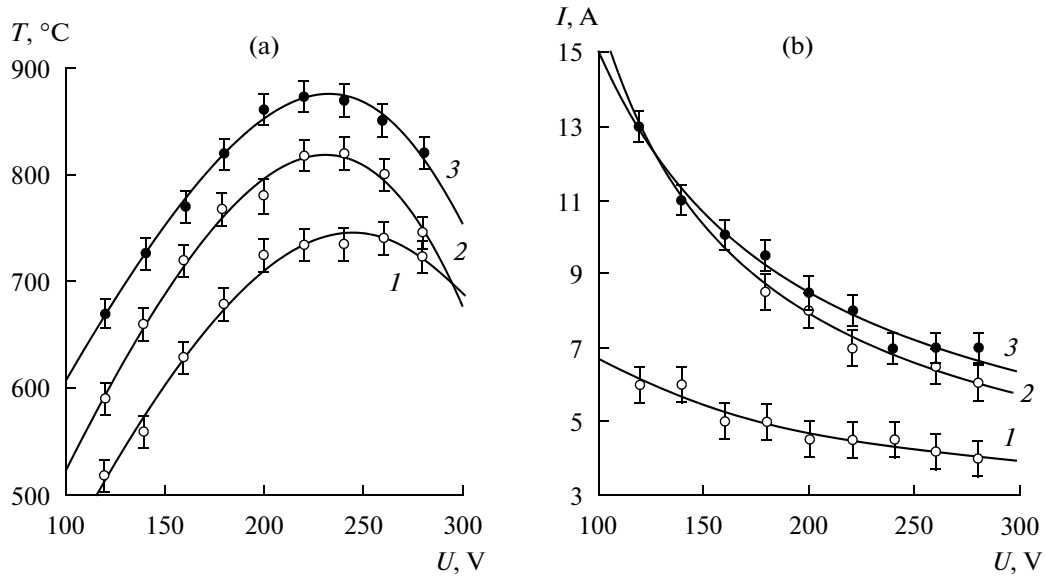

Fig. 2. Volt–temperature (a) and volt–ampere (b) characteristics of heating the 10-mm diameter and 25-mm-long steel specimens in a 10% solution of ammonium chloride. The natural convection and depth of immersion of the upper edge of the specimen, mm: (*1*) 0; (*2*) 45; (*3*) 90.

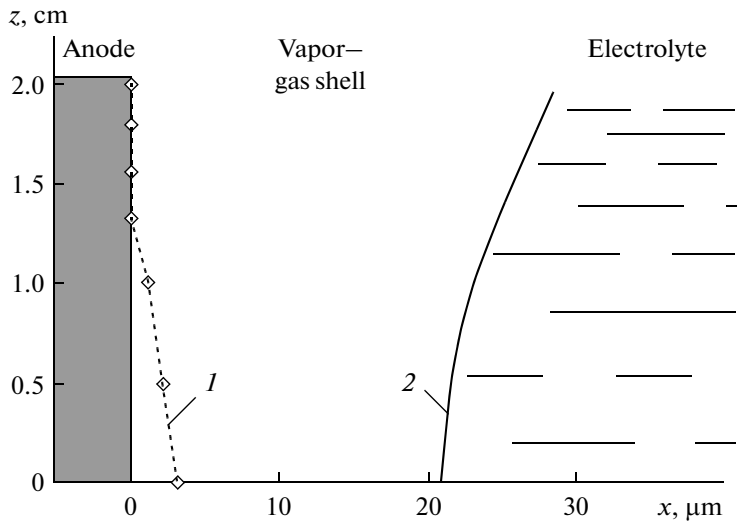

Fig. 3. Surface of maximal temperature (*1*) and profile of the vapor–gas shell (*2*) at a voltage of 240 V.

with the maximal temperature may coincide with the surface of the anode in its upper part, which suggests the change of direction of the heat flows (Fig. 4) [12]. The formally determined heat-transfer coefficient gives average values, which vary from 1900 to 3100 Wt/(m^2 K) in the range of voltages of 180–300 V.

The change of the sign of the density of a heat flow from the VGS to the workpiece is correlated with the presence of the vertical gradient of the temperature, which can be reduced by means of the controlled flowing of the workpiece that is being immersed (Fig. 5). This is done using extra vertical or radial flows of the electrolyte, its rotation, etc.

High rates of heating up to 100 grad/s result from the small inertia of the thin VGS (tens of micrometers). The temperature range from 400 to 1000°C allows thermal treatment of various alloys; rapid heating makes it possible to avoid the growth of the grain and preserve their high diffusion susceptibility. The presence of volatile compounds in the solution creates conditions for the diffusion saturation of the anode–workpiece, and the high-rate heating ensures fast achievement of an equilibrium concentration of the components that were adsorbed. The motion of the vapor–gas blend guarantees the absence of stagnant areas and provides for the inlet of the active medium and products of the reactions. The local treatment of a working section is easily performed by its immersion

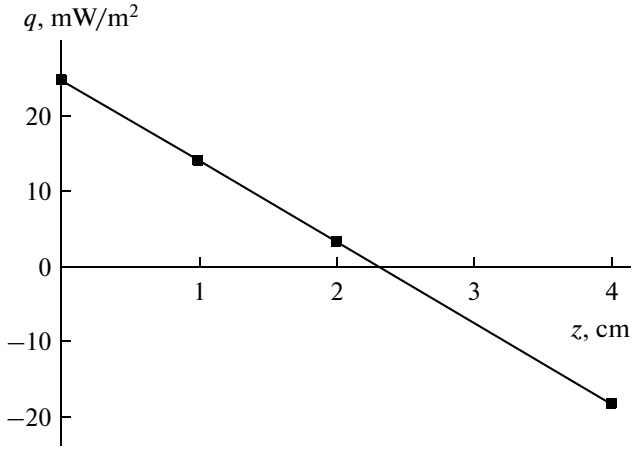

Fig. 4. Density of the heat flow through the side surface of the cylindrical 4-cm-long anode depending on the vertical coordinate.

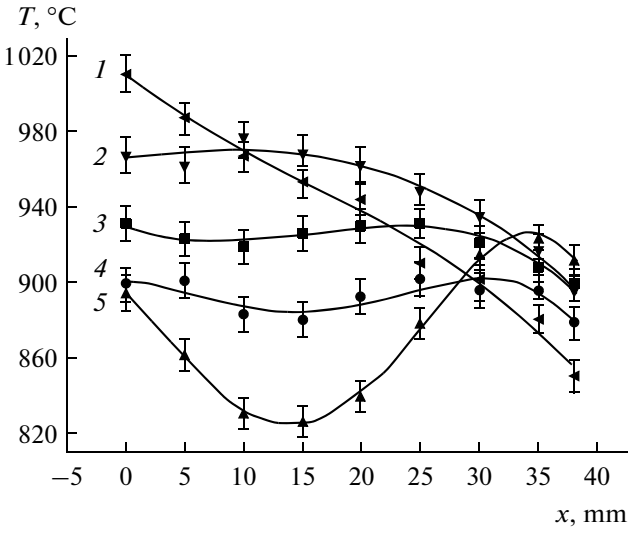

Fig. 5. Temperature dependence on the vertical coordinate at the anode axis. (*1*) flowing with a single jet; (*2*, *3*, *4*, *5*) flowing with four jets. Distance from the cell axis to the axes of the holes, mm: (*2*) 10; (*3*) 13; (*4*) 16; (*5*) 19. The voltage is 200 V.

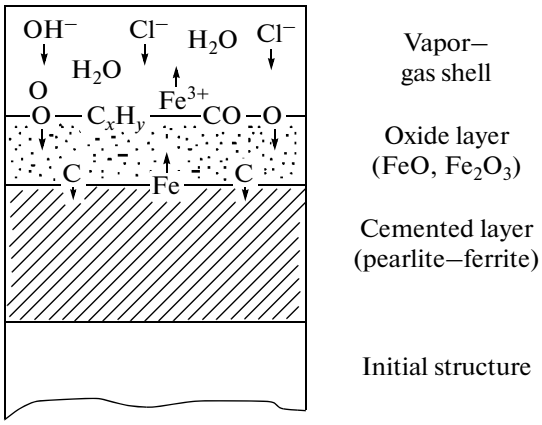

Fig. 6. Scheme of the anode processes of oxidation, dilution, and saturation with carbon upon heating in the aqueous solution of the electrolyte.

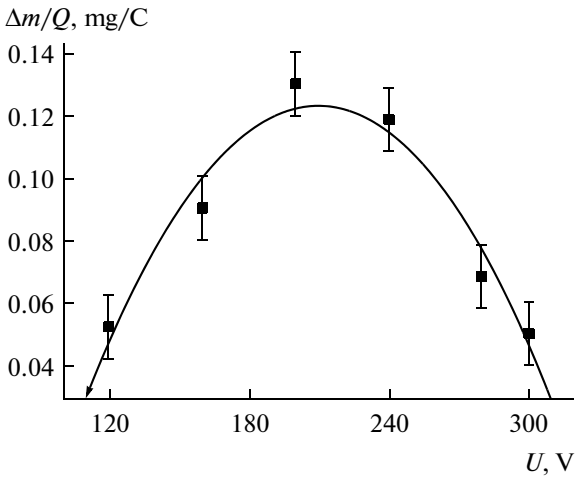

Fig. 7. Dependence of the specific yield of the specimens from steel 20 (12-mm diameter, 10-mm length) on the voltage in a 15% solution of ammonium chloride for 5 min.

into the electrolyte or by the electrolyte jet fed onto it. The voltage switching off leads to hardening in the same electrolyte.

ELECTROCHEMICAL PECULIARITIES OF THE ANODE HEATING

On the interface of the anode–VGS, the processes of oxidation and dissolution of the anode material, along with its absorption (for instance, by carbon upon cementing), occur (Fig. 6). An oxide layer forms due to the electrochemical and chemical processes, including high-temperature oxidation.

The decrease in the mass of the steel anode, which was accounted for by the anode dilution, was found to depend on the electrolyte's composition and the concentration of its components, which was confirmed by the anion mechanism of conduction of the VGS [13]. For example, steel specimens dissolve easily in the solution of ammonium chloride, not so easily in the ammonium nitrate, and still less easily in ammonium sulphate or acetate. The leading role of the electrolyte anions is also supported by the studies of chromium and copper dissolution under conditions of the anode heating [14, 15].

The voltage enhancement and, hence, the heating temperature increase at the VTC rising curve involves a decrease in the anode mass and an increase in the content of the products of the anode dissolution in the electrolyte. The maximal specific yield of the anode material is observed at a voltage of 200 V (Fig. 7), which is relevant to the maximal temperature of heating of 890°C in a 15% solution of ammonium chloride. This resulted from heating the specimens made of 20, 50, and U8 steels in ammonium chloride solutions of various concentrations (5, 10, and 15%).

The significance of the high-temperature corrosion is confirmed by the factor that the temperature (and not the voltage of heating) affects the decrease in the anode mass. In addition, an increase in the concentration of the ammonium chloride from 5 to 10% leads to the increase of the specific yield of the anode material at identical temperature of 950°C. This fact attests to the marked contribution of the electrochemical dissolution itself, which is proportional to the concentration of anions in the shell, in comparison to the high-temperature oxidation. A further increase of the concentration of the ammonium up to 15% inhibits reaching the heating temperature of 950°C. As a result, the specific yield of the anode material decreases despite the higher concentration of anions (Table 1) [16].

Table 1. Characteristics of heating of the specimens from steel 20 (the diameter is 12 mm, the length is 10 mm) in NH_4Cl solutions for 5 min

Solution concentration, %	5	10	15
Max. temperature T_{max}, °C	950 ± 10	950 ± 10	890 ± 10
Voltage, corresponding to T_{max}, V	300	240	200
Current, corresponding to T_{max}, A	7.7 ± 0.3	7.8 ± 0.2	8.5 ± 0.2
Specific yield of metal, mg/C	0.134	0.158	0.137

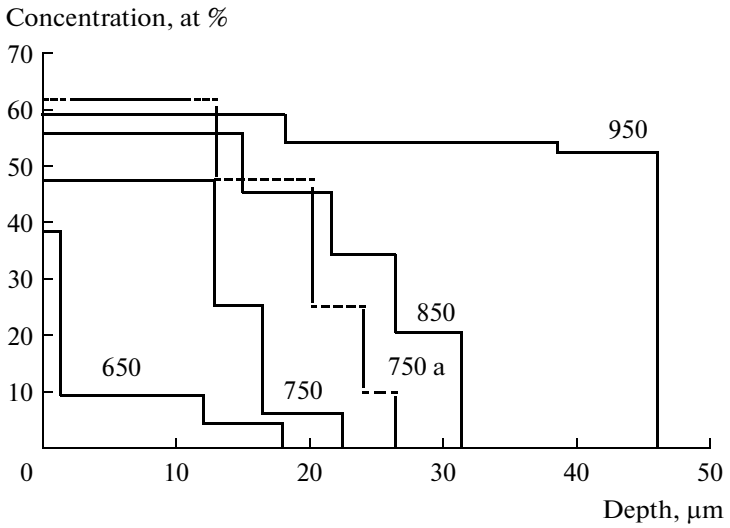

Fig. 8. Concentration profile of oxygen in the steel 10 specimen after the anode heating in the electrolyte, which contains 10% ammonium chloride, 5% nitrogen acid and 10% glycerin. The duration of the heating is 7 min, and the temperature (°C) is indicated on the lines; the cooling occurs in the electrolyte, except for the curve 750 a, which is for cooling in air.

The iron mass in the electrolyte exceeds the decrease in mass of the steel electrode; their difference corresponds to the mass of the oxygen that entered into the surface oxide layer [17]. Owning to this, the decrease of the specimen's mass after its anode heating reflects the integrity of the transfer processes of iron into the electrolyte, oxygen into the heated specimen, and the possible saturation by carbon or nitrogen.

The role of high-temperature oxidation is supported by the data of the nuclear backscattering (NBS) of protons: the oxygen content in the surface layer increases substantially in proportion to the growth of the saturation temperature, particularly, followed by its cooling in air (Fig. 8). An electrolyte that contains nitric acid and glycerin, along with ammonium chloride, involves the formation of thicker oxide layers versus the chloride–carbamide solution. A smaller depth of the oxygen penetration is typical of heating 12X18H10T austenitic stainless steel. Note that the oxygen concentration in most cases is insufficient to form a complete oxide layer of any composition; therefore, it is more correct to talk of a surface layer that is enriched by the iron oxides to a certain extent (Table 2).

Iron oxide is known to be a solid omission solution formed on the basis of a chemical compound but having a defect lattice. First, the free nodes of the lattice, which must be occupied by iron atoms, and, secondly, the nodes that belong to oxygen atoms but are occupied by iron atoms are considered to be the defects. Such a structure facilitates the diffusion mobility of the iron atoms, which can drift to the surface, create new oxides, and accelerate the oxidation process [8]. In addition, the upper oxide layer upon the anode heating contains pores of up to 100 nm and cracks, which enables the transport of iron ions from the specimen to the solution, the oxygen from the shell to the surface layer of the metal, and also allows easy penetration of the nitrogen or carbon atoms into the main metal [16].

Table 2. Maximal oxygen content in the surface layers of the specimens according to the data of the NBS of protons (at %)

Temperature, °C	Composition of the aqueous electrolytes			
	10% ammonium chloride, 20% carbamide	10% ammonium chloride, 5% nitric acid, 10% glycerin	10% ammonium chloride, 20% carbamide	10% ammonium chloride, 8% ammonia, 10% acetone
	Steel 10		12X18H10T	
650	1.8 (43)	11.9 (38)	1.2 (27)	1.1 (27)
750	6.1 (30)	51.7 (47)	1.2 (29)	1.2 (29)
850	8.2 (34)	93.9 (56)	4.1 (31)	1.9 (11)
950	14.5 (53)	102.4 (59)	9.4 (33)	

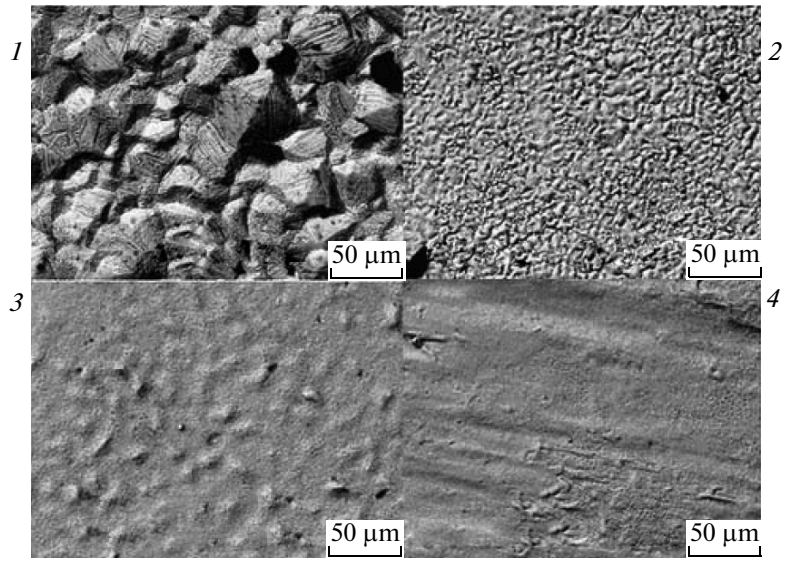

Fig. 9. Surface morphology of steel 20. Heating at 900°C for 10 min, cooling in air. Chloride (*1*), nitrate (*2*), sulphate (*3*) and ammonium acetate (*4*) REM JSM–5610.

The phase composition of the oxide layer was studied using multiple X-ray structural analysis. The iron oxidation depends, firstly, on the electrolyte composition and, secondly, on the composition of the heating material. Upon heating steel 3, FeO oxide was found in the solutions of chlorhydric acid [18]; after the cementation of Armco iron, FeO and γ-Fe_2O_3 [19] were discovered in the solution of ammonium chloride with glycerin; the cementation of steel 08 cf or iron graphites ZhGr1D2 and ZhGr0.5D2 leads to the formation of an oxide layer that contains the superposition of Fe_3O_4 and FeO phases [20]. The same oxides were observed after nitrocementation of steel 10 in a solution of ammonium chloride with carbamide [21]. Steel 45 heating in an ammonium acetate solution also leads to the formation of Fe_2O_3 and Fe_3O_4. The intense oxidation of steel 45 in this solution allows obtaining the thickest oxide layers, which may reach 180 μm, according to the data of metallographic analysis. Such layers have high protective properties in a solution of chlorhydric acid of 0.5 M. Their formation is accompanied by enriching the potential by more than 0.6 V, increasing the resistance, and decreasing the electrode capacity [22]. Similar results were obtained from the study of the corrosion resistance of medium-carbon steels after their nitrohardening in aqueous electrolytes [23, 24].

The combined role of the electrochemical dissolution and formation of the oxide layer determines the different roughness of a steel 20 surface observed after heating in various solutions with the other conditions being equal [9].

The anode dissolution of titanium that is heated in an ammonium chloride solution as well increases with the growth of the voltage and the heating temperature (Fig. 10). Titanium differs from the steels under study in that its quantity in the electrolyte coincides with a decrease of the specimen's mass (the diameter is 8 mm, the length is 10 mm) in the first 10 min of the treatment (Fig. 11). This is indicative of the small mass of the oxide layer. The further divergence of the curves may be accounted for by the analytical errors: the possible delaminating of part of the oxide layer or neglecting other titanium oxides. The estimation of the titanium concentration in the solution suggested that the

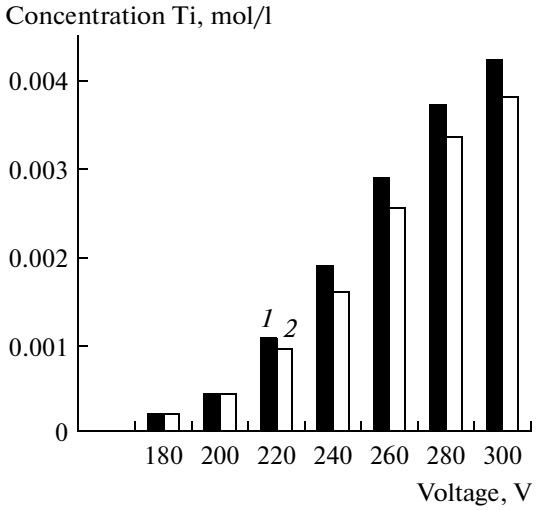

Fig. 10. Effect of the heating voltage on the dissolution of VT1-0 alloy for 30 min. The electrolyte is a 10% solution of ammonium chloride. The temperature of the heating is from 700 to 950°C. (*1*) content of titanium calculated over the absolute change of mass of a specimen; (*2*) content of titanium calculated over the total content of titanium in the solution.

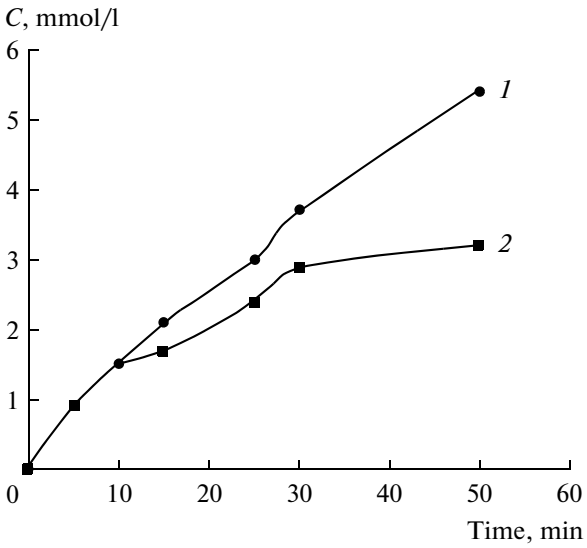

Fig. 11. Dissolution of VT1-0 alloy in a 10% solution of ammonium chloride. The temperature and voltage of heating are 1000°C and 260 V, relatively. (*1*) content of titanium according to the mass change of the specimen; (*2*) content of titanium in the solution.

main product of the dissolution is TiO_2 oxide, which was detected on the surface of the specimens from the X-ray structural analysis [25]. TiO formation is also registered in the first two minutes of treatment, but this phase is not discovered upon more lengthy saturation [26]. Therefore, ignoring the compounds with a high content of titanium might lead to underestimated results.

The concentration of ammonium ions is found to decrease in the process of exploiting the aforementioned electrolytes, owning to their being evaporated into the shell or adsorbed by the finely divided indissoluble compounds (Fig. 12). A saccharose-based electrolyte exhibits a less intensive decrease of ammonium ions versus that of a glycerin electrolyte. The fact that finely divided oxo- and hydrooxocompounds of iron fail to be formed in the saccharose electrolyte may be responsible for the above distinction. Hence, a small share of ammonium ions is adsorbed on the surface of the indissoluble compounds. On the whole, the decrease of the concentration of ammonium ions results mainly from their evaporation from the electrolyte surface. Similarly, the decrease of the concentrations of ammonia and ammonium ions occurs at heating in a 10% solution of ammonium chloride without carbon-bearing additives or in the composition for nitriding [17].

The concentration of chloride ions decreases much slower than that of ammonium ions and, actually, independently of the nature of the carbon-bearing component of the working electrolyte. There are not signs of the release of molecular chloride on the anode. Chloride is assumed to perform a closed cycle of electrochemical conversions [17]. Hydrated chloride ion $Cl^- \cdot nH_2O$ evaporates from the vapor–liquid interface. The hydrate complex disintegrates upon reaching the anode surface. Part of the chloride ions is removed from the vapor–gas shell into the atmosphere, where it is recombined with ammonium ions that are also present in the shell. Ammonium chloride precipitates on the walls of the facility, forming a white coating.

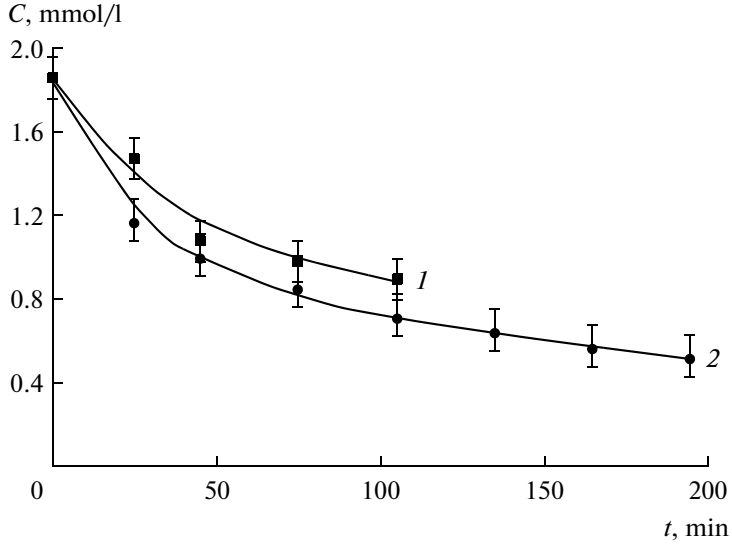

Fig. 12. Change of the concentrations of ammonium ions and ammonia (combined) in exploiting the electrolytes based on ammonim chloride (10 wt %) with an addition (*1*) of 10% of saccharose and (*2*) of 10% of glycerin. The temperature is 880°C, $U = 240$ V, steel 30, the diameter is 10 mm, and the length is 15 mm.

Table 3. Certain characteristics of electrolytes with various additives

Component	Max thickness of the layer after 7-min treatment, μm	Rate of the concentration decrease from 10%, %/h	Cost of 1 kg, rubles	Energy consumption, kW/cm^2	Carbon potential, %
Acetone	139	0.75	125	0.28	0.9
Glycerin	132	0.51	140	0.32	0.8
Saccharose	114	0.41	25	0.36	0.7
Ethyleneglycol	42	0.57	125	0.35	0.6

TECHNOLOGICAL PROCESSES OF THE ELECTRO–THERMAL TREATMENT

The saturation of wares with light elements occurs only in such solutions where the pressure of the vapors of the saturating substance is higher than that of the solvent. The content of the substance in the shell is determined by its temperature of boiling and the conditions of the vapor motion, i.e., by the peculiarities of the supply of the saturating component onto the treated surface.

The kinetic dependences of the thickness of the nitrided or cemented layers on the time have a parabolic character, which is indicative of the steady concentration of diffusants on the surface. The observed phase composition is relevant to the diagrams of the state with account for the additional oxidation in the vapor–gas shell and possible hardening. Below, certain technological procedures of the anode modifying the metals and alloys in aqueous solutions are to be considered.

Nitroquenching. There are electrolytes known to have a nitrogen potential of up to 5%, which make it possible to perform a short-time nitriding followed by quenching in the same electrolyte [27–29]. Ammonia being adsorbed on the surface of the anode–workpiece is assumed to be the source of the atomic nitrogen. The structure (a surface oxide layer, nitride zone, martensite underlayer, and pearlite) obtained on the medium-carbon steels ensures the improvement of the anticorrosion and mechanical characteristics [30]. Saturation with nitrogen at a temperature of 750°C for 5 min followed by quenching allows increasing the strength limit of 45 and 40X steels by 25–30% and the solidity up to 9 Gpa upon a decrease of the layer's plasticity up to 65–70% and increasing the endurance limit more than 2 times.

Cementation. A plurality of compounds for carbon saturation in a cathode or anode processes is offered and patented. Electrolytes containing ammonium chloride (10%) and glycerin (10%) or other compounds have became commonly used for anode cementation (Table 3) [31].

A change of the concentrations of the carbon-bearing components in the cementing affects the heating temperature. The rate of the decrease of the carbon-bearing components owning to evaporation is correlated with the values of their boiling temperatures: 56°C—for acetone, 197°C—for ethyleneglycol, and 290°C—for glycerin. The metallographic analysis of the specimens showed that, in exploiting the electrolyte, the thickness of the pearlite layer changes little, but it is found to be different for each of the compositions of the electrolyte. In the process of the exploitation of acetone and glycerin electrolytes, the thickness of the layer decreases; with a saccharose electrolyte it actually remains the same; and, in the case of an ethyleneglycol electrolyte, it increases. This may occur due to the changes of the anode temperature and the current of the system. Filtering the glycerin electrolyte ensures an increase of its longevity.

The concentration increase of ammonium chloride that contains no carbon was found to increase the thickness of the cemented layer, which is accounted for by the intensifying of the anode dissolution and the decrease of the thickness of the oxide layer, which inhibits the carbon diffusion (Fig. 13). This is indirectly confirmed by the fact that an increase in the concentration of ammonium chloride is accompanied by the current intensity growth due to the enhancement of the conductivity of the solution and the shell.

The effect of the concentrations of the carbon-bearing components is of a more intricate character, and it may be explained by the rivalry of two processes (Fig. 14). Upon an increase of these concentrations from small values to 2%, the growth of the saturating capacity of the medium dominates, which involves an increase of the flow of carbon compounds from the electrolyte to the vapor–gas shell. A further decrease of the thickness of the martensite layer occurs, obviously, because of the less intensive dissolution, i.e., because of the thickness growth of the layer of the inhibiting oxides of iron. This is indirectly confirmed by the current density decrease parallel to the growth of the concentration of the carbon-bearing components found experimentally. The critical value of the content of the organic dopant in the electrolyte (2%) may be regarded as the threshold of the saturating capacity of the latter.

The degree of oxidation in cemented steels may be estimated using the ratio of the intensity of the diffraction maximum of the superposition of Fe_3O_4 (311)–FeO (311) to the ferrite intensity, i. e., to the α–Fe

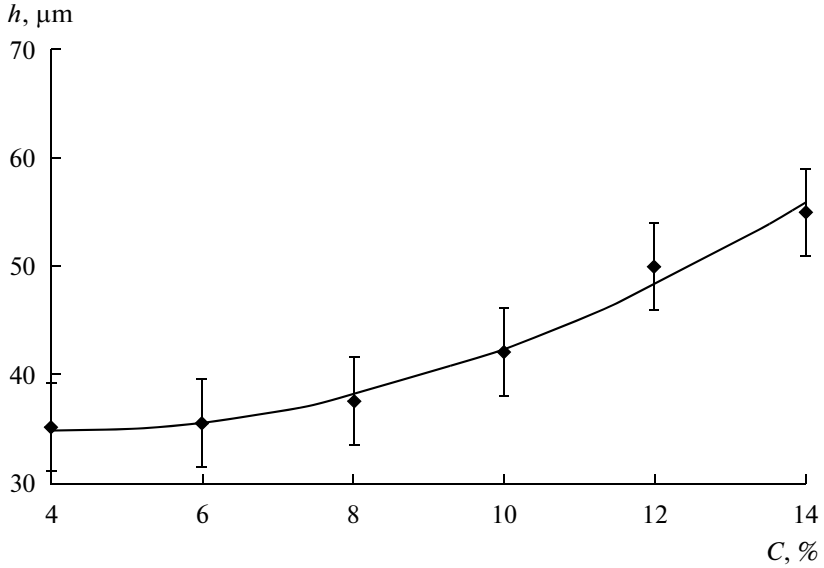

Fig. 13. Change of the thickness of the martensite layer upon an increase of the concentration of ammonium chloride after 10 min of cementation at 900°C in the electrolyte, which contains 10 wt % glycerin.

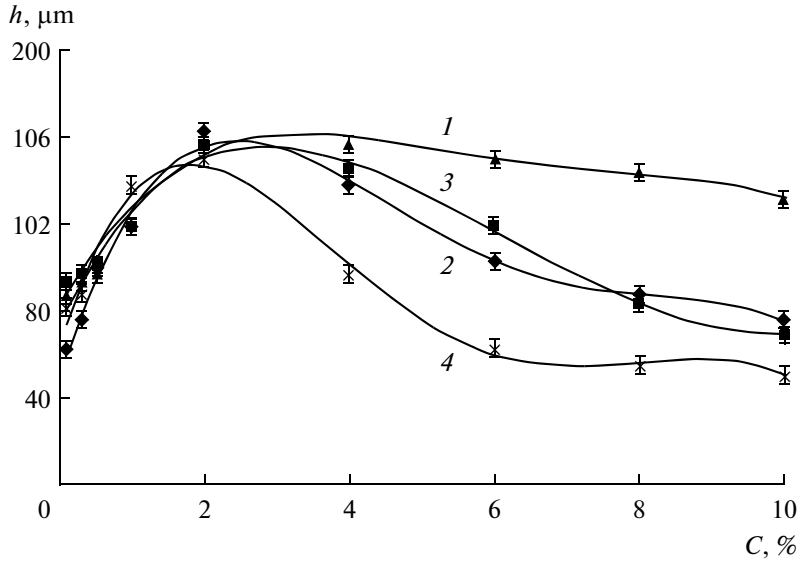

Fig. 14. Change of the thickness of the martensite layer depending on the concentration of the carbon-bearing component (*1*—acetone, *2*—glycerine, *3*—saccharose, *4*—ethyleneglycol) after a 10-minute cementation at a temperature of 900°C in the electrolyte with a concentration of ammonium chloride of 10 wt %.

(110). The minimum oxidation was observed after the treatment in the electrolyte with acetone, the mean with glycerin, and the maximum with saccharose (Table 4). Cementation was carried out for 20 min at 930°C in different solutions. This ratio in the cemented iron–graphites is 1.5–1.75 times more than in the cemented steel 0.8 cf with the degree of oxidation being dependent on the nature of the carbon-bearing components of the solution. It is evident that the processes of oxidation and anode dissolution occur more intensively in the treatment of porous fritted wares due to the more developed surface.

After exploiting the electrolyte for 10 h with account for its total evaporation, it is recommended (as a corrective action) to add any carbon-bearing component into the electrolyte to reestablish its initial concentration and to add water to restore the initial volume of it in the facility. The solution must be filtered while being saturated with indissoluble iron (III) hydroxide.

Nitrocementation. There are electrolytes that allow saturation with nitrogen and carbon simultaneously. A layer with carbonitrides and a martensite underlayer are formed as a result provided that, after the saturation, hardening is performed. The predominant diffusion of nitrogen at low temperatures and the diffusion of carbon dominating at higher temperatures are also characteristic of nitrocementation in electrolytes [32]. Moreover, at enhanced temperatures, the complementary acceleration of the carbon diffusion is observed due to nitrogen: such a conclusion was reached from the analysis of the cross sectional coefficients of the diffusion [33]. A decrease of the corrosion losses of steel 45 by 7–8 times was observed using nitrocementation in an electrolyte containing 10% ammonium chloride and 20% carbamide. The possibility of increasing the surface microhardness of steel 12X18H10T by its nitrocementation in the same electrolyte safe from intercrystalline corrosion was shown.

Other kinds of electrochemical thermal treatment. Positive results were obtained in the boron saturation of steels [34]; a possibility of decarbonization of steels upon the anode heating was shown [35]. The anode saturation of titanium alloys with nitrogen and oxygen for the enhancement of their anticorrosion properties was studied [25, 36–38].

The anode heating may be used combined with other technologies, for example, in modifying composite electrochemical [39] or electrospark coatings [40–42]. A possibility for the improvement of the corrosion resistance of construction steel using complementary oxidation in a sodium nitride solution was shown [43, 44]. Anode nitriding of titanium alloys may be supplemented by vacuum aging and other processes [36, 37].

EQUIPMENT

The first devices for the anode electrolyte heating (UKHTO-type) were developed and produced at the Experimental Plant of the Institute of Applied Physics of the Soviet Socialist Republic of Moldova. The UKHTO-2 device was designed for hardening the spacer bushings of ETSV-type submersible pumps. Six bushings at a time were heated for 1 min, which ensured the productivity of 120 details/h of the hardened bushings upon manual loading and unloading. A rectangular bath with uncontrolled hydrodynamics was used as the working cell. The consumed power of the device amounted to 24 kW.

The UKHTO-3 device (25 kW) ensures hardening, nitro-quenching, and cementation with hardening for various small-scale workpieces having the area of their heating surface up to 100 cm^2. Using a cylindrical heating device with the longitudinal flowing of the workpiece makes it possible to equalize the distribution of the temperature over its surface and to enhance the quality of the hardening along with enlarging the class of the treated workpieces. The device's output is determined by the number of simultaneously treated workpieces and amounts to no less than 30 details/h.

Table 4. Relative intensity of the diffraction maxima of the oxide phases after cementation of the iron-based materials

Specimen material	Acetone	Glycerin	Saccharose
Steel 08	0.24	0.31	0.36
ZhGr0.5D2	0.35	0.48	0.63

The UKHTO-4, UKHTO-5, and UKHTO-6 are equipped with a thyristor power source [45]. A rectifier is used according to Larionov's three-phase bridge scheme with controlled vents. The thyristors are switched on by the phase-pulse converters, which ensure the stability of the start and the possibility of the automatic mode of operation. The UKHTO-5M and UKHTO-5B (50 kW, 30 details/h) became the most popular ones for the speedy hardening of small-scale equipment in light industry using, as a rule, cementation with hardening. For the automatic performance, the voltages and durations of the stages of the treatment are set according to a three-step cycle: heating for saturation with carbon or nitrogen, temperature stabilization prior to hardening with the possibility of cooling down, and the short-time heating of a workpiece before its cooling in the electrolyte for realization of surface hardening.

The UKHTO-6 specialized device was designed for hardening the guide planks of the TCH 3.0 B scraper conveyors by anode nitrohardening. This device provides for the mechanical feed of the workpieces from a supply bin to the heating positions. Local heating of the working surface of each of the holes is performed by the electrolyte jets. The device's output in the automatic mode amounts to 240 details/h at a consumed energy of 50 kW.

The ATO device (30 details/h, 7 kW) was designed for hardening small workpieces of equipment in light industry with an area of the treated surface of 25 cm^2 at the All-Russia Scientific Research Institute of the Flax-Fiber Industry (Kostroma). The unit for the treatment consists of a cylindrical heating device ensuring a longitudinal flow over a workpiece with the solution cooling being performed in a film heat exchanger. The submersion of a workpiece into the solution is done manually by means of a dielectric rod. The supply unit consists of a mains controlled autotransformer with a rectifier, an autotransformer for feeding the pump's electromotor, and switching and measuring equipment.

CONCLUSIONS

The analysis of the available scientific literature of the past twenty years shows that the aspects of anode

electrochemical thermal modifying are studied in Russia, Moldova, Ukraine, Belarus, China, and Great Britain. Among the Russian organizations are the Moscow Aviation Technological Institute–Tsiolkovskii Russian State Technical University (MATI–RGTU), the Scientific Research Institute of Nuclear Physics of Moscow State University (NII of nuclear physics of MGU), the Institute of Chemistry of Nonaqueous Solutions of the Russian Academy of Sciences (Ivanovo), Kostroma Nekrasov State University, Kostroma State Technological University, and the "Fakel" Experimental Design Bureau (Kaliningrad). The objects of the study are the main aspects of the phenomenon: the thermophysical mechanism of heating, the electrochemical processes on the interface of the vapor–gas shell and metal anode, and the aspect of the diffusion saturation of the products in terms of metal materials science. The results of some of the studies and developments were presented in the monographs of V.N. Duradzhi, A.S. Parsadanyan [6], and P.N. Belkin [5].

ACKNOWLEDGMENTS

This work was performed according to the subject plans of the Scientific Research Developments (SRD) under the financial support of the Ministry of Education and Science of the Russian Federation and the Russian Foundation for Basic Research (grant no. 09-08-99069-p_ofi) and reported at a symposium on the Electrical Methods of Material Treatment dedicated to the 100th anniversary of the birth of Boris Romanovich Lazarenko, Academician and first director of the Institute of Applied Physics.

REFERENCES

1. Lazarenko, B.R, Fursov, S.P, Faktorovich, A.A., Galanina, E.K., and Duradzhi, V.N., *Kommutatsiya toka na granitse metal–elektrolit* (Current Commutation at an Interface of Metal–Electrolyte), Kishinev: Rus. Istor. Soc. Acad. Nauk of Soviet Socialist Republic of Moldova, 1971, pp. 11–13.
2. Yasnogorodckii, I. Z., Electrolyte Heating of Metals, in *Elektrokhimicheskaya i elektromekhanicheskaya obrabotka metallov* (Electrochemical and Electromechanical Treatment of Metals), Leningrad: Mashinostr., 1971.
3. Vanin, V.S., Heating Metals in Electrolyte, *Elektrotermiya*, 1967, no. 55, pp. 18–19.
4. Brinza, V.N., Anagorskii, L.A., Frantsenyuk, I.V., Chulkov, V.V., Chernenilov, M.F., Piseukov, B.A., Malyshko, N.F., and Losikhin, V.M., USSR, Inventor's Certifiate no. 296829, Byull. Izobret., 1983, no. 9.
5. Belkin, P.N., *Elektrokhimiko-termicheskaya obrabotka metallov i splavov*, (Electrochemical and Thermal Treatment of Metals and alloys), Moscow: Mir, 2005.
6. Duradzhi, V.N. and Parsadanyan, A.S., *Nagrev metallov v elektrolitnoi plazme* (Electrolyte Plasma Heating of Metals), Chisinau: Shtiintsa, 1988.
7. Belkin, P.N., Ganchar, V.I., and Petrov, Yu.N., Investigation of a Vapor Film Conduction upon Anode Electrolyte Heating, *Dokl. Akad. Nauk of Soviet Union,* 1986,vol. 291, no. 5, pp. 1116–1119.
8. Belkin, P.N., Ganchar, V.I., Davydov, A.D., Dikusar, A.I., and Pasinkovskii, E.A., Anodic Heating in Aqueous Solutions of Electrolytes and its Use for Treating Metal Surfaces, *Surf. Eng. Appl. Electrochem.*, 1997. no 2., pp. 1–15.
9. Belkin, P.N., Thermal and Physical Peculiarities of Anode Heating in Aqueous Electrolytes, *Mater. 2-oi mezhdunarod. konf. po elektrochim. i elektrolitno-plazm. metodam modifik. metal. poverkhnostei* (Proc. 2nd Int. Conf. Electrochem. Electrolyte-Plasmic Meth. Modif. Metal Surf.), Kostroma, Nekrasov Gos. Univ.; Moscow, Inf. Tsentr MATI–Tsiolkovskii RGTU, 2007, pp. 175–189.
10. Belkin, P.N. and Belikhov, A.B., Stationary Temperature of the Anode Heated in Aqueous Electrolytes, *Inzh. Fiz. Zh.*, 2002, vol. 75, no. 6, pp. 19–24.
11. Ganchar, V.I., Parameters of Heat Transfer in the Process of Anode Electrolyte Heating, *Inzh. Fiz. Zh.*, 1991, vol. 60, no. 1, pp. 92–95.
12. Belkin, P.N., Mukhacheva, T.L., and D'yakov, I.G., Peculiarities of Distribution of Heat Flows in the System Anode-Vapor-Gas Shell upon the Anode Electrolyte Heating, *Inzh. Fiz. Zh.*, 2008, vol. 71, no. 6, pp. 1027–1033.
13. Ganchar, V.I., Zgardan, I.M., and Dikusar, A.I., Anode Dissolution of Iron in the Process of Electrolyte Heating, *Elektron. Obrab. Mater.*, 1994. no. 4, pp. 69–77.
14. Ganchar, V.I., Zgardan, I.M., and Dicusar, A.I., Anodic Dissolution of Chromium Upon Electrolyte Heating, *Surf. Eng. Appl. Electrochem.*, 1996. no 5, pp. 13–19.
15. Zgardan, I.M., Ganchar, V.I., and Dicusar, A.I., Anomalous Dissolution of Copper under Conditions of Electrolytic Heating, *Elektrokhimiya.*, 1999, no.4, pp. 542–544.
16. Zhirov, A.V., D'yakov, I.G., and Belkin, P.N., Dissolution and Oxidation of Carbon Steels under Anode Heating in Aqueous Solutions, *Izv. Vyssh. Uchebn. Zaved. Khim. Khimich. Tekhnol.*, 2010, no. 3, pp. 89–93.
17. D'yakov, I.G. and Naumov, A.R., On Electrochemical Reactions under Anode Heating in Aqueous Electrolytes Based on Ammonium Chloride, *Elektron. Obrab. Mater.*, 2006, no. 6, pp. 4–9.
18. Resner, E., Marks, G., Zaitsev, V.A., and Sukhotin, A.M., Electrode Wear upon Treatment of Low-Carbon Steel in Electrolyte Plasma in the Anode Process, *Elektron. Obrab. Mater.*, 1983, no. 3, pp. 59–61.
19. Shkurpelo, A.I., Belkin, P.N., and Pasinkovskii, E.A., Phase Composition and Structure of a Surface Layer of Armco Iron and Austenitic Stainless Cr–Ni Steel 12X18H10T after Nitrocementation upon the Anode Electrolyte Heating, *Fiz. Khim. Obrab. Mater.*, 1993, no. 2, pp. 116–125.
20. Belikhov, A.B. and Belkin, P.N., Peculiarities of Anode Cementation of Iron Graphites, *Elektron. Obrab. Mater.*, 1998, no. 5–6, pp. 23–31.
21. Belkin, P.N., Krit, B.L., D'yakov, I.G., Vostrikov, V.G., and Mukhacheva, T.L., Anode Saturation of Steels with

Nitrogen and Carbon in Aqueous Solutions of Electrolytes that Contain Carbamide, *Metalloved. Termich. Obrab. Met.*, 2010, no. 1, pp. 32–36.

22. Grishina, E.P., Zhirov, A.V., Belkin, P.N., and Dikusar, A.I., Effect of Anode Electrochemical Thermal Oxidation on Corrosion Resistance of Steel 45, *Elektron. Obrab. Mater.*, 2008, no. 5, pp. 57–62.

23. Chernova, G.P., Bogdashkina, N.L., Parshutin, V.V., Revenko, V.G., Tomashov, N.D., Belkin, P.N., Pasinkovskii, E.A., and Factorovich, A.A., Electrochemical and Corrosion Behavior of Steel 40X Nitrided in Electrolyte Plasma, *Zashchita Met.*, 1984, vol. 20, no. 3, pp. 408–411.

24. Revenko, V.G., Chernova, G.P., Parshutin, V.V., Bogdashkina, N.L., Tomashov, N.D., Belkin, P.N., and Pasinkovskii, E.A., Effect of Nitriding in Electrolyte on Protective Properties of Conversion Coatings, *Zashchita Met.*, 1988, vol. 24, no. 2, pp. 204–210.

25. Blashchuk, V.E., Kareta, N.M., Onoprienko, L.M., Belkin, P.N., and Pasinkovskii, E.A., Effect of Electrolyte Nitriding on Corrosion Resistance of Commercial Titanium VT1–0, *Elektron. Obrab. Mater.*, 1986, no. 3, pp. 20–22.

26. Duradzhi, V.N., Morar', N.N., Polotebnova, N.A., and Kiseeva, L.V., On Phase Composition of a Surface of Metals, Treated in Electrolyte Plasma, *Elektron. Obrab. Mater.*, 1986, no. 1, pp. 49–52.

27. Lazarenko, B.R., Duradzhi, V.N., Factorovich, A.A., and Bryantsev, I.V., USSR, Inventor's Certificate no. 461161, Byull. Izobret., 1975, no. 7.

28. Duradzhi, V.N., Bryantsev, I.V., and Tovarkov, A.K., USSR, Inventor's Certificate no. 618447, Byull. Izobret., 1978, no. 29.

29. Factorovich, A.A., Belkin, P.N., and Pasinkovskii, E.A., USSR, Inventor's Certificate no. 621799, Byull. Izobret., 1978, no. 32, p. 97.

30. Belkin, P.N. and Pasinkovskii, E.A., Thermal and Chemicothermal Treatment of Steels upon Heating in Electrolyte Solutions, *Metalloved. Termich. Obrab. Met.,* 1989, no. 5, pp. 12–17.

31. Kusmanov, S.A., D'yakov, I.G., and Belkin, P.N., Effect of Carbon-Bearing Components of Electrolyte on Characteristics of Chemicothermal Cementation, *Vopr. Materialoved.*, 2009, no. 4, pp. 7–13.

32. Yerokhin, A.L., Nie, X., Leyland, A., Matthews, A., Dowey, S.J., Plasma Electrolysis for Surface Engineering, *Surf. Coat. Techn.*, 1999, no. 122, pp. 73–93.

33. Mukhacheva, T.L., D'yakov, I.G., and Belkin, P.N., Peculiarities of Two-Component Saturation of Construction Steels with Nitrogen and Carbon upon Electrolyte Heating, *Vopr. Materialoved.*, 2009, no. 2, pp. 38–45.

34. Kuzenkov, S.E. and Saushkin, B.P., Steel–45 Borating in Electrolytic Plasma, *Elektron. Obrab. Mater.*, 1996, no. 4–6, pp. 24–28.

35. Zemskii, S.V., Factorovich, A.A., Belkin, P.N., and Pasinkovskii, E.A., USSR, Inventor's Certificate no. 969761, Byull. Izobret., 1982, no. 40.

36. Tarasov, A.N. and Prokof'ev, M.A., Hardening of a Stomatologic Point Tool from Titanium Alloys by Electrolyte Nitriding on an UKHTO-5M Device, *Elektron. Obrab. Mater.*, 1991, no. 2, pp. 20–22.

37. Tarasov, A.N., Belkin, P.N., Prokof'ev, M.A., and Machulin, S.A., USSR, Inventor's Certificate no. 1744148, Byull. Izobret., 1992, no. 24.

38. Belkin, P.N., Borisov, A.M., Vostrikov, V.G., D'yakov, I.G., Romanovskii, E.A., and Serkov, M.V., Application of Spectrometry of NBS of Protons for Study of Anode Chemicothermal Treatment of Titanium, *Fiz, Khim. Obrab. Mater.*, 2006, no. 1, pp. 59–61.

39. Gertsriken, D.S., Tyshkevich, V.M., Mazanko, V.F., Fal'chenko, V.M., Mikhailov, V.V., Peretyatku, P.V., Pasinkovskii, E.A., and Yanovich, A.I., Peculiarities of Electroerosion Alloying and Electrolyte Heating of Titanium with Nickel Coating, *Elektron. Obrab. Mater.*, 1996, no. 2–3, pp. 11–17.

40. Mikhailov, V.V., Duradzhi, V.N., Gitlevich, A.E., and Andreeva, L.N., Effect of Electrospark Discharge and Electrolyte Plasma on a Surfac Layer of Metals, *Elektron. Obrab. Mater.*, 1981, no. 5, pp. 26–28.

41. Lazarenko, B.R., Duradzhi, V.N., Bryantsev, I.V., and Mikhailov, V.V., USSR, Inventor's Certificate no. 789629, Byull. Izobret., 1980, no. 47.

42. Ignat'kov, D.A., Michailov, V.V., and Pasinkovskii, E.A., Phase-Structural and Remaining Strain State upon Combined Modification of Metal Surfaces by Electrospark Alloying and Electrolyte Plasmic Nitriding, *Mater. 2-oi mezhdunarod. nauch.–tekhn. konf. po elektrochim. i elektrolitnoplazm. metodam modifik. metal. poverkhnostei* (Proc. 2nd Int. Conf. Electrochem. Electrolyte-Plasmic Meth. Modif. Metal Surf.), Kostroma, Nekrasov Gos. Univ.; Moscow, Inf. Tsentr MATI–Tsiolkovskii RGTU, 2007, pp. 206–211.

43. Parshutin, V.V. and Pasinkovskii, E.A., Enhancement of Corrosion Resistance of Steels Using Chemicothermal Treatment in Electrolytes, *Elektron. Obrab. Mater.*, 2007, no. 6, pp. 26–28.

44. Parshutin, V.V. and Pasinkovskii, E.A., Moldova Patent no. 2959, Byull. Izobret., 2006, no. 1.

45. Khamurar', V.I.,Belkin, P.N., Ganchar, V.I., Govberg, M.G., and Rozental', Ya.Sh., USSR, Inventor's Certificate no. 1349012, Byull. Izobret., 1987, no. 40.

ISSN 1068-3755, Surface Engineering and Applied Electrochemistry, 2010, Vol. 46, No. 6, pp. 570–578. © Allerton Press, Inc., 2010.
Original Russian Text © S.S. Belevskii, H. Cesiulis, N.I. Tsyntsaru, A.I. Dikusar, 2010, published in Elektronnaya Obrabotka Materialov, 2010, No. 6, pp. 42–52.

ELECTRICAL SURFACE TREATMENT METHODS

The Role of Mass Transfer in the Formation of the Composition and Structure of CoW Coatings Electrodeposited from Citrate Solutions

S. S. Belevskii[a], H. Cesiulis[b], N. I. Tsyntsaru[a], and A. I. Dikusar[a, c]

[a] *Institute of Applied Physics, Academy of Sciences of Moldova, ul. Academiei 5, Chisinau, MD-2028 Republic of Moldova*
[b] *Vilnius University, ul. Naugarduko 24, Vilnius, LT-03225 Lithuania*
[c] *Shevchenko Trans Dniester State University, ul. 25 Oktyabrya 128, Tiraspol, Republic of Moldova*
e-mail: dikusar@phys.asm.md

Received April 21, 2010

Abstract—The effect of the hydrodynamic conditions on the electrode process's rate and the composition and structure of cobalt–tungsten coatings electrodeposited from citrate solutions is studied. The rate of the electrode process depends on the hydrodynamic conditions. However, the electrochemical impedance data do not reveal the presence of slow diffusion processes. The analysis of the electrochemical impedance spectra shows the occurrence of slow adsorption processes, such as an intermediate adsorption stage. It is assumed that the hydrodynamic conditions have a strong effect on the surface state rather than on the mass transfer from the solution's bulk to the electrode.

DOI: 10.3103/S1068375510060050

INTRODUCTION

In the mean time the induced codeposition of iron-group metals with refractory metals is studied widely for some reasons. First, this process is an example of the so-called "anomalous" deposition of alloys [1]; its mechanism is not fully understood. Second, in a number of cases, the coatings resulting from the process exhibit unique physicomechanical and anticorrosion properties [1–8]. Third, since the technology for obtaining these coatings is based on the use of environmentally safe electrolytes, it really can replace electrolytic chromium plating, which is associated with ecological risks [8].

It was repeatedly observed that the composition and structure of the coatings in the induced deposition of these metals evidently depend on the hydrodynamic conditions of the electrodeposition [1, 9–11]. This was clearly shown with respect to the electrodeposition of CoW coatings from citrate solutions, in particular, in [12–14]. In this work, we generalized and revise early published results (as well as in [15]) concerning the studied effect of the ionic mass transfer on the composition and structure of CoW coatings. The studies described in [13–15] were carried out using controlled hydrodynamic conditions of electrodeposition, i.e., a rotating cylindrical electrode (RCE) and a so-called Hull cell with an RCE [10, 14, 16, 17].

EXPERIMENTAL

The technique of the polarization measurements using an RCE was described earlier [13—15]. Below, the results obtained at various Reynolds (Re) numbers were providing and are analyzed taking into account the measured values of ohmic drop. The features of the technique regarding the resistive component using an RCE are also given in detail below.

Figure 1 depicts the pattern of the calculation of the ohmic voltage drop between the surface of an RCE and the end of a Luggin capillary. For the geometry shown in Fig. 1 and the values of χ for the electrolyte used (the electrolyte conductivity of $8.76 \times 10^{-2}\ \Omega^{-1}\ \text{cm}^{-1}$, our

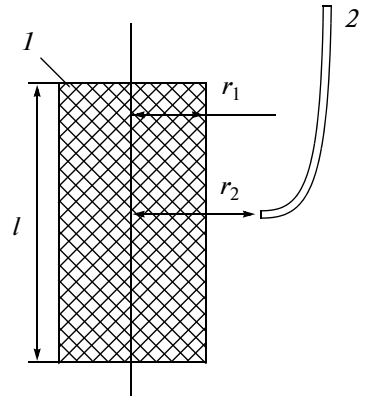

Fig. 1. Diagram and notation of (*1*) an RCE and (*2*) a Luggin capillary.

individual measurements), as well as for $l = 1.5$ cm, $r = 0.5$ cm, and $r_2 = 2.3$ cm, the value of the resistance at a distance of $r_2 - r_1$ from the cylinder's surface ($r_1 = 0.5$ cm) was calculated by (1) [18]:

$$R = \frac{2.3}{\chi l 2\pi} \log \frac{r_2}{r_1}. \quad (1)$$

For these conditions, the resistive component of the measured potential ($R_{ohm}S$) was 8.64 Ω cm^2 (S is the working area of the cylinder's surface). The ohmic potential drop was calculated using Ohm's law ($\Delta E_{ohm} = iRS$). The resulting value is subtracted from the total value of the measured polarization at the respective current density (see Fig. 4 in [13]).

In addition to the measurements using an RCE, to estimate the role of the diffusion processes in the electrodeposition of the coatings under study, the method of electrochemical impedance was used.

The electrochemical impedance spectra at different cathode potentials was recorded using a μAUTOLAB III system, a three-electrode cell, and FRA 4.9 software. The electrochemical impedance was measured at 60°C in the frequency range of 8000–0.1 Hz. In some cases, for example, at relatively high cathode potentials, intense hydrogen evolution occurs and it was difficult to record the interference-free impedance spectrum at low frequencies; therefore, data obtained at 1 Hz were taken for the analysis.

The working electrode was prepared of a cobalt wire (Alfa Aesar, purity of ≥99.9%) with a diameter of 1.5 mm. The working area was the end face of this wire, and the rest of it was insulated with a thermocambric. An Ag/AgCl electrode in a saturated KCl solution served the reference electrode; a Pt wire was used as the anode. Before each experiment, the working surface was polished and washed. Prior to the impedance measurements, the electrode was kept in an electrolyte for 2 min in order to cover it with a layer of Co or CoW.

RESULTS AND DISCUSSION

Ionic Mass Transfer on an RCE

The basic equation for the rate of the ionic mass transfer on an RCE, which was used in this and earlier studies (see [13, 14]), is as follows [16]:

$$k_d = 0.079\omega^{0.7} r^{0.4} \upsilon^{-0.344} D^{0.644}, \quad (2)$$

where k_d is the mass transfer coefficient (the diffusion rate constant, cm/s); ω is the RCE rotation frequency, s^{-1}; i is the RCE radius, cm; υ is the kinematic viscosity coefficient, cm^2/s; and D is the diffusion coefficient, cm^2/s.

As was shown in [13, 16, 17] the equation (2) is valid for $\mathrm{Re} = \omega r^2/\upsilon \geq 200$. In this case, a turbulent flow takes place on the RCE; in the conditions of its occurrence, relation (2) is fulfilled.

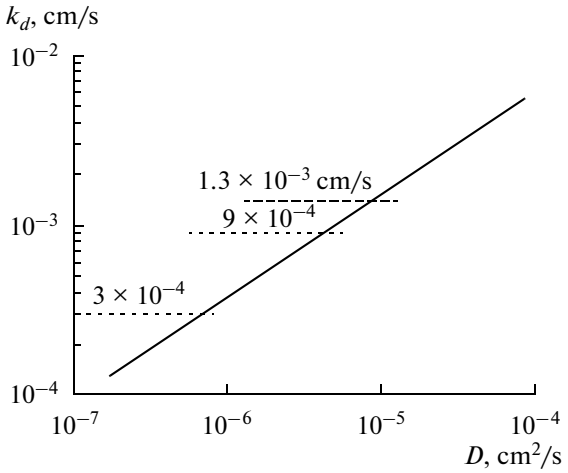

Fig. 2. Dependence of the diffusion rate constant on the diffusion coefficient for the RCE geometry and the physical properties of the solution used in this work at a rate of rotation of 165 rpm (Re = 685 and 600 for the deposition of the Co and CoW, respectively).

For steady-state diffusion, the expression is valid

$$k_d = D/\delta, \quad (3)$$

where δ is the thickness of the Nernst diffusion layer. It follows from (2) and (3) δ is determining by the following expression:

$$\delta = 12.7\omega^{-0.7} r^{-0.4} \upsilon^{0.344} D^{0.356}. \quad (4)$$

The mass transfer coefficient (diffusion rate constant) can be determined experimentally from the value of the diffusion current i_d:

$$i_d = nFk_dC_0, \quad (5)$$

where C_0 is the volume concentration of the electroactive component of the solution and n is the number of electrons transferred in the electrochemical reaction.

For the particular conditions of the electrochemical deposition described in [13, 15] ($\upsilon = 0.63 \times 10^{-2}$ cm^2/s for a citrate solution of Co at 60°C, $\upsilon = 0.72 \times 10^{-2}$ cm^2/s for a citrate solution of Co and W at the same temperature and their concentrations used in the above works, and $r = 0.5$ cm) and at an RCE rotation frequency of 165 rpm (Re = 600 and 685 for the mixed solution and the Co citrate solution, respectively), the dependence of the mass transfer coefficient on the diffusion coefficient will have the form shown in Fig. 2.

Effect of Rotation on the Electroreduction of Co(II) from Citrate Solution at Various pH

It is shown in [15] that the current density of the electrodeposition of Co from a solution containing (mol/l) cobalt sulfate (0.2), citric acid (0.04), sodium citrate (0.25), and boric acid (0.65) at a bulk temperature of 60°C in the potential range more negative than –0.9 V (Ag/AgCl electrode) depends on the rotation

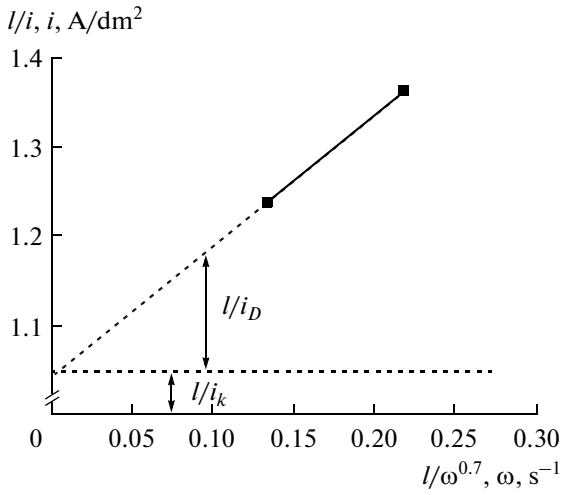

Fig. 3. Dependence of the reciprocal of the partial current density of the Co reduction at pH = 4.4 on the reciprocal of $\omega^{0.7}$.

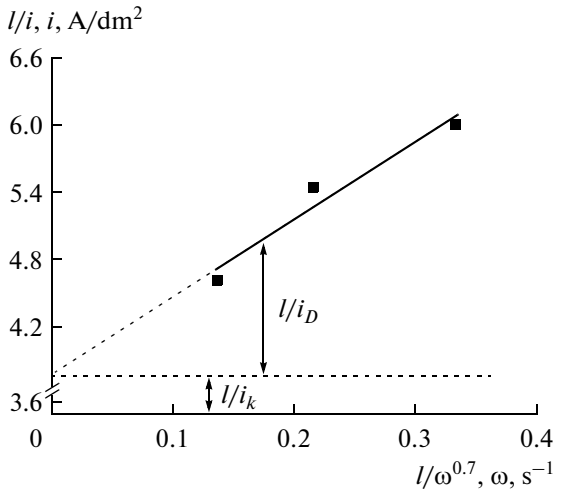

Fig. 4. Dependence of the reciprocal of the partial current density of the Co reduction at pH = 6.7 on the reciprocal of $\omega^{0.7}$.

rate. The rate of rotation of the RCE did not have an effect on the measured current density if it was less than (or equal to) 11 rpm (i.e., at Re numbers less than 50). Obviously, at low rotation rates, the key role was played by the natural convection (e.g., according to (4), the diffusion layer's thickness was 0.44 mm at $D = 10^{-5}$ cm^2/s and a rotation rate of 11 rpm). Starting with rotation rates of 45 rpm (Re = 190), this effect was observed.

Under these conditions, hydrogen evolution concurrently occurred. Both the measured current density and the current efficiency of the electrodeposition depended on the pH of the solution. In an acidic medium (pH = 4.4), both the measured current density and the current efficiency were higher than in a neutral medium with pH = 6.7.

Using the measured values of the current density and current efficiency (see Figs. 8, 9 in [15]), we determined the partial currents of the electrodeposition of Co at various rotation rates for Re >200. It follows from [13] under assumption that the current efficiency in the potentiostatic mode does not depend on the rotation rate. At a potential of −1.0 V, the current efficiency was 67% at a solution pH of 4.4 (acidic solutions) and 48% at $E = -0.95$ V for a neutral solution (pH = 6.7). The resulting values of the partial currents Co electrodeposition were analyzed in the form of $1/i - 1/\omega^{0.7}$ dependences in order to separate the diffusion and "kinetic" components of the measured partial current of the Co reduction. The derived dependences are shown in Figs. 3 (for pH = 4.4) and 4 (for pH = 6.7). In addition, we used the results of [15]; they are represented in Figs. 8 and 10, respectively.

The values of kinetic and diffusion currents obtained at Re = 685 are listed in Table 1. Using the diffusion current values thus obtained, we calculated the mass transfer coefficients according to (4); the diffusion coefficients were determined on the basis of Fig. 2 (at $n = 2$); and the thicknesses of the Nernst diffusion layer were found by (4) (the superscript of 165 for the diffusion current density and the diffusion layer thickness shows that these parameters correspond to an RCE rotation rate of 165 rpm).

It is evident that, for the deposition at pH = 4.4, the resulting values of the diffusion coefficients can be as distinct from, whereas, at pH values close to neutral, the effective values of the diffusion coefficients are anomalously low.

Table 1. Kinetic and diffusion characteristics of the processes of electrodeposition of Co and a CoW alloy from a citrate solution

Coating	pH	i_k, A/dm^2	n	i_D^{165}, A/dm^2	$k_d \times 10^4$, cm/s	D, cm^2/s	δ^{165}, μm
Co	4.4	1.0	2	5.0	13.0	10^{-5}	66
»	6.7	0.3	2	1.1	3.0	7×10^{-7}	26
CoW	6.7	0.4	2	3.7	9.0	4×10^{-6}	44
»	6.7	0.4	6	3.7	3.0	7×10^{-7}	23

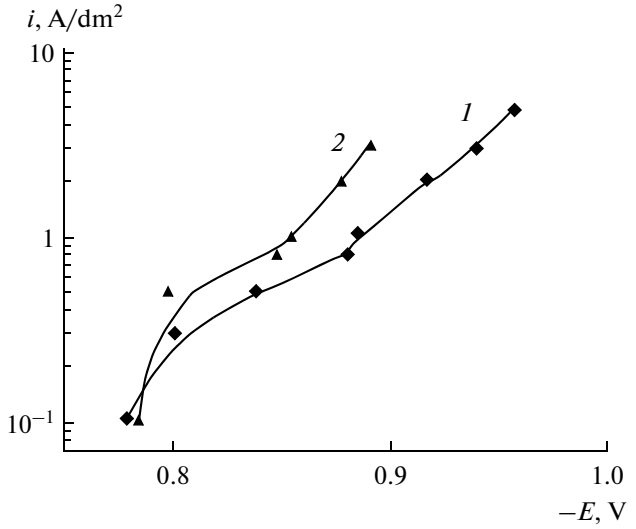

Fig. 5. Polarization curves of the electrodeposition of a CoW alloy [13, Fig. 4] with ohmic drop subtracted: Re = (*1*) 40 and (*2*) 600. Curve *1* corresponds to the curve obtained with natural convection.

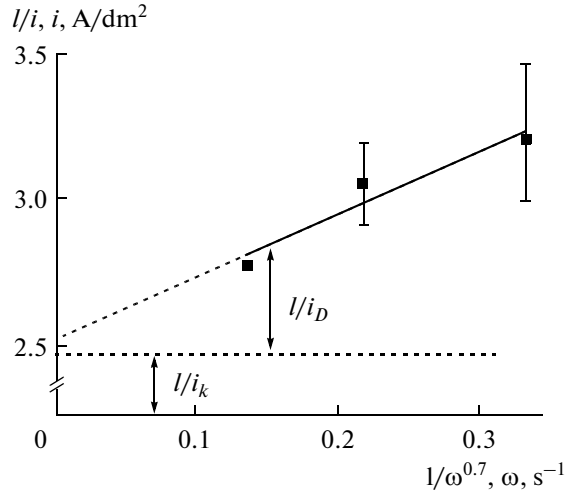

Fig. 6. Dependence of the reciprocal of the partial current density of the deposition of CoW on the reciprocal of $\omega^{0.7}$.

Ionic Mass Transfer in the Electrodeposition of CoW Coatings

The experimental results that are analyzed below were described in detail in [13]. However, the ohmic drop in obtained polarization was taken into account in the further analysis. The polarization curves with regard for the resistive component are shown in Fig. 5.

It should be emphasized that the dependences shown in the figure were obtained for stationary (steady-state) values of the potentials (upon switching on the current, the potential achieved stationary values after a certain number of passed charges). The curves corrected for the ohmic potential drop in Fig. 5 are characteristic of the processes whose rate is determined by the rate of the ionic mass transfer.

The results of the analysis of the partial currents of the deposition (with regard only for the current efficiency; that is, it was assumed that the electrodeposition occurs from a single cobalt–tungsten complex) in the form of the $1/i - 1/\omega^{0.7}$ dependence are represented in Fig. 6; the respective values of the kinetic and diffusion current densities, as well as the effective values of the mass transfer coefficients and the diffusion coefficients, are listed in Table 1.

Since the total number of electrons (in the reduction from a mixed cobalt–tungsten complex) is unknown, the calculation of k_d from the resulting value of the partial diffusion current was carried out for two limiting cases: $n = 2$ and $n = 6$.

In the deposition of the alloy, the following might be concluded:

(a) The kinetic current is close to that observed in the electrodeposition of Co for the same pH values.

(b) The diffusion coefficients are close (if we assume $n = 6$); they will also be fairly close if we take the value of n just greater than 2.

(c) The resulting values of the diffusion rate constants and the diffusion coefficients are anomalously low.

These results (as well as for the deposition of Co and CoW at pH close to neutral) suggest that the process under study is more complex than the classical process of mixed kinetics (slow charge transfer plus slow convective diffusion).

The first complexity lies in the fact that, due to the complex formation at pH > 4, the concentration of the electroactive particles significantly differs from the analytical (given) value; hence, the respective diffusion currents and the diffusion coefficients that are determined on their basis decrease.

The second complexity is due to the possibility of the formation of intermediates (in the bulk solution or on the electrode surface) and their reduction in a multistage process that includes intermediate adsorption and interaction in the adsorption stage.

As applied to the electrodeposition of iron group metals and their codeposition with tungsten and molybdenum, one of these possibilities can be attributed to the following sequence of reactions [11, 19], which include the formation of an adsorbed intermediate and the reduction from the adsorbed complex. These reactions can be described as follows:

$$M(\mathrm{II})\mathrm{L} + e^- \longrightarrow M(\mathrm{I})\mathrm{L}_{ads}; \quad (6)$$

$$M(\mathrm{I})\mathrm{L}_{ads} + e^- \longrightarrow M(\mathrm{s}) + \mathrm{L}. \quad (7)$$

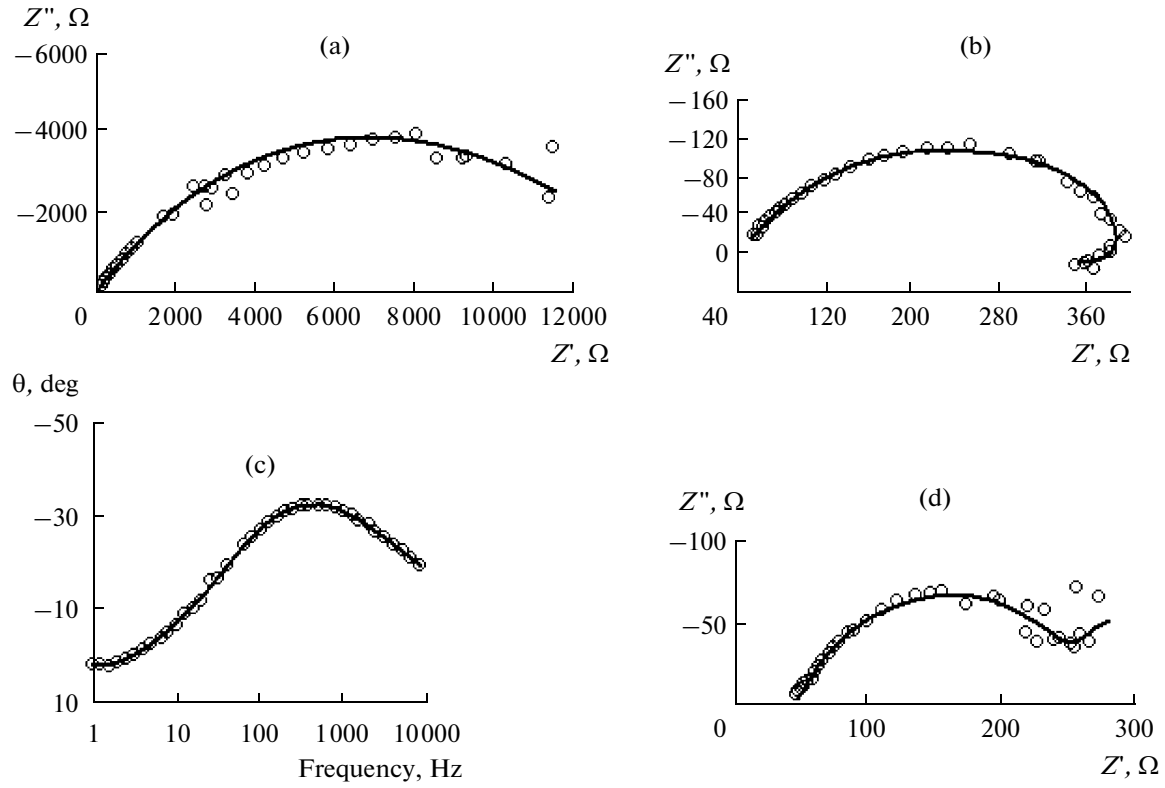

Fig. 7. Comparison of the experimental electrochemical impedance spectra of CoW at pH 6.7 and the results of fitting in Nyquist and Bode coordinates to the equivalent circuit (see Fig. 10). The points stand for the experimental data; the solid line is the fitting. Experimental Nyquist diagrams for the potentials: (a) –0.60, (b) – 0.78, and (d) – 0.86 V; (c) Bode diagram for case (b).

The reduction of tungsten is catalyzed by M(II) particles, and the respective reactions can be represented as

$$WO_4^{2-} + M(II)L + 2H_2O + 2e^- \longrightarrow [M(II)LWO_2]_{ads} + 4OH^-, \quad (8)$$

$$[M(II)LWO_2]_{ads} + 2H_2O + 4e^- \longrightarrow W(s) + M(II)L + 4OH^-. \quad (9)$$

It is shown in [1] that the formation of intermediates is possible in the bulk solution due to the chemical interaction between the electrolyte components (citrate complexes of iron group metals with tungsten and molybdenum). One of the methods for determining the role of the ionic mass transfer (the diffusion in the solution) in this process can be electrochemical impedance spectroscopy.

ELECTROCHEMICAL IMPEDANCE SPECTROSCOPY

Using electrochemical impedance spectroscopy, the electrodeposition of Co at pH 8 and CoW at pH 6.7 and 8.0 were studied in order to compare the features of the deposition and codeposition of Co with W and the effect of the pH on this process. In this case, the compositions of the solutions employed for the deposition did not differ from those described earlier [13–15].

If the inflection of the polarization curve is related to the slowness of the stage of diffusion from the solution to the electrode, then it must affect the impedance spectra. It follows from the theory of impedance with a slow diffusion stage [20] that the phase shift angle represented in Bode coordinates must approach –45° at low frequencies; in the case with a slow discharge or adsorption of an intermediate complex, it approaches 0°; and, if the impedance spectrum is represented in Nyquist coordinates, then a rectilinear dependence of Z'' on Z' with a slope of 45° must be observed at low frequencies.

The data in Figs. 7–9 show that the shape of the impedance spectra does not imply a slow diffusion stage. The presence of two peaks in the Bode diagram excludes a single slow stage of charge transfer. Also note that, if in the case of the deposition of CoW at pH = 6.7 at low cathode potentials the electrochemical impedance spectrum is described without separate adsorption component (Fig. 7a), then an increase in the potential leads to an increase in the hydrogen evolution and hence in the alkalization of the near-electrode layer, which results in the appearance of an

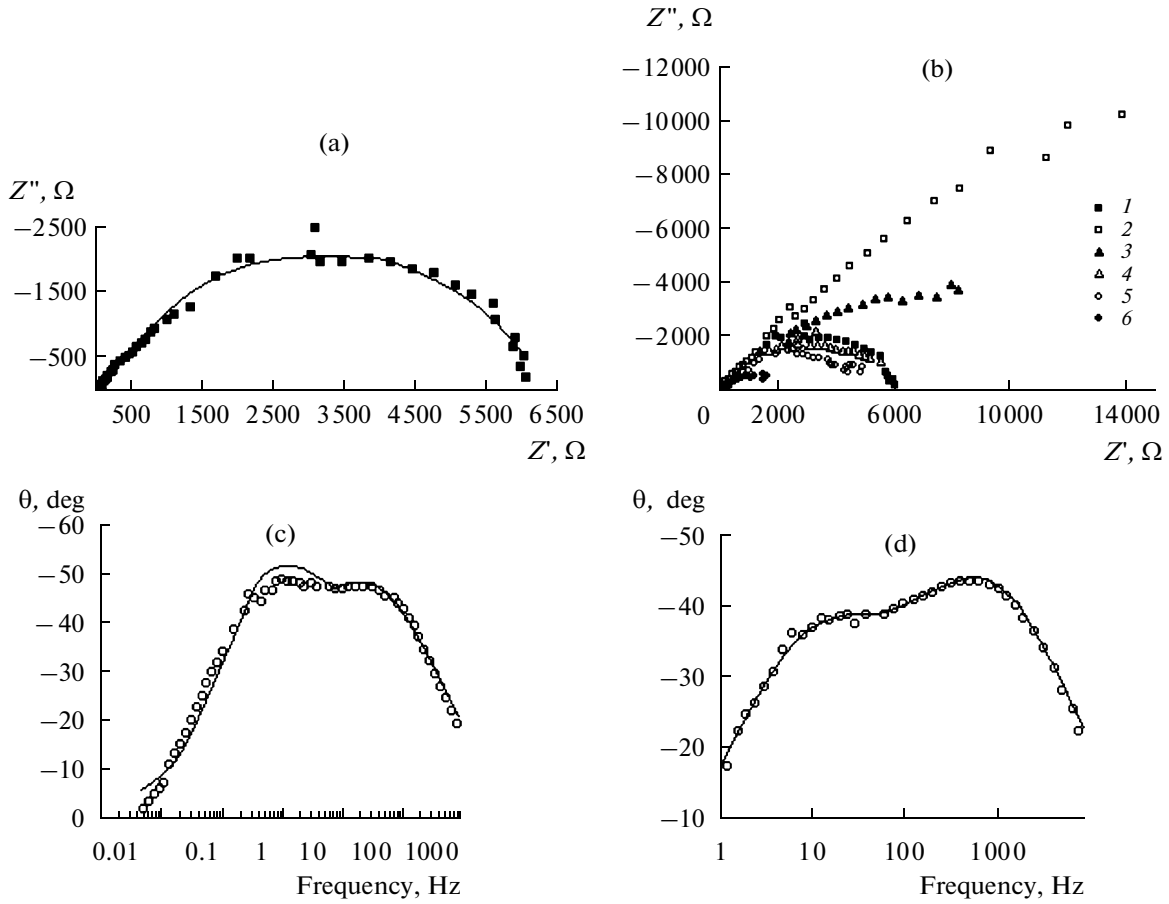

Fig. 8. Comparison of the experimental spectra of the electrochemical impedance of CoW at pH 8 and the results of fitting to the equivalent circuit (Fig. 10) in Nyquist and Bode coordinates. The points stand for the experimental data; the solid line is the fitting. (a) Nyquist diagram for −0.55 V; (b) experimental Nyquist diagrams for the studied potentials; (c) and (d) Bode diagrams for −0.55 and −0.8 V. The values of the equivalent circuit elements are listed in Table 2: (*1*) −0.55; (*2*) −0.60; (*3*) −0.65; (*4*) −0.70; (*5*) −0.75; (*6*) −0.80 V.

adsorption component at potentials above −0.7 V (Figs. 7b, 7d). Meanwhile, at a higher value of the pH (equal to 8), electrochemical impedance spectrum is described by the equivalent circuit with separate adsorption at low and high cathode potentials. The presence of an adsorption complex at high pH values

Table 2. Numerical values of the parameters of the equivalent circuits shown in Figs. 7–9

Experimental conditions		Equivalent circuit element				
System	Potential, V	R_1, Ω cm^2 (uncompensated for resistance)	R_2, Ω cm^2 (charge transfer resistance)	R_3, Ω cm^2 (resistance to adsorption)	CPE_1, μF/cm^2 (double layer capacity)	CPE_2, μF/cm^2 (adsorption capacity)
CoW	−0.70	33.06	6544	–	0.61	–
	−0.78	36.64	1722	402.9	0.61	115.4-*L*
	−0.86	45.07	226.2	136.2	0.68	0.00226-C
CoW pH 8	−0.55	33.23	750.4	5309	0.74	0.78
	−0.80	29.12	432.4	1699	0.74	0.71
Co pH 8	−0.60	28.14	110.3	8152	0.67	0.64
	−0.80	25.33	747.6	2729	0.63	0.61

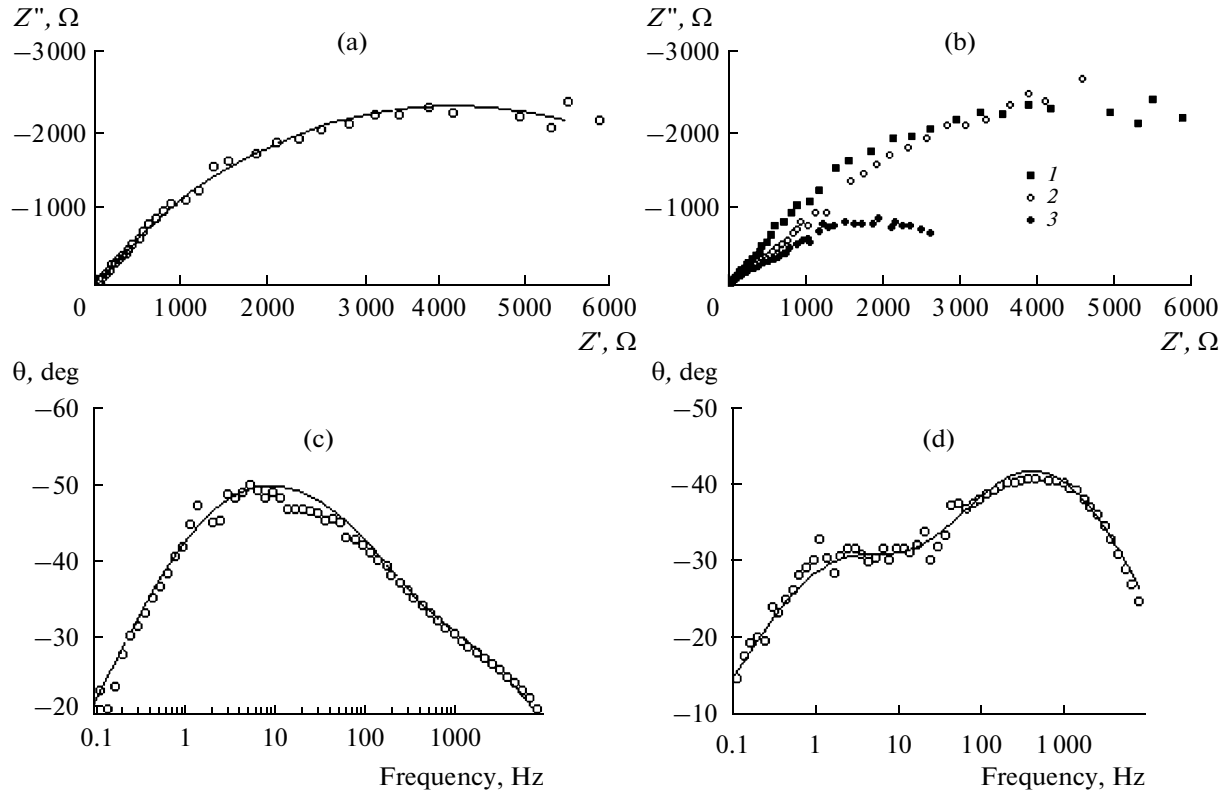

Fig. 9. Comparison of the experimental spectra of the electrochemical impedance of Co at pH 8 and the results of fitting in Nyquist and Bode coordinates with the equivalent circuit (Fig. 10). The points stand for the experimental data; the solid line is the fitting. (a) Nyquist diagram for −0.6 V; (b) experimental Nyquist diagrams for the studied potentials; (c) and (d) Bode diagrams for −0.6 and −0.8 V.

also plays a fundamental role in the deposition of a simpler system, such as the electrodeposition of cobalt (Fig. 9).

Thus, these experimental data are adequately described by an equivalent electric circuit characteristic of the processes that include the adsorption of an intermediate compound. In this work, the double layer capacity and the adsorption capacity are replaced by the respective constant phase elements. The impedance of which (Fig. 10) is described by the equation

$$Z_{CPE} = \frac{1}{C_{dl}(jw)^n}, \quad (10)$$

where j is an imaginary unit, w is the frequency, and n is the factor describing the nonideality of the double layer; in this particular case, $n < 1$.

This equivalent circuit is not the only one describing the impedance spectrum of a process with the adsorption of an intermediate compound. Depending on the ratio of the rates of the reactions of the total process (see, e.g., (6)–(9)), which also depend on the potential, a situation can occur when the resulting phase shift will correspond to the inductance; that is, so-called pseudoinductance will take place. Inductance simulates the situation when the adsorption layer is not constant under cyclic changes in the low-frequency potential [21]. The respective equivalent circuits are shown in Figs. 10c and 10d [19]. In this case, the charge transfer resistance is as follows

$$R_p = \frac{R_{ct}R_0}{R_{ct} + r_0}. \quad (11)$$

Thus, (i) the data of the impedance measurements show the presence of adsorption processes in the systems under study and (ii) the impedance does not specify the chemical composition of the adsorbed layer or the number of adsorption stages; it only shows the presence of a slow adsorption stage that follows from the data. Regardless of the complexes used for the codeposition of Co and W (individual or mixed cobalt–tungsten), the reduction of Co(II) and W(VI) requires a certain number of electrons (two for cobalt and six for tungsten). The simultaneous transfer of this number of electrons is hardly probable; therefore, a partially reduced complex is apparently held on the surface, in particular, by adsorption forces.

The data for the impedance also suggest that the stirring of the electrolyte has an effect on the state of its surface rather than on the mass transfer from the solution to the electrode. It follows from the results of [22]

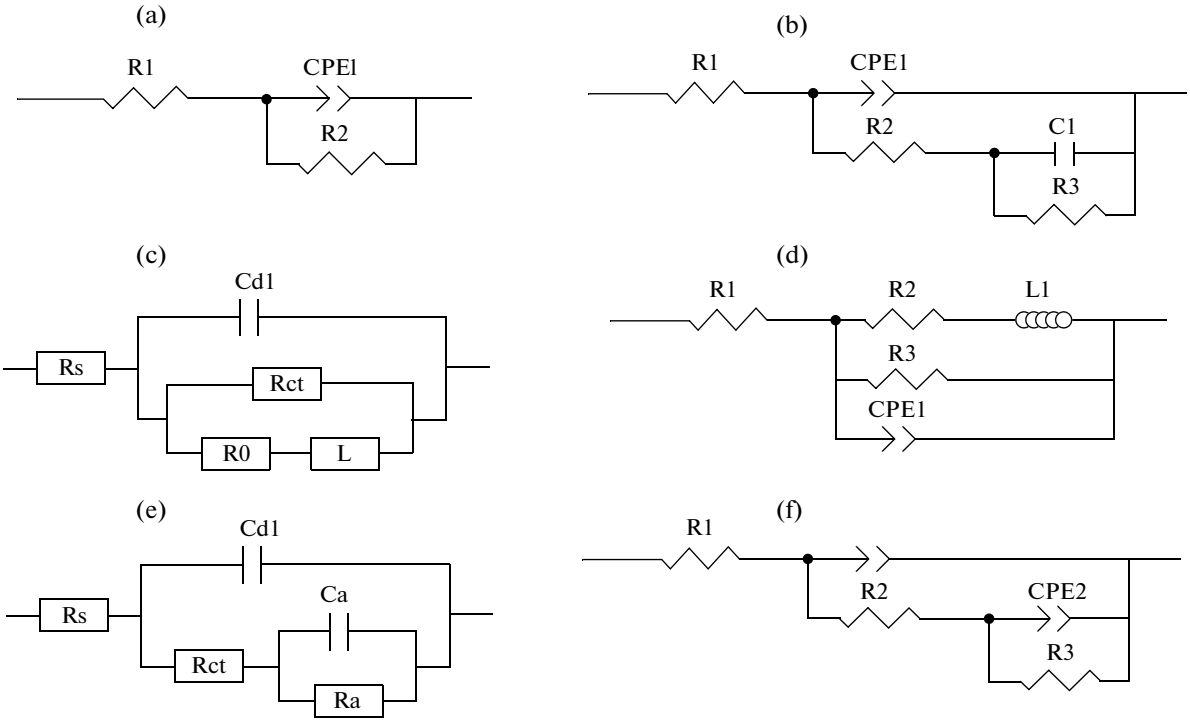

Fig. 10. (a)–(d) Equivalent circuits describing the electrochemical impedance spectrum for the deposition of CoW coatings on a cobalt substrate at pH = 6.7: (a) for potentials more positive than –0.74 V, (b) for potentials more negative than –0.74 V, and (c) and (d) for a potential of –0.78 V. (e) and (f) Equivalent circuits describing the electrochemical impedance spectrum for systems of deposition of Co and CoW coatings on a cobalt substrate at pH = 8. The values of the equivalent circuit elements are listed in Table 2.

that, at pH ≤ 4, the electrochemically active particles are an aquatic complex of Co^{2+}; therefore, the calculated value of the diffusion coefficient is "usual" in this case. At higher pH values, the electrochemically active particles will be both cobalt hydroxocomplexes [19, 23] and citrate complexes of cobalt as well as (possibly) mixed cobalt–tungsten citrate complexes. As the pH increases, their concentration changes and the adsorbed citrate complexes undergo a structuring. It is also known (see, e.g., [15]) that the concentration of the cobalt aquatic complexes in the solution and the current density of the electrodeposition decrease at pH > 5. The hydrogen evolution on the electrode favors a local increase in the pH. With the rotation of the electrode, the local increase in the pH sharply slows down, which leads to a decrease in the concentration of the adsorbed complexes and an increase in the electrodeposition current's density. In a galvanostatic mode, at a constant current density, this results in an increase in the current efficiency; a lowering of the electrodeposition potential; and a decrease in the concentration of tungsten in the coating [13], which, in turn, is one of the causes of changes in its structure [24] and hence properties [14].

CONCLUSIONS

The features of the role of ionic mass transfer in the process of the induced codeposition for obtaining cobalt–tungsten coatings from citrate solutions are analyzed. It is shown that, in a certain range of potentials, the electrode process's rate and the composition of the resulting alloy (and hence its structure) are determined by the hydrodynamic conditions. However, the case under discussion heavily differs from the the case of mixed kinetics (a slow charge transfer complicated by the slow convective diffusion of transfer of the electroactive component (components) to the surface). It is shown that the process's rate and the transfer resistance are also determined by the stage of adsorption of an intermediate complex (intermediate) on the electrode's surface. The composition of the intermediate complex, in turn, is determined by the conditions of the ionic mass transfer, including the pH of the near-electrode layer, which depends on the rotation rate (the hydrodynamic conditions). The elements of the mechanism of the electrode process that follow from the analysis do not confirm the hypothesis proposed in [13] that electrochemical equilibrium takes place at the film–solution interface; however, they are consistent with it in the sense that the conditions of the ionic mass transfer determine the composition of the film (intermediate).

ACKNOWLEDGMENTS

This work was supported in part by the program Micro- and Nanoscale Electrophysicochemical Surface Processes, state programs of the Republic of Moldova (Multilayer Nanostructured Materials Obtained by Electrochemical Methods: the Study and Estimation of the Tribological, Corrosion, and Magnetic Properties; The Study of New Nanostructured Electrochemical Materials Based on Iron Group Alloys and Their Mechanical, Tribological, and Corrosion Properties), and the Research Council of Lithuania (project no. MIP-134/2010).

REFERENCES

1. Eliaz, N. and Gileadi, E., Induced Codeposition of Alloys of Tungsten, Molybdenum, and Rhenium with Transition Metals, *Mod. Aspects Electrochem.*, New York: Springer, 2008, vol. 42, pp. 191–301.
2. Brenner, A., *Electrodeposition of Alloys*, New York: Academic Press, 1963.
3. Santana, R.A.C., Campos, A.R.N., Medierosv, E.A., Oliveira, A.L.M., Silva, L.M.F., and Prasad, Sh., Studies on Electrodeposition and Corrosion Behavior of Ni–W–Co Amorphous Alloy, *J. Mater. Sci.*, 2007, vol. 42, no. 22, pp. 9137–9144.
4. Tsyntsaru, N., Belevskii, S., Dikusar, A., and Celis, J.P., Tribological Behavior of Electrodeposited Cobalt–Tungsten Coatings: Dependence on Current Parameters, *Trans. Inst. Met. Finish.,* 2008, vol. 86, pp. 301–307.
5. Tsyntsaru, N., Belevskii, S., Volodina, G.F., Bersirova, O.N., Yapontseva, Yu.S., Kublanovskii, V.S., and Dikusar, A.I., Composition, Structure, and Corrosion Properties of Coatings of CoW Electrodeposited under Direct Current, *Surf. Eng. Appl. Electrochem.*, 2007, vol. 43, no. 5, pp. 312–317.
6. Bobanova, Zh.I., Dikusar, A.I., Cesiulis, H., Celis, J.P., Tsyntsaru, N.I., and Prosycevas, I., Micromechanical and Tribological Properties of Nanocrystalline Coatings Electrodeposited from Citrate–Ammonia Solutions, *Russ. J. Electrochem.*, 2009, vol. 45, no. 8, pp.895–901.
7. Vasauskas, V., Padgurskas, J., Rukuiza, R., Cesiulis, H., Celis, J.-P., Milcius, D., and Prosycevas, I., Cracking Behavior of Electrodeposited Nanocrystalline Tungsten–Cobalt and Tungsten–Iron Coatings, *Mechanika*, 2008, no. 4, pp. 21–27.
8. Weston, D.P., Shipway, P.H., Harris, S.J., and Cheng, M.R., Friction and Cobalt–Tungsten Alloy Coatings for Replacement of Electrodeposited Chromium, *Wear*, 2009, vol. 267, pp. 934–943.
9. Podlaha, E.J. and Landolt, D., Induced Codeposition: 1. An Experimental Investigation of Ni–Mo Alloys, *J. Electrochem. Soc.*, 1996, vol. 143, no. 3, pp. 885–892.
10. Podlaha, E.J. and Landolt, D., Induced Codeposition: II. A Mathematical Model Describing the Electrodeposition of Ni–Mo Alloys, *J. Electrochem. Soc.*, 1996, vol. 143, no. 3, pp. 893–899.
11. Podlaha, E.J. and Landolt, D., Induced Codeposition: III. Molybdenum Alloys with Nickel, Cobalt, and Iron, *J. Electrochem. Soc.*, 1997, vol. 144, no. 5, pp. 1672–1680.
12. Silkin, S.A., Belevskii, S.S., Tsyntsaru, N.I., Shulman, A.I., Shcuplyakov, A.N., and Dikusar, A.I., Influence of Long-Term Operation of Electrolytes on the Composition, Morphology, and Stress–Strain Properties of Surfaces Produced at Deposition of Co–W Coatings from Citrate Solutions, *Surf. Eng. Appl. Electrochem.,* 2009, vol. 45, no. 1, pp. 1–12.
13. Belevskii, S.S., Tsyntsaru, N.I., and Dikusar, A.I., Electrodeposition of Nanocrystalline Co–W Coatings from Citrate Electrolytes under Controlled Hydrodynamic Conditions: Part 2. The Electrodeposition Rate and Composition of the Coatings, *Surf. Eng. Appl. Electrochem.*, 2010, vol. 46, no. 2, pp. 91–99.
14. Silkin, S.A., Belevskii, S.S., Gradinar, A.S., Petrenko, V.I., Yakovets, I.V., Tsyntsaru, N.I., and Dikusar, A.I., Electrodeposition of Nanocrystalline Co–W Coatings from Citrate Electrolytes under Controlled Hydrodynamic Conditions: Part 3. The Micro- and Macrodistribution of the Deposition Rates, the Structure and the Mechanical Properties, *Surf. Eng. Appl. Electrochem.,* 2010, vol. 46, no. 3, pp. 206–214.
15. Belevskii, S.S., Yushchenko, S.P., and Dikusar, A.I., Electrodeposition of Nanocrystalline Co–W Coatings from Citrate Electrolytes under Controlled Hydrodynamic Conditions: Part 1. Co Electrodeposition, *Surf. Eng. Appl. Electrochem.,* 2009, vol.45, no. 6, pp. 446–454.
16. Eisenberg, M., Tobias, C.W., and Wilke, C.R., Ionic Mass Transfer and Concentration Polarization at Rotating Electrodes, *J. Electrochem. Soc.*, 1954, vol. 101, p. 306.
17. Madore, C., West, A.C., Matlosz, M., and Landolt, D., Design Considerations for a Cylinder Hull Cell with Forced Convection, *Electrochim. Acta*, 1992, vol. 37, no. 1, p. 69.
18. Newman, J.S., *Electrochemical Systems*, Englewood Cliffs: Pentice-Hall, 1973.
19. Grande, W.C. and Talbot, J.B., Electrodeposition of Thin Films of Nickel–Iron: 2. Modelling, *J. Electrochem. Soc.*, 1993, vol. 140, no. 3, pp. 675–681.
20. Lasia, A., Electrochemical Impedance Spectroscopy and its Applications, *Mod. Aspects Electrochem.*, Conway, B.E., Bockris, J., and White, R.E. Eds., New York: Kluwer, 1999, vol. 32, pp. 143–248.
21. Cesiulis, H. and Baltrunas, G., The Study of Surface Passivity and Blocking by the Electrochemical Technique, *Physicochem. Mech. Mater.*, 2006, no. 5, pp. 11–17.
22. Jeffrey, M.I., Choo, W.L., and Breuer, P.L., The Effect of Additives and Impurities on the Cobalt Electrowinning Process, *Miner. Eng.*, 2000, vol. 13, no. 12, pp. 1231–1241.
23. Cesiulis, H. and Budreika, A., Electroreduction of Ni(II) and Co(II) from Pyrophosphate Solutions, *Mater. Sci. (Medziagotyra)*, 2010, vol. 16, no. 1, pp. 52–56.
24. Tsyntsaru, N., Cesiulis, H., Bobanova, J., Croitory, D., Dikusar, A., and Celis, J.-P., Electrodeposition and Tribological Characterization Co–W and Fe–W A, *Proc. Int. Conf. Balttrib 2009*, Kaunas, 2009, pp. 259–264.

ISSN 1068-3755, Surface Engineering and Applied Electrochemistry, 2010, Vol. 46, No. 6, pp. 579–581. © Allerton Press, Inc., 2010.
Original Russian Text © A.N. Mikhailyuk, G.F. Volodina, 2010, published in Elektronnaya Obrabotka Materialov, 2010, No. 6, pp. 53–55.

ELECTRICAL SURFACE TREATMENT METHODS

Structure-Phase Transformations in Electrospark Iron–Carbon Surfaces at Different Heating Temperatures

A. N. Mikhailyuk and G. F. Volodina

Institute of Applied Physics, Academy of Sciences of Moldova, ul. Akademiey 5, Chisinau, MD-2028 Republic of Moldova
e-mail mihalek@yandex.ru

Received May 18, 2010

Abstract—The results of investigation of the surface structure-base transformation of iron specimens subjected to carbonization by the electrospark method and heating in the temperature range of 20–800°C are given. It is known that, after electrospark alloying with graphite, a surface layer consisting of mainly austenite and cementite forms with a carbon content in γ-Fe. The quantity of the austenite reduces with heating, and, at 300°C, it fully turns into a ferrite-cementite mixture (perlite). The heating of the specimens reduces the value of the microstresses, and the diffraction lines narrow down coming nearer to the annealed armco-iron values.

DOI: 10.3103/S1068375510060062

The electrospark alloying of metal surfaces (ESA) opens wide prospects for improving the wear resistance of various friction pairs, which is possible due, in particular, to the formation of highly dispersed structures of antifriction materials on the surfaces in friction [1]. However, the processes in the friction area have not always been considered in the case of choosing the surface alloying materials. For example, outside friction resulting from plastic deformation improves the thermodynamic potential of the friction surfaces (free surface energy γ, the inside energy E, etc.), which makes these surfaces highly active chemically and catalytically. According to the research, the ultimate criterion of seizure of the friction surfaces making them wear and fail is the level of the surface energy γ [2]. It is known that one of the ways to reduce the free surface energy and prevent its increase is surface alloying with nonmetal elements (boron, carbon, silicon, etc.) [2].

A possible solution is to apply electrospark surface alloying with graphite when carbon is injected in the surface layer both as free graphite and as carbide [3]. During iron-based alloying, quite a substantial amount of residual astenite is formed in the surface layer. The carbon dissolved in γ-Fe stabilizes the austenite and impedes the $\gamma \longrightarrow \alpha$ transformation of the iron lattice [4]. Austenite has a higher friction coefficient than α-Fe-based phases and relatively low tribotechnical properties [5]. How will the friction surface behave if relatively high pressure and friction rates makes the friction surfaces heat? How steady will the structure and phase composition of the surfaces be and in what way can they tend to transform? These questions are the basis of this study, where the results of the investigation of the structural-phase transformations in iron-based electrospark surfaces at 20–800°C are presented.

METHOD OF INVESTIGATION

Armco-iron specimens and MPG-6 graphite electrodes were the source materials used. The electrospark processing was realized according to the methods given in the table and with the use of an *Elitron-22* installation made by the IPF pilot plant of the RM AS.

All the samples were X-rayed with a DRON-2.0 diffractometer (CoK_α radiation, an Fe filter, and the θ/2θ method). High-temperature X-raying was conducted with a high-temperature diffractometer attachment (UVD-2000) where the samples were heated in vacuum. The spectra were taken every 100°C.

ESA methods of specimen processing

Sample no.	ESA operating current, A	Discharge energy, J	ESA relative time, min/cm^2
1	0.77	0.185	1
2	1.1	0.24	1
3	1.6	0.33	1
4	2.0	0.43	1
5	2.5	0.585	1
6	2.0	0.43	2
7	2.0	0.43	4

Note: The sample is made of armco-iron and the anode of MPG-6 graphite.

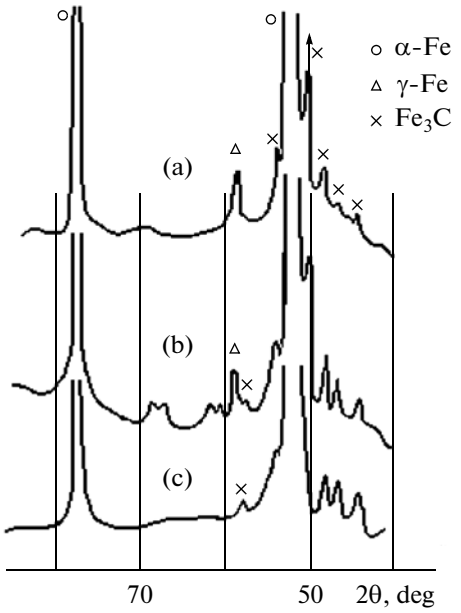

Fig. 1. Diffractograms of sample no. 5 at *t*: 20°C (a), 200°C (b), and 300°C (c).

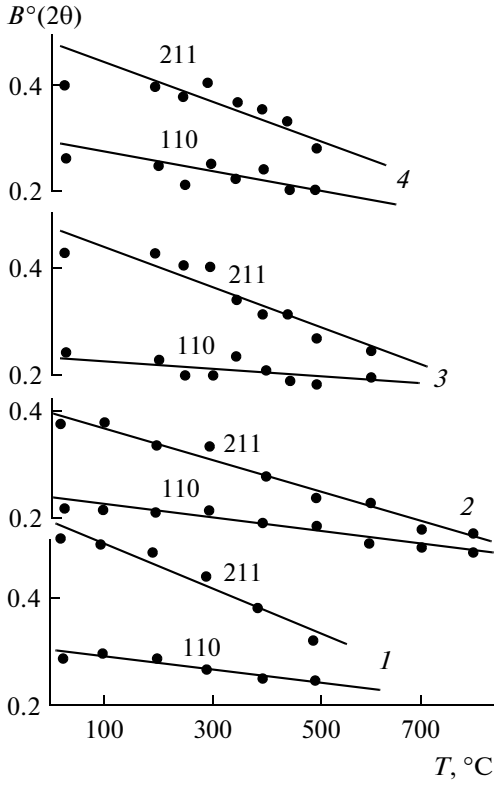

Fig. 2. Temperature dependence of the half-width of lines 110 and 211 α-Fe for sample nos. 2, 3, 4, and 5.

Sample no. 1 appeared to have a very weak diffractogram, whereas the spectra of samples nos. 4, 6, and 7 were identical. Therefore, for the detailed temperature researching, it was decided to use sample nos. 2, 3, 4, and 5.

RESULTS AND ANALYSIS

The diffractograms of all four specimens are similar and contain α-Fe phase spectra, Fe_3C cementite, and a γ-Fe metastable phase (the relations among which depend on the ESA discharge energy). The γ-Fe phase behaved steadily at a moderate cooling rate only down to 723°C [4], although conditions for freezing the phase and preventing its transformation into a ferrite-cementite mixture appeared if the microalloy cooled down rapidly at 10^4–10^5 degrees/s [6]. After the ESA with graphite, for all the processing methods, the period of the γ-Fe lattice substantially increased and was about 3.63 Å as, according to [7], the lattice contained about 2% diluted carbon; that is, high-carbon austenite was generated. As the temperature of the specimens rises, the quantity of austenite in them falls rapidly, and, at 300°C, the lines of that phase go entirely, whereas the α-Fe and cementite lines become more intensive (Fig. 1). The diffractograms of sample nos. 2 and 3 reveal a very blurred unidentified line in the area of angles of about 69–70 degrees (d ~1.6 Å), which is preserved during the entire temperature survey, remains when the second sample cools down, and fades away in the case of the cooling of the third sample.

At room temperature, the α-Fe lattice has a period of 2.86 Å, which is typical for nearly pure iron. In the case of heating the samples, the figure grows to reach 2.90 Å at 800°C, which is due both to the temperature's influence and, possibly, to a high concentration of carbon remaining after the transformation of the high-carbon austenite into ferrite. Therefore, after heating the samples up to more than 300°C, the ESA-processed layer has mainly a ferrite–cementite mixture consisting of cementite and perlite.

In this case, the martensite transformation of austenite is not expectable as it is known to quench entirely [8] if the metal is deformed by more than 30%, whereas, in our case, the study of the diffractograms of the different surfaces shows significant broadening of all the lines. The analysis of the α-Fe spectrum lines (for instance, for sample no. 5, the relation $\beta_{211}/\beta_{110} = 2.25$ approximates the relation $\tan\theta_{211}/\tan\theta_{110} = 2.42$) shows that the blurring is caused mainly by microstresses and the alloyed surface of the samples has mainly chaotically distributed dislocations [9] with a density of about 10^{14}–10^{15} m^{-2}, which is equal to more than 30% deformation [10].

Heating of the specimens reduces the value of the microstresses, the diffraction lines narrow down, and the integral width of the α-Fe line approximates the rates for the reference annealed armco-iron specimens; that is, (0.16 – 0.17)°(2θ) and the dislocations become less dense. The tendencies discovered are typ-

ical of all the samples no matter how they have been processed.

CONCLUSIONS

The results of the study show that, during the heating of a graphitized layer on iron, its phase structure undergoes substantial transformation. The quantity of cementite and ferrite increases, whereas the concentration of austenite falls and goes entirely at 300°C. Alongside with the improved plasticity of the layer due to the weakened density of the dislocations, such a transformation promotes its better antifriction properties.

REFERENCES

1. Gitlevich, A. E., Mikhailov, V. V., Parkanskii, N. Ya., and Revutzkii, V. M., *Elektroiskrovoe legirovaniye metallicheskish poverkhnostey* (Electrospark Alloying of Metal Surfaces), Chisinau: Stiintsa, 1986, 196 pp.
2. Polonskii, Yu. Z., *O kontseptsii skhvatyvaniya metallov i eyo primenenie k oporam granichnogo treniya* (On the Metal Seizure Concept and Its Application to Boundary Friction Supports), Treniye i iznos, 1991, vol. 12, no. 2, pp. 258–266.
3. Mikhailyuk, A. I., Gitlevich, A. E., Ivanov, A. N., etc, Transformations in Surface Layers of Iron Alloys in Case of Graphite Electrospark Alloying, Elektronnaya obranotka materialov, 1986, no. 4, pp. 23–27.
4. Gulyaev, A. P., *Metallovedenie* (Metal Science), Moscow: Metallurgiya, 1986, p. 542.
5. Nazarenko, P. V. and Kostetskii, B. I., *Zavisimost' sily vneshnego treniya ot tipa I parametrov reshyotki par treniya. Trenie, smazka I iznos detaley mashin. Sb. Nauchnykh trudov, vypusk IV* (Dependency of Outside Friction Force from Type and Properties of the Lattice of Friction Pairs, Friction, Lubrication, and Wear of Machine Parts. A Comp. of Scientific Work, Issue IV), Kiev, 1964, pp. 137–139.
6. Zolotykh, B. N., Korobova, I. P., and Strypin, E. M. *Fizicheskie osnovy eletroiskrovoy obrabotki materialov* (Basic Physics of Electrospark Processing of Materials), M.: Nauka, 1966.
7. Mirkin, L. I., *Rentgeno-strukturnyi kontrol' mashinostroitel'nykh materialov. Spravochnik* (X-ray-Structural Control of Engineering Materials. Handbook), M.: Mashinostroeniye, 1979, p. 136.
8. Kurdyumov, G. V., Utevskii, L. M., and Entin, R. I. *Prevrashcheniya v zheleze i stali* (Transformations in Iron and Steel), M.: Nauka, 1977, p. 238.
9. Umanskiy, Ya. S., Skakov, Yu. A., Ivanov, A. N., and Rastorguev, L. M., *Kristallografiya, rentgenografiya i elektronnaya mikroskopiya* (Crystallography, Radiography, and Electronic Microscopy), M.: Metallurgiya, 1982, p. 632.
10. Panin, V. E., Grinyaev, Yu. V., Danilov, V. P., etc., *Strukturnye urovny plasticheskoy deformatsii i razrusheniya* (Structural Level of Plastic Deformation and Desctruction), Novosibirsk: Nauka, Sibirskoe otdelenie, 1990, p. 254.

ISSN 1068-3755, Surface Engineering and Applied Electrochemistry, 2010, Vol. 46, No. 6, pp. 582–588. © Allerton Press, Inc., 2010.
Original Russian Text © F.P. Grosu, M.K. Bologa, 2010, published in Elektronnaya Obrabotka Materialov, 2010, No. 6, pp. 56–64.

ELECTRICAL PROCESSES IN ENGINEERING AND CHEMISTRY

Thermoelectrohydrodynamic Methods of Energy Conversion

F. P. Grosu[a] and M. K. Bologa[b]

[a] *State Agrarian University, ul. Mirchesht' 44, Chisinau, MD-2049 Republic of Moldova*
e-mail: f.grosu@mail.ru

[b] *Institute of Applied Physics, Academy of Sciences of Moldova, ul. Akademiei 5, Chisinau, MD-2028, Republic of Moldova*
e-mail: mbologa@phys.asm.md

Received May 25, 2010

Abstract—The problems connected with the conversion of electrical energy into mechanical energy and vice versa involving heat energy (i.e., using thermoelectrohydrodynamic (TEHD) methods) are considered. It is shown that these conversions depend on the type of the dielectric liquid, which can exhibit ideal dielectric properties or low conductivity. The respective criteria for these cases are given. In an ideal case, mechanical energy can be obtained using only electrical and thermal energy (a TEHD pump). In a low conducting dielectric, there exists the possibility in principle to generate convective currents, i.e., to generate electric energy, using the heat energy and partially the electric energy. The formulas for the calculation of the liquid consumption in TEHD pumps and electroconvective currents for TEHD generators are obtained.

DOI: 10.3103/S1068375510060074

INTRODUCTION

It is well known that electrohydrodynamic (EHD) interactions of external electric fields with ideal or nonideal (low conducting) liquids [1] manifest themselves as electroconvective motions of liquids called electric convection (EC) [1, 2]. In this case, we are dealing with interactions with an initially motionless liquid as well as a moving one too. Electroconvection itself is caused by the medium's nonuniformities with respect to its two electrophysical parameters: its absolute permittivity $\varepsilon \equiv \varepsilon_v\varepsilon_r$ and/or its electric relaxation time $\tau \equiv \varepsilon/\sigma$, where ε_v is the universal electric constant (the vacuum permittivity); ε_r is the relative permittivity; and σ is the specific electric conductivity coefficient. Nonuniformities, in turn, are due to different reasons [3], the most typical being *thermal* ones when a uniform liquid in its mechanical composition is nonuniform in the distribution of the temperature in it, and *mechanical* ones in the case of a heterogeneous medium (emulsions, suspensions, aerosols, etc.). Accordingly, there are recognized *electrothermal* (ETC) and *electromechanical* (EMC) convections. But, as the experiments show, the volumetric electrization of a medium and its motion in an external electric field is also possible at the total absence of thermal and mechanical nonuniformities. In these cases, the electroconvection is commonly called electroisothermal (EITC) [4, 5].

When electric fields interact with liquids, there takes place the interconversion of energies: electric and/or heat energy into the mechanical one and, inversely, mechanical and/or heat energy into the electric one. On the basis of these conversions, it is possible to create various EHD devices to be used in practice, particularly electrohydrodynamic (EHD) or thermoelectrohydrodynamic (TEHD) pumps (of a new type—without moving hard parts) in the first case and EHD or TEHD generators in the second case. These conversions have some peculiar features for every type of electroconvection; thus, it is expedient to consider them separately.

In work [6], the problems of EHD conversions under the conditions of EITC have been discussed. Here we are going to examine and clear up the practical aspects of EHD conversions as applied to the electrothermal case (ETC) when a liquid being uniform in its mechanical composition is nonuniform in temperature, i.e., $T \neq \text{const}$, and, consequently, along the liquid $\varepsilon = \varepsilon(T) \neq \text{const}$; $\tau = \tau(T) \neq \text{const}$.

In order to understand the physical essence of the regularities and to find out the TEHD flows that can be used in practice for different aims, we proceed from formulas for the density of an electric force acting on a liquid dielectric in an electric field [7, 8]:

$$f = \rho E - (1/2)E^2\nabla\varepsilon + (1/2)\nabla[\gamma(\partial\varepsilon/\partial\gamma)E^2], \quad (1)$$

and the electric current density, which in the most general case when magnetic effects are absent has the form [8]:

$$j = \sigma E + \rho\upsilon - D\nabla\rho + \partial(\varepsilon E)/\partial t + \nabla\times(P\times\upsilon), \quad (2)$$

where ρ is the density of the space *free* charges; υ is the vector of the convective velocity; D is the coefficient of theion diffusion assumed the same for both positive and negative ions; and P is the vector of the electric polarization of the liquid. Hereafter, in formula (1), we neglect the last electrostriction summand, which is the "exact" gradient of some scalar function (in square

brackets) and does not produce any work in the closed bulk of the liquid limited by solid walls [3]. The estimations also show that, for the cases of interest, in also the equation for the current density (2), the diffusion current (the third summand) may be omitted. As for the last summand, which can be called *the convective current of polarization* [8], it is solenoidal, and it is usually automatically dropped out of the consideration (its divergence is identically zero). Nevertheless, this summand is kept as it is the only component of the current remaining in an ideal dielectric in the stationary case.

Formula (1) explains the reasons for the appearance of electroconvective flows and the pumping effect, i.e., the ordered convective flow. The action of an EHD generator is explained in outline by the second summand of formula (2); that is, by a common electroconvective current. In the electric field, the liquid is charged; then, it is set in motion; if it is performed by the field forces, we have here electric convection and we are simply dealing with the growth of the charge transfer at the expense of the additional, convective component of the total current. These effects are widely used and can be employed in different automatic EHD devices [9]. If the motion is due to an external hydrodynamic head (forced motion) or thermal (natural) convection, we are dealing with a generator effect with the same convective current $j_k = \rho\upsilon$ being generated, and electric energy is produced at the expense of the mechanical one in the first case or the hermal one in the second case.

In accordance with the general approach to the study of electroconvective phenomena, let us separately consider the cases of ideal and nonideal (low conducting) dielectrics. In practice, these cases are stated according to the following criteria: $\tau/t_* > 1$ is an ideal dielectric, and $\tau/t_* < 1$ is a nonideal one, where t_* is the characteristic time of the external field change; it is an oscillation period in the typical case of a sinusoidal alternating field [3, 4].

Ideal Liquid Dielectrics ($\tau/t_* > 1$)

By assumption, charges are not brought into an ideal dielectric ($\sigma = 0$) from the outside, and there are no free ones by definition. Thus, the first purely coulomb component of the force ($f_1 \equiv \rho E$) disappears due to $\rho \equiv 0$; thus, only the second summand remains, which with regard for the thermal nonuniformity of the medium may be written as

$$f \equiv f_2 \equiv -(E^2/2)\nabla\varepsilon = (E^2/2)\varepsilon\beta_\varepsilon\nabla T, \qquad (3)$$

where $\beta_\varepsilon \equiv -(1/\varepsilon)(d\varepsilon/dT)$ is the temperature coefficient of the dielectric permittivity at some average liquid temperature. The second equation in the case under examination has the form

$$j \equiv \partial(\varepsilon E)/\partial t + \nabla\times(P\times\upsilon). \qquad (4)$$

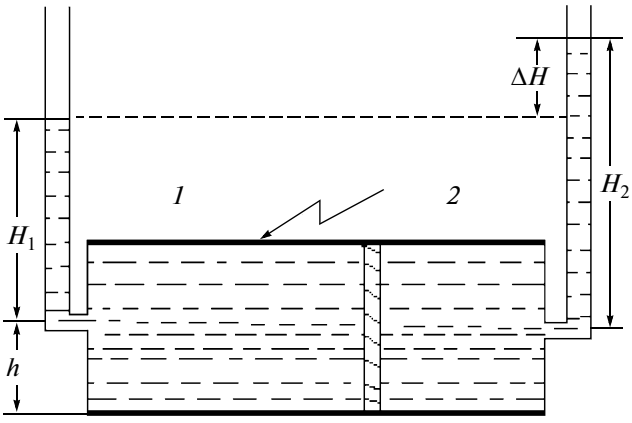

Fig. 1. Pull of the interface into the electric field.

Under the action of force (3), there is possible the electroconvective motion of a medium in a steady mode ($\partial/\partial t \equiv 0$) being the result of the conversion of heat energy into mechanical energy, and there is conceivable the creation of a TEHD pump on this basis. As for the TEHD generation of electric energy with such a statement of the problem (under the conditions of the complete absence of the liquid electrization), it is impossible because $\rho \equiv 0 \Rightarrow j_k = 0$. Thus, we restrict ourselves to the search for a possible one-dimensional TEHD flow between the plates of a plane-parallel horizontal capacitor as applied to the creation of a TEHD pump for ETC in an ideal dielectric liquid.

To understand better the physical essence of this flow, we begin with the solution of a simple problem on the pulling in of the interface of two immiscible liquids into a plane-parallel horizontal capacitor.

Pulling in of the Interface into a Plane Capacitor

In Fig. 1, the interface between two liquids *1* and *2* is presented in the form of a thin dielectric piston. By the assumption that $\varepsilon_1 > \varepsilon_2$, the pulling in apparently happens from the left to right, resulting in the rising of the liquid level by some magnitude $\Delta H \equiv H_1 - H_2$. The further problem consists in searching for this magnitude as the corresponding pressure drops $\Delta P \equiv \gamma g \Delta H$, where γ is the liquid's density ($\gamma_1 \approx \gamma_2 \equiv \gamma$), which is the most important static characteristic of any pump. To solve this problem, we proceed from a general expression for the free energy $\tilde{F} = \tilde{F}_1 + \tilde{F}_2$ of the whole liquid mass at the prescribed intensity (potentials) of the electric field E [7].

Omitting the a fortiori constant summands containing in particular the inner energy for the free ener-

gies of each liquid, including the potential and electric (with the sign "–") ones, we find

$$\begin{aligned}\tilde{F}_1 &= (m_1 g H_1)/2 + M_1 g h - (\varepsilon_v/2)(\varepsilon_{r1} - 1)E^2 V_1;\\ \tilde{F}_2 &= (m_2 g H_2)/2 + M_2 g h - (\varepsilon_v/2)(\varepsilon_{r2} - 1)E^2 V_2,\end{aligned} \quad (5)$$

where m_1, m_2 are the masses ofthe liquid columns H_1 and H_2; M_1, M_2 are the masses of parts of liquids *1* and *2*; V_1 and V_2 are the corresponding volumes; $\varepsilon_1 = \varepsilon_v\varepsilon_{r1}$; and $\varepsilon_2 = \varepsilon_v\varepsilon_{r2}$. Substituting the quantities $m_1 = \gamma_1 S_0 H_1$; $M_1 = \gamma_1 V_1$; $m_2 = \gamma_2 S_0 H_2$; $M_2 = \gamma_2 V_2$ into formulas (5), we obtain for the total free energy

$$\tilde{F} = (g/2)S_0(\gamma_1 H_1^2 + \gamma_2 H_2^2) + (\gamma_1 V_1 + \gamma_2 V_2)gh - (\varepsilon_v E^2/2)[(\varepsilon_{r1} - 1)V_1 + (\varepsilon_{r2} - 1)V_2].$$

It is known that, at the state of thermodynamic equilibrium, presuming mechanical equilibrium too, the thermodynamic potential $\tilde{F}$ should have a minimum which we ascertain assuming the variation $\delta\tilde{F}$. Taking into account $H_1 + H_2 = \text{const} \Rightarrow \delta H_2$ and $V_1 + V_2 = \text{const} \Rightarrow \delta V_2 = -\delta V_1$, we find

$$\delta\tilde{F} = gS_0(\gamma_1 H_1 - \gamma_2 H_2)\delta H_1 + (\gamma_1 - \gamma_2)gh\delta V_1 + (E^2/2)(\varepsilon_1 - \varepsilon_2)\delta V_1 = 0.$$

Considering also that $\delta V_1 = S_0\delta H_2 = -S_0\delta H_1$, we obtain the final result:

$$\gamma_1 H_1 - \gamma_2 H_2 = (\gamma_1 - \gamma_2)h - [E^2/(2g)](\varepsilon_1 - \varepsilon_2).$$

The second equation for H_1 and H_2 is of purely geometric character (see Fig. 1) and has the form $H_1 + H_2 + l \approx L = \text{const}$—the total length of the EHD channel, where l is the length of the cell (capacitor). This is the general solution of the problem. Usually $\gamma_1 \approx \gamma_2 \equiv \gamma$, and then from (5) for the hydrostatic head there is obtained the formula

$$\Delta P \equiv \gamma g(H_2 - H_1) \equiv \gamma g \Delta H = (E^2/2)(\varepsilon_1 - \varepsilon_2). \quad (6)$$

This result is achieved at once considering that $P_E = (\varepsilon E^2/2)$ is none other than the electric pressure.

From the point of view of energy, the pulling in of a liquid with great dielectric permittivity into a field is explained by the simultaneous increase of the surface density of the free charges on the electrodes coming from the field source because it is necessary to maintain the potentials of the electrodes as constant. Thus, the work to produce a liquid head (6) is performed thanks to the power supply, i.e., to the capacitor's charging power.

One-Dimensional TEHD Flows

It is obvious that, if the difference of the dielectric constants in formula (6) is produced due to the difference of the temperatures at the ends of the channel with the liquid, according to the formula

$$\begin{aligned}\varepsilon_1 - \varepsilon_2 &= \varepsilon\beta_\varepsilon(T_{02} - T_{01}) \equiv \varepsilon\beta_\varepsilon\Delta T;\\ \Delta T &\equiv T_{02} - T_{01},\end{aligned} \quad (7)$$

where T_{01}, T_{02} are the temperatures at the inlet and outlet of the TEHD channel, the hydrodynamic head ΔP can be supported by this temperature difference:

$$\begin{aligned}\Delta P \equiv \gamma g \Delta H &= (1/2)E^2\varepsilon\beta_\varepsilon\Delta T\\ \Rightarrow\ \Delta H &= (1/2)E^2\varepsilon\beta_\varepsilon(\Delta T/\gamma g),\end{aligned} \quad (8)$$

where ΔH is the difference of the levels at the inlet and outlet of the TEHD channel (the pressure gauge indications, Fig. 1).

Formula (8) may be the basis for the design of TEHD pumps operating according to the considered electrothermal principle. Really, for this purpose, in the first approximation, it is sufficient to substitute ΔP from (8) into the design equations of Poiseuille type or other hydraulics formulas expressing the fluid flow through the hydrostatic characteristics (head).

However, below, we try to establish the peculiar features of TEHD flows analytically. Proceeding from the general form of the expression for the electrothermal force (3), we assume that the flows that can be expected follow the direction of the temperature gradient, so we will seek for the flows under such boundary conditions when along the capacitor plates there are maintained constant gradients of the temperatures: A_1 and A_2 according to Fig. 2.

The calculation of the intensity is carried out approximately, assuming that the medium is in the state of equilibrium at some average constant temperature:

$$E = \frac{\varphi_2 - \varphi_1}{2h} = \frac{\varphi_s}{2h} = \text{const}. \quad (9)$$

It is easy to notice that the equilibrium at any distribution of the temperature $T_0 \neq \text{const}$ is impossible ($\text{rot}\vec{f}_0 \neq 0$); thus, no-threshold electrothermal convection should be observed at any $\nabla T \neq 0$. We proceed from the TEHD general equations [3]. Assuming $\vec{\upsilon} = \vec{i}\upsilon_x = \vec{i}\upsilon(z)$, we obtain

$$\begin{cases}-(\partial p/\partial x) + (E^2/2)\varepsilon\beta_\varepsilon(\partial T/\partial x) + \eta(d^2\upsilon/dz^2) = 0;\\ -(\partial p/\partial z) + (E^2/2)\varepsilon\beta_\varepsilon(\partial T/\partial z) - \gamma g = 0;\\ \upsilon\dfrac{\partial T}{\partial x} - a\left(\dfrac{\partial^2 T}{\partial x^2} + \dfrac{\partial^2 T}{\partial y^2}\right) = 0;\\ \gamma = \gamma_0(1 - \beta T).\end{cases} \quad (10)$$

In the approximation under consideration, the parameters E, η, a, ε, β_ε, β are assumed constant and

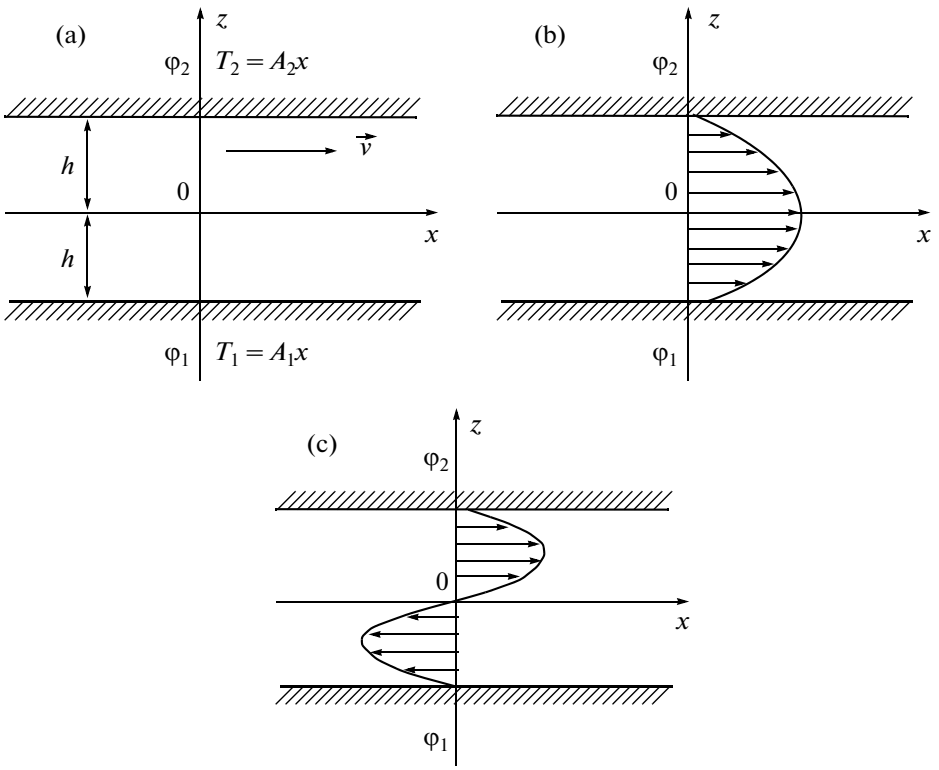

Fig. 2. Diagram of a one-dimensional TEHD flow in a plane-parallel channel.

equal to the average across the volume values. The boundary conditions for system (10) have the form

$$\upsilon(\pm h) = 0; \quad T(\pm h) = T_{1,2} = A_{1,2}x. \tag{11}$$

It follows from the equations of motion and the boundary conditions that the flows sought can be realized if the temperature along the liquid changes in conformity with the relation

$$T = xA(z) + \theta(z), \tag{12}$$

where $A(z)$, $\theta(z)$ are unknown functions of z. The substitution of (12) into the third equation of (10) gives the relations

$$\begin{gathered} A(z) = cz + b; \quad c = (A_2 - A_1)/(2h); \\ b = (A_2 + A_1)/2, \end{gathered} \tag{13}$$

in terms of which system (10) takes the form

$$\begin{cases} -(\partial p/\partial x) + (E^2/2)\varepsilon\beta_\varepsilon(cz + b) + \eta\upsilon''(z) = 0; \\ -(\partial p/\partial x) + (E^2/2)\varepsilon\beta_\varepsilon(cx + \theta') - \gamma_0 g \\ + \gamma_0 g\beta(cxz + bx + \theta) = 0; \\ \upsilon(z)(cz + b) - a\theta''(z) = 0. \end{cases} \tag{14}$$

Integrating the second equation of (14) and substituting the obtained expression for the pressure p into the first equation, we find

$$\eta\upsilon''(z) = \gamma_0\beta g(cz^2/2 + bz) - (1/2)\varepsilon\beta_\varepsilon E^2 b + B, \tag{15}$$

where B is the arbitrary integration constant having the meaning of the pressure gradient in the absence of the field ($B = -dp_0/dx$). Without any forced pumping of the liquid and the channel being open at its ends, the greatest flow rate determined by the field can be estimated assuming $B = 0$.

The solution of equation (15) satisfying boundary conditions (11) has the form

$$\begin{gathered} \upsilon(\xi) = -\frac{\gamma_0\beta g c h^4}{24\eta}(1 - \xi^4) + \frac{h^2}{2\eta}[(\varepsilon\beta_\varepsilon E^2 b/2) - B] \\ \times (1 - \xi^2) - \frac{\gamma_0\beta g b h^3}{6\eta}\xi(1 - \xi^2), \end{gathered} \tag{16}$$

where $\xi \equiv z/h$ is the dimensionless coordinate. Notice that, in a particular case of the absence of an electric field ($E = 0$), these formulas go into the known solution of the problem on natural convection in a plane horizontal layer of liquid [10].

It is seen from formula (16) that the flow rate profile presents a superposition of even profiles of the type in Fig. 2b or odd ones of the type in Fig. 2c.

As applied to the design of a TEHD pump, it is of interest that the ensured liquid volume flow rate is (per unit of channel width)

$$Q = \int_{-h}^{h} \upsilon(z)dz = -\frac{\gamma_0 \beta g c h^5}{15\eta} + \frac{2h^3}{3\eta}\left(\frac{1}{2}\varepsilon\beta_\varepsilon E^2 b - B\right). \quad (17)$$

The first summand of the right side of this formula is a part of the flow rate caused by the natural convection of the liquid, and the second one, by the electric field with consideration for the hydraulic losses (parameter B).

Formula (17) in the general form can be suitable with the aim to study the effect of isolated factors on the liquid flow rate, in particular, of boundary gradients of the temperatures A_1 and A_2, but we are esspecially interested in the case of the presence of only electroconvection ($g = 0$), which is tantamount to $c = 0$; that is, $A_1 = A_2 \equiv A \Rightarrow b = A$. Then, it follows from (17) that

$$Q = \frac{2h^3}{3\eta}\left(\frac{1}{2}\varepsilon\beta_\varepsilon E^2 A - B\right). \quad (18)$$

Considering the meaning of the constant B under static mode ($Q = 0$), we find one of the pump characteristics—the hydrostatic head that the TEHD pump can produce and that can be measured by a manometer (a graduated vertical tube, Fig. 1):

$$\Delta P = \frac{1}{2}\varepsilon\beta_\varepsilon E^2 A l = (\varepsilon\beta_\varepsilon \varphi_s^2 \Delta T)/(8h^2) \equiv \gamma g \Delta H, \quad (19)$$

where l is the horizontal EHD channel's (capacitor) length, ΔH is the reading of the manometer, ΔT is the difference of the temperatures at the TEHD channel ends, which, taking $E = \varphi_s/(2h)$ into account, coincides with result (8).

It is seen that, with the given field (φ_s), with increase in the heat flow rate (the increasing heat flux A), the liquid flow rate grows; that is, the direct conversion of heat energy into mechanical energy occurs through the mechanism of the liquid depolarization. As the colder liquid enters into the interelectrode space and moves into the hotter region, its electric energy decreases due to the reduction of the dielectric permittivity with the growth of the temperature. This diminution of the electric energy of the system is attended by the increase of its mechanical part.

As follows from (18), the greatest liquid flow rate caused by the electric field action is obtained at $B = 0$, and, thus, the flow rate (per unit of the channel width) is limited at the top according to the inequality

$$Q < Q_{\max} = \frac{\varepsilon\beta_\varepsilon \varphi_s^2 \Delta T}{12\eta l},$$

where the channel length $l \gg h$—the spacing between the capacitor plates (Fig. 2).

This formula shows that the only ways to increase the efficiency of the liquid pumping are the increases of electric voltage in the TEHD channel and the longitudinal temperature gradient $A = \Delta T/l$. It is noteworthy that the flow rate does not depend on the interelectrode spacing h; thus, it is possible to increase the voltage with the simultaneous growth of this spacing to obtain the designed results.

Low Conducting Liquids ($\tau/t_* < 1$)

This case differs greatly from the previous one, as taking account of the nonzero (though little) electric conductivity ($\sigma \neq 0$) causes the loss by the liquid of its electric neutrality, that is, $\rho \neq 0$, in contrast to the case of an ideal dielectric. In the simplest case, it is easily demonstrated [3] with the help of the classic Maxwell equations

$$j = \sigma E; \quad \nabla j = 0; \quad \rho = \nabla(\varepsilon E),$$

leading to the formula

$$\rho = j\nabla\tau. \quad (20)$$

According to this formula, the threading of a nonuniform medium by a through conductivity current not normal to $\nabla\tau$ uniquely results in the generation of free spatial charges. Therefore, the role of the nonuniformities of the medium is important in its electrization. In the case of thermal nonuniformities, we are interested in, considering the dependence $\tau(T)$, a purely coulomb force; that is, the first summand of formula (1) takes the form

$$f \equiv f_1 \equiv \rho E = -\varepsilon\beta_\tau (E\nabla T)E, \quad (21)$$

where $\beta_\tau \equiv -(1/^t)(d\tau/d\mathrm{T} = \beta_\varepsilon + \beta_\sigma$; $\beta_\sigma \equiv (1/\sigma)(d\sigma/dT)$ are the temperature coefficients of τ and σ, respectively. The second summand in (1), being the only one in the case of an ideal dielectric, now becomes negligible in comparison with the first one as $|f_1|/|f_2| \sim \beta_\tau/\beta_\varepsilon = 1 + (\beta_\sigma/\beta_\varepsilon) \gg 1$, because usually $\beta_\sigma/\beta_\varepsilon \gg 1$. In this case, $\rho \neq 0$; therefore, it is rightful to search not only for the production of mechanical energy (a TEHD pump) as in the case of an ideal dielectrics but also for TEHD methods of generation of electric energy, that is, for convective electric currents ($j_k = \rho\upsilon$).

One-Dimensional TEHD Flow of Low Conducting Liquid

We seek a solution of the same problem as in the previous case (see Fig. 2) with the fundamental distinction that the moving force of the electroconvection is not force (3) but that given by formula (21),

implying some complications. Instead of equations (10), we have

$$\begin{gathered} -(\partial p/\partial x)+\eta(d^2\upsilon/dz^2)=0;\\ -(\partial p/\partial z)+\rho E-\gamma g=0,\\ \upsilon(\partial T/\partial x)-a(\partial^2 T/\partial x^2+\partial^2 T/\partial y^2)=0;\\ \tau\upsilon(\partial\rho/\partial x)+\rho+\varepsilon\beta_\tau E(\partial T/\partial z)=0;\\ \gamma=\gamma_0(1-\beta T) \end{gathered} \quad (22)$$

under the same boundary conditions (11). The fourth equation of this system, absent in (10), is the equation of continuity of the total current density (2) ($\nabla j=0$), in which only the two first summands are taken into account as the most significant [3].

The stated problem has been previously solved [3, 11]. We present the final formulas for the velocity distribution depending on the dimensionless coordinate $\xi=z/h$ and the problem's parameters:

$$\upsilon(\xi)=M\xi(1-\xi^2)-N(1-\xi^4)+K(1-\xi^2), \quad (23)$$

where

$$\begin{gathered} M\equiv-(\gamma_0\beta gb-\varepsilon\beta_\tau E^2c)(h^3/6\eta);\\ N\equiv c\gamma_0\beta gh^4/24\eta;\\ K\equiv(\varepsilon\beta_\tau E^2b-B)(h^2/2\eta);\\ B\equiv dp_0/dx;\quad \xi\equiv z/h. \end{gathered} \quad (24)$$

It is seen that, as in the previous case, the joint action of the electric and gravitation fields results in the superposition of the even and odd profiles of the velocity. It is possible to follow the contribution to TEHD flow of the summands of (23) and (24).

Production of Mechanical Energy: Pumping Effect

The density of the electric energy is determined by the general formula $w=jE$, from which, with consideration for the first two summands of (2), for the whole mass of the liquid we obtain

$$W=\int\limits_{(V)}jEdV=\int\limits_{(V)}\sigma E^2dV+\int\limits_{(V).}(\rho E)\upsilon dV$$

The first summand of the sum in the right side of this expression makes the contribution of the common joule heating into the total power, which is not of any interest for us as it is negligibly small. The mechanical part of the power is given by the last integral, presenting the total power of the coulomb forces, which are taken into account in this problem. From the point of view of producing a TEHD pumping effect, we are interested in the liquid flow rate through the channel cross section, which, with regard for (23)–(24), similar to (17), is

$$Q=\int\limits_{-h}^{h}\upsilon(z)dz=-\frac{\gamma_0\beta gch^5}{15\eta}+\frac{2}{3}\frac{\varepsilon\beta_\tau E^2b-B}{\eta}h^3. \quad (25)$$

As before, the first summand of the right side of (25) gives the flow rate caused by the natural convection. However, we are interested in the electrothermal effect; therefore, following the same pattern, as in the case in p. 1.2, we assume $c=0\Rightarrow b=A$. Then, for the liquid flow rate, instead of (18), we obtain the formula

$$Q=\frac{2h^3}{3\eta}(\varepsilon\beta_\tau E^2A-B), \quad (26)$$

which almost coincides with (18), the only difference being that it contains the electric relaxation time coefficient $\beta\tau$ instead of the dielectric permittivity thermal coefficient $\beta\varepsilon$. Similarly, for the hydrostatic head, we obtain

$$\Delta P=\varepsilon\beta_\tau E^2Al=(\varepsilon\beta_\tau\varphi_s^2\Delta T)/(4h^2)\equiv\gamma g\Delta H, \quad (27)$$

and the limitation for the flow rate has the form

$$Q<Q_{\max}=\frac{\varepsilon\beta_\tau\varphi_s^2\Delta T}{6\eta l}. \quad (28)$$

Having analyzed the obtained results from the point of view of the final formulas (18) and (19) for ideal dielectrics and the similar (27) and (28) for low conducting ones, we make the following conclusions.

Firstly, using the principle of the electrothermal convection (ETC), it is possible to change the electric and thermal energy into mechanical energy, creating a TEHD pump for pumping of both ideal liquid dielectrics and low conducting liquids.

Secondly, it should be expected that the effects will be qualitatively the same, but quantitatively, in the second case, they should exceed those in the first case by the approximate relation $2\beta_\tau/\beta_\varepsilon\gg 1$ because $\beta_\sigma/\beta_\varepsilon\gg 1$.

Thirdly, it is well to bear in mind that the notions of ideal and nonideal dielectrics should be interpreted according to the definitions presented in the Introduction. It is good practice to carry out the experiments with the necessary pumping of a medium using alternating fields and selecting the frequencies in accordance with the parameter τ/t_*.

On Production of Electric Energy by the TEHD Method

As is known, to produce electric energy, it is necessary to have a source of extraneous forces moving the electric charges opposite to the generated field such as the hydrodynamic forces arising at the forced motion of the medium or wind forces [12]. In the considered case of the ETC of a low conducting liquid, there are generated electric convective currents $j_k=\rho\upsilon$, where υ is the convective velocity of the liquid, determined by

the flow rate of two types of energy: the electric one from the TEHD channel power supply and the thermal one from the heater. Just the latter thermal part of the total energy will transfer into the useful electric one in the TEHD generator.

It is shown in works [3, 11] that, at antiparallel boundary gradients of the temperatures, that is, at $A_1 = -A_2 \Rightarrow b = 0$ and $c = A_1/h$, the flows have a cubic profile of their velocities (Fig. 2c), and, in this case, there arises the longitudinal component of the convective electric current with the average cross section value

$$\bar{j}_k = \frac{1}{2}\int_{-1}^{1}\rho(\xi)\upsilon(\xi)d\xi = 1.102\times 10^{-5}\frac{\varepsilon^3\beta_\tau^3 A_1^2\varphi_s^5}{\eta^2 a}\left(1-\frac{6\tau a}{h^2}\right), \quad (29)$$

where a is the temperature conductivity coefficient. For the examined liquids ($\tau \le 10^{-1}$ s, $a \le 10^{-6}$ m^2/s), the second summand within the brackets can be neglected in comparison with unity.

It is characteristic that the average density of the convection current depends not on the field's intensity and the spacing between the capacitor plates but on the potential difference between them; therefore, by increasing h, it is possible to enlarge φ_s up to ~10^2 kV. The estimations show that, in transformer oil at $A_1 \sim 10$ C/cm, $j \sim 2$ A/cm^2, to maintain such currents and the liquid's motion, it is necessary, as follows from the above mentioned formulas, to ensure the given thermal conditions (A_1). This is connected with the expenditures of heat energy; i.e., we are dealing with the TEHD generation of convection currents as in conventional EHD generators.

To isolate the convection convective current, besides the main power circuit of the whole channel, there is necessary a second electric circuit with additional electrodes at the ends of the TEHD channel. There have been made some efforts aimed at the experimental isolation of these currents, which could not be considered successive, as besides weak currents in the circuit of the external power supply, no other stronger ones, as expected in the experiments, have been registered. Nevertheless, this does not mean the invalidity of the theoretical assumptions. The truth is that the collecting of the convection current is a separate problem, as on solid current-collecting electrodes the normal component (as well as the tangential one due to the adhesion conditions) is zero. Therefore, the question of a TEHD generator calls for further experimental and theoretical investigations.

REFERENCES

1. Ostroumov, G.A., *Vzaimodeistvie elektricheskikh i gidrodinamicheskikh polei*, (Interaction of Electric and Hydrodynamic Fields), Moscow: Nauka, 1979.
2. Ostroumov, G.A., Electric Convection, *Inzh. Fiz. Zh.*, 1966, vol. 10, no. 5, pp. 683–695.
3. Bologa, M.K., Grosu, F.P., and Kozhukhar, I.A., *Elektrokonvektsia i teploobmen* (Electroconvection and Heat Transfer), Kishinev: Shtiintsa, 1977.
4. Grosu, F.P. and Bologa, M.K., Peculiar Features of Heat Transfer under Conditions of Electric Convection, *Elektr. Obrab. Mater.,* 2010, no. 4, pp. 41–55.
5. Bologa, M.K. and Grosu, F.P., Physical Aspects of Electrohydrodynamic Phenomena, *Elektr. Obrab. Mater.*, 2006, no. 3, pp. 118–127.
6. Grosu, F.P. and Bologa,M.K., Conversion of Energy under Conditions of Electroisothermal Convection, *Elektr. Obrab. Mater.*, 2010, no. 5, pp. 45–55.
7. Landau, L.D. and Lifshits, E.M., *Elektrodinamika sploshnykh sred*, (Electrodynamics of Continuous Media), Moscow: Nauka, 1959.
8. Panovskii, V. and Filips, M., *Klassicheskaya elektrodinamika*, (Classic Electrodynamics), Moscow: Fizmatgiz, 1963.
9. Denisov, A.A. and Nagornyi, V.S., *Elektrogidro- i elektrogazodinamicheskie ustroistva avtomatiki* (Electrohydro- and Electrogasdynamic Automation Devices), Leningrad: Mashinostroenie, 1979.
10. Birikh, P.O., On Small Disturbances of Plane-Parallel Flow with Cubic Profile, *Prikl. Mat. Mekh.*, 1966, vol. 30, no. 2, pp. 366–369.
11. Grosu, F.P. and Bologa, M.K., One-Dimensional Thermoelectrodynamic Flows of Low Conducting Liquids, *Magn.Gidrodin.,* 1974, no. 1, pp. 7–19.
12. Rubashov, I.B. and Bortnikov, N.S., *Elektrogazodinamika*, (Electrogasdynamics), Moscow: Atomizdat, 1971.

ISSN 1068-3755, Surface Engineering and Applied Electrochemistry, 2010, Vol. 46, No. 6, pp. 589–595. © Allerton Press, Inc., 2010.
Original Russian Text © S.M. Kuz'min, S.A. Chulovskaya, V.I. Parfenyuk, 2010, published in Elektronnaya Obrabotka Materialov, 2010, No. 6, pp. 65–71.

ELECTRICAL PROCESSES IN ENGINEERING AND CHEMISTRY

The Features of Mass Transfer in the Electroreduction of Copper from Aqueous Ethanol Solutions of Copper Sulfate

S. M. Kuz'min[a], S. A. Chulovskaya[a], and V. I. Parfenyuk[a, b]

[a] *Institute of Solutions Chemistry, Russian Academy of Sciences, ul. Akademicheskaya 1, Ivanovo, 153045 Russia*
[b] *Ivanovo State University of Chemistry and Technology, pr. Engel'sa 7, Ivanovo, 153000 Russia*
e-mail: vip@isc-ras.ru

Received May 25, 2010

Abstract—The process of electroreduction of copper from aqueous ethanol solutions of copper sulfate on a copper electrode is studied using the polarization and impedance techniques. It is shown that, at the working electrode potentials in a range of –0.6 to –0.8 V, the rate-limiting step of the process is the diffusion of copper ions to the electrode's surface. The diffusion coefficient of copper ions at an ethanol concentration of about 0.08 m. f. takes the minimum value due to the restructuring of the near-electrode layer at the given concentration of alcohol.

DOI: 10.3103/S1068375510060086

INTRODUCTION

It is of fundamental importance to study the state of the interface in the conditions of an electrochemical process for both solving the basic problems of electrochemistry and their further implementation. This work is a continuation of the series of studies of the electrochemical production of copper-bearing nanopowders from aqueous organic electrolyte solutions [1–5]. It is shown that the use of a nonaqueous component crucially changes the physicochemical characteristics of the synthesized copper-containing powders [3, 4].

The process of the electrodeposition of copper in aqueous media has been studied rather thoroughly [6–9]. It is found that the electrochemical reaction occurs by a two-step mechanism:

$$Cu^{2+} + e \rightleftharpoons Cu^{+}, \quad \text{(a)}$$

$$Cu^{+} + e \rightleftharpoons Cu^{0}. \quad \text{(b)}$$

The rate-limiting step of the electrodeposition in both acidic and neutral media is the reaction of the addition of the first electron (a). In some cases, the formation of a passivating layer in the interaction between the deposited copper and water molecules was observed [10, 11]:

$$4Cu + 2H_2O \rightleftharpoons 2Cu_2O + 4H^{+} + 4e, \quad \text{(c)}$$

$$Cu_2O + H_2O \rightleftharpoons 2CuO + 2H^{+} + 2e, \quad \text{(d)}$$

$$Cu_2O + (3 - 2x)H_2O \rightleftharpoons 2CuO_x(OH)_{2-2x} + 2H^{+} + 2e. \quad \text{(e)}$$

The effect of the electrolyte's composition on the behavior of the electrode process can significantly change the ratio of the copper oxides that appear in the formation of loose cathode deposits [3].

The aim of this work is to study the process of the electroreduction of copper in aqueous ethanol solutions of copper sulfate using voltammetry and electrochemical impedance spectroscopy.

EXPERIMENTAL

To study the kinetics of the electrochemical reduction, polarization measurements were carried out. The working electrode was polarized using a Pi-50-1 potentiostat (equipped with a PR-8 programming unit). The polarization curves were recorded using a PDA-1 recording two-coordinate potentiometer.

The studies were carried out in a three-electrode cell. The working electrode was the end face of a copper cylinder embedded into a fluoroplastic sleeve. A platinum electrode was selected to be the auxiliary electrode; a saturated silver chloride electrode served the reference electrode.

To decrease the ohmic error in the measurements, we used a Luggin capillary, which was brought to the electrode at a distance equal to its outer diameter (50 μm). The distance between the capillary and the surface under study was controlled using an MPB-2 measuring microscope with an accuracy of 0.01 mm.

The diffusion coefficients were determined by polarization measurements on a rotating disk electrode (RDE) at rates of rotation of 0, 200, 400, 900, and 1600 rpm.

The electrochemical impedance was measured using a Solartron 1260A analyzer. In the experiment, the amplitude of the applied alternating voltage was

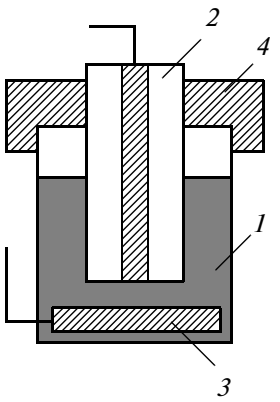

Fig. 1. Diagram of an electrochemical cell: (*1*) electrolyte solution, (*2*) working electrode, (*3*) auxiliary electrode, and (*4*) vinyl plastic cap.

10 mV. The frequency range was 0.1 to 2×10^7 Hz. The electrochemical cell was connected to an impedance meter by a two-electrode four-wire circuit, which made it possible to exclude the impedance of the conducting wires from the total impedance of the system. The resulting impedance spectra of the systems under study were processed using ZView 2 software, which gives the possibility to simulate the impedance of an electrochemical cell using equivalent circuits that contain up to 20 different elements. The model parameters were determined through finding the composite function coefficients by a simplex method. The values of the equivalent circuit elements obtained in several experiments were averaged.

The electrochemical cell that was used for the impedance measurements (Fig. 1) is a temperature-controlled glass vessel with the solution under study (*1*), in which the working electrode (*2*) and the auxiliary electrode (of platinized platinum) (*3*) are placed opposite to one another at a distance of 5 mm.

The working electrode was a copper rod with a diameter of 3 mm embedded into a fluoroplastic sleeve with an outer diameter of 10 mm. The working electrode was rigidly fixed in the cell using a fluoroplastic cap (*4*). The use of the auxiliary electrode of platinized platinum in the form of a disk with a diameter of 25 mm makes it possible to neglect its capacity owning to the large surface (the current density on the auxiliary electrode is negligible).

The stationary potential of the working electrode in the solutions under study was determined with respect to the silver chloride electrode using a digital pH meter (Precision Digital pH OP-208/1, Hungary). The potential values stabilized within ~10 min after the immersion of the working electrode.

To prepare the solutions, we took analytically pure $CuSO_4 \cdot 5H_2O$ salt and chemically pure ethanol, which were subjected to additional purification according to [12]. The solutions were prepared in distilled water using the gravimetric method. A portion of the salt was weighted using a VLR-200 g-M laboratory balance with a maximum error of weighing of ±0.5 mg. The solvents were weighted using a VL-E144 laboratory electronic balance with a maximum error of weighing of ±30 mg.

RESULTS AND DISCUSSION

Figure 2 shows the polarization curves of the copper deposition from aqueous ethanol solutions of 0.1 M copper sulfate. The polarization curves have a classical shape characteristic of multistage processes with diffusion control. This is shown through the presence of plateaus that correspond to the limiting values of the currents.

As the concentration of the organic component increases, a decrease in the limiting cathodic currents is observed. The rise of the current that follows these

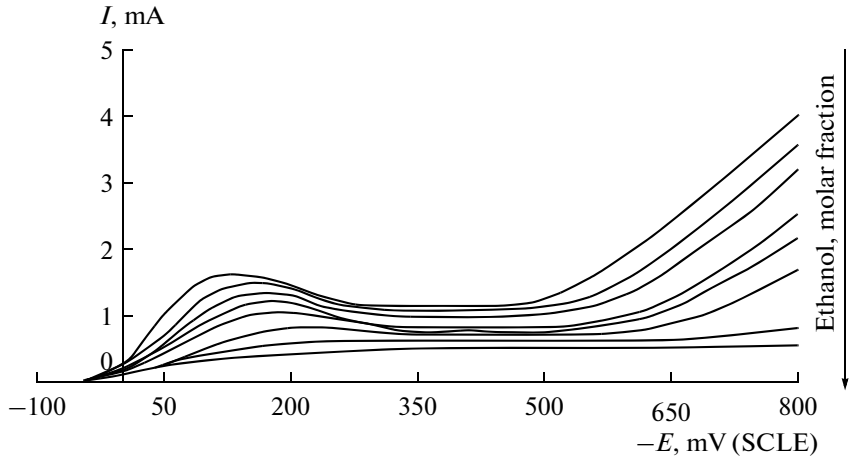

Fig. 2. Cathodic polarization curves of copper deposition. The content of C_2H_5OH: 0.00, 0.02, 0.04, 0.06, 0.08, 0.10, 0.12, and 0.14 m. f.

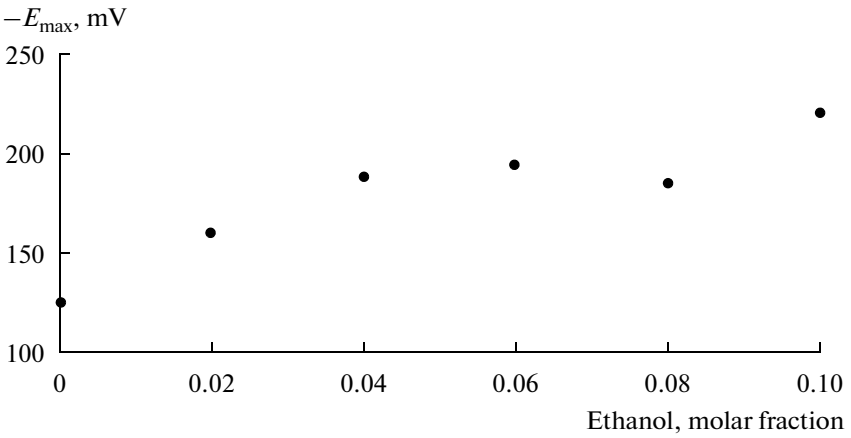

Fig. 3. Effect of the ethanol concentration on the peak's position in the polarization studies.

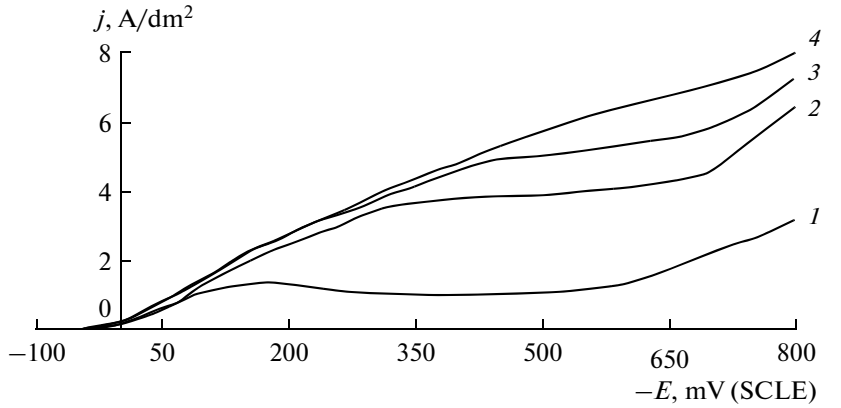

Fig. 4. Polarization curves of the cathodic deposition of copper. The RDE rate: (*1*) 0, (*2*) 200, (*3*) 400, and (*4*) 900 rpm.

regions is caused by hydrogen evolution. For solutions that contain up to 0.1 m. f. ethyl alcohol, the polarization curves exhibit peaks that are due to the occurrence of cathodic passivation. The decrease in the maximum and the shift of its position to the negative range upon the addition of ethyl alcohol to the electrolyte solution (Fig. 3) indicate that the organic component has a significant effect on the formation of the passivated layer on the electrode's surface.

The polarization curves measured at the different rates of rotation of the RDE (Fig. 4) show that the stirring of the electrolyte appreciably increases the cathodic currents. This suggests that the diffusion transfer of electroactive ions to the electrode surface is the rate-limiting step of the electrode process.

The stirring of the solution leads to a decrease in the diffusion layer's thickness and, as a consequence, to an increase in the intensity of the mass transfer of the reagents in the diffusion layer. At the limiting current density, the dependence of j on $\sqrt{\omega_{rot}}$ obeys the Levich equation [13]:

$$j = \pm 0.62 z F D_k^{2/3} \omega_{rot}^{1/2} \nu^{-1/6} c_k^0 = k \omega_{rot}^{1/2}. \quad (1)$$

where z is the number of electrons in the electrode reaction, $F = 96487$ C/mol is the Faraday number, D_k is the effective diffusion coefficient of an electroactive ion, ω_{rot} is the angular velocity of rotation of the electrode, ν is the kinematic viscosity of the solution, and c_k^0 is the concentration of electroactive ions in the bulk electrolyte.

In our case, the $j - \sqrt{\omega_{rot}}$ dependences are linear and extrapolated to the origin of the coordinates for the potential $E = -0.4$ to -0.6 V. The slope ratio of the straight line (the slope factor k) decreases with the increasing concentration of the alcohol and achieves an almost constant value at 0.08 m. f. of ethyl alcohol

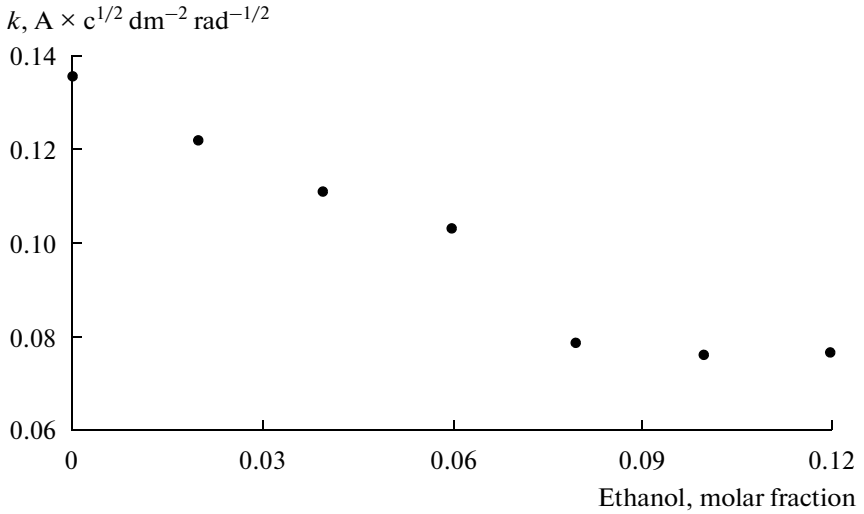

Fig. 5. Effect of the ethyl alcohol concentration on the slope factor of the linear $j-\sqrt{\omega_{rot}}$ dependence.

(Fig. 5). In our opinion, the observed change in the slope of the dependence of the current density j on $\sqrt{\omega_{rot}}$ must be attributed to the change in the effective diffusion coefficient in the near-electrode space upon the transition from an aqueous electrolyte solution to aqueous organic media, because, according to (1), the dependence of the current density on the viscosity of the medium is fairly weak.

The nearly constant value of k at a concentration of ethyl alcohol of ~0.08 m. f. can be explained if we assume that, beginning with this concentration, the diffusion layer in the near-electrode space almost entirely consists of alcohol molecules. This assumption is consistent, in particular, with the data of Jakuszewski [14].

Another approach to studying the properties of the interface and the features of the electrode process in aqueous organic media is possible on the basis of using the method of electrode impedance. The impedance hodographs for a copper electrode–aqueous ethanol solution of copper sulfate system at different potentials are shown in Fig. 6. We can see that, at high frequencies (1×10^7 to 6×10^4 Hz), which correspond to the relaxation processes in the bulk solution and the occurrence of the electrochemical stage of charge transfer on the electrode surface, the hodograph has the form of an off-centered semicircle, the radius of which increases with the increasing potential. At lower frequencies, we observe a hodograph region that corresponds to the diffusion and adsorption processes at the interface. In addition, at potentials of –0.6 to –0.8 V, the shape of the diffusion potential branch is closest to the Warburg dependence, which is consistent with the yield of limiting currents in the polarization curves in the same range of potentials.

In the case of the electrode polarization by a potential of about –0.6 V, the low-frequency region of the impedance is adequately approximated by a circuit that contains series-connected resistance (Z_R) and a generalized Warburg element (W_s) (Fig. 7).

The value of Z_R is equivalent to the length of the segment that is intercepted by the high-frequency edge of the hodograph along the axis of the abscissas (Fig. 6). The dependence of Z_R on the molar fraction of ethanol, which was obtained under conditions of electroreduction of copper (Fig. 8), monotonically increases with the increasing concentration of alcohol. In this case, the dependence is in good agreement with the classical concepts of the variation of the electric conductivity with the changing viscosity of the medium [15], according to which the following relation holds true:

$$\lambda\eta^{\alpha} = \text{const}, \qquad (2)$$

where λ is the electric conductivity, η is the viscosity, and α is a constant value less than or equal to 1. The value of the viscosity of the aqueous ethanol mixtures linearly increases with the increasing molar fraction of alcohol [16] in the concentration range under study; therefore, the dependence of the logarithm of the solution's resistance Z_R on the molar fraction of alcohol must be close to linear, which in our case is fulfilled with a high degree of validity (Fig. 8).

The generalized Warburg element [17] is described by the relation

$$W_s = \frac{R_d \tanh((iB\omega)^P)}{(iB\omega)^P}, \qquad (3)$$

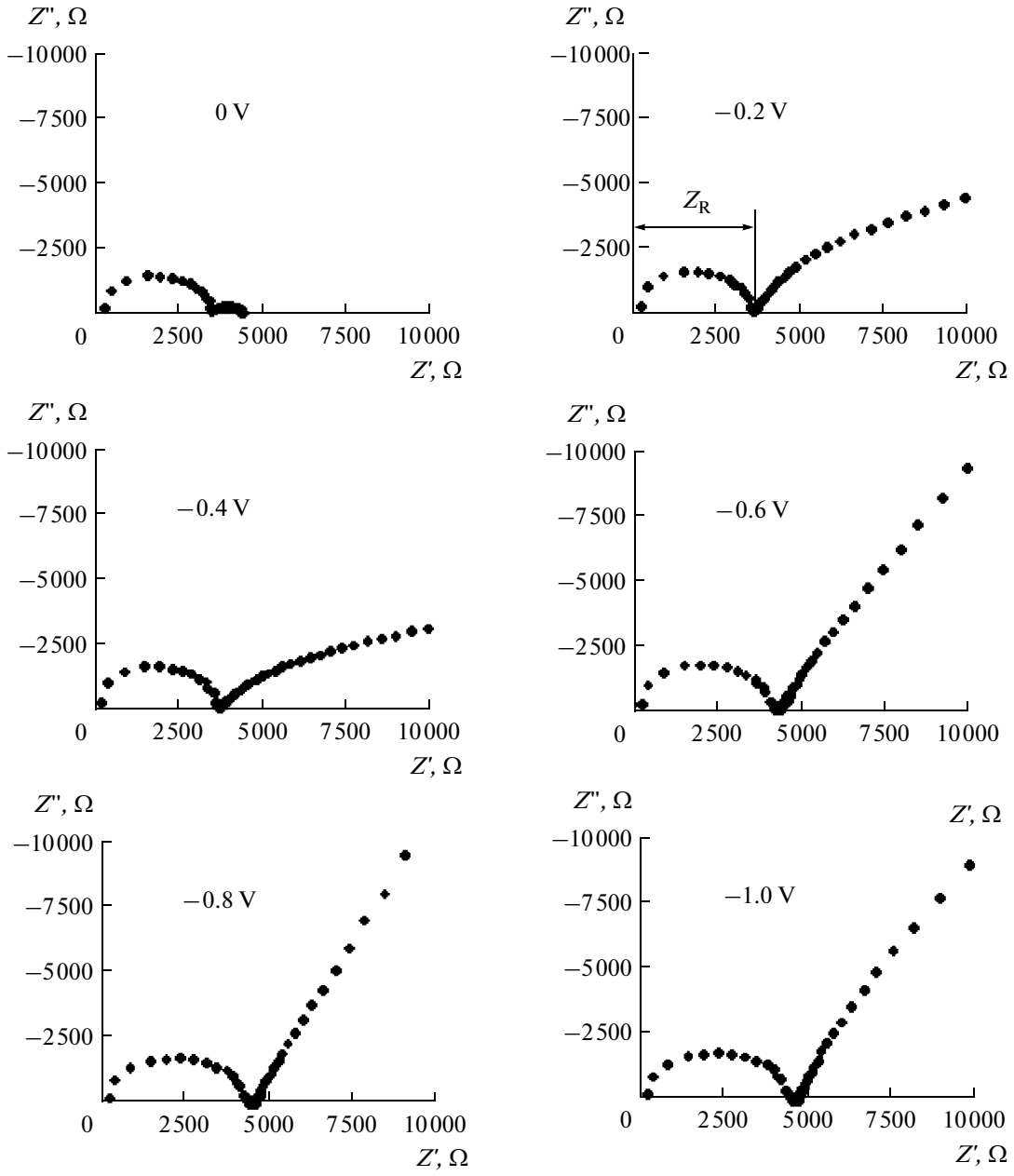

Fig. 6. Frequency impedance spectrum of aqueous ethanol solutions of copper sulfate. The molar fraction of alcohol is 0.04.

where $R_d = \dfrac{RT}{\sqrt{2z^2F^2D_kc_k^0S}}$ is the resistance of the diffusion mass transfer, $B = \dfrac{L^2}{D_k}$ is the characteristic time of the diffusion transfer, and P is the dimensionless exponent that can take values of 0 to 1. Here, R is the universal gas constant, S is the effective electrode area, T is the temperature, and L is the effective thickness of the diffusion layer. The rest of the notations correspond to those adopted in formula (1).

In the case of the transfer of electroactive particles between two parallel homogeneous boundaries, the value of P will be close to 0.5; in the case $p \neq 0.5$, a more complex process of diffusion transfer should be

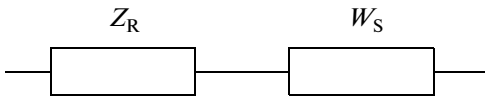

Fig. 7. Equivalent circuit for analyzing the characteristics of the diffusion impedance branch.

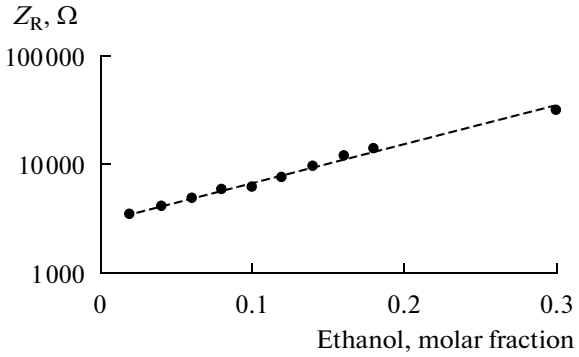

Fig. 8. Effect of the molar fraction of ethanol on the active resistance Z_R of the electrochemical cell: $y = 3031, 8e^{8.1766x}$; $R^2 = 0.9925$.

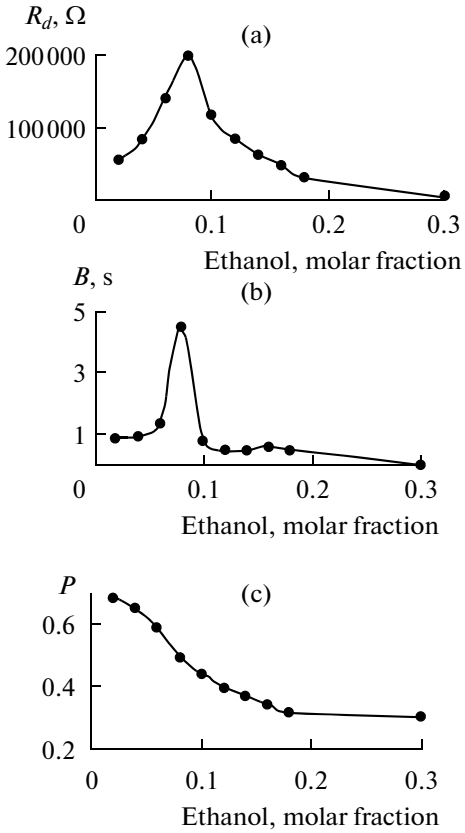

Fig. 9. Dependences of the diffusion impedance parameters on the m. f. of ethanol.

assumed, for example, the diffusion to an irregular surface [18].

Figure 9a shows that the resistance of the diffusion mass transfer R_d increases in the range of 0–0.08 m. f. of alcohol and then decreases. The characteristic time of the diffusion transfer (Fig. 9b) also exhibits a sharp peak at a concentration of alcohol of 0.08 m. f.. The exponent P was closest to a value of 0.5 in the solutions with ethanol concentrations close to 0.08 m. f. For the same concentration, the slope of the dependence of this parameter on the molar fraction of alcohol was maximal (Fig. 9c).

In this particular case, we should assume that the dependence of R_d on the molar fraction of alcohol is characterized, first of all, by a change in the diffusion coefficient of copper ions in the near-electrode space. In addition, the value of the diffusion coefficient of copper ions is minimal at a concentration of ethyl alcohol of about 0.08 m. f. It is most probable that the change in the diffusion coefficient in the near-electrode space is due to the restructuring of the near-electrode layer at the given concentration of alcohol. The sharp increase in the diffusion time can also be attributed to the increase in the effective thickness of the diffusion layer in this range of ethanol concentrations, which can also be a consequence of the restructuring of the near-electrode space.

Note that the data of the polarization measurements in Fig. 5 confirm the sharp change in the near-electrode space at the same concentrations of alcohol. This is shown through the sharp decrease in the slope ratio of the linear $j-\sqrt{\omega}$ dependence at ethanol concentrations of 0.06–0.08 m. f., which is explained by the decrease in the effective diffusion coefficient.

CONCLUSIONS

Based on the polarization and impedance measurements, it is shown that, at a concentration of alcohol of about 0.08 m. f., the near-electrode space undergoes a restructuring that hinders the transfer of copper ions to the electrode surface in the process of the electroreduction of copper from aqueous ethanol solutions.

REFERENCES

1. Chulovskaya, S.A., Lilin, S.A., Parfenyuk, V.I., and Girichev, G.V., Physicochemical Properties of Ultrafine Copper-Containing Powders Synthesized by Cathode Reduction, *Zh. Fiz. Khim.*, 2006, vol. 80, no. 2, pp. 332–335 [*Russ. J. Phys. Chem. A*, (Engl. Transl.), vol. 80, no. 2, p. 264].
2. Chulovskaya, S.A., Lilin, S.A., Balmasov, A.V., and Parfenyuk, V.I., Electrochemical Production of Ultradisperse Copper-Containing Particles from Organo-Aqueous Electrolyte Solutions, *Zashch. Met.*, 2006, vol. 42, no. 4, pp. 430–433 [*Prot. Met. Phys. Chem. Surf.* (Engl. Transl.), vol. 42, no. 4, p. 394].
3. Chulovskaya, S.A. and Parfenyuk, V.I., Influence of the Electrolytic Solution Composition on the Process of Electrochemical Synthesis of Nanodimensional Cupriferous Powders, *Elektron. Obrab. Mater.*, 2008, no. 1, pp. 58–63 [*Surf. Eng. Appl. Electrochem.* (Engl. Transl.), vol. 44, no. 1, p. 50].
4. Chulovskaya, S.A. and Parfenyuk, V.I., Effect of Isopropyl Alcohol on Cathodic Deposition of Ultradispersed Copper-Containing Powders from Electrolyte Solutions, *Zh. Prikl. Khim.*, 2007, vol. 80, no. 6,

pp. 952–955 [*Russ. J. Appl. Chem.* (Engl. Transl.), vol. 80, no. 6, p. 930].

5. Chulovskaya, S.A., Kuz'min, S.M., and Parfenyuk, V.I., Morphological and Dimensional Properties of Ultradispersed Powders Produced by the Electrochemical Method from Electrolyte Solutions, *Elektron. Obrab. Mater.*, 2009, no. 5, pp. 24–29 [*Surf. Eng. Appl. Electrochem.* (Engl. Transl.), vol. 45, no. 5, p. 370].
6. Murashova, I.B., Ostanina, T.N., and Yankelevich, I.N., Change in Conditions of Electrocrystallization of Dendrites near the Loose Deposit Growth Front in Galvanostatic Electrolysis, *Elektrokhimiya*, 1992, vol. 28, no. 7, pp. 967–973.
7. Murashova, I.B., Potapov, O.A., and Pomosov, A.V. Electrodeposition of Disperse Copper with Homogeneous Structure, *Poroshk. Metall.*, 1988, no. 8, pp. 5–11.
8. Krzewska, S., Impedance Investigation of the Mechanism of Copper Electrodeposition from Acidic Perchlorate Electrolyte, *Electrochim. Acta*, 1997, vol. 42, nos. 23–24, pp. 3531–3540.
9. Slaiman, Q.J.M. and Lorenz, W.J., Investigations of the Kinetics of Cu/Cu^{2+} Electrode Using the Galvanostatic Double Pulse Method, *Electrochim. Acta*, 1974, vol. 19, pp. 791–798.
10. Souto, R.M., Gonzales, S., Salvarezza, R.C., and Arvia, A.J., Kinetics of Copper Passivation and Pitting Corrosion in Na_2SO_4 Containing Dilute NaOH Aqueous Solution, *Electrochim. Acta*, 1994, vol. 39, pp. 2619–2628.
11. Metikos-Hukovic, M., Babic, R., and Paic, I., Copper Corrosion at Various pH Values with and without the Inhibitor, *J. Appl. Electrochem.*, 2000, vol. 30, pp. 617–624.
12. Karyakin, Yu.V. and Angelov, I.I., *Chistye khimicheskie veshchestva* (Pure Chemical Substances), Moscow: Khimiya, 1974.
13. Damaskin, B.B., Petrii, O.A., and Tsirlina, G.A., *Elektrokhimiya* (Electrochemistry), Moscow: Khimiya, 2001.
14. Jakuszewski, B., Partyka, S., and Przasnyski, M., Potencjaly ladunku zerowego rteci w mieszaninach etanolowo-wodnych, *Roczniki Chemii Ann. Soc. Chim. Polonorum*, 1972, vol. 46, pp. 921–927.
15. Robinson, R. and Stokes, R., *Electrolyte Solutions*, London: Butterworths, 1955.
16. Afanas'ev, V.N., Efremova, L.S., and Volkova, T.V., *Fiziko-khimicheskie svoistva binarnykh rastvoritelei. Vodosoderzhashchie sistemy* (Physicochemical Properties of Binary Solvents: Water-Bearing Systems), Ivanovo: Inst. Khim. Nevodnykh Rastvorov, 1988, Part II.
17. *Zplot for Windows, Electrochemical Impedance Software Operating Manual: Version 2.4*, Southern Pines: Scribner Associates, 2001.
18. Pajkossy, T. and Nyikos, L., Diffusion to Fractal Surfaces: II. Verification of Theory, *Electrochim. Acta*, 1989, vol. 34, no. 2, pp. 171–179.

ISSN 1068-3755, Surface Engineering and Applied Electrochemistry, 2010, Vol. 46, No. 6, pp. 596–599. © Allerton Press, Inc., 2010.
Original Russian Text © G.A. Barbashova, 2010, published in Elektronnaya Obrabotka Materialov, 2010, No. 6, pp. 72–75.

ELECTRICAL PROCESSES IN ENGINEERING AND CHEMISTRY

Hydrodynamic Processes in High-Speed Impact Welding of Two Plates

G. A. Barbashova

Institute of Impulse Processes and Technologies, National Academy of Sciences of Ukraine, pr. Oktyabrskyi 43a, Nikolaev, 54018 Ukraine

e-mail: dpte@iipt.com.ua

Received June 10, 2010

Abstract—The hydrodynamic processes of high-speed impact welding of two plates are studied numerically. The hydrodynamic load on the thrown plate is determined.

DOI: 10.3103/S1068375510060098

INTRODUCTION

Works [1, 2] provide some results of the theoretical research of the hydrodynamic processes caused by an explosion in an unlimitedly long tube of a conductor placed in a cylindrical polyethylene cartridge filled with water. Such research is necessary to develop tube beading technology for grids of heat exchangers [3]. A cartridge of the same type is used in the high-speed impact (HSI) welding of two plates [4]. In this case, a polyethylene cartridge filled with water is placed into a thick cylindric bush with holes in the butts. Note that the length of the cartridge and the height of the bush are identical. One base of the cartridge is closed with polyethylene, whereas the other one bears one of the plates welded, that is, the driver plate. The cartridge has a spiral conductor, after the electrical explosion of which, a plasma-filled cavity (discharge channel) appears. The expansion of the cavity leads to a sharp increase in the fluid pressure inside the cartridge. Pressured by the hydrodynamic load, the driver plate starts to move until hitting the second, fixed, plate.

The quality of the welding joint depends on a lot of factors including the amount of the hydrodynamic load, the motion rate of the driver plate at the moment of hitting the fixed one, and the angle between the plates [5]. Therefore, it will be essential to define how such factors influence the welding process in the case of developing an appropriate discharge-pulse technology [3]. Experimental studies of the process are very difficult, whereas some parameters of the process are even impossible to be measured. Thus, a theoretical study is needed about modeling the HSI welding mathematically.

This work aims to present a theoretical study of the hydrodynamic processes during the HSI welding of two plates.

PROBLEM DEFINITION AND SOLUTION

The following assumptions were made during the development of the mathematical model:

—the wall of the bush holding the socket is absolutely firm;

—the conductor is placed on the symmetry axis of the socket and is shaped as a straight round cylinder of a finite length;

—the conductor explodes instantaneously;

—the driver plate is shaped as a disk, does not deform, and moves according to the law of the motion of rigid bodies;

—the socket fills with a perfect compressible fluid whilst the discharge channel fills with a perfect low-temperature plasma.

According to the assumptions accepted, the mathematical model in question consists of the following:

—a system of two-dimensional nonlinear equations of gas dynamics recorded in a cylindrical coordinate system [1];

—a two-term equation of state [1];

—an equation of the energy balance in the discharge channel [1] in the water–plasma contact discontinuity (the inner limit of the computational domain);

—a condition of nonpercolation on a fixed hard surface [1];

—equal rates of motion of the border between the liquid and the plate and the plate proper, respectively;

—a condition on the free surface [1] on the socket base where the fluid is initially limited by the polyethylene, as well as on the water–gas border of the outcoming fluid at the opposite butt.

The problem was solved using the finite-difference Godunov method [1] and in view of the area filled with

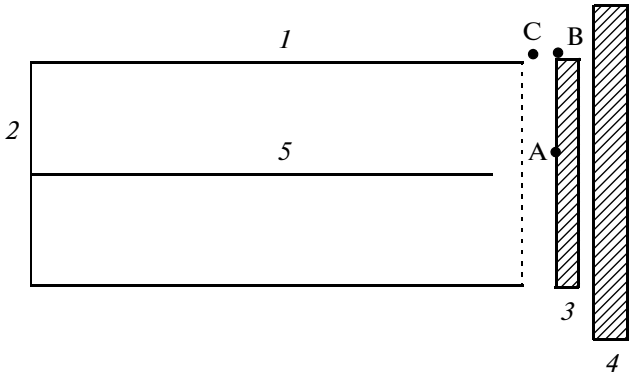

Fig. 1. The scheme of the rated operating conditions. (*1*) inside surface of the bush; (*2*) polyethylene bottom; (*3*) driver plate; (*4*) fixed plate; (*5*) exploding conductor; A, B, C—points on the surface of the plate and in the fluid.

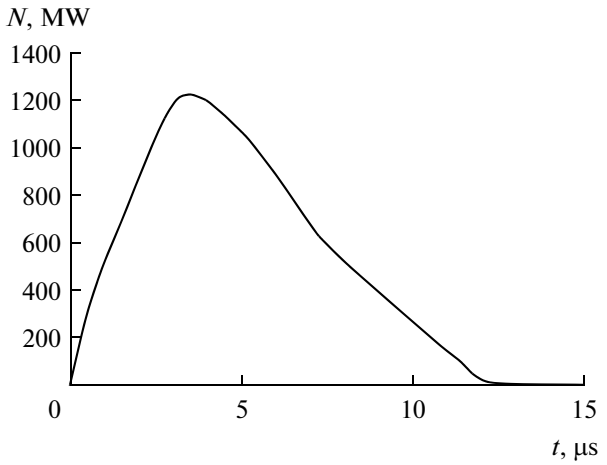

Fig. 2. Power input into the discharge channel.

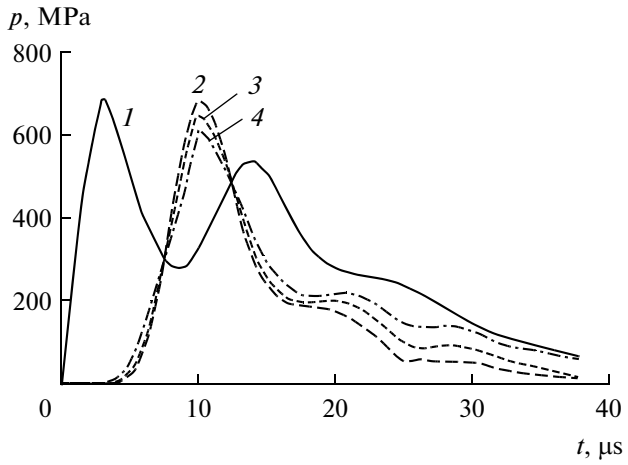

Fig. 3. Pressure in the discharge channel and on the driver plate. (*1*) pressure in the channel; (*2*) at point $r = 0.5R$ on the plate; (*3*) at point $r = 0.75R$; (*4*) at point $r = 0.95R$;

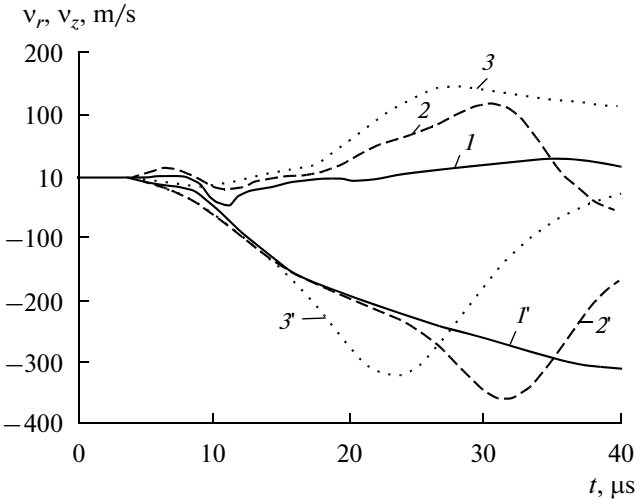

Fig. 4. Radial (v_r) and axial (v_z) components of the fluid velocity vector. (*1, 1'*) v_r, v_z at point A (Fig. 1), respectively; (*2, 2'*) v_r, v_z at point B; (*3, 3'*) v_r, v_z at point C.

the outcoming water near the plate. A movable grid was used.

SOLUTION RESULTS

The computational domain is shown in Fig. 1. The inside radius of the bush and the cartridge and the radius of the driver plate are equal to R, the weight m of the driver plate is 8 g, and the initial distance to the fixed plate is $x = 10$ mm. The law of the power input into the discharge channel [1] is shown in Fig. 2.

The pressure inside the plasmatic cavity resulting from the explosion is way higher than the pressure in the surrounding fluid. Therefore, the discharge channel undergoes rapid expansion and generates a shock wave. The fluid pressure in the cartridge sharply increases. Thus, the cartridge explodes and the water leaves the initially occupied space. The wave reflected from the cylindrical surface reaches the wall of the discharge channel, which decreases the size of the channel and increases the pressure inside it (Fig. 3, curve *1*). The second peak pressure in the channel is lower than the first one, which is explained by the end of the power input into the channel and the increased space filled with the fluid [1]. After reaching the maximum, the fluid pressure sharply decreases in the entire area including the driver plate (Fig. 3, curves *2–4*). It should also be borne in mind that the wave front reaches different parts of the plate almost simultaneously, whereas the hydrodynamic load distributes nearly homogeneously (Fig. 3).

After the socket has exploded and the plate has started to move, the fluid flows out of the bush at a rate of up to 380 m/s. The direction and level of the components of the velocity vector (Fig. 4) show that, after a certain period, the water flow goes around the plate

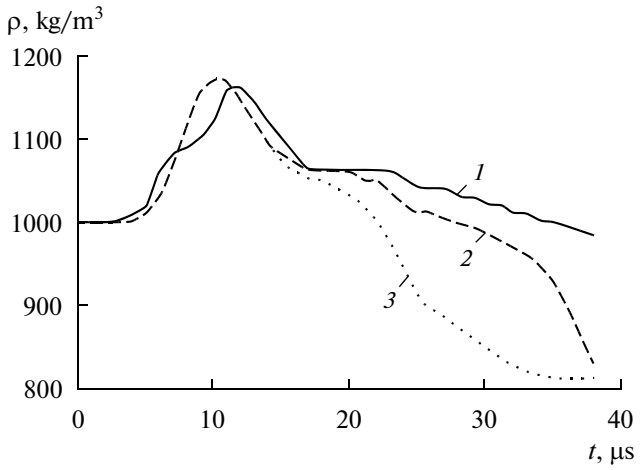

Fig. 5. Fluid density: (*1*) at point A; (*2*) at point B; (*3*) at point C.

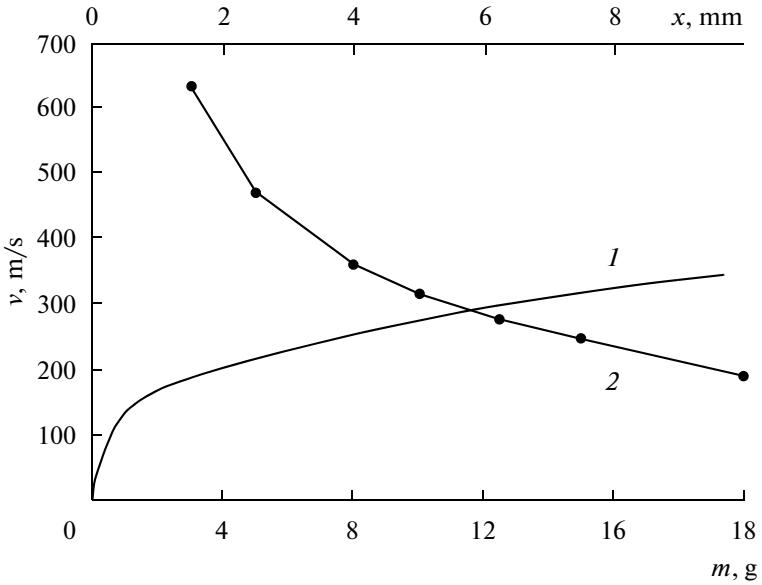

Fig. 6. Motion rate of the driver plate: (*1*) dependence on the motion x; (*2*) dependence on the plate's weight at $x = 10$ mm.

(Fig. 4, curves *2* and *2*'). This fact also makes it difficult to study HSI welding.

After reaching its peak, the fluid density quickly becomes lower than the density of the fluid at rest: $\rho = 1000$ kg/m^3 (Fig. 5). It occurs due to the larger space filled with the fluid; that is, the destruction of the fluid leads to breakaways [6]. As assumed in [6], the destroyed fluid is a continuum with zero pressure and less dense than the fluid at rest.

Figure 6 shows the dependency between the velocity and the motion of the driver plate, $\dot{x}(x)$ (curve *1*), and the dependency of the velocity at the moment of hitting the fixed plate, $\dot{x}(m)$ (curve *2*). After a rapid decrease of the hydrodynamic pressure on the plate (Fig. 3), its acceleration falls, whereas the velocity grows, which may result from the fact that the fluid medium and the material of the plate are in perfect motion. If we analyze curve *2* in Fig. 6 we will see that, according to the hyperbolic law, the motion rate of the plate falls as the weight of the plate increases.

CONCLUSIONS

Therefore, the case of HSI welding of the two plates in question shows that the hydrodynamic pressure distributes along the entire surface of the driver plate almost homogeneously.

According to the hyperbolic law, the motion rate of the plate falls as the weight of the plate increases.

REFERENCES

1. Barbashova, G.A., Research of Hydrodynamic Processes in Case of an Electric Discharge in a Low Quantity of Fluid, Elektronnaya obrabotka materialov, 2008, no. 1, pp. 35–39.
2. Barbashova, G.A., Research of Hydrodynamic Processes in a Limited Part of the Tube in Case of Explosion of a Microconductor, Elektronnaya obrabotka materialov, 2009, no. 1, pp. 44–47.
3. Mazurovskii, B.Ya. *Elektroimpul'snaya zapressovka trub v trubnykh reshyotkakh teploobmennykh apparatov* (Electric Pulse Press Fitting of Tubes in Tube Plates of Heat Exchangers), Kiev: 1980.
4. Yurchenko, E.S., Polovinko, V.D., and Shlenskyi, P.S., HSI Welding of Heterogeneous Materials with Electroblast of A Conductor, Tezisy dokladov VII Mezhdunarodnoy shkoly-seminara implul'snye protsessy s mekhanike sploshnykh sred (Reporting Theses of VII International School Seminar *Pulse Processes in Continuum Mechanics*), Nikolaev, 2007, pp. 69–70.
5. Lavrentyev, M.A. and Shabat, B.V., *Problemy Gidrodinamiki I ikh matematicheskiye modeli* (Problems of Hydrodynamics and Their Mathematical Models), Moscow: 1977.
6. Atanov, G.A., *Gidroimpul'snye ustanovki dlya razrusheniya gornykh porod* (Rock Disintegration Hydroimpulsive Plants), Kiev: 1987.

ISSN 1068-3755, Surface Engineering and Applied Electrochemistry, 2010, Vol. 46, No. 6, pp. 600–604. © Allerton Press, Inc., 2010.

ELECTRICAL PROCESSES IN ENGINEERING AND CHEMISTRY

Influence of the Electromagnetic Field on the Nonlinear Electron Localization Dynamics in the Nanocluster with Two Redox Centers[1]

O. V. Yaltychenko[a], E. Yu. Kanarovskii[a], and N. N. Gorinchoy[b]

[a] *Institute of Applied Physics, Academy of Sciences of Moldova, 5, Academy str., Kishinev, MD-2028, Republic of Moldova*

[b] *Institute of Chemistry, Academy of Sciences of Moldova, 3, Academy str., Kishinev, MD-2028, Republic of Moldova*

e-mail: oialt@mail.ru

Received June 16, 2010

Abstract—The localized properties of electron in the nanocluster with two redox centers were studied using of the semi-classical approach. In this consideration nanocluster interacts with an external electromagnetic field. It is shown, that the external electromagnetic field can operate by the localized properties of the system. In resonance case the regimes of the electron localization and delocalization and also conditions of the switching between them are revealed. The used approach allows to describe the localized properties of the electron in the dimer nanocluster for the different parameters of the system, and also specifies ways of parametrical management by these properties.

DOI: 10.3103/S1068375510060104

INTRODUCTION

Phenomenon of electron localization-delocalization in the molecular cluster systems for the device applications in the molecular electronics and optoelectronics has the key aspects such as the control ways of the localization degree and its duration [1]. Many perspective multifunctional nanomaterials contain the metal-organic nanoclusters, which elementary representative is the nanocluster with two redox centers or dimer nanocluster [2–4]. The degree of the localization of the electron strongly depends basically on the ratio of constant of the electron-vibrational interaction to the tunneling constant between the electron states on the centers and in a less degree other parameters of the system. In the absence of an external field owing to the electron-vibration interaction the electron in such molecular system is either fully localized on one of centers or partially delocalized. The conformation reorganization yielded by the additional electron on given centre through the electron-vibrational interaction creates the potential well for this electron and so eventually leads to less its transition probability on other centre. The metal-organic complexes with redox centers in which metal ions are build in the polymeric matrix, characterized by the π-electron conjugation and the high degree of the delocalization of the electron gained from the ion of the metal have the good transport properties and find the various application in the molecular electronics and optoelectronics [2, 3]. The external field essentially influences on the properties of the cluster systems, changing in particular their transport properties and changing the degree of the localization of the electron [5, 6]. The dynamics of the nonstationary electron state in the nanocluster with two redox centers is studied in [7].

The aim of the given investigation is the theoretical study of the influence of the electromagnetic field on the electron transport in the nanocluster with two redox centers. The analysis is based on the calculation of the difference of the probabilities of electron detection on the first and second centers of the nanodimer, respectively.

THEORETICAL MODEL

Let's view the nanocluster consisting of two redox centers with one additional electron. The system is prepared so that the electron in the initial moment of time is localized on the first centre of the nanodimer. We propouse that electron, being on each of nanodimer centers, interacts only with full-symmetrical vibrations of the nearest environment Q_i ($i = 1, 2$) and can be tunneling from one centre to another centre (for detail, see also [6]).

Let's enter normal coordinates:

$$Q = (Q_1 + Q_2)/\sqrt{2}, \quad q = (Q_1 - Q_2)/\sqrt{2}. \qquad (1)$$

The first of two normal coordinates is excluded from viewing because this full-symmetrical coordinate is multiplied by unit electron matrix. From the made assumptions, the kinetic properties of the dimer nanocluster can be described by means of the model Hamiltonian of the two-level electron system, which includes the external electromagnetic field [6].

The presented approach is semi-classical as the vibrational mode is quantized, and the electromag-

[1] The article is published in the original.

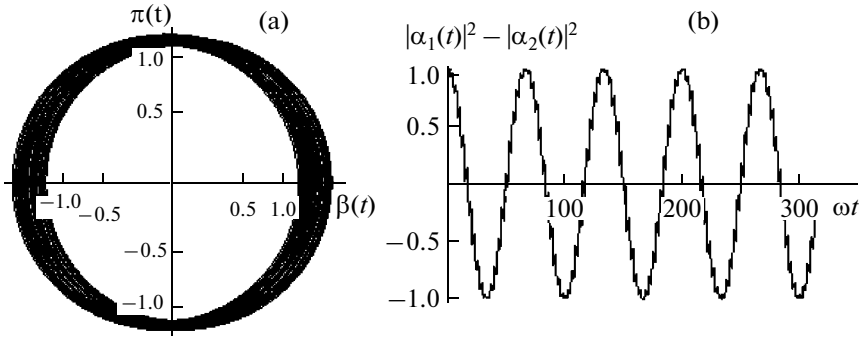

Fig. 1. The phase portrait for cluster mode (a). The time dependence of the difference of the average values of the electron populations on the nanodimer centers (b). System parameters are $\nu = 0.2$; $g = 0.1$; $(d_0E_0) = 4.9$; $\Omega = \omega = 1$; $\pi(0) = 1$.

netic field is considered classically. Thus, the Hamiltonian of the considered system is:

$$H(t) = \frac{1}{2}(p^2 + \omega^2 q^2) + \nu\sigma_x + gq\sigma_z + (d_0E_0)\cos(\Omega t)\sigma_z. \quad (2)$$

Here p, q—the momentum and coordinate of the vibrational mode q with frequency ω; σ_x, σ_z, σ_y—Pauli's matrixes; ν, g—the tunneling constant and constant of the electron-vibrational interaction; E_0, Ω—the amplitude and frequency of the monochromatic electric field, d_0—the electron dipole moment of the dimer. All parameters are taken in $\hbar\omega$ units.

For the description of model in the quasi-classical approximation Hamilton's canonical equations were applied. The time evolution of studied system describes with using Davydov's time-dependent wave function:

$$\psi(t) = \exp[-i(\beta(t)p - \pi(t)q)]\sum_{j=1}^{2}\alpha_j(t)\cdot a_j^+|0\rangle. \quad (3)$$

The expression (3) contains the variation functions $\alpha_j(t)$ and $\beta(t)$, $\pi(t)$, which are the time-dependent amplitude of the probability of the electron detection on the j-centre of the nanodimer and the average values of the coordinate and momentum of the vibrational mode, correspondently. The time dependent electron-vibrational wave function (3) is presented in the factorized form, and the electronic part of the wave function is chosen in the form of superposition of electron states of system. The vibrational subsystem is presented in the form of the vibrational wave package.

Solving the variation problem, it is obtain the system of the differential equations concerning the functions $\alpha_j(t)$ and $\beta(t)$, $\pi(t)$. Thus, the system of the linkage nonlinear differential equations for the values $\alpha_j(t)$ and $\beta(t)$, $\pi(t)$ is:

$$\begin{aligned} i\frac{d\alpha_1}{dt} &= \nu\alpha_2 + g\beta\alpha_1 - (d_0E_0)\alpha_1\cos(\Omega t),\\ i\frac{d\alpha_2}{dt} &= \nu\alpha_1 - g\beta\alpha_2 + (d_0E_0)\alpha_2\cos(\Omega t),\\ \frac{d\pi}{dt} &= \omega\beta + g[|\alpha_1|^2 - |\alpha_2|^2],\\ \frac{d\beta}{dt} &= -\pi. \end{aligned} \quad (4)$$

The system (4), which describes nonlinear dynamics both the electron and vibrational subsystems, is solved numerically. For the vibrational subsystem the numerical solution is presented by the phase portrait to planes "coordinate-momentum". On the phase portrait of the vibrational mode it is possible to observe dynamics of the vibrational wave package in depending from the examined parameters—ν, g, Ω, ω and (d_0E_0). The evolution in the electron subsystem is presented by the time dependence of the difference of the average values of the electron populations on the dimer centers. In the given research it is shown what specific features of the behavior are realized in the electron and vibrational subsystems for the chosen values of the electron-vibrational interaction constant and the tunneling constant in depending from the intensity of the electromagnetic field.

RESULTS AND DISCUSSIONS

The main results of given consideration, which follows from the numerical solution of (4) are presented on the Figs. 1–5. On the each of Figs. 1–5 are displayed the time evolution for the electron and vibrational subsystems, respectively.

The further increase of the value (d_0E_0) up to the value 6.75 leads to the return of dynamics in the time behavior of the difference of the average values of the electron populations on the centers of the dimer nano-

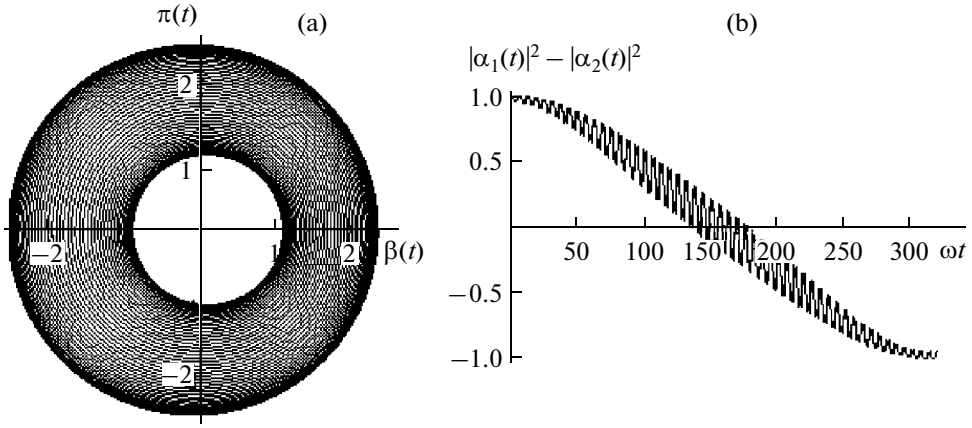

Fig. 2. The phase portrait for cluster mode (a); The time dependence of the difference of the average values of the electron populations on the nanodimer centers (b). System parameters are $\nu = 0.2$; $g = 0.1$; $(d_0E_0) = 5.815$; $\Omega = \omega = 1$; $\pi(0) = 1$.

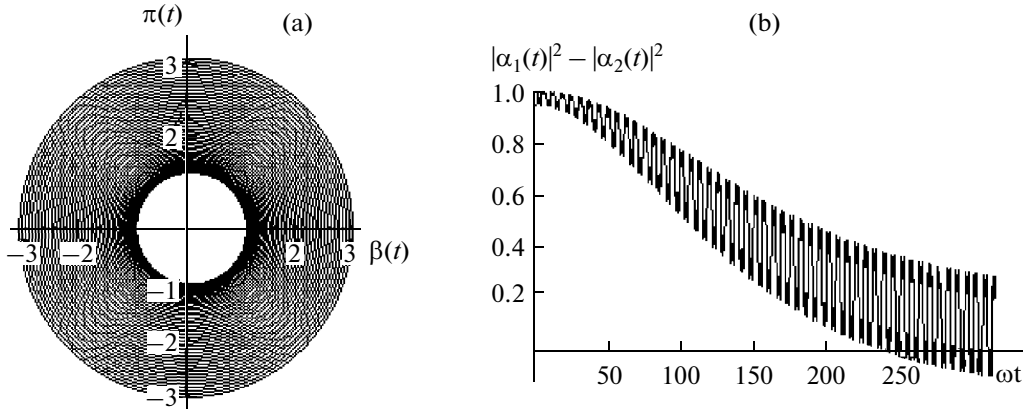

Fig. 3. The phase portrait for cluster mode (a); The time dependence of the difference of the average values of the electron populations on the nanodimer centers (b). System parameters are $\nu = 0.2$; $g = 0.1$; $(d_0E_0) = 5.83$; $\Omega = \omega = 1$; $\pi(0) = 1$.

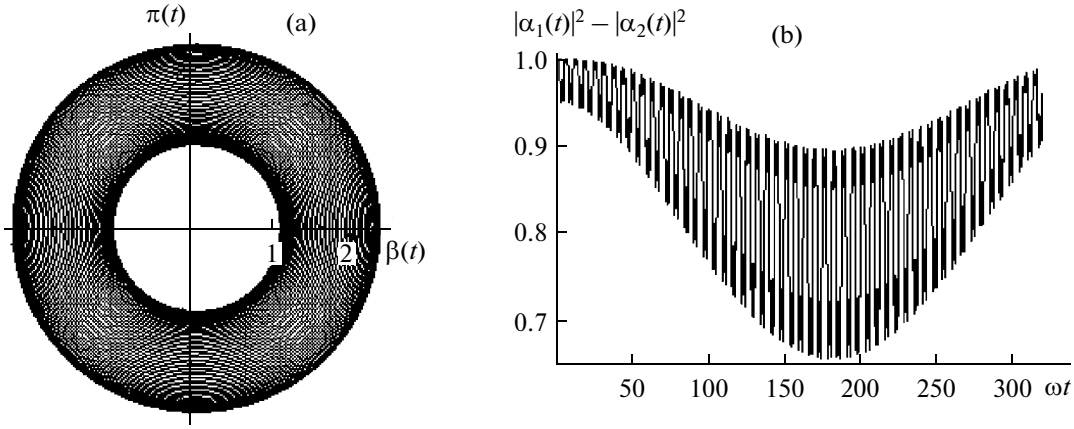

Fig. 4. The phase portrait for cluster mode (a); The time dependence of the difference of the average values of the electron populations on the nanodimer centers (b). System parameters are $\nu = 0.2$; $g = 0.1$; $(d_0E_0) = 5.85$; $\Omega = \omega = 1$; $\pi(0) = 1$.

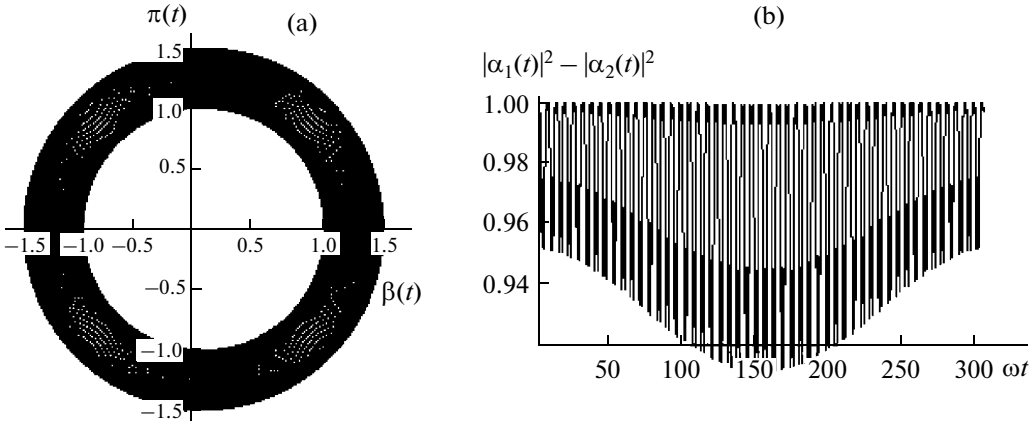

Fig. 5. The phase portrait for cluster mode (a); The time dependence of the difference of the average values of the electron populations on the nanodimer centers (b). System parameters are $\nu = 0.2$; $g = 0.1$; $(d_0E_0) = 5.87$; $\Omega = \omega = 1$; $\pi(0) = 1$.

cluster. For the value (d_0E_0) =6.75 the dynamics of electron subsystem almost completely coincides with the case given on the Fig. 1. Further change of the value of (d_0E_0) outside of the studied interval from 4.9 to 6.75 leads to the complete resumption of evolution in the considered system.

As known, in the quasi-classical approximation the dynamics of vibrational wave package is characterized by the motion of its gravity center on the classical trajectory. Note that in the studied case the vibrational subsystem and the electromagnetic field are interconnected through electronic subsystem, which interacts with each of them separately. Thus, the electromagnetic field and vibrational subsystem linked indirectly and between them the energy exchange occurs. Note also that the time dependence of the difference of the average values of the electron populations of centers in the nanodimer has beats. These beats take place in all the subsequent cases below (Figs. 1–5). Such features of the nonlinear electron dynamics may be connected with the changing of the package form.

The case of the time evolution of the considered system for the value of the interaction energy with electromagnetic field $(d_0E_0) = 4.9$ and for time interval corresponding to the value 100π (in dimensionless unities ωt) is presented on the Fig. 1. In this case the electron, which initially localized on the first center of the nanodimer, 10 times passes from centre to center, i.e. there are 10 switchings. Herewith, at the each switching in the electron subsystem the phase trajectory center of the wave package has uniform shift along the axe of coordinates. Such behavior of the electron subsystem can be interpreted, as a regime of the periodically renewable full localization of the electron for time corresponding to the value of order 10π, and switching on other center with the subsequent localization on it.

The case (d_0E_0) = 5.815, when for time corresponding to the value 100π only one switching of the electron from the center to the center was made, is presented on Fig. 2. In this case switching of the electron localization on other center is carried out during of order 100π in unities ωt. While the wave package moves so that its phase trajectory lies between two non-concentric circles in the phase plane "coordinate-momentum", i.e. the phase trajectory center of the wave package still continues to shift.

On the Fig. 3 was presented the case $(d_0E_0) = 5.83$, when for the observed time interval can assume that the electron completely delocalized between the centers of the dimer. The studied system relatively slowly goes to the delocalization state, whose duration is very sensitive to the field intensity.

The results presented on the Fig. 4 and Fig. 5 for $(d_0E_0) = 5.85$ and 5.87 correspond to cases of the partial localization and almost full localization of the electron on the first center, accordingly. In these cases the phase trajectory of the wave packet lies between two already concentric circles on the phase plane "coordinate-momentum".

CONCLUSIONS

Thus, the gradual change of the interaction energy of the electron subsystem with the electromagnetic field leads to the realization of the several regimes in the time evolution of the electron in the dimer nanocluster.

Firstly, it is the regime with switching of full localization of the electron from one center to another. The time of the electron switching is strong depending from the interaction energy of the electron subsystem with the electromagnetic field (d_0E_0) (compare Fig. 1 and Fig. 2).

Secondly, it is the regime of the full delocalization of the electron in the dimer nanocluster (see Fig. 3). The main feature of this regime is that the duration of the time period of the existence of delocalization is

very sensitive to the value (d_0E_0). The performed calculations show, that the gradual increase of the field at first increases the duration of the derealization, and then to its decrease. And finally, in dependence of the value (d_0E_0), the electron either switches to another center or remain or remains at the same center.

Thirdly, it is the regime of the partial or practically full localization of the electron on the first dimer center—the case of the locked electron (see Fig. 4 and Fig. 5).

Thus, the electromagnetic field plays the role of the external driving parameter. Herewith, the electron-vibrational dynamics in the studied system is so that at the fixed value (d_0E_0) one of the specified regimes of the localization of the electron is realized.

REFERENCES

1. *Molecular Electronic Devices*, Carter, F.L. et al., Eds., Amsterdam: Elsevier, 1988.
2. Roche, S., Jiang, J., Foa Torres, L.E.F., and Sailo, R., Charge Transport in Carbon Nanotubes: Quantum Effects of Electron-Phonon Coupling, *J. Phys. Condens. Matter.*, 2007, vol. 19, 183203 doi: 10.1088/0953-8984/19/18/183203.
3. Choukroun, R. and Lorber C., Adventures in Vanadocene Chemistry, *Eur. J. Inorg. Chem.*, 2005, vol. 23, pp. 4683–4692.
4. Kenkre, V. and Wu, H., Time Evolution of the Nonlinear Quantum Dimer, *Phys. Rev. B*, 1989, vol. 39, no. 10, pp. 6907–6913.
5. Kalinin, S.V., Morozovska, A.N., Chen, L.Q., and Rodriguez, B.J., Local Polarization Dynamics in Ferroelectric Materials, *Rep. Prog. Phys.,* 2010, vol. 73, 056502 doi: 10.1088/00344885/73/5/056502.
6. Yaltychenko, O.V., Dynamic Localization Effect of the Electron in the Dimer, *Sensor Electronics and Microsystem Technologies.*, 2009, vol. 4, pp. 18–25.
7. Yaltychenko, O.V. and Kanarovskii, E.Yu., Dynamics of the Non-Stationary State in the Dimer Nanocluster, *Surface Engineering and Applied Electrochemistry*, 2009, vol. 45, no. 4, pp. 300–305.

ISSN 1068-3755, Surface Engineering and Applied Electrochemistry, 2010, Vol. 46, No. 6, pp. 605–611. © Allerton Press, Inc., 2010.
Original Russian Text © E.G. Sprincean, 2010, published in Elektronnaya Obrabotka Materialov, 2010, No. 6, pp. 81–87.

ELECTRICAL TREATMENT OF BIOLOGICAL OBJECTS AND FOOD PRODUCTS

The Optimization of Protein Extraction during Electrophysical Whey Processing

E. G. Sprincean

Institute of Applied Physics, Academy of Sciences of Moldova, ul. Akademii 5, Kishinev, MD-2028 Republic of Moldova
e-mail: vrabie657@yahoo.com

Received March 23, 2010

Abstract—The properties of milk whey protein fractions are analyzed. The need for obtaining them is outlined; the possible mechanisms of complexing and coagulation during the electrophysical processing of secondary raw milk products are explained. The possible methods for optimizing the conversion of the protein fractions into a protein–mineral concentrate, as well as the fractional analysis of the minerals, are described, and their role in the complexing of the concentrate is estimated. The electrophysical parameters under the conditions of the optimization, the different compositions of the anode liquid, and the types of separating of the elements are analyzed. The fields of future investigations aimed at obtaining high quality products during developing nonwaste electrotechnologies of milk whey processing are identified.

DOI: 10.3103/S1068375510060116

Complete and zero-waste milk processing are among the major problems facing the milk industry and have particularly sharpened during the last 10–15 years due to the increase in the output of milk products. The following valuable milk components pass into the milk whey (MW) remaining after the primary milk processing: carbohydrates, proteins, vitamins, and mineral substances. The weight of the MW dry matter (DM) is about 7–8%, which accounts for 50% of the milk DM. Lactose, the milk whey component that is the weightiest quantitatively (70–80% of the MW DM) and occurs in nature only in milk, passes into the milk whey almost completely after the primarily milk processing and gets into the sewage with a probability of 50%. The transformation of lactose into lactulose, which is a very important prebiotic, remains one of the urgent problems of using MW characterized by a high content of the salts that do not differ in composition from those that are present in whole milk. The biological value of MW is primarily due to the fact that the whey proteins containing all the essential amino acids have immune functions, are highly digestible, and pass into it almost completely. These proteins do not precipitate during the milk setting under the action of the fermentation and/or acid and, therefore, get into the whey.

The protein composition of milk whey is represented by the main protein fractions: β-lactoglobulins, α-lactalbumins, immunoglobulins, and bovine serum albumin (BSA) [2]. β-lactoglobulins are the quantitatively major protein fraction of milk whey (50–55%); they occur only in the milk of ruminants. These proteins are a good source of essential amino acids with branched chains; β-lactoglobulins do not show allergenicity in the hydrolyzed state and are used in different formulas for infant feeding. α-lactalbumins account for about 20–25% of the MW proteins and are the main protein of breast milk. Thanks to the balanced amino acid composition, they supply essential amino acids into a child's body (particularly, tryptophan and cystine), are able to bind calcium as well as zinc [3], and accelerate their absorption in the alimentary process. α-lactalbumin is known to enter into the composition of lactose synthetase. 5–10% of the MW proteins represent bovine serum albumin (BSA), which is notable for the sufficiently large size of its molecules (see Table 1), its balanced amino acid composition, and can be bound by fats. The experiments with radioactive carbon have shown that BSA gets into milk from blood. The immunoglobulins of milk whey (10–15%) also get into milk from blood. They have the activity of antibodies against the corresponding antigens and, being the major protein fraction of colostrum, promote strengthened immunity in newborns.

The composition of the whey proteins also includes lactoferrin ranked among the so-called "minor" proteins contained in an insignificant quantity, which do not have a particular nutritional value but perform other very important functions. In particular, lactoferrin is a good antioxidant, has bactericidal properties, and is supposed to take part in protecting the mammary gland from the penetration of infections. This protein occur in breast milk in a significant quantity (17%); however, its content is much higher in any colostrum (by a factor of four). It is thanks to lactoferrin that the immunity and resistance of an organism increase in the first days of life. Thanks to its property to bind iron, lactoferrin suppresses the growth of

Content of the main protein fractions in milk whey

Protein	Content in MW, g/l	Molecular weight, kDa	Isoelectric point
α-lactalbumin	0.7	14.1	4.8
β-lactoglobulin	3.0	18.2	4.9–5.4
Bovine serum albumin	0.3	66	4.8
Lactoferrin	0.1	78–80	8.0–8.8
Lactoperoxidase	0.04	78–80	8.6–9.6
Immonoglobulins	0.5	150–900	5.8–7.3

pathogenic bacteria and fungi but promotes the growth of bifidobacteria, thus ensuring the normal functioning of gut organisms in newborns. The "minor" whey proteins also include lactoperoxidase inhibiting the growth of iron-consuming bacteria. Proteose-peptones account for nearly 25% of the whey proteins. This fraction is inhomogeneous in content and consists of four components, one of which represents a whey protein with a molecular weight of about 41000 and a high content (up to 17%) of carbons (a glicomacroproteid). The remaining components are phosphopeptides formed (together with [gamma]-caseins) during the hydrolysis of β-casein under the action of milk proteinases.

The milk whey proteins have the greatest rate of proteolysis in the alimentary process among whole proteins. The concentration of amino acids and peptides in blood abruptly increases as early as the first hour after taking foodstuffs based on whey proteins. The amino-acid composition of the MW proteins is most similar to that of human muscular tissue; as for the contents of essential amino acids (lysine, tryptophan, methionine, and threonine), they are superior to many proteins of animal and plant origin. The assimilability of milk whey proteins is exclusively high [4]. At present, demineralized whey is used widely enough for nutrition and fodder purposes [5–7]. There are different known methods for processing MW with the view to obtaining protein concentrates used as different additions, including biologically active ones [8–11].

Particular attention is devoted to the extraction of separate whey protein fractions in order to prepare different formulas for infant feeding [12, 13]. Analyzing the fields of milk whey processing permits one to conclude that the technologies based on combining different methods for extracting the milk whey components are the most efficient. Considerable promise is shown by the development of the electrophysical method yielding a protein–mineral concentrate and lactulose isomerized from lactose [14, 15].

The goal of this research was to optimize the protein extraction process by combining electrophysical MW processing and the chemical reagents admissible in the food industry.

The milk whey processing was performed in a two-chamber electrolyzer. Membranes of different types served as the separating element: canvas, ultrafiltration, and ion-selective membranes. A protein concentrate was extracted in the foamy form as a result of the processes taking place in the cathode chamber. Meanwhile, anode liquids of different compositions were used. The current density and the rate of income of the liquids into the chambers, where the voltage and the temperature of the solutions were registered, were supported constant during the MW processing. The active acidity and the content of proteins and mineral salts were determined in the partially deproteinized and demineralized whey (DW) that remained after separating the protein-mineral concentrate (PMC) into the mass-force field [16].

The electrochemical activation yielding a mixture of different valence-unsaturated particles (radicals) is one of the moving factors in extracting proteins by this method. According to the well-known theory of V.M. Bakhir [17], the electrochemical activation (ECA) is the assembly of the electrochemical and electrophysical impacts on water and the dissolved particles contained in it under the conditions of minimum heat evolution. The process takes place in the area of the spatial charge near the electrode surface (anode or cathode) of the electrochemical system during the nonequilibrium charge transfer through the electrode–electrolyte boundary by electrons. The particles (radicals) formed in this way have an increased reaction capability. In addition, the electric current behaves as a strong oxidizer or reducer [18].

The proteins contained in whey mainly have a globular structure. A protein globular is formed so that most of the polar hydrophilic amino-acid residues turn out to be outside and contact with a solvent, and most of the nonpolar (hydrophobic) residues are inside and isolated from the interaction with water. The ionogenic R-groups (radicals) of the amino-acid residues that are on the surface manifest acid–base properties determining the amphotericity and the charge of the protein molecules. The proteins contained in the solution bear a negative or positive charge depending on the medium's reaction and the ratio between the acid and base amino acids. A protein molecule in the solution is surrounded by a hydrate (sol-

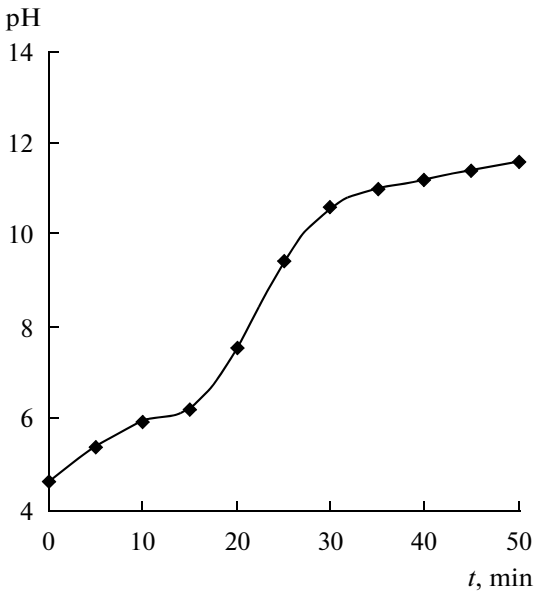

Fig. 1. Change in pH of the DW (the canvas membrane).

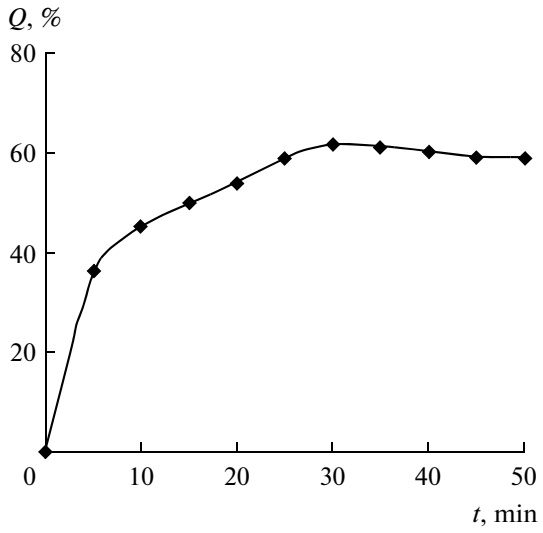

Fig. 2. Degree of the protein extraction into the PMC (the canvas membrane), Q—protein passing into the PMC (in % of its content in the initial MW).

vate) shell, i.e., water dipoles oriented around the polar groups. The proteins in the solution are kept in the native state owing to the factors of the stability including the charge of a molecule and the hydrate shell around it, which prevents the protein molecules from adhesion. The removal of these factors results in the coagulation of the proteins and their precipitation.

The destruction of the hydrate shell of the MW proteins resulting from the EHA of the water molecules' decomposition in the near-cathode area leads to their coagulation and ensures the protein extraction into the concentrate from the first minutes of the processing. In addition, the rupture of noncovalent bonds supporting the globular proteins' structure under the action of the electric current and the activation of the ionogenic R-groups of the amino-acid residues can result in the formation of new bonds and, consequently, the aggregation of the protein molecules.

A significant role in extracting the whey proteins is likely to be played by the R-groups of cysteine residues representing the reaction-capable sulfhydryl (thiol) groups. The oxidation of the sulfhydryl groups of two cysteine residues and the formation of a (covalent) disulfide bond (–S–S–) in the proteins yields cystine, which is a dimer of cysteine, thus supporting the spatial structure of the protein molecules along with the hydrogen, ion, and hydrophilic bonds. The intermolecular bridges between cysteine radicals dissociated either as a consequence of the ECA or during the increase in pH up to 8.3 analogously. The participation of cysteine residues in the complexing of the whey proteins in this treatment process is confirmed by the results of blocking of the sulfhydryl groups by sodium iodine acetate. The introduction of the latter in the initial whey decreases the protein yield owing to the aggregation of the proteins being excluded according to this mechanism [18].

The degree to which the R-groups of the amino-acid residues are ionized depends on the pH of the medium. In an acid medium, the increase in the proton concentration results in suppressing the dissociation of carboxyl radicals and decreases the negative charge of the proteins. In an alkaline medium, it leads to binding of the hydroxyl excess with the proteins formed during the dissociation of NH_3^+-groups with the formation of water, thus resulting in a decrease of the positive charge of the proteins. The pH value at which the number of positively and negatively charged groups is analogous, that is, the protein acquires a summary zero charge, is called the "isoelectric point" pI. If there is a zero charge of the protein, the hydrate shell is destroyed, since there naturally can be no interaction between the water dipoles and an electrically neutral protein molecule. Separate molecules join, thus forming large aggregates that are not able to stay in the solution and precipitate.

The active acidity of the DW increases during conducting the process from pH 4.55 to 11.60. The pI of the MW proteins are in this pH range (see the table) [19, 20]. However, it is very difficult to monitor the dependence of their isoelectric precipitation on the pH of the DW (Fig. 1, 2). The DW accumulates for some time interval, which already averages its parameters. The change in the active acidity in the volume of the electrolyzer chamber does not take place analogously and is determined by its width as well as the income of the initial solutions under the stream processing mode, which extends in time the process of reaching the pI by the proteins of one fraction. In

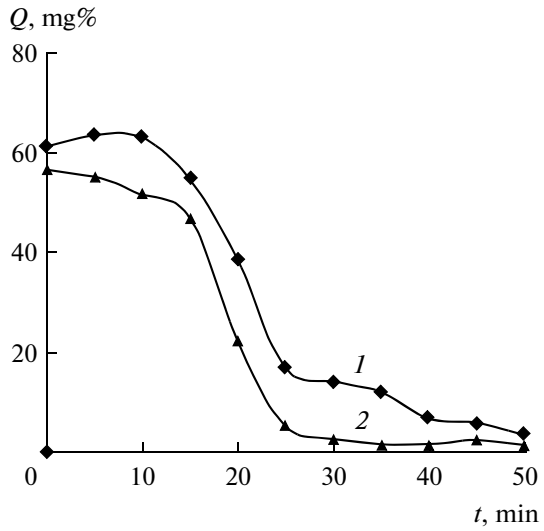

Fig. 3. Change in the content of calcium (*1*) and phosphor (*2*) in the DW (the colorimetric determination with a Beckman analyzer).

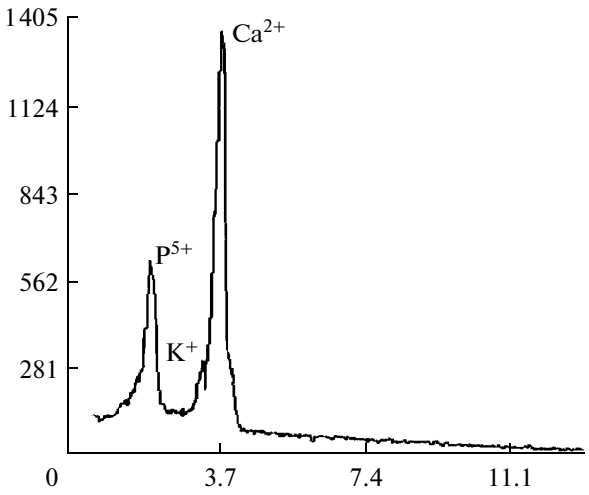

Fig. 4. Spectrogram of the summary PMC obtained by the electron probe X-ray analysis

addition, the protein extraction by this method of processing is due to several mechanisms of their complexing and coagulation acting simultaneously.

The predominant significance of calcium for the protein extraction by the suggested method is evidenced, on the one hand, by the decrease in its quantity in the DW during the process (Fig. 3) and, on the other hand, by the predominance in the mineral composition of the PMC. Phosphor is the second ash constituent by the content in the concentrate, since the almost complete phosphate-ion depletion of the DW (Fig. 3) is due to the phosphate ions only partially passing into the concentrate. A significant part of these ions migrates to the anode chamber. According to the data of the X-ray analysis, the Ca : P ratio in the PMC is 2.23 (Fig. 4); meanwhile, according to the literary sources [1], this ratio in the MW is about 1.09.

To precipitate proteins, the salting-out reaction is widely used, which is based on the phenomenon of the proteins' solubility with an increase in the concentration of neutral salts. The physicochemical basis of salting out has not been completely revealed; the destruction of a bond between a polymer and the solvent is known to be primary in this mechanism. When a salt is introduced, a part of the solvent molecules that were in the solvate bond with the polymer and solvate the molecules of the introduced salt. When a protein is salted out, the molecules are dehydrated and the charge is removed. The process is affected by the relative molecular weight, charge, and hydrophilicity of the protein. There is a direct dependence between the size of the water shell of the protein molecules and the salt concentration: the smaller the hydrate shell, the smaller the amount of salts is required. Thus, large and heavy molecules that have a small water shell precipitate if the salt saturation of a solution is incomplete, and smaller molecules surrounded by a large water shell precipitate if the saturation is complete. The neutral salts of alkaline and alkaline-earth metals are used to salt out proteins. When whey is processed, the electrolysis of the salts contained in it and the electrodialysis result in the fact that the ion concentration in the near-electrode zones can multiply (by orders of magnitude) exceed the latter in the initial solution, creating conditions ensuring the effect of the protein salting out.

In milk (pH 6.47–6.67), calcium salts are mainly represented by phosphates that have a small solubility and an insignificant degree of dissociation. Only a small part of them is contained in the form of a true solution, and a greater part is contained in the form of a colloid solution. Colloid calcium phosphate joined with calcium caseate is contained in milk in the form of the so-called "calcium caseate–phosphate" complex (CCPC). The composition of the colloid calcium phosphate that is present in the CCPC and the character of its bond with casein are still unknown. Calcium caseate is formed when calcium ions interact with the carboxyl and serine phosphate groups of casein. This being the case, calcium can react with two closely located –COOH and –OH-groups, forming intermolecular calcium bridges: –R–Ca–R. It is believed that hydrophosphate ions –R–Ca–HPO_4–Ca–R or –R–Ca–HPO_4–Ca–HPO_4–Ca–R can also take part in forming cross-linking bridges (between two phosphoserine radicals).

Lactic acid formed due to the activity of the lactic-acid microflora transfers the calcium milk salts from the colloid state to the ion-molecule state. Under the action of the acid, the structure of the CCPC is destroyed—inorganic and organic calcium phosphate (of phosphoserine) are both detached from it. Lactic acid inhibits the dissociation of the free carboxyl groups and acidic groups of casein phosphate: the

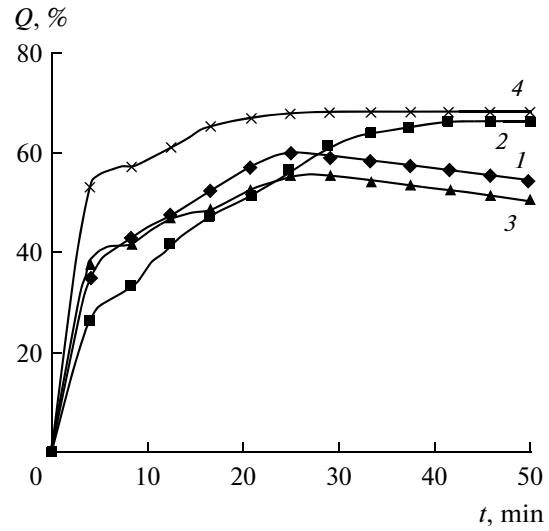

Fig. 5. Dependence of the degree of the protein extraction into the PMC on the composition of the AL and the type of membrane. The variants of the composition of the AL: (*1*) MW (the canvas membrane); (*2*) 5% solution $CaCl_2$ in MW (the canvas membrane); (*3*) MW (the ultrafiltration membrane); (*4*) 2% solution $CaCl_2$ in water (the MK-40 ion-selective membrane); *Q*—the protein passage into the PMC (in % of its content in the initial MW).

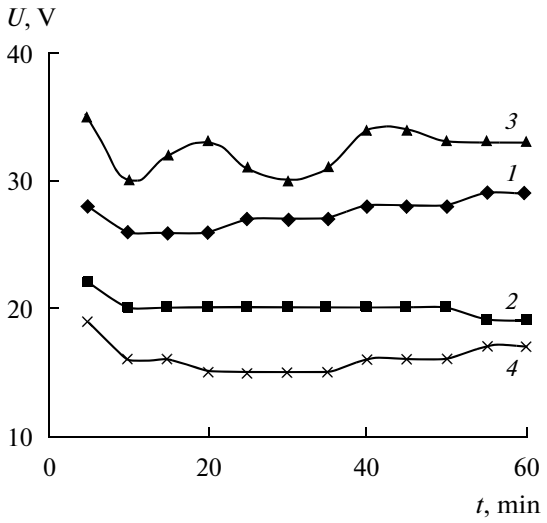

Fig. 6. Change in the voltage depending on the composition of the AL and the type of membrane. The variants of the composition of the AL: (*1*) MW (the canvas membrane); (*2*) 5% solution $CaCl_2$ in MW (the canvas membrane); (*3*) MW (the ultrafiltration membrane); (*4*) 2% solution $CaCl_2$ in water (the MK-40 ion-selective membrane).

COO groups transform into COOH, and PO_3^{-2}, into PO_3H_2. In whey (at pH 4.6–4.7), calcium hydrophosphates (mono- and predominately dihydrophosphates) are soluble; that is, they are electrolytically dissociated. They attain an equilibrium, whose shift depends on the pH of the medium (the whey's pH): as the pH increases, dihydrophosphates transform into monohydrophosphates, reacting with hydroxylion.

It is supposed that, under the conditions of electrophysical milk whey processing at a pH of more than 6, bonds analogous to the bridges between the casein molecules entering into the composition of the CCPC are formed between the ionized acetate groups and the phosphoserine residues of both the phosphopeptides (proteose-peptones) and whey proteins, particularly those which are conformationally unchanged [18]. As the active acidity grows, the calcium orthophosphates weakly associated in the initial whey pass into the molecular-dispersed state completely and can get into the PMC together with protein.

To make the protein extraction process more intensive, experiments differing mainly in the heightened concentration of calcium ions in the processed whey were conducted according to these mechanisms. Calcium chloride, which is a well-soluble salt, was used as an additionally introduced electrolyte. To avoid the formation of chlorine-bearing organic compounds in the CC and to increase the conductivity of the system, calcium chloride was introduced into the anode liquid (AL). The salt (an electrolyte) was dissolved either in MW or in (distillated) water. Three types of membranes were used: a canvas membrane, an MK-40 ion-selective membrane, and an ultrafiltration membrane. The current density (20 mA/cm^2) and the rate of the liquids incoming to the electrolyzer chambers (5 ml/min) are analogous in the presented variants of the experiments.

Using 5% calcium chloride in the MW as the AL and canvas as a separating element increases the protein extraction into the PMC by almost 10% in comparison with using only MW (Fig. 5, variants *1*, *2*). The lower protein yield in variant 2 compared to variant 1 is explained by the lower initial acidity of the processed whey. Meanwhile, the voltage (Fig. 6, variants *1*, *2*) and power inputs (Fig. 7, curves *1*, *2*) decrease, and, correspondingly, the profitability of the process rises. However, after 25 working cycles, the canvas diaphragm is observed to be gradually choked up [22]. The efficiency of the device concerning the protein yield into the PMC falls by a factor of two, which is accompanied by an abrupt increase in the voltage and results in a heightened temperature of the processed whey. It is evident that the area of the separating element involves some of the supposed processes of the precipitation of the proteins migrating through the canvas diaphragm in both directions due to the difference in the charges of the molecules. The concentrate formed in the near-membrane area is held up on its surface on the side of both cathode and anode chambers.

A low protein yield is observed when using the ultrafiltration membrane with the properties caused by its destination. The increase in the voltage consump-

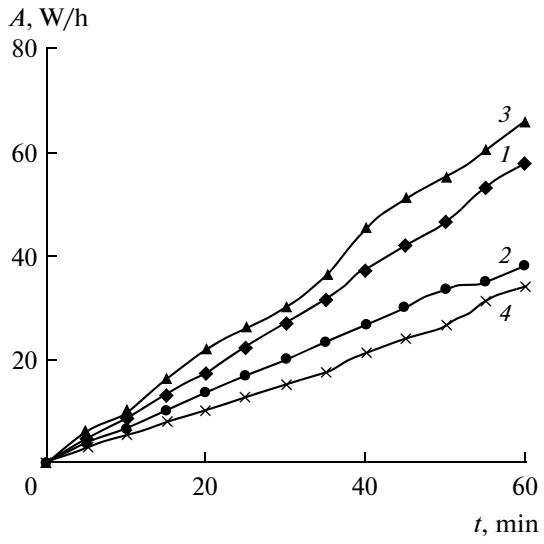

Fig. 7. Change in the power inputs depending on the composition of the AL and the type of membrane: (*1*) MW (the canvas membrane); (*2*) 5% solution $CaCl_2$ in MW (the canvas membrane); (*3*) MW (the ultrafiltration membrane); (*4*) 2% solution $CaCl_2$ in water (the MK-40 ion-selective membrane).

tion (Fig. 6, variant *3*) in comparison with the previous variant of the experiment and, correspondingly, the growth in the power inputs (Fig. 7, variant 3) speak for the increase in the resistance owing to the membrane's pores being choked up by the protein substances aspiring to migration. This hampers the displacement of the ions and charged molecules from one chamber into another, including the calcium cations, which are important for the aggregation of the whey proteins. The choice of the ion-selective membrane (MK-40) as a separating element meets all the requirements of the method presented. The membrane is not choked up, which promotes a decrease in the voltage and power inputs (Figs. 6, 7; curve *4*). Intensive foaming in almost the entire volume of the working chamber is observed. Using 2% calcium chloride in distillated water as the AL raises the protein yield in comparison with variant 3 (Fig. 5, variants *3*, *4*) by almost 13%, which enabled the 70% extraction of the whey proteins. Although the content of calcium chloride is much lower (by a factor of almost three) than in the AL representing the 5% solution of this salt in the MW, the protein extraction into the concentrate is observed to be almost equal (Fig. 5, variants *2*, *4*).

Consequently, using the ion-selective membrane permits the degree of the protein passing into the PMC to be increased with lowering the power inputs, enables the protein salting out to be regulated, and permits the whey to be saved (economized) only for processing in the cathode chamber.

The conducted research is the next stage in the chain for optimizing the suggested method, thanks to which there is success in reaching the maximum protein extraction with decreasing power inputs and in obtaining concentrates with the assigned composition and properties by combining the different parameters and conditions of the milk whey processing. The electrophysical methods are a promising field in the nonwaste processing of secondary raw milk products; they enable the valuable fractions to be extracted without directly applying chemical reagents.

REFERENCES

1. Khramtsov, A.G., *Molochnaya syvorotka* (Milk Whey), Moscow: Agropromizdat, 1990.
2. Khramtsov, A.G., Evdokimov, I.A., Ryabtseva, S.A., Vinogradskaya, S.E., Dunchenko, N.I., Myachin, A.F., and Polishchuk, D.O., The Scientific-Technical Bases of Expert Examination of Secondary Raw Milk Products and Derivative Products, *Sb. Nauch. Tr. SevKavGTU, Ser. "Prodovol'stviye"*, 2003, no. 6, pp. 36–39.
3. Permyakov, S.E., Uversky, V.N., Veprintsev, D.V., Cherskaya, A.M., Brooks, C.L., Permyakov, E.A., and Berliner, L.J., Mutating Aspartate in the Calcium-Binding Site of α-Lactalbumin: Effects on the Protein Stability and Cation Binding, *Protein Engineering*, vol. 14, no. 10, pp. 785–789.
4. Lodygin, A.H. and Kiselev, S.A., The Urgency of Using Milk Whey Proteins When Producing Concentrates with an Intermediate Moisture, *Sb. Nauch. Tr. SevKavGTU, Ser. "Prodovol'stviye"*, 2005, no. 1, www.ncstu.ru.
5. Avtyan, K.V., Lodygin, A.N., and Lodygina, S.V., The Prospects for Using Demineralized Milk Whey in Confectionery, *Sb. Nauch. Tr. SevKavGTU, Ser. "Prodovol'stviye"*, 2010, no. 6, www.ncstu.ru.
6. Molochnikov, V.V., Nesterenko, P.G., Bogdanova, N.A., Kovaleva, O.G., Vodolazov, L.I., and Astakhov, E.S., The Effect of the Ionite Weight and Duration of the Process on the Degree of Mineralization of Milk Whey, *Tezisy dokl. Mezhdun. Nauchno-Prakt. Konf. "Energosberegayushchiye tekhologii pererabotki sel'skokhozyaistvennogo syrya"* (Theses of Reports at the International Scientific-Practical Conference "Energy-Saving Technologies for Processing Raw Agricultural Products"), Minsk, 1996.
7. Chebotarev, E.A., Perfecting the Technological Schemes for Separation of Milk Whey and Its Concentrates, *Vestn. SKO ATN RF* "*Technologiya zhivykh sistem*", 2001, no. 1, pp. 84–88.
8. Evdokimov, I.A., Volodin, D.N., and Dykalo, N.Ya., Electrodialysis is a Challenging Method for Milk Whey Processing, *Pererabotka moloka*, 2001, no. 2, pp. 5–7.
9. Khramtsov, A.G., Basilisin, S.V., Evdokimov, I.A., Vinogradov, B.D., and Roslyakova, I.V., RF Inventor's Certificate no. 5061562/13, March 27, 1995.
10. Shuvaev, V.A., New Physico-Chemical Processes of Obtaining Milk-Whey Concentrates, *Sb. Nauch. Tr. SevKavGTU, Ser.* "*Prodovol'stviye*", 1999, no. 2, pp. 55–58.
11. Chebotarev, E.A., Vasilisin, S.V., and Sanzharovskii, S.A., Expert Assessment of the Methods for Coagulation of Milk Whey Proteins, *Sb. Nauch. Tr. SevKavGTU, Ser.* "*Prodovol'stviye*", 2001, no. 4, pp. 69–70.

12. Maketin-Kijunen, S. and Sorva, R., Bovine β-Lactoglobulin Levels in Hydrolised Protein Formulas for Infant Feeding, *Clin.Exp.Allergy*, 1993, vol. 23, pp. 287–291.

13. Khramtsov, A.G., Evdokomov, I.A., Ryabtseva, S.A., Polovyanova, A.V., Kozlova, E.A., and Ereshova, V.D., New Fields in Developing Functional Nutrition Products, *Sb. Nauch. Tr. SevKavGTU, Ser. "Prodovol'stviye"*, 2005, no. 8, pp. 14–20.

14. Bologa, M., Sprincean, E., and Maximuc, E., a. nr. 3793, Procedeu de prelucrare a produselor lactate secundare.

15. Bologa, M., Sprincean, E., Bologa, A., Stepurina, T., Policarpov, A., a nr. 3924, Procedeu de proscesare a zerului.

16. Sprincean, E.G., Optimizing the Technological Modes for Obtaining the Protein-Mineral Concentrate from Secondary Raw Milk Products, *Electron. Obrab. Mater.*, 2009, no. 1, pp. 73–80.

17. Bakhir, V.M., *Electrokhimicheskaya aktivatsiya* (Electrochemical Activation), Moscow: VNIII Med. Tekhniki, 1992, part 2.

18. Bologa, M.K. and Pyrgaru, Yu.M., Processes of Electrocontact Coagulation of Whey Proteins, *Electron. Obrab. Mater.*, 1993, no. 6, pp. 46–50.

19. Rytchenkova, O.V. and Krasnoshtanova, A.A., Development of the Methods for Protein Extraction from Milk Whey, *6-ya Mezhdun. Konf. "Sotrudnichestvo dlya resheniya problemy otkhodov"* (The 6-th Intern. Conf. "The Cooperation for Solving the Problem of Waste"), April 8–9, 2009, Moscow, Russia.

20. Bogatova, O.V. and Dogareva, R.G., *Khimiya i fizika moloka* (Chemistry and Physics of Milk), Orenburg: GOU OGU, 2004.

21. Gorbatova, K.K., *Khimiya i fizika belkov moloka* (Chemistry and Physics of Milk Proteins), Moscow: Kolos, 1993.

22. Sprincean, E.G. and Bologa, M.K., The Salt Composition of the Whey-Protein Concentrate Obtained by the Electrocontact Method, *Electron. Obrab. Mater.*, 2006, no. 6, pp. 50–55.

ISSN 1068-3755, Surface Engineering and Applied Electrochemistry, 2010, Vol. 46, No. 6, pp. 612–614. © Allerton Press, Inc., 2010.
Original Russian Text © S.N. Maslobrod, L.B. Korletyanu, A.I. Ganya, 2010, published in Elektronnaya Obrabotka Materialov, 2010, No. 6, pp. 88–90.

ELECTRICAL TREATMENT OF BIOLOGICAL OBJECTS AND FOOD PRODUCTS

The Influence of Millimetric Radiation on Plant Viability: 2. The Changes in Seeds' Metabolism after the Treatment of Soaked Seeds

S. N. Maslobrod, L. B. Korletyanu, and A. I. Ganya

Institute of Plant Genetics and Physiology, Academy of Sciences of Moldova, ul. Pedurii 20, Kishinev, MD-2002 Republic of Moldova

e-mail: maslobrod37@mail.ru

Received June 16, 2010

Abstract—At the influence of millimetric radiation (MMR) with wavelength of 5.6 mm; density of stream of capacity of 6–10 mwt/sm^2 and several minutes' expositions on dry and presoaked seeds of tomato, castor-oil plant and dope we observed stimulation of sprouting energy and seeds germinating power, change of protein synthesis and enzymatic activity of sprouts and also decrease of the number of chromosomal infringements in cells of rootlets. It has been drawn the conclusion that water is a primary receptor of millimetric radiation in seeds of plants.

DOI: 10.3103/S1068375510060128

The given work represents the logical continuation of the previous one [1]. The aim was to find out how soaked seeds respond to MMR. The primary receptor of MMR in such objects is water. It can provoke initial changes of the metabolism of seeds treated by MMR. A comparative experiment using both dry and swelled (soaked) seeds as the objects was conducted. The following parameters served as indicators of the efficiency of the MMR's influence on the seeds: the germinating and viability energy, the o–IAA and easily soluble proteins (ESPC) content in the seedlings, and the number of chromosome aberrations (NCA) in the cells of the primary roots (the methods of estimation of these parameters are described in [1]).

When irradiating dry seeds of tomatoes (cv., Muromskii), the stimulation of the seeds' germinating capacity was observed for all the expositions; the most expressed effect was reached after 10 min of exposition for all the terms of screening of the seeds' germination (five to seven days). The increase of the germinating capacity reaches 24% (figure). The irradiation of similar seeds soaked in distilled water for three hours leads to the alteration of the "dose–effect"curve: two stimulation peaks are observed at expositions of six and ten minutes. The exposition for eight minutes indicates an effect on the control level. The absolute meanings of the stimulation of the objects in the different physiological states are almost similar (figure).

The following results were obtained for another object (dry and soaked for 24 h in distilled water)—onion seeds. The irradiation of the dry seeds provoked two stimulation expositions, two and eight minutes, while three peaks were observed in the case of the treatment of the soaked seeds (2, 6, and 10 min). Hence, the first curve is bimodal and the second is trimodal. The stimulation in the case of the MMR's influence on the soaked seeds is 10–16% higher than in the case of the dry seeds (Fig.).

The analysis of the two experiments reveals the better manifestation of the nonlinearity of the "dose–effect" curve for the soaked seeds. The stimulation curves do not coincide for the dry and soaked seeds, which may evidence the different nature of the MMR receptors in these objects.

The most probable basic MMR receptor in case of the soaked seeds is the water present both inside the object and on its surface, which is in accordance with the known concept concerning the dominant role of water in MMR reception [2].

In the case of dry seeds, except for the water present in the bound state, other MMR receptors seem to significantly contribute to the total effect viz. the cell membranes, their fragments, and single organic molecules [2, 3]. This phenomenon leads to differences in the character of the dose curves obtained from the treatment of the dry and soaked seeds.

The next experiment was connected with the MMR's influence on the dry and soaked seeds of other plant species. Both the dry and soaked (24 h) seeds of the castor-oil plant of reproductions of 2002 and 2003 together with dry seeds of thorn apple (reproduction of 2006) were used for the work. These seeds represent different periods of conservation and possess a low germinating capacity. They were treated with MMR with a wave length of 5.6 mm; a power flux density of 7–10 mWt/cm^2; and expositions of 2, 8, and 30 min.

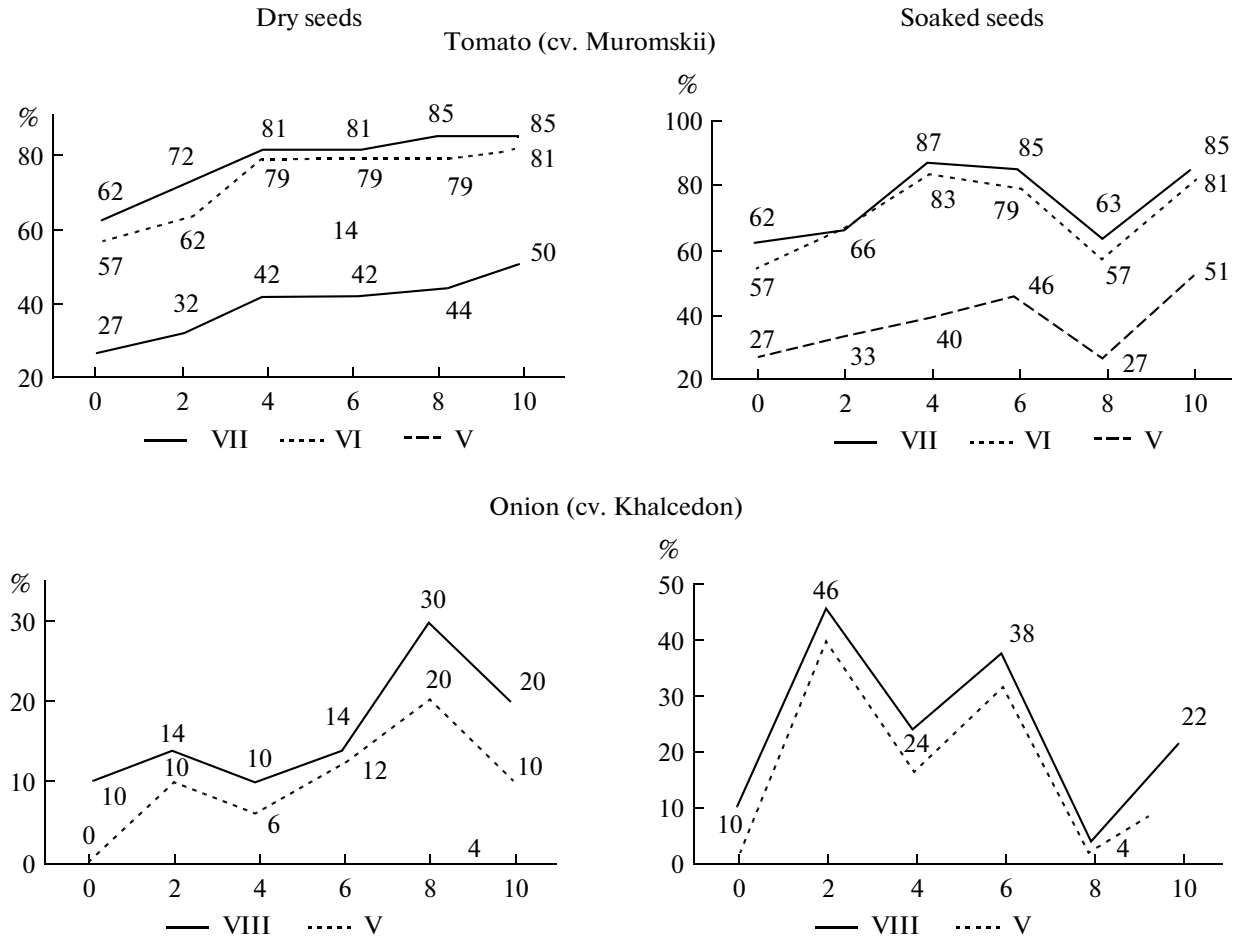

The dynamics of the germinating capacity of the tomato and onion seeds after the MMR treatment of the dry and soaked seeds, %. 4, 6, 8, and 10 min exposition to the radiation; the V, VI, VII, and VIII days of the seeds' germination.

When irradiating the dry castor-oil plant, the stimulation of the germinating energy was observed for all the expositions, but 2 and 30 min appeared to be the most effective (table). The level of the stimulation reached 30%. The maximum effect on the germinating efficiency was 11.6% in the case of the exposition for 30 min. The maximum root length was observed after two and eight minutes of exposition. In the case of the irradiation of soaked samples, the stimulation of the seeds' germinating energy and capacity was also observed for these expositions. The excess of the germinating energy compared with the control comprised ca. 12% and 9% for the germinating capacity. In general, similar results were obtained for the germinating of both the dry and soaked seeds. In accordance with our data [4], one may propose a common mechanism of the MMR's action on the plant seeds with water (intra- and extracellular) serving as the primary MMR receptor, as in [2, 3]. The highest t level of the stimulation is observed in the case of the irradiation of soaked seeds as compared with dry ones.

The o–IAA enzyme content in the seedlings obtained from the treated dry seeds (exposition of 30 min) practically coincides with the control; a similar situation is observed for the ESPC in the roots of the seedlings. In this case, the maintaining of high growing activity in the castror-oil plants is accompanied by high ESPC. The optimal exposition of the dry seeds for reaching the most effective germinating energy and capacity comprises 8 min; after 2 min of treatment, the activity of the o–IAA is two times lower. A stimulating exposition of 8 min was also confirmed for the soaked seeds. A decrease of the o–IAA activity is associated with an increase of the growing activity as indicated by the root length. The ESPC is higher in the soaked seeds than in the dry ones due to the higher hydrophilicity of the former.

The MMR treatment of the dried thorn apple seeds led to a decrease of a number of the chromosome abnormalities (NCA) in the cells of the primary roots of the seedlings; i.e., the treatment factor promoted the more rapid elimination of the cells with chromosome aberrations, thus increasing the percentage of the normally dividing cells.

Changes in the physiological, biochemical, and genetic parameters of the seeds and the seedlings of the castor-oil plants and the thorn apples after the MMR treatment of their seeds

Object	State	Exposition, min	Germinating energy, %	Germinating capacity, %	o–IAA, arb. units	ESPC, μg/g	NCA, %
Castor-oil plants	Dry seeds	0	21.9 ± 8.13	84.8 ± 4.81	0.0306	526	6.6 ± 1.64
		2	59.9 ± 1.23*	83.8 ± 4.81	0.1163	390	5.2 ± 1.40
		8	27.2 ± 1.41	91.4 ± 2.11	0.0566	390	3.2 ± 0.81*
		30	31.4 ± 2.05*	96.2 ± 1.20	0.0305	567	2.4 ± 0.54*
	Soaked seeds	0	85.6 ± 1.28	89.5 ± 1.20	0.1017	975	–
		2	93.5 ± 4.18	95.2 ± 3.30	0.1328	1050	–
		8	97.1 ± 1.20*	98.1 ± 1.00	0.0898	885	–
		30	87.6 ± 4.67	87.7 ± 4.67	0.3080	795	–
Thorn apples	Soaked seeds	0	21.9 ± 1.72	29.9 ± 3.42	0.1756	100	7.4 ± 1.35
		2	32.0 ± 1.31*	44.2 ± 1.60*	0.0730	109	6.2 ± 1.56
		8	30.4 ± 1.00	40.0 ± 1.18*	0.0196	150	3.8 ± 0.63*
		30	25.6 ± 1.01	34.3 ± 2.96	0.4151	75	5.0 ± 1.26

Note: * The differences are significant comparing with control values.

The MMR treatment of the thorn apple seeds led to the stimulation of the germination energy and capacity at expositions of 2 and 8 min, but no effect was observed for the exposition of 20 min. These data coincide with the earlier original results obtained for seeds of other plant species.

The content of the o–IAA decreased at short expositions and increased at longer ones, which, as in the case with the castor-oil plants, evidences an increase of the intensity of the seeds' germination. The ESPC in the roots increases after short expositions (2 and 8 min) and decreases after 20 min of exposition. The NCA significantly decreases at the exposition of 8 min and insignificantly at the expositions of 2 and 30 min. Conclusively, the healthy influence of MMR on the chromosome apparatus of the seedlings was confirmed.

Hence, the MMR treatment of the castor-oil plants and the thorn apple seeds revealed the stimulation of the germination energy and capacity, the protein synthesis stimulation in the roots of the seedlings, and a decrease of the o–IAA activity and the frequency of the chromosome aberrations in the seedlings' roots.

The method of millimeter irradiation of old seeds of medicinal plants (with examples of thorn apples and castor-oil plants) in order to increase their viability is proposed.

REFERENCES

1. Maslobrod, S.N., Karletyanu, L.B., and Ganya, A.I., Influence of Millimeter Radiation on Plant Viability. 1. Changes in Seed Metabolism after Treatment of Dry Seeds, *(see given issue)*, 2009.
2. Betskii, O.V., Lebedeva, N.N., and Kotrovskaya, T.I., The Unusual Water Characteristics under Weak Electromagnetic Fields, *Biomeditsinskiye Tekhnologii I Radioelektronika*, 2003, vol. 1, pp. 37–44.
3. Devyatkov, N.D., Golant M.B., and Betskii, O.V., *Millimetrovye volny i ikh rol' v processakh zhiznedeyatel'nosti* (Millimeter Waves and Their Role in Processes of Life Activity), Moscow, 1991.
4. Maslobrod, S.N., Korletyanu, L.B., Ganya, A.I., and Gaidei, N.A., Water "Memory" of Millimeter Radiation for Criterion of Seeds' Germination Capacity, in *Voda: ekologiya i tekhnologiya, EKVATEK–2006* (Water: Ecology and Technology, EKVATEK–2006), vol. 2, Moscow, 2006, pp. 1049–1050.

ISSN 1068-3755, Surface Engineering and Applied Electrochemistry, 2010, Vol. 46, No. 6, pp. 615–619. © Allerton Press, Inc., 2010.
Original Russian Text © E.M. Godzhaev, A.M. Magerramov, Sh.A. Zeinalov, S.S. Osmanova, E.A. Allakhyarov, 2010, published in Elektronnaya Obrabotka Materialov, 2010, No. 6, pp. 91–96.

EQUIPMENT AND INSTALLATIONS

Coronoelectrets Based on Composites of High Density Polyethylene with a $TlGaSe_2$ Semiconductor Filler

E. M. Godzhaev[a], A. M. Magerramov[b], Sh. A. Zeinalov[a], S. S. Osmanova[a], and E. A. Allakhyarov[a]

[a] *Azerbaijan Technical University, pr. G. Dzhavida 25, Baku, AZ1000 Azerbaijan*

[b] *Institute of Radiation Problems, National Academy of Sciences of Azerbaijan, ul. F. Agaeva 9, Baku, AZ1143 Azerbaijan*

e-mail: geldar-04@mail.ru

Received June 25, 2010

Abstract—In the thesis reports concerning the results of the study of the thermally stimulated depolarization and electret properties of the compositions of HDPE + x%, where x = 1, 3, 5, 7, 10, it is found that the composites with x = 5 and 7 are valuable electret materials with a lifetime of 360 days, 50 times higher than the lifetime of pure high density polyethylene.

DOI: 10.3103/S106837551006013X

INTRODUCTION

The production of new polymer compositions with interesting electrophysical, tensosensitive, electret, sensor, and other properties mainly depends on the nature of the filler, on the shape, on the size, on the distribution character and particle connectivity type, and on the degree of interaction between the components. Usually, new fillers lead to the extension of the possibilities of the practical application of the composite materials. Electroactive (electret, piezo-, pyro- and ferroelectric, photoelectric, acoustophotovoltaic, etc.) polymer composite materials of polymer–semiconductor filler type are of special interest [1–3].

Depending on the polymer matrix's nature and the filler type, various methods of production of an electroactive state are applied, and, to study the peculiarities of the charge stabilization, various thermoactivation methods are used.

Experimental investigations show that the electroactive properties of the polymer–filler type are mainly determined by the charge state of the phases and the structure's peculiarities, the connectivity type, the intraphase interaction, and the distribution and polarization in the composite [4–6]. For the control of the accumulation during the charge relaxation in polymer composites under the action of a corona discharge in air, it is of great research and practical interest to find out the interconnection of the parameters of the polarization with the peculiarities of the structure and interphase interaction.

The selection of high density polyethylene (HDPE) as a binder is conditioned by the good study of the electrophysical properties of this material and by the fact that the oriented PE state exhibits the stability of the electret effect with the effective surface of the charge density equal to 10^{-5}–10^{-4} C/m^2 [7]. The selection as a filler of $TlGaSe_2$ is connected, on the one hand, with the search for the possibilities of the creation of flexible electroactive elements with arbitrary configurations and, on the other hand, with the study of its interaction with polymers as a nucleating agent. It should be noted that $TlGaSe_2$ has high photosensitivity to the infrared and visible region of the spectra [8, 9]. Besides, the contact phenomena, the changes of the electrophysical and electroactive properties of the heterogeneous polymer–semiconductor systems, the peculiarities of the interphase phenomena, the presence of the effects of percolation, and the formation of the volume charges during the polarization processes in these systems are poorly explored.

EXPERIMENTAL

From PE powders and a $TlGaSe_2$ semiconductor (with particle sizes of ≤63 μm), via mechanical mixing of the components in a laboratory mixer, a homogeneous mixture for which the method of hot pressing of films with thicknesses of 100–150 μm was used. The polarization of the samples in the needle-space system was performed via the effect of a corona discharge at a voltage of 6 kV for 5 minutes. The distance between the polarizing electrodes (the needle–plane) was 10 mm. The electret difference of the U_e potentials was measured using the compensation method without contact, and its values σ were calculated [4].

The spectra of the currents of the thermostimulated depolarization (TSD) were taken by the standard method [5, 10]. Samples of the compositions (using a U5-11 electrometric amplifier) were placed between two short-circuited electrodes into a heated measuring cell [5]. The recording of the TSD in the temperature range of 293–543 K was performed at the linear increasing of the sample's temperature at a rate of

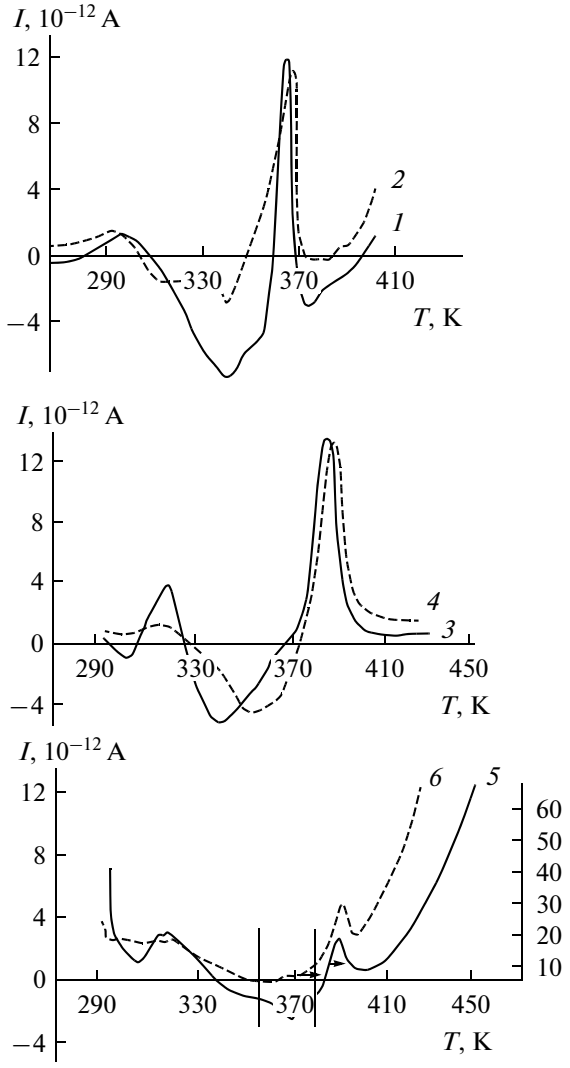

Fig. 1. Spectra of the thermostimulated depolarization of HDPE + x vol % $TlGaSe_2$ compositions, where x equals the following: (*1*) 1; (*2*) 3; (*3*) 7; (*4*) 10; (*5*) 20; *6*) 30.

2.5 K/min. All the samples of the composite electrets had the connectivity type of 0–3 [3–6].

RESULTS AND DISCUSSION

In Fig. 1 are given the TSD spectra for the samples of the HDPE + x vol % $TlGaSe_2$ compositions at various contents of the filler. As is seen (curve *1*) for the HDPE + 1 vol % $TlGaSe_2$ composite, on the TSD curve, a maximum at 295 K, a current inversion at 310 K, a minimum at 337 K, a current inversion at 357 K, a pronounced maximum at 366 K, current inversions at 370 K and 396 K, and a minimum at 375 K are observed. For the HDPE + 3 vol % $TlGaSe_2$ composite, on the TSD curve (curve *2*), the first maximum at 293 K, the current inversion at 303 K, the minimum at 340 K, the second current inversion at 350 K, the pronounced maximum at 359 K, and the current inversion at 373 K are observed. As a whole, the TSD curve's character for compositions with $x = 1$ and 3 does not significantly differ. On the TSD curve for the HDPE + 7 vol % $TlGaSe_2$ composite (curve *3*), the first maximum at 318 K, the current inversion at 325 K, the minimum at 340 K, the current inversion at 368 K, and the pronounced maximum at 384 K are observed. For the HDPE + 10 vol % $TlGaSe_2$ composite, on the TSD curve (curve *4*), a weak maximum at 316 K, a current inversion at 329 K, a minimum at 355 K, a current inversion at 373 K, and a pronounced maximum at 387 K are detected. Similar investigations were performed for the HDPE + 20 vol % $TlGaSe_2$ and HDPE + 30 vol % $TlGaSe_2$ compositions. For the HDPE + 20 vol % $TlGaSe_2$ composite (curve *5*), on the TSD curve, a minimum at 303 K, a maximum at 316 K, a current inversion 336 K, a minimum at 365 K, a current inversion at 379 K, a relatively pronounced maximum at 385 K, a minimum at 395 K, and further growth of the current of the thermostimulated depolarization are revealed. On the TSD curve of the HDPE + 30 vol % $TlGaSe_2$ composite (curve *6*), a weak minimum at 317 K, a pronounced maximum at 386 K, a minimum at 393 K, and further growth of the TSD are revealed.

When analyzing the TSD spectra, it can be noted that the introduction of a 1–10% filler into the high density polyethylene leads to the formation of deeper carrier traps. At that, the amount of the injected charge traps during the corona effect increases (the rise of the intensity and the square of the corresponding maximum) as well as the depth of their accumulation (the temperature position shifts to the high-temperature region).

The nature of the appearance of the inversion peak in the 310–370 K region for the composites with $x = 1-10$ can be explained in the following way: during the electreting under the action of the corona discharge, the volume charge is formed, and, in the field of the volume charges (VC) on the boundaries of the $TlGaSe_2$ particles and the polymer, the interphase polarization (IP) prevails [11]. The direction of that polarization is opposite to the field of the volume charges. In this case, during the depolarization, in the TSD spectra, the inversion currents caused by the IP are observed. The explanation proposed by us of the inversion peak's formation in principle agrees with the Maxwell–Wagner effect, according to which the charge accumulation on heterogeneous materials (in our case, composites) is caused by the conductivity difference in the amorphous and crystalline phases. During the electrization of such materials, the carriers will either accumulate nearby this interphase boundary or, on the contrary, go from it depending on which of the two conduction currents is higher. A difference in the local conduction currents also leads to the dissipation of the charges during the collecting of the TSD currents, since, in this case, the currents already flow in the opposite direction. It should be noted that this maxi-

mum is connected with the charge relaxation on the $TlGaSe_2$ particles' surfaces, since, as the filler content increases in the compositions, the peak value increases.

Effects of the TSD sign inversion are also observed for other electroactive dielectrics, electrets, and polymer composites [12]. However, the interpretation of these phenomena up to the present time remains controversial. Depending on the temperature position of the inversion peak, the surface state, the nature of the polymer matrix and the filler, the nature of the polarization, and other factors, the observed currents with opposite signs on the TSD curves are also connected with the reorientation of the dipoles existing in the polymer.

In our opinion, via the comparison of various α–, β^-–, β^+–, etc., for the structural transitions in polymorphines [4–6, 10], the maximums observed at certain temperatures have the same nature; i.e., they are connected with α-relaxation in the PE. The observed inversion at certain temperatures occurs as a result of a decrease of the $TlGaSe_2$ conductivity during the repolarization of the volume charges in the IP in the VC field. It can be assumed that the volume content of the $TlGaSe_2$ in the composite can influence the temperature position of the α-relaxation process.

The high-temperature maximums on the TSD curves can be connected with the increase of the conductivity of the filler, since the value of the peak changes as the filler content in the composition increases.

For the quantitative evaluation of the thickness of the interphase layer in heterogeneous polymer compositions, in some cases, the concept about the formation of a double layer is used (such a point of view is held for impurity semiconductors, where the difference of the conductivity leads to the formation of a double layer).

In polymer blends and composites, the thickness of the interphase layer can be estimated using the formula

$$d_m^2 = \frac{2\varepsilon_1\varepsilon_2\varepsilon_0 kT}{ne^2},$$

where ε_1 and ε_2 are the dielectric conductivities of each phase, ε_0 is the electric constant, and n is the concentration of the charge carriers (for polymer dielectrics, $n = 10 \times 21$ m^{-3}, e is the electron charge, k is the Boltzmann constant, and T is the absolute temperature). The calculations of the values of d_m using this equation show that it is about 0.4×1.2 μm.

Thus, the investigation results of the TSD currents of the electret films based on the samples of HDPE- + $TlGaSe_2$ compositions crystallized under the conditions of hardening at 273 K show that, on the TSD curves, a series of depolarization peaks in the temperature regions relating to the release of charges from traps connected both with the individual components (HDPE + $TlGaSe_2$) and the formed interphase polarization in the field of the volume charges are observed.

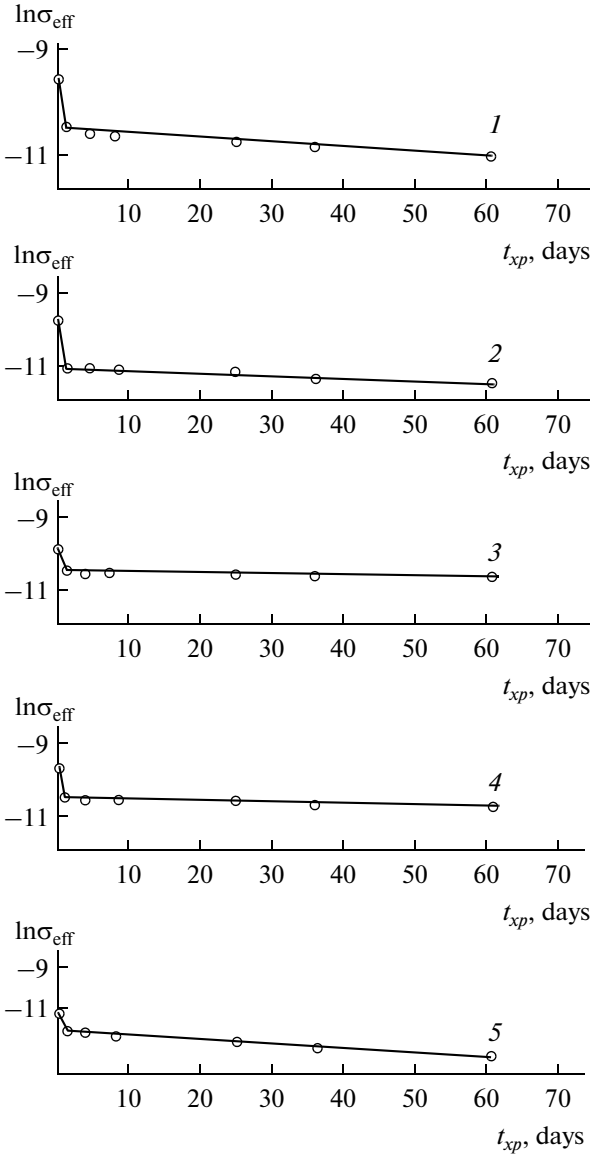

Fig. 2. Dependence of the surface density of the charge on the storage time for coronoelectrets from HDPE + x vol % $TlGaSe_2$ polymer compositions, where x equals the following: (*1*) 1; (*2*) 3; (*3*) 5; (*4*) 7; (*5*) 10.

In this work, the surface density of the charges of the HDPE + x vol % $TlGaSe_2$ compositions depending on the additive amounts was investigated. Measurements of the surface density of the charge were performed by the technique described in [5].

The surface density of the electret charge was measured using the induction method with compensation and determined by the equation

$$\sigma_{\text{eff}} = \frac{\varepsilon\varepsilon_0 U_c}{d},$$

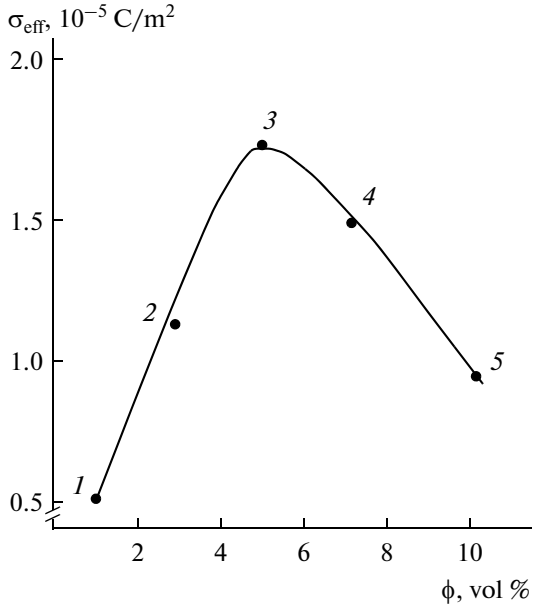

Fig. 3. Dependence of the surface density of the coronoelectret charge from the HDPE + x vol % $TlGaSe_2$ polymer composition (where x equals the following: (*1*) 1; (*2*) 3; (*3*) 5; (*4*) 7; (*5*) 10) on the volume content of the filler.

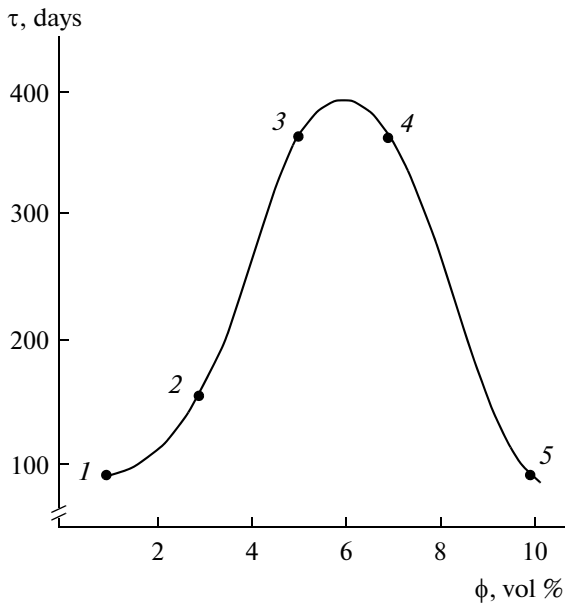

Fig. 4. Dependence of the lifetime of the coronoelectrets from the HDPE + x vol % $TlGaSe_2$ polymer composition (where x equals the following: (*1*) 1; (*2*) 3; (*3*) 5; (*4*) 7; (*5*) 10) on the volume content of the filler.

where σ_{eff} is the surface density of the charge (C/m^2), ε_0 is the electric constant, ε is the dielectric conductivity of the sample, d is the electret sample's thickness (m), and U_c is the compensational voltage (V).

The lifetime was determined by the treatment of the experimental results $\sigma_{eff} = f(t_{xp})$ by the equation

$$\tau = \frac{t_{xp1} - t_{xp2}}{\ln\sigma_2 - \ln\sigma_1},$$

where σ_1 and σ_2 are the surface densities of the charge corresponding to the storage time t_{xp1} and t_{xp2}, respectively.

The obtained results of the investigation of the surface charge density are given in Fig. 2. The figure shows the curves of the charge drop (the dependences of the surface charge's value on the time) for the HDPE + $TlGaSe_2$ samples with the volume ratios of 99 : 1 (curve *1*), 97 : 3 (curve *2*), 95 : 5 (curve *3*), 93 : 7 (curve *4*), and 90 : 10 (curve *5*).

The obtained results of the investigation of the surface charge density of the HDPE + x vol % $TlGaSe_2$ compositions with $x = 1, 3, 5, 7, 10$ are given in Fig. 3. The analysis of these results shows that the optimal value of the surface density of the electret charge is observed at the filler content from 5–7%. At that, the value of the surface charge density σ_{eff} of these compositions is 1.5–2 times higher than for pure oriented 50% hardened HDPE films.

Thus, the lifetime of the investigated coronoelectrets from the HDPE + x vol % $TlGaSe_2$ compositions depending on the $TlGaSe_2$ additive's content is presented in Fig. 4. It follows that the lifetime τ for the charges of the HDPE + x vol % $TlGaSe_2$ compositions is much higher than for pure PE; particularly, for compositions with $x = 1, 3, 5, 7$, and 10, the lifetime is 7, 93, 152, 362, 360, and 92 days, respectively. These results show that the value of the electret charges σ_{eff} and the lifetime τ_{eff} of the electret charges of the HDPE + 5–7 vol % $TlGaSe_2$ compositions are considerably superior with the introduction of the structure forming HDPE $TlGaSe_2$ filler at 5–7 vol % [13] compared to the lifetime of the electret from pure HDPE.

CONCLUSIONS

In this work, the phenomenon of thermostimulated depolarization in HDPE + x vol % $TlGaSe_2$ for compositions with $x = 1, 3, 5, 7, 10, 20$, and 30 in the temperature range of 300–500 K and their electret properties were investigated. It was revealed that the composite materials based on HDPE with a $TlGaSe_2$ filler are promising electret materials with a lifetime considerably superior to the lifetime of HDPE.

REFERENCES

1. Galikhanov, M.F., Eremeev, D.A., and Deberdeey, R.Y., Electret in compounds of polystyrene with aerosil, *Russian Journal of Appl. Chem*, 2003, vol. 76, no. 10, pp. 1651–1654.

2. Trakhtenberg, L.I., Gerasimov, G.N., Potapov, V.K., et al., Nanocomposite metal-polymer films: sensor, catalytic and electrophysical properties, *Vestn. MGU*, 2001, vol. 42, no. 5, pp. 325–331.
3. Sessler, G.M. and Gros, B., And Evolution of Modern Electret Research, *Braz. J. Phys.*, 1999, vol. 29, no. 2, pp. 220–225.
4. *Elektrety* (Electrets), Sesler, G., Ed., Moscow: Mir, 1983, p. 487.
5. Lushcheikin,,G.A., *Polimernye elektrety* (Polymer electrets), Moscow: Khimiya, 1984, p. 184.
6. Magerramov, A.M., *Strukturnoe i radiatsionnoe modifitsirovanie elektretnykh, p'ezoelektricheskikh svoistv polimernykh kompozitov* (Structural a and radiation modification of electret, piezoelectric properties of the polymer composites), Baku: Elm, 2001, p. 327.
7. Abutalybov, G.I., Larionova, L.S., and Ragimova, N.A., Excitons in absorption and photoconductivity of $TlGaSe_2$ monocrystal, *FTT*, 1989, vol. 31, no. 11, pp. 375–377.
8. Bagirzade, E.F. and Aliev, V.S., Photoconductivity induced by electric field in $TlGaSe_2$, *FTT*, 1986, vol. 20, no. 11, pp. 1517–1518.
9. Gorokhovatskii, Yu.A. and Bordovskii, G.A., *Termoaktivatsionnaya tokovaya spektroskopiya vysokoomnykh poluprovodnikov i dielektrikov* (Thermoactivated current spectroscopy of high-resistance semiconductors and dielectrics), Moscow: Nauka, 1991, p. 248.
10. Oshmyak, V.G., Timak, S.G., and Shamaev, M.Yu., Modeling of plastic fracture of polymer blends and composites with consideration of the interphase layer formation, *Vysokomolek. Soed. Ser. A*, 2003, vol. 45, no. 10, pp. 1689–1698 [Pol. Sci. Ser. A, vol. 45, no. 10, pp.].
11. Magerramov, A.M., Sherman, M.Y., Lesnykh, O.D., Kovchagin, A.G., Turyshev, B.I., The Polarization and Piezoelectric Properties of a Vinylidene Fluoride-Tetrafluoroethylene copolymer, *Pol. Sci. Ser. A*, 1988, vol. 40, no. 6, pp. 590–595.
12. Magerramov, A.M., Nuriev, M.A., Veliev, I.A., and Safarova, S.I., Coronoelectrets based on composites of polypropylene dispersed by semiconducting $Tl_xCe_{1-x}Se_2$ filler, *Electron. Treat. Mat.*, 2007, no. 2, pp. 84–88.
13. Zakrevskii, V.A., Pakhotin, Z.A., and Fomin, V.A., USSR Inventor's Certificate no. 734901 (25.05.1980).

ISSN 1068-3755, Surface Engineering and Applied Electrochemistry, 2010, Vol. 46, No. 6, pp. 620–627. © Allerton Press, Inc., 2010.
Original Russian Text © G.P. Gaidar, 2010, published in Elektronnaya Obrabotka Materialov, 2010, No. 6, pp. 97–106.

OPERATING EXPERIENCE

Provision of the Stability of Semiconductor (Nanostructure) System Parameters Against Effective External Disturbances

G. P. Gaidar

Kiev Institute for Nuclear Research, National Academy of Sciences of Ukraine, pr. Nauki 47, Kiev, 03680 Ukraine
e-mail: gaidar@kinr.kiev.ua

Received July 2, 2010

Abstract—The particularities of size and structure of nanoobjects leads to set of specific properties. So, the developed surface determines the increased chemical reactivity; the high level of discontinuity results in lack of lattice constant and disturbance translation symmetry; the size of intrinsic variations of potential on distance, which may be commensurable with inter-atomic distances, prejudices the appropriateness of effective mass method; etc. The presence of huge mechanical stresses and difference of thermal expansion coefficients can stimulates the structure degradation processes under change of temperature conditions. The preventive measures to decrease the rate of degradation processes in the nanostructures will be discussed.

DOI: 10.3103/S1068375510060141

INTRODUCTION

Thermal and radiation stability may be considered among the most important performance characteristics of any semiconductor device, especially when nanostructures or nanoobjects (NObj) being miniature in volume, such as quantum dots (QD) or superlattices (SL), are discussed. The reason is that their use is often related to significant energetic overloads, which may, in turn, lead to local overheating, being a topical problem for the operation of microvolumes of small-scale semiconductor devices or their critical functional parts, such as interphase boundaries and *p*–*n*- or *p*–*i*–*n*-transitions.

Nanoobjects and, particularly, their areas characterized by enhanced resistivity ρ or the presence of heterogeneities, either residual or caused by construction peculiarities, in the spatial distribution $\rho(\vec{r})$ are especially sensitive to the effect of radiation fields [1]. It has to be taken into account when the corresponding NObj is used in the radiation field, which is significantly higher than the background radiation.

As silicon and germanium are among the most thoroughly studied semiconductors, the distinct and unambiguous interpretation of the NObj peculiarities may be acquired when these crystals are the ones under consideration.

The main peculiarities of NObj responsible for their thermal and radiation instability may include the following.

(1) The presence of boundaries between materials with different chemical structures (when talking about SL and heterostructures) and the utmost heterogeneity of the QD by its chemical structure.

(2) Enormous internal (and related to the presence of boundaries) mechanical stresses (~GPa) occur in SL due to certain mismatches of the constant crystal lattices of the materials on the basis of which SL are created or due to the different thermal expansion coefficients of these materials. The presence of mechanical stress gradients in QD is, first of all, related to the heterogeneity of the substance distribution in their volume and the effects of the substrate and medium in which they're grown.

(3) The presence of residual (uncontrolled) impurities of technological origin and Frenkel pairs (vacancies and interstitial atoms), which don't lose their mobility completely even at cryogenic temperatures.

(4) The interaction of electrically low active impurities (such as N, H, and O in Si and Ge) with each other and Frenkel pair elements (in the case of NObj usage, as well as in case of their long-term storage). Such interaction results in the appearance of electrically active complexes, which provide changes not only in the average $\bar{\rho}$ but also in the spatial distribution $\rho(\vec{r})$ of semiconductor materials as well [1].

THE FACTORS THAT PREDETERMINE THE DEVELOPMENT OF THE RADIATION AND THERMAL INSTABILITY OF NANOOBJECTS

Thermal and radiation instability of NObj is predetermined by a series of critical factors including the following:

—the mobility of Frenkel pair components and atoms of background (electrically low active) impuri-

ties under normal conditions and even at lower temperatures (close to cryogenic ones);

—the tendency of Frenkel pair components and electrically low active background impurities to interact with each other (and with dislocation-type defects of the structure) leading to the formation of electrically and recombinationally active centers capable of changing the concentration of both the major and minor charge carriers and their spatial distribution in the microvolumes of NObj;

—the relatively low activation energy levels of the aforementioned interdefect interaction processes; and, moreover,

—the NObj storage regime and usage related to the current passage of significant density through the current conduction channels of the NObj (at atomic and molecular scales), which don't satisfy the condition $T \longrightarrow 0$ K.

The problem of the possible effect of such gases as nitrogen and a mixture of argon and hydrogen (which formed the medium for the crystal growth) on the electrophysical, mechanical, and other properties of Ge and Si crystals raised strong protest and sometimes almost resentment among engineers in the early 1950s, i.e., at the initial development stages of industrial production of the mentioned crystals.

Materials science gathered enormous factual material all over the world in the second half of the XX and the early XXI centuries, which persuasively shows that even hydrogen and nitrogen in volumes of Ge and Si form electrically (or optically) active complexes with their annealing temperatures often higher than 300–600°C with doping impurity atoms and crystals' defects (Frenkel pair components) under certain conditions (especially under high energetic electron, proton, or γ-quantum radiation of crystals). Only the most illustrative examples of such complexes will be selected and presented below with paying attention to their formation conditions as well.

The static and dynamic properties of monoatomic hydrogen dissolved in crystalline silicon in various charge states were quantitatively described for the first time in [2]. These states included H^+, H^0, and H^-, as well as PH complexes (where P represents phosphor atoms), which create an energy level lower than the bottom conduction band by 0.16 eV in the band gap as a response to donor *E*3' centers arising in the case of proton implantation into interstitials of initial single crystals and the acceptor level being lower than the medium band gap by 0.07 eV. The authors state that these theoretical predictions agree with the experimental data.

The authors of [3] investigated theoretically predicted $\{I, H_n\}$ complexes, where *I* represents an interstitial silicon atom and H_n represents several ($1 \le n \le 4$) hydrogen atoms, using infrared spectroscopy. The experimentally studied $\{I, H_n\}$ complex appeared to be the most stable.

When the author of [4] obtained hydrogenised Si by thermal annealing (TA) at 1300°C within an H_2 and/or D_2 medium with further hardening; carried out irradiation of *n*-S⟨P⟩, *p*-Si⟨B⟩, and highly purified Si by electrons with energy of ~3 MeV (at 300 K); and investigated the optical absorption, it was shown that the absorption peaks at 1870 and 2072 cm^{-1} were related to the development of complexes of interstitial atoms (*I*) with H and vacancies (*V*) with H, respectively. In addition, the proportionality of the intensities of both absorption peaks to the square electron irradiation dose (in the low dose area) indicated the structure of these complexes as I_2H_2 and V_2H_2. The peaks at 1870 and 2072 cm^{-1} disappear as a result of the isochronous TA below 200 and 300°C, respectively.

It is also shown [5] that interstitial hydrogen (H_2) forms $O-H_2$ complexes with interstitial oxygen (O). Two closely adjacent lines of $O-H_2$ complexes observed at $T > 10$ K in the infrared absorption spectrum are related to the development of orto- and parahydrogen molecules in these complexes.

The effectiveness of introducing thermal donors (TD-1) by TA of oxygen-containing Si at 450°C after the preceding hydrogenization in hydrogen plasma and γ-irradiation (^{60}Co) is investigated in [6]. These procedures result in atomic hydrogen release from the bound state, which stimulates the introduction of TD-1 in the process of the mentioned TA.

Annealing of divacancies (V_2) in nonhydrogenized Si and hydrogenised Si:H was investigated as well. V_2O complexes are formed in the process of annealing of V_2 in nonhydrogenized Si, while mostly V_2H_2 are formed in the hydrogenised one [7]. Moreover, it is shown in [8] that complex V_2H_2 is a deep trap for electrons; i.e., it acts as an acceptor.

According to [9], the interaction of atomic hydrogen (H) with interstitial palladium atoms (Pd) results in the formation of seven electrically active and at least one electrically passive PdH_4 complex, while the electrically active complexes include different numbers of hydrogen atoms.

The investigation of the effect of additionally implanted electrically inactive impurities C, N, and F on the formation of donor centers (DC) in Si in which erbium (Er) was implanted before showed [10] that the coimplantation of the mentioned impurities (as well as the coimplantation of oxygen impuritys) leads to an increase in the DC concentration and the shift of the DC distribution maximum towards the implanted surface as opposed to the case when only Er is implanted. When the annealing temperature increases, the overall DC concentration falls, and the position of their distribution maximum is shifted deeper into the sample. The results obtained in [11] show that not only Er atoms (and point defects I and V) participate in DC formation but also the implanted electrically low active impurities listed above as well.

The study of the dislocation generation and motion peculiarities in Si⟨N⟩ grown using Czochralski method (Cz) showed [12] that nitrogen doping of Cz–Si leads to a significant increase in the critical voltages of the start of the dislocation motion (τ_{cr}) from the surface sources (indentations) and a decrease in the dislocation motion velocity as opposed to the crystal without nitrogen doping. Moreover, nitrogen doping affects the decay rate of the oxygen solid solution in Cz–Si⟨N⟩ in process of its postcrystallization cooling. The dislocation generation and motion may be reliably observed only at $T \sim 500$–600°C within the shear stress interval of ~30–130 MPa. Nitrogen doping results in strengthening of Cz–Si⟨N⟩ wafers. The most considerable changes in Cz–Si⟨N⟩ are observed when the nitrogen concentration is $\sim 1.6 \times 10^{14}$ cm^{-3}. The value of τ_{cr} becomes twice as high with such a nitrogen doping level (at ~600°C), and the activation energy of the dislocation motion becomes 1.15 times as high as opposed to the crystal without nitrogen doping. The dynamic properties of the dislocations in Cz–Si⟨N⟩ change considerably for a nitrogen concentration of $\sim 10^{14}$ cm^{-3}, while the required concentration of the traditional donor and acceptor impurities for comparable changes in the dislocation dynamics should be three to four orders as high.

The nitrogen concentration distribution $C_N(z)$ after the diffusion from the sample's volume to its surface was obtained by the authors of [13] by further TA at medium temperatures (~650°C). Small nitrogen–oxygen TD generated during the process were distributed by depth according to the $C_N(z)$ profile under any diffusion TA. Given the enhanced oxygen concentration in Cz–Si⟨N⟩, the nitrogen transport is simplified due to the accelerated dissociation of the nitrogen dimmers. On the other hand, the transport is slightly complicated due to the partial oxidation of nitrogen monomers (however, this effect doesn't prevail). Therefore, the diffusion profile is controlled by the combination $D_1K^{1/2}$, where D_1 is the diffusion coefficient for nitrogen monomers, and K is the dissociation constant. Nitrogen dimmers N_2 are practically immobile and dissociate into mobile monomers N, which implement nitrogen transport.

As a result of studying the effect of nitrogen doping on the vacancy aggregation in Si, it was shown [14] that two nitrogen atoms form a stable complex with two vacancies in Si, which leads to the inhibition of the oversaturation of isolated vacancies. This circumstance also complicates the formation of voids in Cz–Si doped by nitrogen impurities. Nitrogen pairs are more stable than single atoms (the degradation energy of a pair N_2 in the interstitial position is 4.3 eV), and, therefore, N_2 pairs are present in Si even at a temperature near its melting point [15].

The study of the growth defects, including oxygen inclusions (OI) in Cz–Si doped by a nitrogen impurity showed [16] that a considerable OI increase in size due to the N_2–V_z–O_x complexes generated at ~1150°C, while small OI appear (and grow) due to N_mO_n complexes generated at 750°C and lower temperatures. It is found that the OI behavior in nitrogen doped crystals of Si was strongly different from the OI behavior in crystals of Si without nitrogen doping, which underwent one-step (at 1050°C for 32 hours) and two-step (at 800°C for four hours and at 1050°C for 16 hours) thermal annealing.

Nitrogen-vacancy complexes in Si are of interest due to their ability to inhibit the formation of large vacancy defects (pores) in the process of single crystal growing [16].

In highly purified crystals of *n*- and *p*-Si, which were freshly grown by floating zone melting (FZ), the nitrogen impurity doesn't show electric activity. However, when these crystals are annealed at rather high temperature (~900 or 1000°C), deeply embedded centers (with concentrations of $\sim 10^{13}$ cm^{-3}) arise in them. A possible reason for the appearance of deep centers is the interaction of well diffusing interstitial nitrogen centers with other impurity atoms [17].

The effect of annealing at 720–920 K under the enhanced pressure (up to 1.4 GPa) in an argon medium on the electric properties of the urface layer in Cz–Si and FZ-Si crystals doped by a nitrogen impurity (up to concentrations of $\sim 10^{14}$–10^{15} cm^{-3}) and germanium doped Cz–Si (up to 7×10^{17} cm^{-3}) was investigated in [18]. In addition, decreases in the electron concentration in Cz–Si⟨N⟩ annealed at 720 K under normal pressure were discovered. The pressure induced growth of n_e in Cz–Si⟨N⟩ didn't depend on the nitrogen doping level within the interval of 10^{14}–5×10^{14} cm^{-3}. Even given a high nitrogen doping level ($\sim 5 \times 10^{15}$ cm^{-3}), no changes of n_e occurred under the hydrostatic pressure in the crystals of FZ-Si⟨N⟩. A sharp acceleration of the thermal donor generation was observed in germanium doped Cz-Si under the pressure of ~1.1 GPa. The authors explain the investigated effects by the development of oxygen-nitrogen complexes in Cz–Si⟨N⟩ and the generation of TD in nitrogen and germanium doped silicon stimulated by the hydrostatic pressure.

Shallow embedded donor centers (such as NO_3) are investigated in [19].

NO_n complexes in crystals of Si remain poorly investigated in contrast to N_2O_m complexes. The authors of [20] consider that NO_2 complexes are actually responsible for the experimentally observed absorption lines at 1002, 973, and 855 cm^{-1}.

The energetically deepest donor center among the nitrogen-oxygen inclusions in Si crystals has the structure NO. Other (energetically shallower) centers may include up to three oxygen atoms [21].

Nitrogen, hydrogen, and oxygen impurities in silicon are considered in detail due to their technological importance.

POSSIBILITIES FOR RAISING THE RADIATION AND THERMAL STABILITY OF NANOOBJECTS THROUGH THE OPTIMAL SELECTION OF THE USAGE CONDITIONS

By no means all the aforementioned factors, which predetermine the development of the radiation and thermal instability of NObj, may be eliminated or even minimized. However, with these factors recognized, it is necessary to do everything possible to reduce their negative effect on NObj properties to a minimum.

We leave aside the trivial requirements on the substrate temperature reduction (when talking about molecular beam epitaxy) to avoid possible chaos in the spatial distribution of the doping (and residual) impurities and ensure their spatial changes under the known physical laws, etc. Instead, we focus on those hidden possibilities for improvement in the situation when positive results in the thermal and radiation stability enhancement of NObj may only be reached due to the optimal selection of the usage conditions under which the corresponding NObj will be exploited considering the physically justified selection of its certain construction peculiarities. It will be demonstrated by several specific examples.

Frenkel pair components (V and I) are rather mobile in Si even at temperatures close to cryogenic ones, and their effective interaction with electrically active impurities under usage conditions (generally, strongly different from $T \longrightarrow 0$ K) results in the thermal instability of nanoobjects. On the other hand, it is known [22] that the energy of the vacancy generation in the presence of hydrogen atoms in Si may be changed by a value of 1.8 to 3.5 eV, while the same parameter for divacancies varies from 2 to 5.4 eV. However, the presence of hydrogen atoms in Si makes it less sensitive to pressure and may completely suppress the tendency for the generation of additional vacancies in the case of significant concentrations, which will make the material (or a device on its basis) more thermally stable.

It is shown in [23] that lead, as opposed to other isovalent impurities in Si, doesn't participate directly in the generation of electrically active radiation defects. However, lead doping of silicon results in the inhibited accumulation of the main radiation defect in silicon, namely, a VO complex (*A*-centers), and the inhibited accumulation of radiation defects (7–13 times as low for C_iC_s and 20–25% as low for VO) under electron irradiation. Furthermore, lead doping of silicon increases the lifetime of the minor charge carriers while having no considerable effect on the current carrier scattering. All these results may be used to increase the radiation stability of silicon-based NObj as is shown in [23].

Finally, the mechanical stresses are perhaps the most critical reserve, which isn't used in nanotechnology to its full potential. First, the mechanical stresses (~GPa) can't be technically eliminated when working with heterostructures. Second, the change of the zone structure (at least in multivalley semiconductors) under oriented stresses is rather thoroughly studied both theoretically and experimentally [24, 25], which favors the problem statement of their practical application in nanotechnology. It will be demonstrated by the example for superlattices, which include layers with various band gap widths. Considering that the lateral tension of layers based on multivalley semiconductors results in compression along the normal direction towards them (and vice versa), pairs for layers should necessarily be selected solely to make conditions for the electric current passage along the SL axis (along the normal line towards the layers) better.

The authors of [26] showed that the increase in the electron irradiation temperature ($E = 2$ MeV with the intensity of $5–10^{12}$ cm^{-2}s^{-1}) within the interval of 20–400°C raises the effectiveness of introducing multivacation phosphor- or oxygen-containing radiation defects. It may, in turn, lead to an increase in the radiation stability of *n*–Si, as soon as two to three times as many unbalanced vacancies are spent for the generation of PV_2, V_2O, V_2O_2, and V_3O complexes, as in the case of the generation of *E*- or *A*-centers.

The radiation stability of Si is increased through doping by an Sn impurity due to the formation of SNC [27] complexes and through doping of silicon grown by the Czochralski method by a germanium impurity [28].

It follows from the results presented in [29] that there is a possibility of increasing the radiation stability of Cz–Si by several times due to short TA (~1 hour) at 450°C.

The authors of [30] investigated the radiation stability of crystals of *p*–Si ($n_p \approx 3 \times 10^{12}$ cm^{-3}) and *n*-Si ($n_e \approx 2 \times 10^{12}$ cm^{-3}) grown by floating zone melting and showed that *p*-Si was more radiation stable than *n*-Si under the same conditions.

It was found possible to increase the hermal stability of Cz–Si through dissolved oxygen (or vacancy) binding in crystal by a nitrogen impurity introduced into the crystal [31, 32] or by a phosphor doping impurity in the case of vacancies [33].

The main defects and conditions for their development in silicon grown by different methods (the Czochralsi method (CZ) and the loating zone method (FZ)) are presented in the table composed on the basis of data from literature sources [8, 10, 34–45]. Not only the roles of the most important elements (nitrogen, hydrogen, and oxygen) in silicon may be judged based on the data from the table but also the contributions of other electrically low active impurities.

Thermal annealing may be analyzed most reliably using equations that are similar to the ones applied in chemical kinetics. The annealing of each defect (or structural change accompanied by a change of the concentration) independently from the others is a decisive characteristic of first order TA. Vacancy-type defects are annealed in the process of the annihilation

Defects in the irradiated crystals of Cz–Si and FZ–Si

No.	Energetic position, eV	Irradiated material	Energy of particles of g-quants, MeV	Type of defect(-s), and their concentration	Annealing temperature	Reference
1	$E_c - 0.30$	p-Si⟨B⟩ ⟶ converted into n-Si under irradiation	Electrons with $E \sim 1$ MeV, dose $\sim 10^{17}$ cm^{-2}	N_{RD} (for radiation defect) $\cong 1.5 \times 10^{14}$ cm^{-3} N_V (for vacancy) $\approx 9.5 \times 10^{13}$ cm^{-3}		[34]
2	$E_c - 0.29 \pm 0.01$ $E_c - 0.61 \pm 0.02$	Cz n-Si⟨Sn⟩	Protons with $E = 61$ MeV		These traps for e^- dissociate at $T < 120$°C	[35]
3	$E_c - 0.214$ $E_c - 0.501$	FZ n-Si⟨Sn⟩ $N_{Sn} \sim 10^{18}$ cm^{-2}	Electrons with $E \sim 2$ MeV	SnV		[36]
4	$E_c - 0.17$ $E_c - (0.30 \pm 0.16)$ $E_c - (0.19 \pm 0.20)$	n-Si	γ-quants of ^{60}C	VO C_iO_i		[37]
5	Deep traps for carriers	Si		V_2H_2–acceptor V_2H–amphoteric		[8]
6		Highly purified n-Si	Ion implantation of Er^+ and O^+ with further TA	ErO_n $n \geq 4$		[10]
7	$E_c - 0.06$ acceptor	Cz n-Si		VO_2–bistable VO_2^* –metastable		[38]
8	$E_c - 0.11$ $E_c - 0.13$ $E_c - 0.18$ } in n-Si $E_V + 0.43$ $E_V + 0.24$ $E_V + 0.36$ $E_V + 0.53$ } in p-Si	Cz p-Si⟨P⟩ Cz p-Si⟨B⟩	β-particles of low intensity: with $E = 0.20$ Mev and $E = 0.93$ MeV	C_i, C_iC_s and/or VO in n-Si V, B, C_iC_i, V_2OC in p-Si		[39]
9	$E_V + 0.22$	Cz p-Si⟨B⟩	Electron irradiation with $E = 8$ MeV at 300 K	Annealing of V_2 leads to the formation of B_SV_2	Within the interval of (360–440°C)	[40]
10	$E_V + 0.16$ $E_V + 0.21$ $E_V + 0.27$ $E_V + 0.31$	Cz n-Si	High-speed electrons $T_{irr} = 340$–770 K	VO_2		[41]
11	$E_c - (0.21 \pm 0.27)$	n-Si⟨Er⟩ p-Si	Electron irradiation			[42]
12	$E_c - 0.25$	Cz p-Si⟨B⟩ $6 \times 10^{13} \leq N_B \leq 2 \times 10^{15}$		B_iO_i	~175°C	[43]
13		Irradiation of (100) Si by ions of Si^+	Ions of Si^+: with $E = 20$ keV, dose $\sim 10^{14}$ cm^{-2}	BSi_i	The first TA at 815°C for five minutes. Complexes develop after the repeated TA at 815 and 1000°C for the time from 10 seconds to 16 hours	[44]
14	$E_c - 0.45$ $E_c - 0.37$ $E_V + 0.23$	Hydrogenized n–Si⟨P⟩	Electron irradiation e^- with $E = 6$ MeV, dose 5×10^{12} cm^{-2}	VO, V_2, C_iO_i; $VO + H_x \longrightarrow VOH_x$; $V_2 + H_x \longrightarrow V_2H_x$		[45]

with mobile interstitial defects having a migration energy depending on their charge state [46].

The disappearance of the P_i property determined by the concentration of the radiation defects (RD) as a result of the first order TA may be defined using the velocity constant K_i from the relationship

$$\frac{dP_i}{dt} = -K_i P^j. \quad (1)$$

The appearance of the property P^j determined by the concentration of defects (up to the maximum value P^j_m) may be defined using the velocity constant K_j, respectively:

$$\frac{dP^j}{dt} + K_j(P^j - P^j_m) = 0. \quad (2)$$

Generally, the velocity constant (in the case of several TA channels) is $K_{i,j} = A^{i,j}\exp(-E^{i,j}_a/kT)$, where $A^{i,j}$ represents the frequency factors; $E^{i,j}_a$ represents the process's activation energies; k is the Boltzmann constant; T is the absolute temperature; and i, j represent the number of annealing and defect accumulation channels, respectively.

VO and V_2 RD are stable and low mobile at room temperature, when I and I_2 are already mobile. VO and V_2 become mobile at higher temperatures and move to sinks (O_i, C_s).

When we integrate (1) and (2) (considering the different channels of isothermal annealing or accumulation of the property defined by the concentration of defects), we obtain a change in this property depending on the annealing time in the form of the following relationship:

$$P(t) = \sum_{i=1}^{k} P^j_0 \exp[-A^i t \exp(-E^i_a/kT)] + \sum_{j=1}^{m} P^j_m \exp[1 - \exp(-A^j t \exp(-E^j_a/kT))] - \sum_{l=1}^{n} P^l_{00}. \quad (3)$$

Item P^l_{00} is caused by the fact that the annealing process occurs not completely. Here, P^j_0 is the share of annealing of the property defined by the concentration of defects in the ith way; P^j_m is the share of the accumulation of the property defined by the concentration of defects in the jth way; and t represents the annealing time. For example, such defect accumulation is possible due to the dissociation of other defects with lower the annealing temperature. Different ways of annealing are implemented through the defect's annihilation with interstitial atoms or diinterstitial in the process of the capture at sinks or defect dissociation, or when the energy and frequency factor of the defect's annealing change under condition of its reorientation.

A coherent theory of diffusion-controlled reactions in solids was developed in [47]. The case of atoms with different diffusion coefficients in solids participating in quasi-chemical interactions was considered in this paper. Only one component in the interacting pairs is mobile in our case.

If the frequency of the mobile defect jumps ν is known, then the frequency factor D_0 may be evaluated using the relationship $D_0 = (2a^2\nu)/3\pi$, where $a = 5.43$ Å is the silicon lattice constant. If it is impossible to define the frequency of the mobile defect jumps ν but sink concentration N_s is known, then the frequency factor D_0 may be obtained using the expression

$$D = \frac{1}{t}\left(\frac{3}{4\pi N_{Cm}}\right)^{2/3}, \quad (4)$$

where t is the annealing time, as soon as $D = D_0\exp(-E_a/kT)$ at the temperature of 50% of the defects under isochronous annealing and at the moment of 50% under isothermal annealing. The annealing activation energy should be set equal to the diffusion activation energy for mobile defects. It is assumed in this case that the mobile defects move an average distance to the sink, which is equal to the sink's atomic radius ($L = Ra$) at the maximum annealing speed. The radiuses of the radiation defects capture (including vacancies, divacancies, A-centers, etc.) by the interstitial oxygen and nodal carbon fit in the interval of 3–4 silicon lattice constants according to estimations from [48] (see the table in the cited paper). It should be considered that the deformation fields of the defect clusters reduce the annealing energy of the A-centers in the conduction matrix n-Si irradiated by high-speed (reactor) neutrons.

CONCLUSIONS

(1) As a matter of fact, the distribution of the substance in nanoobjects (such as heterostructures, thin films, and quantum dots) can't be uniform, which states the upper limit of the operating temperatures and their reliable lifetime (due to the diffusion processes). It should necessarily be taken into account in the case of using nanoscale heterosystems in critical components of state-of-the-art electronic devices.

(2) The main peculiarities of nanoobjects that cause their thermal and radiation instability are considered. These peculiarities should necessarily be taken into account to provide reliable operation under the usage conditions (which are often complicated).

(3) When heterostructures and quantum dots (for example, germanium on a silicon substrate or vice versa) are used, the operating temperature range is to be selected considering the significant differences in the thermal expansion coefficients of the different materials, which leads to the inevitable growth of the

internal mechanical stresses and all the consequences that come with it.

ACKNOWLEDGMENTS

The author thanks Professor P.I. Baranskii for his interest and useful discussions.

REFERENCES

1. Baranskii, P.I. and Semenyuk, A.K., Resistivity Gradient Variation in *n*- and *p*-Ge under γ-Irradiation, *Fiz. Tekh. Polupr.*, 1967, vol. 1, no. 8, pp. 1150–1154.
2. Herring, C., Johnson, N.M., and van de Walle, C.G., Energy Levels of Isolated Hydrogen in Si, *Phys. Rev. B.*, 2001, vol. 64, p. 125209 (27).
3. Gharaiben, M., Estreicher, S.K., Fedders, P.A., and Ordejón, P., Self-Interstitial-Hydrogen Complexes in Si, *Phys. Rev. B.*, 2001, vol. 64, p. 235211 (7).
4. Suezawa, M., Formation of Defect Complexes by Electron-Irradiation of Hydrogenated Crystalline Silicon, *Phys. Rev. B.*, 2000, vol. 63, p. 035201 (7).
5. Chen, E.E., Stavola, M., and Fowler, W.B., *Orto*- and *Para* O-H_2 Complexes in Silicon, *Phys. Rev. B.*, 2002, vol. 65, p. 245208 (9).
6. Bolotov, V.V., Kamaev, G.N., Noskov, A.V., Chernyaev, S.A., and Roslikov, V.E., The Effect of Hydrogen State in Lattice on the Effectiveness of Donor Center Introduction in Oxygen-Containing Si, *Fiz. Tekh. Polupr.*, 2006, vol. 40, no. 2, pp. 129–132.
7. Monakhov, E.V., Ulyashin, A., Alfieri, G., Kuznetsov, A.Yu., Avset, B.S., and Svensson, B.G., Divacancy Annealing in Si, *Phys. Rev. B.*, 2004, vol. 69, p. 153202 (4).
8. Coutinho, J., Torres, V.J.B., Jones, R., Öberg, S., and Briddon, P.R., Electronic Structure of Divacancy-Hydrogen Complexes in Silicon, *J. Phys. Cond. Mat.*, 2003, vol. 15, pp. S2809–S2814.
9. Sachse, J.U., Weber, J., and Lemke, H., Deep-Level Transient Spectroscopy of Pd-H-Complexes in Silicon, *Phys. Rev. B.*, 2000, vol. 61, pp. 1924–1934.
10. Aleksandrov, O.V., Zakhar'in, A.O., Sobolev, N.A., and Nikolaev, Yu.A., The Effect of Electrically Inactive Impurities on Donor Center Formation in Layers of Si with Implanted Erbium, *Fiz. Tekh. Polupr.*, 2000, vol. 34, no. 5, pp. 526–529.
11. Voronkov, V.V., Voronkova, G.I., Batunina, A.V., Golovina, V.N., Arapkina, L.V., Tyurina, N.B., Gulyaeva, A.S., and Mil'vidskii, M.G., Small Thermal Donors in Nitrogen-Doped Single Crystals of Silicon, *Fiz. Tverd. Tela*, 2002, vol. 44, no. 4, pp. 700–704.
12. Mezhennyi, M.V., Mil'vidskii, M.G., and Reznik, V.Ya., Peculiarities of Dislocation Generation and Motion in Nitrogen-Doped Single Crystals of Silicon, *Fiz. Tverd. Tela*, 2002, vol. 44, no. 7, pp. 1224–1229.
13. Voronkov, V.V., Batunina, A.V., Voronkova, G.I., and Mil'vidskii, M.G., Generation of Small Nitrogen-Oxygen Donors as a Method of Nitrogen Diffusion Investigation in Silicon, *Fiz. Tverd. Tela*, 2004, vol. 46, no. 7, pp. 1174–1179.
14. Kageshima, H., Taguchi, A., and Wada, K., Theoretical Investigation of Nitrogen-Doping Effect on Vacancy Aggregation Processes in Si, *Appl. Phys. Lett.*, 2000, vol. 76, no. 25, pp. 3718–3720.
15. Sawada, H. and Kawakami, K., First-Principles Calculation of the Interaction between Nitrogen Atoms and Vacancies in Silicon, *Phys. Rev. B.*, 2000, vol. 62, pp. 1851–1858.
16. Jones, R., Hahn, I., Goss, J.P., Briddon, P.R., and Öberg, S., Structure and Electronic Properties of Nitrogen Defects in Silicon, *Solid State Phen.*, 2004, vols. 95–96, pp. 93–98.
17. Voronkova, G.I., Batunina, A.V., Moiraghi, L., Voronkov, V.V., Falster, R., and Mil'vidskii, M.G., Deep Level Generation in Nitrogen-Doped Float-Zoned Silicon, *Nucl. Instrum. and Meth. in Phys. Res. B.*, 2006, vol. 253, pp. 217–221.
18. Jung, W., Misiuk, A., and Yang, D., Effect of High Pressure Annealing on Electrical Properties of Nitrogen and Germanium Doped Silicon, *Nucl. Instrum. and Meth. in Phys. Res. B.*, 2006, vol. 253, pp. 214–216.
19. Wagner, H.E., Alt, H.Ch., Ammon, W.v., Bittersberger, F., Huber, A., and Koester, L., N-O Related Shallow Donors in Silicon: Stoichiometry Investigations, *Appl. Phys. Lett.*, 2007, vol. 91, p. 152102 (3).
20. Fujita, N., Jones, R., Öberg, S., and Briddon, P.R., First-Principles Study on the Local Vibrational Modes of Nitrogen-Oxygen Defects in Silicon, *Phys. B Cond. Mat.*, 2007, vols. 401–402, pp. 159–162.
21. Alt, H.Ch., Wagner, H.E., Ammon, W.v., Bittersberger, F., Huber, A., and Koester, L., Chemical Composition of Nitrogen-Oxygen Shallow Donor Complexes in Silicon, *Phys. B Cond. Mat.*, 2007, vols. 401–402, pp. 130–133.
22. Zavodinskii, V.G., Gnidenko, A.A., Misyuk, A., and Bak–Misyuk, Ya., The Effect of Pressure and Hydrogen on Generation of Vacancies and Divacancies in Crystalline Silicon, *Fiz. Tekh. Polupr.*, 2004, vol. 38, no. 11, pp. 1281–1284.
23. Voitovich, V.V., *Cand. Sci. Dissertation*, Kiev, 2005.
24. *Elektricheskie i gal'vanomagnitnye yavleniya v anizotropnykh poluprovodnikakh* (Electric and Galvanomagnetic Phenomena in Anisotropic Semiconductors), Baranskii, P.I., Ed., Kiev: Naukova dumka, 1977.
25. Baranskii, P.I., Nontraditional Piezoresistance Mechanisms in Single-Axis Deformed Multivalley Semiconductors, *Neorg. mater.*, 1997, vol. 33, no. 2, pp. 147–152.
26. Pagava, T.A., The Effect of Irradiation Temperature on Effectiveness of Introduction of Multivacancy Defects in *n*-Si Crystals, *Fiz. Tekh. Polupr.*, 2006, vol. 40, no. 8, pp. 919–921.
27. Lavrov, E.V., Fanciulli, M., Kaukonen, M., Jones, R., and Briddon, P.R., Carbon-Tin Defects in Silicon, *Phys. Rev. B.*, 2001, vol. 64, p. 125212 (5).
28. Dolgolenko, A.P., Gaidar, G.P., Varentsov, M.D., and Litovchenko, P.G., Germanium Impurity Effect on Radiation Stability of Silicon with High Hydrogen Concentration, *Vopr. Atom. Nauki Tekh. Ser. Fiz. Rad. Povrezhd. Rad. Mater.*, 2008, vol. 2, pp. 28–36.
29. Korshunov, F.P., Marchenko, I.G., and Zhdanovich, N.E., Electron Irradiation Induced Changes of Electric

Parameters of Structures with p-n Transitions on Strained Silicon after Preliminary Thermal Annealing at 400–550°C, in *Dokl. Mezhdunarod. konf. "Aktual'nye problemy fiziki tverdogo tela"* (Proc. Int. Conf. "Topical Problems of Solid State Physics"), Minsk: BGU, 2007, vol. 2., pp. 52–55.

30. Dolgolenko, A.P., Varentsov, M.D., Gaidar, G.P., and Litovchenko, P.G., Dependence of the Defect Introduction Rate on the Dose of Irradiation of p Si by Fast-Pile Neutrons, *Semicond. Phys. Quant. Electron. Optoelectron*, 2007, vol. 10, no. 4, pp. 9–14.
31. Yang, D.R., Wang, H.J., Yu, X., Ma, X.Y., and Que, D.L., Thermal Stability of Oxygen Precipitates in Nitrogen-Doped Czochralski Silicon, *Solid State Phen.*, 2004, vols. 95–96, pp. 111–116.
32. Karoui, F.S., Karoui, A., Rozgonyi, G.A., Hourai, M., and Sueoka, K., Characterization of Nucleation Sites in Nitrogen Doped Czochralski Silicon by Density Functional Theory and Molecular Mechanics, *Solid State Phen.*, 2004, vols. 95–96, pp. 99–104.
33. Peaker, A.R., Markevich, V.P., Auret, F.D., Dobaczewski, L., and Abrosimov, N., The Vacancy-Donor Pair in Unstrained Si, Ge, and SiGe Alloys, *J. Phys. Cond. Mat.*, 2005, vol. 17, no. 22, pp. S2293–S2302.
34. Matsuura, H., Uchida, Y., Nagai, N., Hisamatsu, T., Aburaya, T., and Matsuda, S., Temperature Dependence of Electron Concentration in Type-Converted Silicon by 1×10^{17} cm^{-2} Fluence Irradiation of 1 MeV Electrons, *Appl. Phys. Lett.*, 2000, vol. 76, no. 15, pp. 2092–2094.
35. Simoen, E., Claeys, C., Neimash, V.B., Kraitchinskii, A., Krasko, N., Puzenko, O., Blondeel, A., and Clauws, P., Deep Levels in High-Energy Proton-Irradiated Tin-Doped *n*-Type Cz–Si, *Appl. Phys. Lett.*, 2000, vol. 76, no. 20, pp. 2838–2840.
36. Larsen, A.N., Goubet, J.J., Mejlholm, P., Sherman Christensen, J., Fanciulli, M., Gunnlaugsson, H.P., Weyer, G., Petersen, J.W., Resende, A., Kaukonen, M., Jones, R., Öberg, S., Briddon, P.R., Svensson, B.G., Lindström, J.L., and Dannefaer, S., Tin-Vacancy Acceptor Levels in Electron Irradiated n-Type Silicon, *Phys. Rev. B.*, 2000, vol. 62, pp. 4535–4544.
37. Makarenko, L.F., Re-Evaluation of Energy Levels of Oxygen-Vacancy Complex in *n*-Type Silicon Crystals: I. Weak Compensation, *Semicond. Sci. and Technol.*, 2001, vol. 16, no. 7, pp. 619–630.
38. Murin, L.I., Markevich, V.P., Medvedeva, I.F., and Dobaczewski, L., Bistability and Electric Activity of Complex Consisting of Vacancy and Two Oxygen Atoms in Si, *Fiz. Tekh. Polupr.*, 2006, vol. 40, no. 11, pp. 1316–1320.
39. Badylevich, M.V., Blokhin, I.V., Golovin, Yu.I., Dmitrievskii, A.A., Kartsev, S.V., Suchkova, N.Yu., and Tolotaev, M.Yu., Nonmonotonic Changes in Concentration of Donor and Acceptor Radiation Defects in Si Induced by Fluxes of β-Particles with Low Intensities, *Fiz. Tekh. Polupr.*, 2006, vol. 40, no. 12, pp. 1409–1411.
40. Pagava, T.A., Peculiarities of Radiation Defect Annealing in Irradiated *p*-Si Crystals, *Fiz. Tekh. Polupr.*, 2007, vol. 41, no. 6, pp. 651–653.
41. Korshunov, F.P., Bogatyrev, Yu.V., Murin, L.I., Markevich, V.P., and Lastovskii, S.B., Radiation Defects with Deep Levels in Silicon *p–n*-Structures Irradiated by High-Speed Electrons at 340–770 K, in *Dokl. Mezhdunarod. konf. "Aktual'nye problemy fiziki tverdogo tela"* (Proc. Int. Conf. "Topical Problems of Solid State Physics"), Minsk: BGU, 2007, vol. 2., pp. 56–58.
42. Belova, O.V., Shabanov, V.N., Kasatkin, A.L., Kuznetsov, O.A., Yablonskii, A.N., Kuznetsov, M.V., Kuznetsov, V.P., Kornaukhov, A.V., Andreev, B.A., and Krasil'nik, Z.F., Electrophysical Properties of Si⟨Er⟩/Si Layers Grown by Sublimation Molecular Beam Epitaxy, *Fiz. Tekh. Polupr.*, 2008, vol. 42, no. 2, pp. 136–140.
43. Vines, L., Monakhov, E.V., Kusnetsov, A.Yu., Kozłowski, R., Kaminski, P., and Svensson, B.G., Formation and Origin of Dominating Electron Trap in Irradiated *p*-Type Si, *Phys. Rev. B.*, 2008, vol. 77, no. 8, p. 085205 (7).
44. Boninelli, S., Mirabella, S., Bruno, E., Priolo, F., Cristiano, F., Claverie, A., De Salvador, D., Bisognin, G., and Napolitani, E., Evolution of Born-Interstitial Clusters in Crystalline Si Studied by Transmission Electron Microscopy, *Appl. Phys. Lett.*, 2007, vol. 91, no. 3, p. 031905 (3).
45. Bleka, J.H., Pintilie, I., Monakhov, E.V., Avset, B.S., and Svensson, B.G., Rapid Annealing of the Vacancy-Oxygen Center and the Divacancy Center by Diffusing Hydrogen in Silicon, *Phys. Rev. B.*, 2008, vol. 77, no. 7, p. 073206 (4).
46. Kimerling, L.C., Blood, P., and Gibson, W.M., Defect States in Proton-Bombarded Silicon at $T < 300$ K, *Proc. Conf. "Defects and Radiation Effects in Semiconductors"*, London, 1979, pp. 273–280.
47. Waite, T.R., Theoretical Treatment of the Kinetics of Diffusion-Limited Reactions, *Phys. Rev.*, 1957, vol. 107, no. 2, pp. 463–470.
48. Gaidar, G.P., Dolgolenko, A.P., and Litovchenko, P.G., *Ukr. Fiz. Zh.*, 2008, vol. 53, no. 7, pp. 691–696.

ISSN 1068-3755, Surface Engineering and Applied Electrochemistry, 2010, Vol. 46, No. 6, pp. 628–631. © Allerton Press, Inc., 2010.
Original Russian Text © V.F. Zhitar, V.I. Pavlenko, T.D. Shemyakova, 2010, published in Elektronnaya Obrabotka Materialov, 2010, No. 6, pp. 107–111.

OPERATING EXPERIENCE

Anisotropy of Optical Transmission and Photoluminescence in $ZnIn_2S_4$ and $ZnIn_2S_4$:Cu Single Crystals

V. F. Zhitar, V. I. Pavlenko, and T. D. Shemyakova

Institute of Applied Physics, Academy of Sciences of Moldova,
ul. Akademiei 5, Chisinau, MD-2028 Republic of Moldova
e-mail: shemyakova@yahoo.com

Received July 27, 2010

Abstract—Significant anisotropy of the optical transmission associated with the exponential increasing of the absorption coefficient and the anisotropy of the photoluminescence were found in $ZnIn_2S_4$ and $ZnIn_2S_4$:Cu single crystals. It was shown that the peculiarities of the investigated photoluminescence spectra are associated with optical transitions involving donor and acceptor levels. The possibility was found to control the spectra's shape and intensity using doping and variation of the technological parameters to allow preparing $ZnIn_2S_4$ single crystals with alternation of three and one packet polytypes.

DOI: 10.3103/S1068375510060153

INTRODUCTION

The wide-gap ternary semiconductor compound $ZnIn_2S_4$ forms layered crystals that refer to a hexagonal-rhombohedral structure with the space group R3m [1, 2]. This material is promising for application in optoelectronics. UV sensors, electrochemical solar cells, and other devices have been proposed on the basis of this material [3, 4]. Recently, recombination properties of $ZnIn_2S_4$ single crystals activated by doping with high Cu concentrations were reported [5]. It was shown that copper impurities, similar to ZnSe:Cu, substantially enhance the efficiency of red radiation [6]. The main optical properties of undoped platelet crystals were studied and described earlier and are summarized in [2]. The layered structure and polarity of the multilayer packages should lead to a dependence of the physical characteristics of the material on the crystallographic directions. Taking this into account, one can expect that the compound should exhibit a pronounced anisotropy of its physical properties.

Judging by the publications, the study of optical anisotropy attracts the special attention of researchers. An overview of the recent studies of optical anisotropy in heterostructures with quantum wells, quantum wires, and quantum dots based on ZnSe/BeTe semiconductors with a cubic structure is provided in [7]. It is also known that, in layered semiconductors such as GaSe, the luminescent properties strongly depend on the structural disorder of the lattice layers [8]. In particular, it was suggested that the three bands in the GaSe photoluminescence spectrum could be ascribed to the three crystal modifications of this material [9].

The above gives evidence that the study of the anisotropy of the optical transmission and photoluminescence (PL) in $ZnIn_2S_4$ single crystals with a polymorph structure is an interesting research problem. In the given paper, the results are presented of investigations of the photoluminescence spectra in single crystals undoped and activated by doping with copper $ZnIn_2S_4$.

EXPERIMENTAL

The undoped and doped with copper $ZnIn_2S_4$ single crystals were grown using a method of chemical transport reactions with iodine as the transport agent. In the initial load, especially pure chemical elements were used; hyperstoichiometric copper was introduced in a quantity of 1.6 at %. The growth regimes were studied earlier and are summarized in [2]. The doped samples were mirror-like platelets of darker color if compared with the undoped crystals.

The PL spectra were registered under the excitation of the samples by a monochromatic LGI-21 N_2 laser ($\lambda = 337.1$ nm). The radiation from the single crystals was registered using an OVA-284 analyzer at a temperature of 20°C. The spectral resolution of the installation was 21 nm. The method is described in detail in [10]. As differs from [5], in this work, the excitation was performed from the face (0001) or from the end face as is schematically shown in Fig. 1. The C axis of the monocrystal is perpendicular to the face (0001). The measurements were carried out at room termperature on platelets with different thicknesses of 40, 100, and 150 μm. The spectra of the optical transmission T were registered using the same installation with a film polarizer inserted before or after the sample.

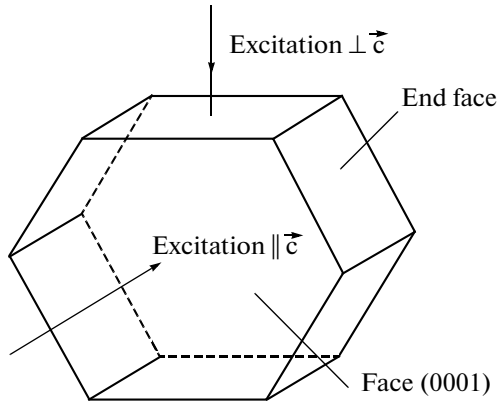

Fig. 1. Scheme of the geometry of the experiment for the registration of the $ZnIn_2S_4$ PL spectra.

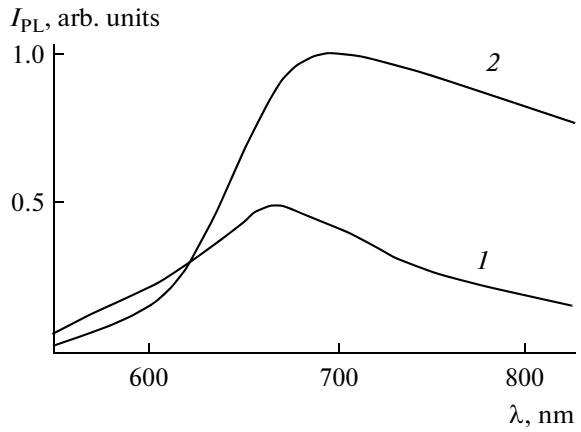

Fig. 2. PL spectra of $ZnIn_2S_4$ single crystals at room temperature. (*1*) Excitation from the end face; (2) excitation from the face (0001). The sample's thickness is $d = 100$ μm.

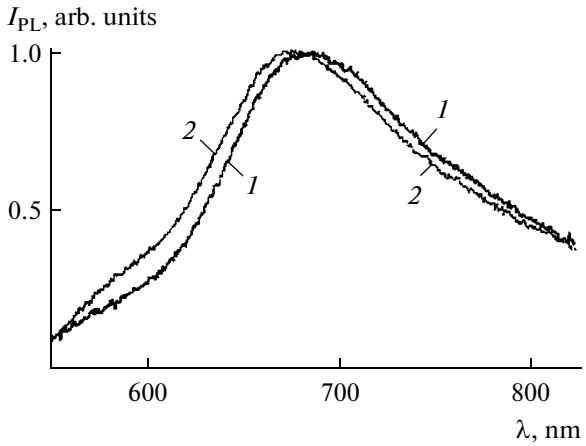

Fig. 3. PL spectra of single $ZnIn_2S_4$:Cu crystals at room temperature. (*1*) Excitation from the end face; (*2*) excitation from the (0001) face. The sample's thickness is $d =$ 150 μm.

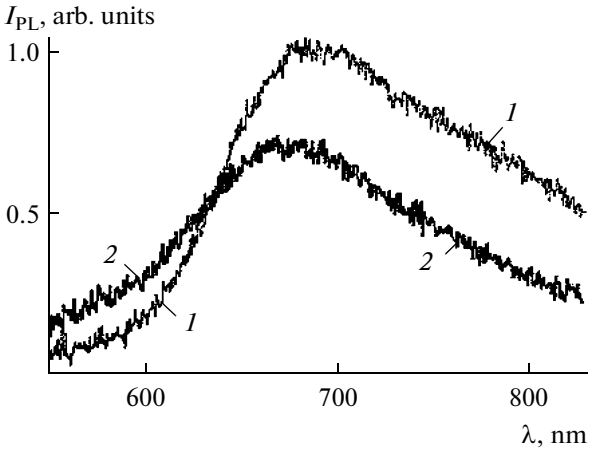

Fig. 4. PL spectra of $ZnIn_2S_4$:Cu single crystals at room temperature. (*1*) Excitation from the end face; (*2*) excitation from the (0001) face. The sample's thickness is $d =$ 40 μm.

RESULTS AND DISCUSSION

The PL spectra of the undoped $ZnIn_2S_4$ samples measured at room temperature are shown in Fig. 2. The spectra obtained under the laser excitation ($\lambda = 337.1$ nm) from the end face and from the (0001) face contain one wide band centered at 668 (curve *1*) and 682 nm (curve *2*), respectively. The halfwidth of the band measured from the end face $\Delta h\nu = 0.4$ eV. The anisotropic shift (AS) amounted to $\Delta\lambda = 14$ nm. The spectra of the X-ray induced luminescence in this material registered from the face showed a maximum at 775 nm with $\Delta h\nu = 0.46$ eV and a plateau at 710 nm [11].

Figure 3 shows the typical PL spectral characteristics for $ZnIn_2S_4$ single crystals doped with copper. At room temperature, they exhibit a wide band centered at 673.9 nm under the excitation from the end face and centered at 682.6 nm under the excitation from the face (0001). The anisotropic shift $\Delta\lambda$ amounted to 8.7 nm; $\Delta h\nu = 0.4$ eV for both these cases.

The PL spectra of a thin sample are shown in Fig. 4. They contain a wide band centered at 677.6 and 691.4 nm under the excitation from the end face and from the (0001) face, respectively. The AS $\Delta\lambda$ amounted to 13.8 nm; $\Delta h\nu$ was in the range from 0.36 to 0.40 eV for both these cases (Fig. 5). As was shown earlier [5], the radiation is associated with the donor–acceptor recombination. The traps exponentially distributed near the conduction band act as donors.

This is confirmed by the wide-band PL spectra for all the cases ([5], the model in Fig. 5, transition 5). We showed earlier that, in the similar $ZnGa_2O_4$ compound activated with Mn and Yb [12], the radiation

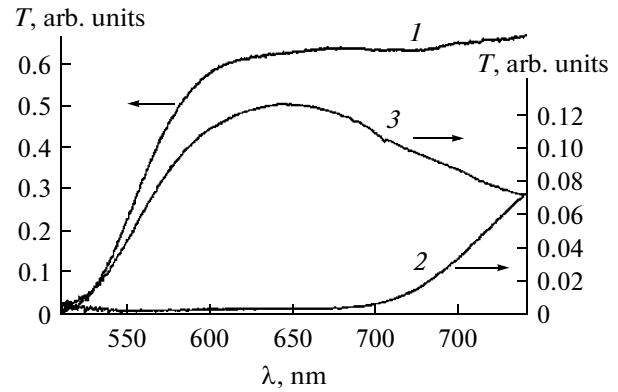

Fig. 5. Optical transmission spectra of $ZnIn_2S_4$:Cu single crystals in natural (*1*) and polarized light. (*2*) Polarization before the sample; (*3*) polarization after the sample. The sample's thickness is $d = 150$ μm.

enhances owing to the doping and exhibits narrow peaks. The PL is induced by the intracenter transitions. Evidently, the results differ from $ZnIn_2S_4$, since a ceramic method of the preparation of the material and different impurities were used; the spinel structure also influences the effect.

Obviously, the $ZnIn_2S_4$ single crystals exhibit a substantial effect of PL anisotropy. As was shown in [13], one can shift the PL spectra or increase their intensity using doping (with Ni, for example). Our technolgical growth method allows one to grow crystals with the alternation of three and one packet polytypes [2]. The variation of the doping and technological parameters also allows one to control the AS, and this is promising for the potential practical application of this effect. There are other possibilities to shift the PL spectra, since a family of related compounds is known, such as $Zn_2In_2S_5$, $Zn_3In_2S_6$, and $Zn_5In_2S_8$ [2, 14]. The strong optical anisotropy owing to the corrugated heterojunction interface is a decisive factor for the development of vertical lasers with polarization stabilized radiation and other devices [15].

The spectra of the optical transmission T of a $ZnIn_2S_4$:Cu platelet crystal with the thickness $d =$ 150 μm are shown in Fig. 5. Curve *1* is a usual transmission curve, which exhibits a sharp edge. The signal starts to increase at 450 nm and reaches ~60% in the wavelength range greater than 600 nm. For curve *2*, the transmission starts to increase at 700 nm and continues until 800 nm. Curve *3* starts to increase at 500 nm, peaks near 625 nm, and slowly decreases until 800 nm. According to the data obtained for the optical transmission in natural light [2] for undoped samples, in the wavelength range of 445–570 nm at room temperature, the absorption coefficient α exponentially depends on the energy $h\nu$. The increase of the optical transmission corresponds to this spectral range. It can be seen from Fig. 5 that, owing to the anisotropy, the polarization substantially influences the effect. One should take into account that doping with copper slightly shifts the absorption spectrum into the long wavelength region.

The results of the measurements of the conductivity along ($\sigma_{\parallel C}$) and perpendicular to the C axis and its temperature dependence in a $ZnIn_2S_4$ three-packet polytype were published in [16]. A significant anisotropy $\sigma_{\parallel C}/\sigma_{\perp C} = 10^{-3}$ at 300 K was found. At $T = 50$ K, this ratio amounted to 10^{-4}. One of the probable interpretations of the anisotropy was associated with the defect composition; this was also confirmed by the electron microscope studies. We can also agree with this point of view.

In the case of $ZnIn_2S_4$, a pronounced anisotropy appears owing to the strong covalent bonds of atoms within the layers and the weak Van der Waals bonds between the layers. The anisotropy of the electrical properties in InSe with a similar layered crystalline structure containing intercalated magnesium also confirms this point of view [17].

Results of research related to the anisotropy of the photoconductivity and PL in $ZnIn_2S_4$ single crystals both undoped and activated with Cu have been published recently [18]. It was shown that the polarization changes the recombination mechanism of the carriers.

Note that $ZnIn_2S_4$ exhibits intensive photo-, cathodo- and X-ray induced luminescence, which were studied in detail for the case when the excitation from one of the faces was performed [5, 11]. The anisotropy of the optical transmission and photoluminescence in this material was measured for the fist time. On the basis of this compound, ZnO/In_2O_3 multilayer structures were prepared, which consist of alternating ultrathin ZnO (0001) and In_2O_3 (111) layers [19]. When the time and temperatures of the technological cycle were reduced, we have also obtained a ZnO/In_2O_3–$ZnIn_2S_4$ composite [20]. Recently, the PL has been studied in a similar $CdGa_2S_4$: Eu compound. The activation energy, the depth of the traps, and the lifetime of the excited states were determined.

CONCLUSIONS

Substantial anisotropy of the optical transmission and PL in single $ZnIn_2S_4$ platelet crystals undoped and doped with copper was shown for the first time. The found peculiarities of the spectra appear due to the exponential increasing of the absorption coefficient and the optical transitions involving donor and acceptor levels. The possibility was shown to shift the PL spectra in a definite wavelength range and to change their intensity by virtue of doping or variation of the growth regimes, which allowed obtaining the alternation of three and one packet polytypes in the crystal. These factors are promising for practical application.

REFERENCES

1. Donika, F.G., Radautsan, S.I., Semiletov, S.A., Kiosse, G.A., and Mustya, I.B., Crystallographic Structure of a Two-Packet Polytype $ZnIn_2S_4$(II), *Kristallografiya*, 1972, vol. 17, no. 13, pp. 663–667.
2. Donika, F.G., Zhitar, V. F., and Radautsan, S.I., *Poluprovodniki v sisteme ZnS–In_2S_3* (Semiconductors in the ZnS–In_2S_3 System), Chisinau: Stiinta, 1980.
3. Arama, E., Ababii, I., Zhitar, V., and Shemyakova, T., UV-Detectors Based on $Zn_xIn_2S_{3+x}$ and Related Compounds, *Proc. Int. Semicond. Conf. CAS 2003*, Sinaia, Romania, vol. 1, 2003, pp. 147–151.
4. Tsiuleanu, I., Simashkevich, A., and Sprincean, A., Formation of Double Electric Layer at $Zn_mIn_2S_{m+3}$ (m = 1, 2, 3) – H_2O (S^{2-}/S_2^{2-}) Interface, *Proc. Int. Semicond. Conf. CAS 2001*, Sinaia, Romania, vol. 2, 2001, pp. 315–319.
5. Zhitar, V., Pavlenko, V., Arama, E., and Shemyakova, T., Recombination Properties of $ZnIn_2S_4$:Cu Single Crystals, *Proc. Int. Semicond. Conf. CAS 2008*, Sinaia, Romania, vol. 2, 2008, pp. 241–244.
6. Bolboshenko, V.Z., Ivanova, G.N., Kalmykova, I., Kasiyan I.A., Nedeoglo, D.D., and Novikiv, B.V., Copper Influence on the Radiation Spectra of ZnSe Crystals, *Fiz. Tekh. Popluprovodn*,, 1990, vol. 24, no. 11, pp. 1929–1933.
7. Kochereshko, V.P., Platonov, A.V., and Gurevich, A.S., Optical Anisotropy of Cubic Crystals, from Bulk to Quantum Dots, *J. Lumin.*, 2007, vol. 125, no. 1–2, pp. 33–46.
8. Capozzi, V. and Montagna, M., Optical Spectroscopy of Extrinsic Recombinations in Gallium Selenide, *Phys. Rev. B*, 1989, vol. 40, pp. 3182–3190.
9. Fan, Y., Schittkowski, T., Bauer, M., Kador, L., Allakhverdiev, K. R., and Salaev, E. Yu., Confocal Photoluminescence Studies on GaSe Single Crystals, *J. Lumin.*, 2002, vol. 98, pp. 7–13.
10. Deneprovskii, V.S., Dobynda, I.I., Zhukov, E.A., and Santalov, A.N., Retardation of the Relaxation over Quantum-Well Energy Levels in CdSe/ZnS Quantum Dots with Increasing Number of Excited Carriers, *Phys. Solid State*, 2007, vol. 49, no. 4, pp. 780–784.
11. Machuga, A., Radu, R., Pintea, V., Arama E., Zhitar V., and Shemyakova T., X-Ray Luminescence in $ZnIn_2S_4$, $CdGa_2S_4$, and $Zn_3In_2S_6$, *Proc. Int. Semicond. Conf. CAS 2007*, Sinaia, Romania, vol. 2, 2007, pp. 377–380.
12. Zhitar, V.F., Muntean S.P., and Pavlenko V.I., Photoluminescence of $ZnGa_2O_4$ Doped with Mn, Yb, Sm, and Tb, *Inorg. Mater.*, 2009, vol. 45, no. 3, pp. 278–280.
13. Zhitar, V.F., Machuga, A.I., and Arama, E.D., Optical Absorption and Photoconductivity of Ni-Doped $ZnIn_2S_4$ Single Crystals, *Inorg. Mater.*, 2002, vol. 38, no. 6, pp. 542–544.
14. Machuga A.I., Zhitar V.F., Muntean S.P., and Arama E.D., Growth and Cathodoluminescence Properties of $Zn_5In_2S_8$ Single Crystals, *Inorg. Mater.*, 2000, vol. 36, no. 12, pp. 1192–1193.
15. Ledentsov, N.N., Litvinov, D., Gerthsen, D., et al., Quantum Wires and Quantum Dots on Corrugated (311) Surfaces: Potential Applications in Optoelectronics, *Proc. SPIE*, vol. 4656, 2002, pp. 33–42.
16. Anagnostopoulos, A.N., Manolikas, C., Papadopoulos, D., and Spyridelis, J., Composition Faults in $ZnIn_2S_4$(III) Layered Crystals and Their Influence on the Anisotropic Conductivity of This Compound, *Phys. Status Solidi A*, 1982, vol. 72, no. 2, pp. 731–736.
17. Kovalyuk, Z., Kushnir, O., Mintyanskii, I., Electrical Properties of Magnesium-Intercalated InSe, *Inorg. Mater.*, 2009, vol. 45, no. 8, pp. 846–850.
18. Zhitar, V.F. and Pavlenko V.I., Anisotropy of Photoconductivity and Luminescence in $ZnIn_2S_4$ and $ZnIn_2S_4$:Cu Single crystals, *Inorg. Mater.*, 2010, vol. 46, no.1, pp. 1–4.
19. Volodina, G., Zhitar, V., Muntean, S., Grabko, D., and Shikimaka. O., Orientation Relationships in ZnO/In_2O_3 Structures, *Inorg. Mater.*, 2007, vol. 43, no. 7, pp. 720–723.
20. Ursaki, V., Tiginyanu, I., Burlaku, A., Zalamai, V., and Zhitar, V,, Luminescence Properties of a ZnO–In_2O_3 Composite, *Phys. Status Solidi C*, 2006, vol. 3, no. 8, pp. 2754–2757.
21. Tagiev, B.G., Abushev, S.A., and Tagiev O.B., Luminescence of $CaGa_2Se_4$:Eu, *J. Appl. Spectrosc.*, 2009, vol. 76, no. 1, pp. 101–106.

ISSN 1068-3755, Surface Engineering and Applied Electrochemistry, 2010, Vol. 46, No. 6, pp. 632–633. © Allerton Press, Inc., 2010.
Original Russian Text © T.A. Man'ko, 2010, published in Elektronnaya Obrabotka Materialov, 2010, No. 6, pp. 112–113.

OPERATING EXPERIENCE

Preparation of Fiberglass Plastic Constructions with the Application of Physical Fields

T. A. Man'ko

Dnepropetrovsk National University, per. Nauchnyi 13, Dnepropetrovsk, 49050 Ukraine
e-mail: naza@ua.fm

Received June 2, 2010

Abstract—The questions of the intensification of technological process are considered at created plastic flows of wares by the search for effective technologies for applying energy to speed up electrons and the possibilities of reducing power expenses.

DOI: 10.3103/S1068375510060165

The existing technology of the preparation of fiberglass plastic articles includes the curing of the formed constructions in thermal chambers with convective heating. When applying phenol-formaldehyde binders to remove the volatile substances released during the polycondensation, vacuum-suction systems are used, and the required density of the materials is obtained at the expense of the performance of curing under pressure. The heat flow during the convective heating goes from the external layers to the internal ones, which hinders the removal of the volatile substances from the internal layers and can lead to the deterioration of the articles' integrity. To exclude the appearance of the thermal stresses and the provision of the fiberglass's plastic integrity, continuous modes of thermochemical curing (TCC) are applied, which extend the cycle of the construction's production.

An urgent problem during the production of fiberglass plastic articles is the intensification of the technological process at the expense of a reduction of the curing time with the improvement of the parameters of the material's quality provided by the existing technology. One of the promising directions of the search for effective technologies is the application of the energy of accelerated particles. Radiation curing (RC) differs from TCC by its high rate, simplicity of operation and control, and the possibility to decrease the power consumption.

The investigations were performed on samples of fiberglass laminate based on silica fabric KT-11 and bakelite varnish LBS-4. The radiation curing of plane prepreg samples was carried out using an ElT-1.5 serial accelerator of electrons. The samples sequentially placed on a transporter were delivered into the zone of the accelerator output port and irradiated by a parallel beam of electrons. The irradiation process's parameters were chosen taking into account the positive experience of the application of accelerated electrons in the production technology of fiberglass plastics based on thermoreactive binders of the polymerization type [1, 2]. During the investigations, the following modes of the RC were applied:

—the electron energy was, MeV	1.0
—the power of the radiation dose was, Mrad/s	2.33
—the absorbed dose was, Mrad	40; 60; 80
—the beam current was, mA	7

The preliminary formation of the fiberglass laminate samples with the shape of rectangular plates with a size of 200 × 200 × 3.5 mm was performed in a mold under a pressure of 0.5–1.5 MPa. The formed blanks were thermostated at a temperature of 353 ± 2 K for 0.5 h. After the rising of the temperature, the pressure was increases up to 0.8–1.0 MPa. Part of the samples was subjected to the following thermal treatment (FTT) for 1–1.5 H at temperatures of 373 and 393 K with the aim to combine the methods of TCC in ovens with additional radiation polymerization [3]. Blanks were cooled to room temperature with free cooling of the oven. To estimate the adhesion strength between the layers of the fiberglass laminate, samples were prepared to determine the shear interlayer deformation. They were superposed "overlapping" strips of prepreg with sizes of 120 × 20 mm with 25 mm overlaping (the thickness of the covering was 0.5 mm). The irradiation time of the samples with 3.5 mm thickness was 108 s, and the samples with 0.5 mm thickness were held in the radiation zone for 60 s. For comparative tests, control samples were prepared whose TCC was performed using a mode including the temperature being increased up to 335 K during 5 h, the smooth transition of the temperatures from 353 to 433 K during 4 h, exposure at 433 K for 1 h, and the following free cooling in the oven.

During the investigations, the tensile strength, the polycondesation degree, and the characteristics of the

fiberglass plastic's thermostability during the heating were determined. The breaking strengths characterizing the binder's curing completeness were defined by the method of extraction of the soluble fraction, and the thermal processes occurring during the fiberglass plastic's heating were studied using the derivatographic method.

The results of the strength tests showed that the decrease of the radiation dose RC to 40 Mrad leads to a decrease of the breaking strength, and the FTT promotes the increase of the breaking loads in comparison with the RC at the dose of 80 Mrad. The preliminary thermal treatment of the prepreg at a temperature of 393 K for 1.5 h increases the strength of the radiation cured fiberglass plastic providing breaking load values close to the values of the breaking strength of the samples prepared by the method of TCC. FTT leads to the partial curing of the binder, whose polycondesation degree is determined by the thermal-time mode, and the following radiation by the flow of accelerated electrons promotes almost complete curing. In the samples prepared with the application of the combined curing (FTT + RC), the polycondensation degree in the fiberglass plastic was 97.2–98.5%. The data of the derivatographic analysis showed that the value of the thermal stability of the fiberglass laminate samples prepared both with the application of the FTT + RC and thermally cured are approximately the same.

As a result of the experimental investigations, it was established that the combined thermoradiation curing by the scheme of FTT + RC decreases the duration of the process by approximately 4 times while providing the retention of the strength characteristics, the thermal stability, and the degree of curing of the fiberglass plastic.

The performed investigations allow one to suggest a preparation technology of thin-walled fiberglass plastic constructions formed by the method of winding including FTT wound to the required thickness of the article with the following additional radiation curing of the rotating construction by a flow of accelerated electrons. To increase the efficiency of the curing process in the scheme of the thermoradiation curing, the replacement of the FTT operation in the ovens is worthy of layer-by-layer sequential curing by infrared heating. The realization of the suggested technology will promote a significant decrease of the preparation cycle of articles made from fiberglass plastics based on phenol-formaldehyde binders.

REFERENCES

1. Omel'chenko, S.I. and Shlapatskaya, V.V., Adhesion of binders to fiberglass fillers during radiation curing and plastics, 1980. no. 8.
2. Tsaplin, A.I. and Bochkarev, S.V., Nonstationary temperature field of a rotating fiberglass cylinder irradiated with parallel electron beam, *Mekh. Comp. Mat.*, 1980, no. 5 [*Mech. Comp. Mat.*, vol. 16, no. 2, pp. 229–232].
3. Kalinchev, V.A. and Makarov, M.S., *Namotannye stekloplastiki* (Wound fiberglass plastics), Moscow: Khimiya, 1986, p. 286.

ISSN 1068-3755, Surface Engineering and Applied Electrochemistry, 2010, Vol. 46, No. 6, pp. 634–645. © Allerton Press, Inc., 2010.
Original Russian Text © B.I. Stavitskii, 2010, published in Elektronnaya Obrabotka Materialov, 2010, No. 6, pp. 114–126.

INFORMATION

Glimpses of the History of Electrospark Machining of Materials (Dedicated to the Centenary of B.R. and N.I. Lazarenko—the Inventors of the Method of Electrospark Machining of Metals, Alloys, and Other Conducting Materials)

B. I. Stavitskii

Candidate of Engineering, Senior Researcher, Lenin Prize Laureate, Chief Designer of Electrospark Equipment for the Electronics Industry, Fryazino, Russia

DOI: 10.3103/S1068375510060177

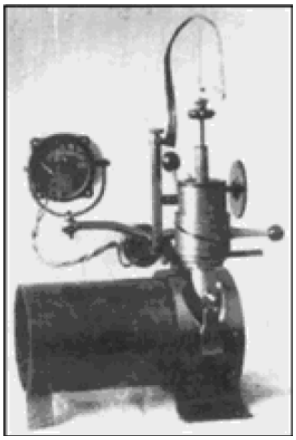

B.R. Lazarenko in the laboratory: a scene from the movie of 1950. Device for removing broken instruments from the shells of Katyusha projectiles (the early 1940s). Author's certificate of invention of the method of machining metals and other conducting materials no. 700010 dated April 3, 1943, issued to N.I. Lazarenko and B.R. Lazarenko.

Fate brought me to Boris Romanovich Lazarenko on March 5, 1949, at Moscow State Aviation Technology Institute (MATI) at the scientific and technical conference of students dedicated to the XI Congress of the All-Union Leninist Young Communist League at the section of electrospark machining, which was headed by State Prize laureate, associate professor, Candidate of Engineering B.R. Lazarenko. Reports at the section were made by diploma students S.P. Milyutin, F.G. Zaremba, A.A. Tabachnikova, and G.Ya. Bernshtein.

I had to study at the institute one more year, i.e., to prepare and defend my graduation paper, the theme of which had not been chosen yet. Therefore, this conference occurred at a good hour for me.

The Laboratory of Electrospark Machining of Materials at the MATI was organized in the late 1940s on the initiative of Boris Romanovich. It was equipped with electrospark installations for various purposes (for cutting metals, broaching, circular grinding, etc.), which were designed mostly on the basis of metal-cutting machines (Fig. 1). In those years, the director of the MATI was Mikhail Andreevich Popov, who actively supported new methods of material machining and created all the conditions for their development.[2]

The training of the first specialists in the domain of electrospark machining of materials began at that time.

Figure 2 depicts B.R. Lazarenko among the graduates of the MATI in the Laboratory of electrospark machining of materials.

In April 1963, Dmitrii Zakharovich Mityashkin, who is standing next to Boris Romanovich in the

[1] This is a continuation; see the beginning in *Surf. Eng. Appl. Electrochem.*, 2010, nos. 1–5.

[2] After his transfer to Bauman State Technical University, the director was A.N. Zhuravlev; the chairman of the Scientific and Technical Society of the students was Doctor of Engineering and Professor Aleksandr Ivanovich Kashirin.

Fig. 1. In the laboratory of electrospark machining of materials of the MATI, 1948.

photo, was awarded the Lenin Prize for the development of new methods of electrochemical production of components of aviation engines.[3]

Tat'yana Ivanovna Makeeva became an active researcher of the Central Research Laboratory for Electrical Machining of Materials (TsNIL-Elektrom); Aleksandr Mikhailovich Belov became the head of the electrospark laboratory of the MATI, which in those years was situated at the corner of Petrovka and the Boulevard Ring (nos. 14–16).[4] Next to him, we can see MATI's graduate Boris Nikolaevich Lyamin, who later, after the transfer of the TsNIL-Elektrom to the Ministry of the Machine Building and Toolmaking Industry of the Soviet Union (Minstankoprom), was appointed its director.

On March 5, 1949 (when I was a five-year student of the MATI (group TM-5-25), I took an interest in the section of electrospark machining at the conference of students and reports of graduate students. I listened to the report of B.R. Lazarenko, who summarized the work of the section, with great attention. The eloquent speech of Boris Romanovich left a lasting impression, and I felt an irresistible desire to partake in the mysteries of this advanced process of material machining, which, according to Boris Romanovich, will govern the near future. This revolutionary process was breaking all the notions of the machinability of materials, and its prospects seemed to be truly infinite. I inexorably decided to devote my forthcoming graduate work and life to this wonderful process.

After awhile, I met Boris Romanovich, and my problem of choosing the theme was solved. He proposed to study the electrospark grinding of hard-to-machine cast magnetic alloys, such as Alnico and Magnico, and agreed to be my supervisor. **As a matter of fact, this meeting with Boris Romanovich Lazarenko determined the rest of my life.**

The theme of my graduation project was to study the electrospark grinding of cast magnets of YuNDK-type alloys. We intended to carry out experimental works in the MATI's electrospark laboratory using a redesigned circular grinding machine (see Fig. 1, photo at the right). However, an unexpected event took place. Boris Romanovich, having no support from the new leadership of the institute (A.N. Zhuravlev) with respect to the organization of training of highly skilled experts with a specialization in the electrospark machining of materials in the aircraft industry (which should be specified in the diploma), was forced to cease the cooperation with the MATI, and the electrospark laboratory was, properly speaking, closed down. The theme of my graduation project became open to question because Boris Romanovich could not officially be my supervisor any longer. The Dean's board suggested that I should choose another theme; I flatly refused. A way out was found by the head of the Department of Electrical Engineering Professor Sergei Aleksandrovich Sinitsyn, who became a formal supervisor of my graduation project; Boris Romanovich kindly invited me to carry out the necessary experimental works in one of the laboratories of the TsNIL-Elektrom and became the real supervisor of my diploma.

The TsNIL-Elektrom was organized on June 16, 1948, according to the USSR Government decree signed by I.V. Stalin, and B.R. Lazarenko was

Fig. 2. In the laboratory of electrospark machining of materials of the MATI. From left to right: T.I. Makeeva, D.Z. Mityashkin, B.R. Lazarenko, A.M. Belov, and B.N. Lyamin, 1948.

[3] I met him at that time in the Kremlin at the ceremony of the presentation of Lenin Prize diplomas.

[4] In the mid-1940s, senior students were actively involved in the repair of this building. Our group mounted scaffolds for the repair of the front face.

Fig. 3. Electrospark circular grinding of magnetic alloys.

appointed its head. At first, it was a part of Research Institute 627 (NII-627) of the Ministry of the Electrotechnical Industry of the Soviet Union.[5]

Therefore, I studied the new method of electrospark machining of metals and electrospark grinding of cast magnetic alloys in one of the laboratories of the TsNIL-Elektrom (Fig. 3).

Here it is pertinent to slightly excurse and to explain the reasons for my entrance into the MATI. I believe in my destiny. I was destined to commit myself to the electrospark machining of materials.

In 1942, when we lived in the Trans-Baikal region (6500 km from Moscow, between Shilka and Nerchinsk) and I was an eight-form pupil of the Kholbon secondary school, it was announced that the pupils who successfully completed first-level education would be admitted to the Krasnodar Military Aviation School. At that time I, like many boys, cherished the dream of becoming a pilot!

However, when I was preparing the documents, an unexpected obstacle occurred: a medical certificate stated that I am physically healthy but suffer from myopia. This broke all my dreams.

Only in 1943, when I was finishing the ninth form of the Saltykovka secondary school in Moscow oblast, some institutes in Moscow announced the admission of ninth-form pupils to preparatory courses. The MATI was among these institutes. Together with Pavel Snegirev, we decided to take this opportunity and entered into these courses. After we finished them, we enrolled in the MATI's Faculty of Technology of Metal Machining in Aircraft Engineering in the fall of 1944. So, I became related to aviation.

Meanwhile, on April 3, 1943, N.I. and B.R. Lazarenko filed application for invention no. 8959/321923 to the People's Commissariat of the Aviation Industry of the Soviet Union. On May 31, 1947, the State Committee of the Soviet Union for the implementation of advanced technology in the national economy registered inventor's certificate no. 70010 for the method of machining metals, alloys, and other conducting materials using spark electric discharges into the State Register of Inventions of the Soviet Union with the priority dated April 3, 1943. The front page of the certificate is shown in the photograph at the head of this work.

APPEARANCE OF NEW METHODS OF THE ELECTROSPARK PRODUCTION OF HIGH-PRECISION PIECES

It is symbolic that, according to the Resolution of the State Defense Committee of the Soviet Union dated July 4, 1943, with the view to providing new developments and large-scale production of radars with modern high-quality vacuum-tube devices, the Electrovacuum Institute (NII-160) with a pilot-production plant was organized on the territory of plant no. 747 of the People's Commissariat of the Electrical Industry (the former factory Radiolampa in the village of Fryazino).

Within 60 years, it developed microwave electronics as the advanced domain of domestic electronics intended to meet the challenges of national security with respect to the design of radioelectronic weapons for various applications.

Among other things, specialists of the NII-160 developed the theoretical foundations of precision electrospark machining; new methods of electrospark producing of high-precision pieces, which were awarded the Lenin Prize in 1963; and the world's first electrospark installations for producing pieces using an electrode wire with a diameter of 10 μm to 0.2 mm, including electrospark machining systems with a microcomputer-based NC control. More than 100 models were designed; more than 3000 units of equipment were produced.

The development of new methods of the electrospark production of high-precision pieces is associated with the names of Mstislav Mikhailovich Fedorov, who was the director of the NII-160 from 1953 to 1961, and B.R. Lazarenko, who was the head of the group of postgraduates of the institute (B.I. Stavitskii, V.L. Kravchenko, E.V. Kholodnov, K.K. Gularyan, and I.I. Sazhin).

Through the efforts of M.M. Fedorov and B.R. Lazarenko (Fig. 4), the middle of 1960–1965 is the stage of formation and effective development of the latest electrospark technologies, which was unfortunately accompanied by constant opposition from malevolent forces.

After I entered the postgraduate courses of the Fryazino NII-160, I had my second meeting with M.M. Fedorov, who was the director of the NII-160 at

[5] In 1953, the TsNIL-Elektrom was separated into an independent organization; in 1955, it was transferred to the system of the USSR Academy of Sciences.

Fig. 4. B.R. Lazarenko and M.M. Fedorov.

that time (together with the supervisor B.R. Lazarenko).[6]

He became interested in the theme of the thesis and the first results of studying the possibility of using the electrospark method in the manufacture of microwave vacuum-tube devices (klystrons, backward-wave tubes (BWTs), and millimeter-wave magnetrons, as well as special receiving amplifier tubes).

Believing in the inexhaustible possibilities of this method, Mstislav Mikhailovich made every endeavor: he organized a laboratory of electrospark machining of materials, allotted more than 500 m^2 for it in the new main building of the institute, equipped it with the facilities necessary for research scientific works, and assigned technicians and engineers to the laboratory.

This decision was timely and coincided with the appearance of the problem of manufacturing high-precision components of microwave devices in the early 1950s.

In early October 1959, director of the institute M.M. Fedorov represented the achievements of the laboratory in the development of electrospark technologies for the high-precision production of components of vacuum-tube devices to Deputy Minister of the Radioelectronics Industry of the Soviet Union Aleksandr Ivanovich Shokin. Shokin, who had been listening to our reports very thoughtfully, took an active interest in the new possibilities of the process, praised the results, recommended extending them to enterprises of the industry, and wished every success in this domain.

Since the inception of the laboratory, which was transformed into the Department of electrospark machining of materials, Mstislav Mikhailovich paid much attention to the development of this new direction, believing in its inexhaustible possibilities in the improvement of the technological process for the manufacture of vacuum-tube devices. It was important that the pilot-production division produced major components of devices under development (klystron grids, slow-wave structures of centimeter and millimeter BWTs, various cathodes of refractory and rare-earth materials, magnets, etc.) for the scientific departments of the institute. This made it possible not only to promptly improve their production technology but also to design new electrospark equipment; it was without equal in the country and even in the world.

The close relationship with the designers of major microwave tubes, on the one hand, stimulated the development of electrospark technologies and, on the other hand, it opened boundless possibilities for designing crucially new devices and improving the ones designed earlier. In the decades prior to the early 1990s, the department actively worked, being at the forefront in the domain of high-precision electrospark machining of materials.

As early as 1953, there were attempts to use the electrospark method to produce components of vacuum-tube devices and process tools in some departments of the institute and in the tool shop of the pilot-production plant.

ORIGINATION OF THE ELECTROSPARK PROCESS OF CUTTING USING A WIRE WITH A DIAMETER OF 20–40 μm

In early 1954, in the NII-160, for the first time in the world, the electrospark method (using a slowly rewinding tungsten wire with a diameter of 0.02–0.04 mm) was applied to cut narrow grooves with a width of 50–60 μm in the end faces of tool electrodes for simultaneous electrospark "broaching" of 95 to 200 square meshes (0.25 × 0.25 mm) with connecting strips between them (30 μm) directly in copper diaphragms of klystrons of radio-relay communication lines (Fig. 5).

[6] The first meeting with M.M. Fedorov (at that time, he was the head of the Fifth General Board of the Ministry of the Communication Industry of the Soviet Union) took place in 1950. I turned to him with a request for his consent to my transfering to the electrospark laboratory that was under formation at the Sergo Ordzhonikidze plant in order to continue working in the domain of electrospark grinding of magnetic alloys.

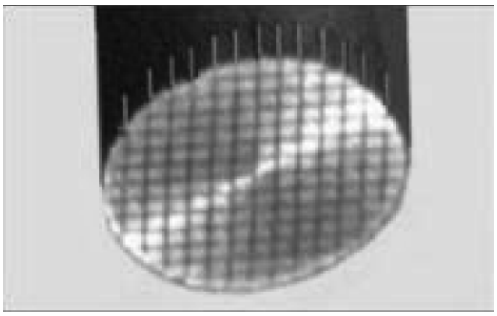

Fig. 5. Electrode with a diameter of 7 mm with 26 grooves with a width of 50 μm cut in its end face to a depth of 2.5 mm.

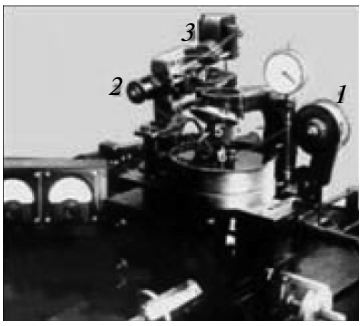

Fig. 6. The world's first electrospark installation with an electrode wire with a diameter of 20–40 μm.

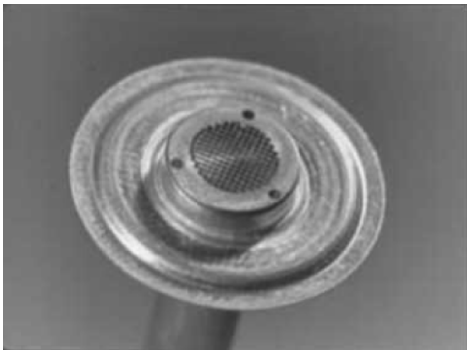

Fig. 7. Grid with a diameter of 7 mm having 152 square meshes with a size of 0.45 × 0.45 mm and connecting strips between them of ≤30 μm prepared in the diaphragm of a klystron.

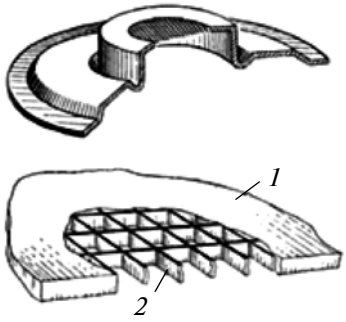

Fig. 8. Klystron diaphragm with a grid made directly in the diaphragm by the electrospark method and a schematic representation of a grid with high connecting strips (at the bottom): (*1*) a fragment of the diaphragm and (*2*) connecting strips of the grid.

Using a VA-3 tungsten wire with a diameter of 30 μm, we can cut grooves with a width of 45–60 μm; a wire with a diameter of 40 μm cuts grooves with a width of 55–70 mm. Wider grooves were cut in two passes with the displacement of the wire by a respective distance.

For this purpose, an experimental electrospark installation for producing pieces using an electrode wire with a diameter of 20–40 μm was designed for the first time in the world (Fig. 6).

Using this electrode, a grid with 152 square meshes with a size of 0.45 × 0.45 mm with connecting strips between them of up to 30 μm was "broached" in a copper klystron diaphragm by the electrospark method (Fig. 7).

Wicker grids of a tungsten wire were replaced with one-piece copper ones; the width of the connecting strips in them is equal to the wire diameter (to preserve the transparency of the grids for electrons) and the height is five- to tenfold. Owning to the increase in the cross section of the connecting strips due to the increase in their height, the higher heat conduction of copper than that of tungsten (approximately twofold), and the production of grids directly in copper diaphragms, the heat removal from the grids is tens times as much (Fig. 8). In turn, this inevitably leads to a significant increase in the lifetime of the devices.

One female worker produced up to 6000 grids per month and at least a hundred copper electrodes for producing grids. Brass LS-59, which usually was widely used as electrodes for electrospark machining, was not suitable for manufacturing components of vacuum-tube devices.

The requirements for grids of reflex klystrons are extremely severe: the allowable spread of the width of the connecting strips must not be higher than its one-tenth (i.e., it must not exceed 0.002 mm)! The spacing of the connecting strips must not have a deviation of more than 0.005 mm, and the roughness of the machined surface of the connecting-strip walls must be ≤0.4 μm.

The electrospark production of one-piece grids became possible owning to the use of special tool electrodes that provided simultaneous broaching of all the grid meshes. They were copper rods with a respective profile; grooves were cut in their end faces to a depth

of 2–2.5 mm (for grids with a thickness of a few tenths of a millimeter); the groove width depended on the size of the connecting strips of the grid, and the spacing was equal to that of the connecting strips (usually 02–0.5 mm). The preparation of these tool electrodes with narrow grooves in the end faces with a width of 0.04–0.05 mm, an error not exceeding 0.002 mm, and a depth of no less than 2–3 mm was a certain technical problem.

Earlier, there was no method for producing these grids with a hundred square meshes (with a size of no more than a few tenths of a millimeter with connecting strips between them of 0.02–0.03 mm) in materials with a thickness of no less than 0.1–0.15 mm. The author joined the work on this problem, because he thought that a possible way to solve it was the application of the simultaneous electrospark broaching of all 100 to 150 meshes with a size of 0.22×0.22 mm using a tool electrode that had grooves with a width of 0.04–0.05 mm cut in its end face to a depth of no less than 1.5–2 mm in two mutually perpendicular directions. For this purpose, we prepared the necessary equipment (based on MBI biological microscopes) and a tool electrode composed of plates of an FeNi42 alloy (Fe–Ni) with a thickness of 20–30 μm and copper gaskets between them whose thickness was less than the grid mesh by a double value of the interelectrode gap.

Using this electrode, we intended to solve the problem of cutting grooves with a width of 0.04–0.05 mm in the electrode end face. However, the FeNi42 alloy exhibits an extremely high electric resistance (almost 40-fold that of copper). Employing one hybrid electrode, using two of its sides, it was possible to prepare only one tool electrode for producing grids due to the severe wear of the plates; grooves were cut to a depth of no more than 0.5 mm. Attempts to use plates made of other materials did not give significantly better results.

In November 1953, the first experimental electrospark installation EPS-2 based on a BMI-1 biological microscope was constructed; it was designed for the production of klystron grids directly in copper diaphragms with the simultaneous electrospark broaching of tens to over hundreds of square meshes with connecting strips of 20–30 μm (Fig. 9).

Figure 10 shows a microscope image of a grid with a diameter of 3 mm in a 0.1-mm-thick copper plate from the first samples. Figure 11 depicts samples of grids produced in a copper plate with a thickness of 0.15 mm. A copper tool electrode (prepared by the electrospark method using a hybrid foil electrode) was moved to a depth of 0.14 mm. The production time of a grid was 2.5 min.[7]

[7] These photographs are published for the first time.

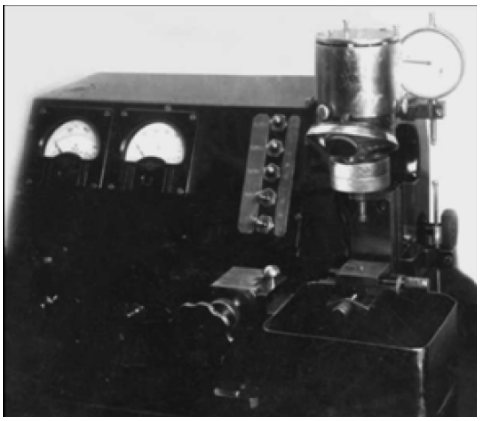

Fig. 9. First EPS-2 electrospark installation with a power supply for producing klystron grids.

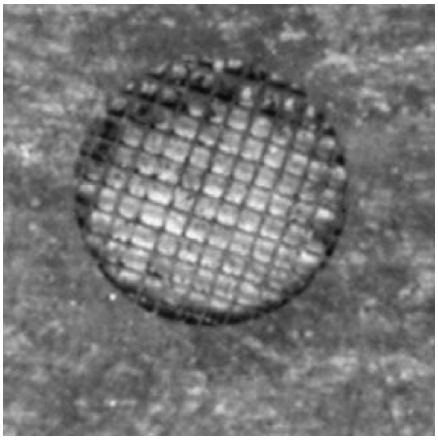

Fig. 10. Grid with a diameter of 3 mm with square meshes "broached" in a 0.1-mm-thick copper plate (from the first samples in a medium of kerosene and without purification from products of erosion).

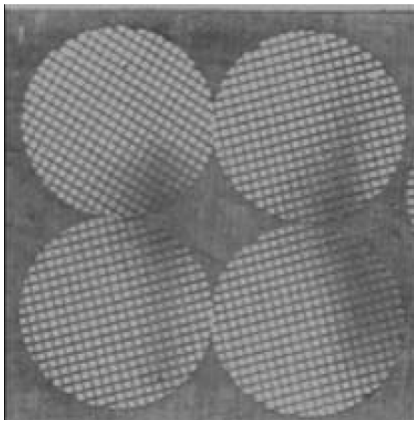

Fig. 11. Samples of grids with a diameter of 5 mm made in a copper plate with a thickness of 0.15 mm.

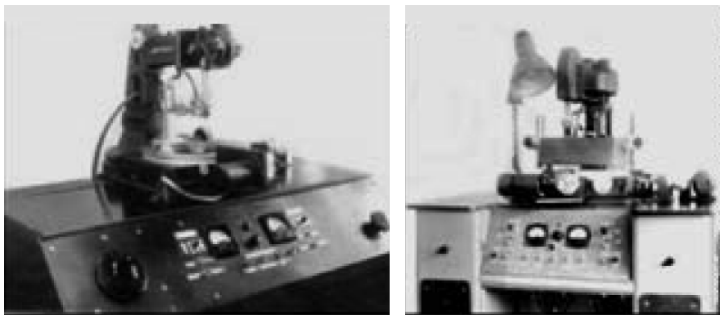

Fig. 12. First experimental installation for producing M-type millimeter-wave device anode blocks (to the left) and an EKU-1 electrospark installation with RC oscillators (to the right).

THE USE OF NEW ELECTROSPARK METHODS FOR PRODUCING MAGNETRONS AND AMPLITRONS

The development of precision electrospark machining of metals was also stimulated by the intensive growth in the production of magnetrons. For the first time, the method was used for producing millimeter-wave magnetron anode blocks (of the vane or "rising sun" types) in the mid-1950s.

The method of copying the profile of a tool electrode and cutting a resonator using a wire with a diameter of 0.03–0.04 mm was applied. In this case, the largest resonator diameter was 5–20 mm, the height was 2–5 mm, and the lamella width was 0.1–0.5 mm. The number of resonators was 10 to 80. The time of the production of these anode blocks using a tool electrode and employing an experimental installation with no software control was 2–6 h with the roughness of the machined surface $R_a \le 0.5$–1.2 μm. At first, the interelectrode medium was lamp kerosene.

In order to solve the emerged problem of producing anode blocks of microwave tubes of the M-type, an EKU-1 electrospark coordinate installation was constructed on the basis of a large BMI toolmaker's microscope in 1954.

Figure 12 shows the first experimental installation for the production of M-type millimeter-wave device anode blocks and an EKU-1 electrospark installation with RC oscillators, which was designed somewhat later.

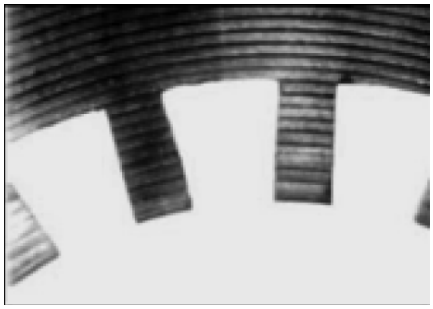

Fig. 13. Fragment of a 4-mm-thick block with ten resonators (D = 6.7 mm and d = 5.4 mm; lamellae: a width of 0.4 mm and a length of 0.82 mm).

These installations were prepared in the mid-1950s on the basis of a BMI-1 microscope (using a microscope base with a measuring revolving table and a support, as well as a stack of second-class gage blocks). A workpiece of a block was placed in a frame that is installed on an arm fixed on the revolving table of the microscope and providing the turning of the table with an accuracy of ±3″. The micron-accurate displacement of the coordinate table was performed using micrometer screws.

Figure 13 shows a fragment of a 4-mm-thick millimeter-wave magnetron anode block with ten resonators prepared using one of these installations.

The first 20-resonator anode block was prepared on February 9, 1956, using a VA-3 tungsten wire with a diameter of 30 μm (Fig. 14a).

Soon after, in 1960, the Ministry of the Electronics Industry of the Soviet Union was constituted, and A.I. Shokin was appointed the Minister.

On December 1, 1960, the Laboratory of Electrospark Machining of Materials of the NII-160 was transformed into a department consisting of laboratories of the technology (E.V. Kholodnov), power supply equipment (V.L. Kravchenko), and automation (K.K. Gularyan); a design bureau (D.K. Dmitrov); and electrospark and mechanical pilot-production divisions (Yu.A. Shevelev).

Therefore, the department of electrospark machining of materials moved to a new production area of the main building; in accordance with the order of the Minister of the Electronics Industry of the Soviet Union, it became the parent enterprise in the domain of electrospark machining of materials.

Anode blocks are the most time-consuming and critical components of modern magnetrons and amplitrons. They are made mainly of oxygen-free copper. Sometimes, their lamellae are reinforced with

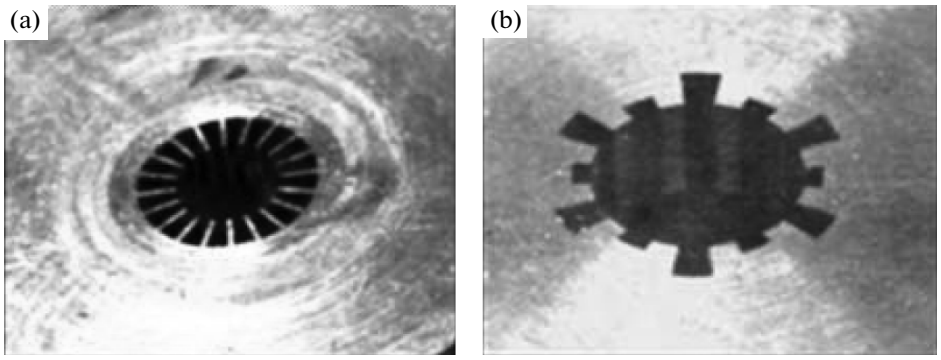

Fig. 14. Examples of small-sized magnetron anode blocks: with (a) 20 and (b) 12 resonators.

refractory metals (tungsten or molybdenum). The sizes of the anode blocks are listed in the table.

The sizes of the anode blocks of magnetrons and amplitrons

Outer diameter D, mm	20–120
Height H, mm	20–135
Inner diameter d, mm	3–35
Number of resonators, pieces	10–80
Resonator diameter D_1, mm	20–80
Resonator lamella height, mm	2–115

For the production of large-sized anodes, special installations were designed: A207.19 with an RC oscillator (Fig. 15), A207.27 (Fig. 16), and A207.33 (Fig. 17) with embedded thyratron pulse generators, which provided for machining materials in water.

The technological process of manufacturing pieces (see Fig. 14) can be carried out using two copper wires with a diameter of 0.1–0.2 mm, which are guided by hard-alloy inserts fixed on a bracket *6* (Fig. 15).

A wire is rewound from coils *1* to coil *2*. Each wire is stretched independently using respective gears. The value of the stretching is usually chosen to be 0.6–0.8 of the maximum breaking tension of the wire.

A workpiece of an anode block is placed on revolving table *3* and can be revolved using servomotor *4*.

The wire winding speed is varied from 0.12 to 1.5 m/min. It is significantly lower, at least by an order of magnitude, than that of foreign electrospark cutting machines that appeared in the mid-1960s.

An important feature of the method was that the implementation of this amazing technology did not require the preparation oyed a thinnest wire whose diameter was smaller than the thickness of the hair of a blonde person. In addition, all these process operations were performed by women.

Unfortunately, these processes were carried out in a medium of lamp kerosene and required the adherence to certain conditions of fire safety and gas removal from the working zone as well as storage and transportation of the manufactured products to the cleaning department in closed vessels with pure kerosene.

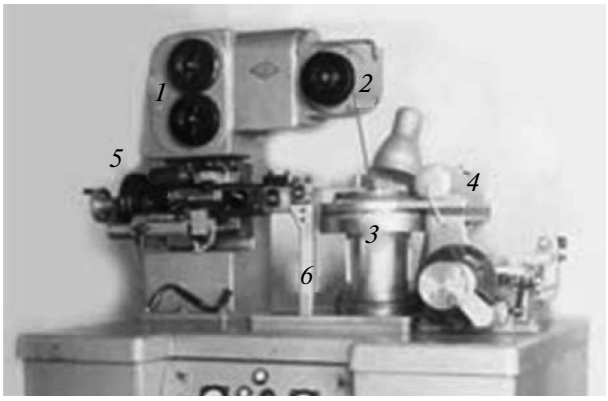

Fig. 15. A207.19 electrospark machine for producing M-type device anode blocks using two wires with an embedded thyratron pulse generator.

Fig. 16. A207.27 electrospark machine for producing M-type device anode blocks using two wires with an embedded thyratron pulse generator.

Fig.17. A207.33 installation with an embedded thyratron pulse generator.

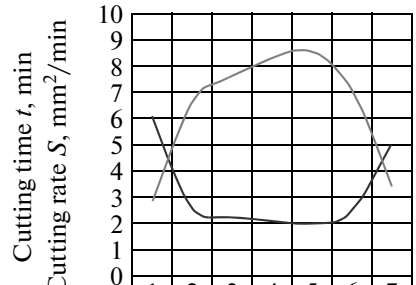

ethanol, %	0	10	25	35	40	50	100
— *t*, min	6	2.6	2.3	2.1	2.0	2.4	5
— *S*	2.8	6.6	7.6	8.3	8.6	7.1	3.4

Fig. 18. Cutting rods of molded tungsten VT-15 with a diameter of 4.67 mm (17 mm^2) using a VA-3 wire with a diameter of 0.03 mm in water with ethanol.

To reveal the possibility of replacing kerosene, which was used for the electrospark machining of components of vacuum-tube devices, with other interelectrode media containing a less amount of hydrocarbons, rods of molded tungsten VT-15 were cut using a VA-3 electrode wire with a diameter of 0.03 mm.

The rate of cutting rods of molded tungsten VT-15 with a diameter of 4.67 mm ($S = 17$ mm^2) using a VA-3 electrode wire with a diameter of 0.03 mm at a wire winding speed of 14 mm/s and a distance between the current-carrying rollers of 17 mm (at $U_0 = 110$ V, $U_1 = 90$ V, and $I_{SC} = 0.45$ A) versus the content of ethanol in water is shown in Fig. 18.

The graphs show that an increase in the content of ethanol in the water up to 10% leads to a 2.36-fold increase in the cutting rate; from 10 to 35%, by a factor of 1.26 more; and, at a content of ethanol in the water of 40%, the cutting rate is maximal; it is 3 times as much as that in water. However, as the content of ethanol in the water increases from 40 to 100%, the cutting rate decreases by a factor of 2.5; it exceeds the rate of cutting in water only by 21%.

Although **the first anode blocks prepared by the electrospark method were small-sized, the possibility of their production marked a new era in the manufacture of components of electronic devices.**

It was clear that it was necessary to concentrate the available resources in one place without dissipating them over several departments of the institute. More than 20 engineers and technicians were transferred to the laboratory along with workers for the newly created pilot production division. We can mention among them K.K. Gularyan, V.L. Kravchenko, I.I. Sazhin, and Yu.A. Shevelev.

M.M. Fedorov organized the exposing of the advances of the NII-160 in the development of new methods for high-precision electrospark producing of components of magnetrons and amplitrons for ground-based radar stations and airborne and shipborne air defense missile systems to chairman of the Military Industrial Complex D.F. Ustinov. He was shown original samples of components and process tools as well as souvenirs demonstrating the possibilities of the new methods and their advantages over traditional techniques of machining of materials.

In the early 1960s, the members of the Laboratory of Power Supply Equipment of Department 62 of the NII-160, which was headed by V.L. Kravchenko, designed experimental thyratron generators with pulse transformers on the basis of thyratrons developed in the NII-160. They made it possible to perform electrospark machining in ordinary water from a public water supply without its purification and deionization. In addition, the electrospark process was carried out not only with water delivery to the working zone but also with the full immersion of the workpieces into the bath without electrochemical processes in the working zone. Moreover, it was possible not only to produce pieces using an electrode wire but also to successfully carry out broaching operations.

Figure 19 depicts the circuit schematic of a thyratron pulse generator with a pulse transformer.

A condenser *C* is charged by a high-voltage power supply *PS* through a throttle *Thr*. After that, a trigger pulse is fed to a thyratron grid *Thyr* from a trigger pulse generator *PG*. The thyratron is triggered, and the condenser *C* is discharged to the primary winding of a pulse transformer *Ptr*. A voltage pulse induced in the secondary winding excites a spark discharge between a tool electrode *TE* and a workpiece WP. A signal from the spark gap is fed to the input of a servo amplifier *SA*; the voltage is fed from its output to the electric motor *EM* of the tool electrode actuator.

Figure 20 shows an experimental installation for producing pieces via copying the profile of the tool electrode with a pulse transformer embedded into a

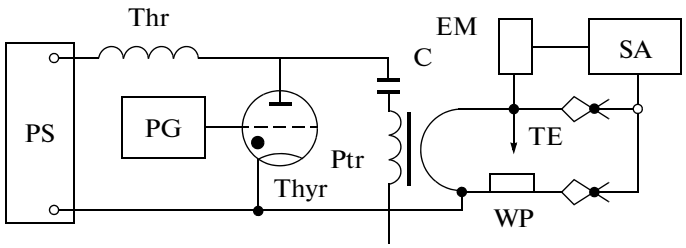

Fig. 19. Circuit schematic of a thyratron pulse generator with a pulse transformer.

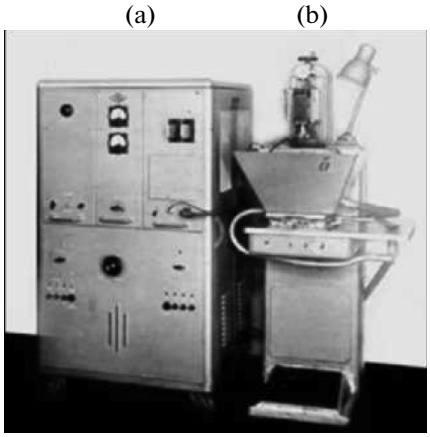

Fig. 20. (a) Thyratron generator and (b) experimental installation for producing pieces via copying the profile of the tool electrode with a pulse transformer embedded into a bath.

Fig. 21. A207.05 two-position installation (c) with one of the heads connected to the ends of the pulse transformer embedded into the generator (a).

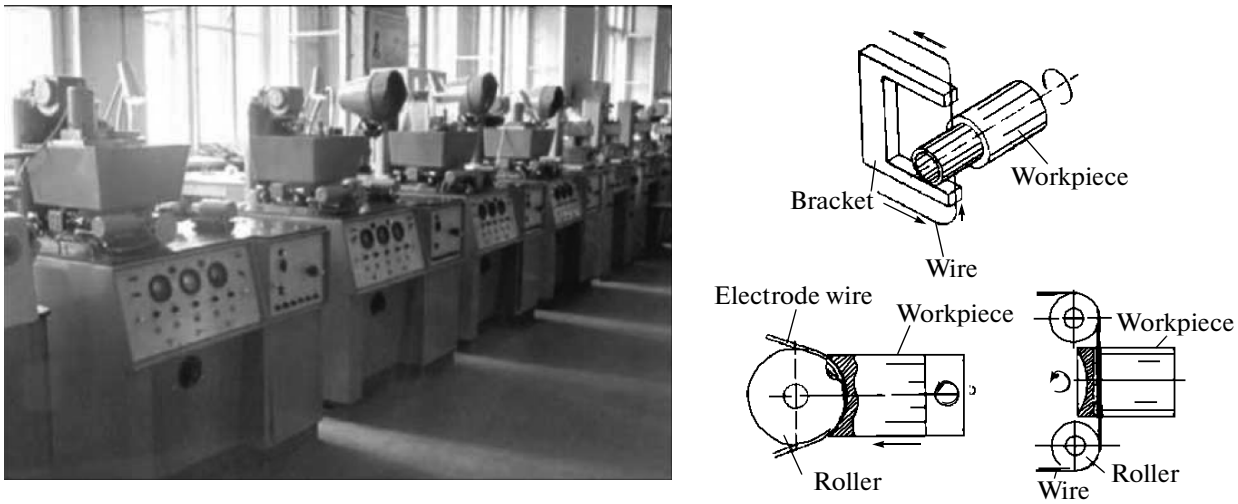

Fig. 22. Group of A207.33 installations with an embedded thyratron pulse generator and replaceable facilities for producing anode blocks, cathodes, and other components of electronic devices.

bath (b). Another pulse transformer is built into the generator frame (a). The ends of its secondary winding are at the top of the generator frame to the right.

Figure 21 depicts an A207.05 two-position installation (c) for producing klystron grids; one of the heads is connected to the ends of a pulse transformer embedded into the generator (a).

A group of A207.33 installations with an embedded thyratron pulse generator is shown in Fig. 22.

A207.33 installations are equipped with a device for producing anode blocks and solids of revolution (e.g., cathodes) by turning using an electrode wire (Figs. 22–23).

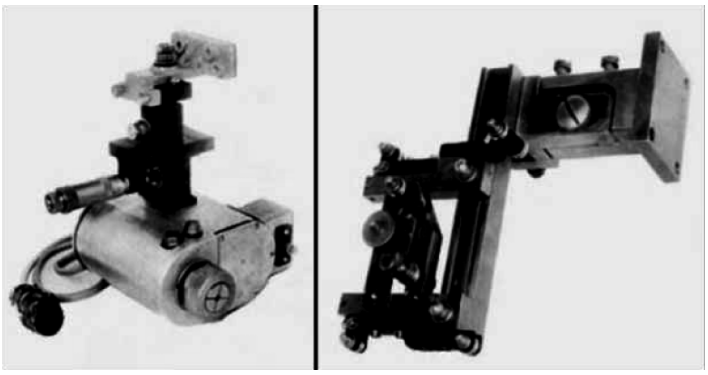

Fig. 23. Replaceable facilities for A207.33: for positioning workpieces during turning (to the left) and for guiding the electrode wire (to the right).

Fig. 24. Salyut amplitron anode block. Lamellae: a width of 4 mm and a height of 12 mm. D = 62 mm and d = 14 mm. The accuracy of manufacturing the components is 0.01 mm. The wastes are shown on the right-hand side.

Fig. 25. Amplitron anode block: a height of 50 mm, D = 62 mm, and d = 14 mm. The lamellae are 4 mm. Seven resonators are cut.

Large-sized anode blocks of magnetrons and amplitrons that were produced using two wires are shown in Figs. 24–26.

The photo of a Salyut anode block with wastes of removed material lying next to it is convincing evidence of the fact that, in the generation of the geometry using an electrode wire, an insignificant part of the metal is removed in the form of "cuttings," which, immediately melting, are discharged from the interelectrode space in the form of micron-sized beads.

Only seven resonators are cut in the nine-resonator amplitron block (an analog to the Salyut block) that is depicted in Fig. 25. The photo shows parallel grooves with a width of 0.12 mm, which were cut using two wires. After the sequential cutting of nine pairs of parallel grooves using two wires (the formation of nine lamellae), one of the wires breaks. After that, nine resonators are sequentially cut using one wire due to turning the table with the removal of wastes.

The use of two wires for cutting lamellae provides their absolute identity, the highest precision of the width, and the best quality of the machined surface in addition to the extremely simple process of machining. The accuracy of manufacturing the components is 0.01 mm, and the angle's accuracy is ±6'; R_a = 0.8–1.0 μm.

Figure 26 shows the largest ten-resonator anode block of the vane type. The lamella width is 4 mm, its height is 82 mm, d = 24 mm, and D = 68 mm. The angle's accuracy is ±6'; the machined surface's roughness R_a = 0.8–1.0 μm.

Figure 27 represents an Anakonda magnetron anode block with ten resonators; its body is made of MB copper with an insert of molybdenum. The inner diameter of the resonators d = 6 mm, and the outer diameter D = 10 mm; the lamella's height is 10 mm, and its width is 1.5 mm.

Figure 28 shows a Romashka original anode block with 12 resonators in the form of chamomile petals. The inner diameter is 0.5 mm, the maximum diameter is 2.5 mm, and the outer diameter of the body is 20 mm.

Intricate-shaped open-work pieces of small-sized components of M-type electronic devices for prefabricated blocks with a diameter of 20 mm are depicted in Fig. 29. These pieces were used to assemble anode blocks of devices.

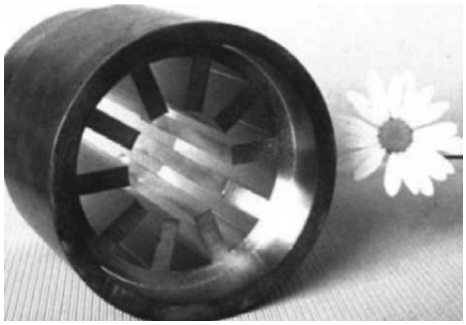

Fig. 26. Anode block. Lamellae: a width of 4 mm, a height of 82 mm, $d = 24$ mm, and $D = 68$ mm.

Fig. 27. Anakonda anode block with an insert of molybdenum.

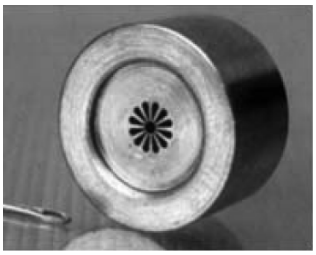

Fig. 28. Romashka anode block with 12 resonators: $d =$ 0.5 mm, $D = 2.5$ mm, and $h = 6$ mm.

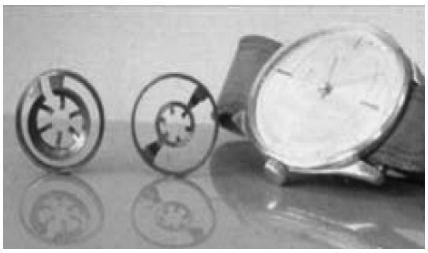

Fig. 29. Components of prefabricated blocks with $D =$ 20 mm.

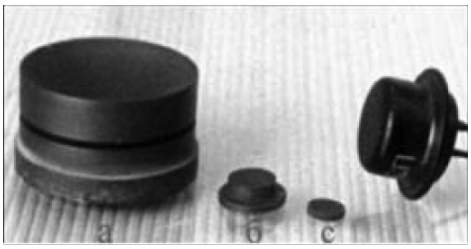

Fig. 30. Cathodes of lanthanum boride LaB_6: (a) a diameter of 16 mm, the end face has a spherical recess to 4.5 mm, and $R = 20$ mm; (b) a diameter of 5 mm, $h = 2.5$ mm, and $R = 10$ mm; and (c) a diameter of 3 mm, $h = 1.5$ mm, and $R = 6$ mm.

Figure 30, by way of illustration, shows photographs of cathodes of lanthanum boride.

Great difficulties arose in the manufacture of products with cathodes of such materials as lanthanum boride (LaB_6) and other rare-earth materials that are hard-to-machine by traditional methods. The electrospark machining using a moving electrode wire and special equipment proved to be the most efficient for their production. The electrospark processes of the generation of geometry using an electrode wire were applied: the turning of cylindrical surfaces, the formation of concave spherical end faces using a wire guided by a roller with an appropriate diameter, and the cutting off of the prepared cathode from the work piece.